



UNIVERSIDADE ESTADUAL DE CAMPINAS
Faculdade de Engenharia Elétrica e de Computação

Ruby Stella Bravo Ospina

**Parameter Estimation in Space-Division
Multiplexing Transmission Systems Based on
Digital Signal Processing
Estimação de Parâmetros em Sistemas de
Transmissão com Multiplexação Por Divisão
Espacial Baseada em Processamento Digital de
Sinais**

Campinas

2023

Ruby Stella Bravo Ospina

**Parameter Estimation in Space-Division Multiplexing
Transmission Systems Based on Digital Signal Processing**
**Estimação de Parâmetros em Sistemas de Transmissão
com Multiplexação Por Divisão Espacial Baseada em
Processamento Digital de Sinais**

Thesis presented to the School of Electrical and Computer Engineering of the University of Campinas in partial fulfillment of the requirements for the degree of Doctor in Electrical Engineering, in the area of Telecommunications and Telematics.

Tese apresentada à Faculdade de Engenharia Elétrica e de Computação da Universidade Estadual de Campinas como parte dos requisitos exigidos para a obtenção do título de Doutora em Engenharia Elétrica, na Área de Telecomunicações e Telemática.

Supervisor: Prof. Dr. Darli Augusto de Arruda Mello

Este exemplar corresponde à versão final da tese defendida pela aluna Ruby Stella Bravo Ospina, e orientada pelo Prof. Dr. Darli Augusto de Arruda Mello.

Campinas

2023

Ficha catalográfica
Universidade Estadual de Campinas
Biblioteca da Área de Engenharia e Arquitetura
Elizangela Aparecida dos Santos Souza - CRB 8/8098

Os6p Ospina, Ruby Stella Bravo, 1992-
Parameter estimation in space-division multiplexing transmission systems based on digital signal processing / Ruby Stella Bravo Ospina. – Campinas, SP : [s.n.], 2023.

Orientador: Darli Augusto de Arruda Mello.
Tese (doutorado) – Universidade Estadual de Campinas, Faculdade de Engenharia Elétrica e de Computação.

1. Multiplexação por divisão espacial. 2. Processamento digital de sinais. I. Mello, Darli Augusto de Arruda, 1976-. II. Universidade Estadual de Campinas. Faculdade de Engenharia Elétrica e de Computação. III. Título.

Informações Complementares

Título em outro idioma: Estimação de parâmetros em sistemas de transmissão com multiplexação por divisão espacial baseada em processamento digital de sinais

Palavras-chave em inglês:

Space-division multiplexing

Digital signal processing

Área de concentração: Telecomunicações e Telemática

Titulação: Doutora em Engenharia Elétrica

Banca examinadora:

Darli Augusto de Arruda Mello [Orientador]

Carmelo José Albanez Bastos Filho

Jacklyn Dias Reis

Hugo Enrique Hernandez Figueroa

Renato da Rocha Lopes

Data de defesa: 04-04-2023

Programa de Pós-Graduação: Engenharia Elétrica

Identificação e informações acadêmicas do(a) aluno(a)

- ORCID do autor: <https://orcid.org/0000-0003-0980-8519>

- Currículo Lattes do autor: <http://lattes.cnpq.br/7927299490404963>

COMISSÃO JULGADORA - TESE DE DOUTORADO

Candidato: Ruby Stella Bravo Ospina, RA: 163653

Data da Defesa: 04 de abril de 2023

Título da Tese: "Parameter Estimation in Space-Division Multiplexing Transmission Systems Based on Digital Signal Processing (Estimação de Parâmetros em Sistemas de Transmissão com Multiplexação Por Divisão Espacial Baseada em Processamento Digital de Sinais)".

Membros:

Prof. Dr. Darli Augusto de Arruda Mello
Prof. Dr. Carmelo José Albanez Bastos Filho
Dr. Jacklyn Dias Reis
Prof. Dr. Hugo Enrique Hernandez Figueroa
Prof. Dr. Renato da Rocha Lopes

A ata de defesa, com as respectivas assinaturas dos membros da Comissão Julgadora, encontra-se no SIGA (Sistema de Fluxo de Dissertação/Tese) e na Secretaria de Pós-Graduação da Faculdade de Engenharia Elétrica e de Computação.

To my parents Luis and Rubiela.

To my sisters Claudia, Diana, and Ana.

To my nephews Jose, Felipe, Samuel, and Santiago.

To my niece Luciana.

To Daniela, my friends, brothers in law, and relatives.

Acknowledgements

I thank God above all things.

I am deeply grateful to my supervisor, Professor Darli Mello, for his invaluable support and collaboration throughout my Doctorate. I thank him for his strong guidance and motivation whenever it was necessary.

I thank my parents, Luis and Rubiela, for their constant encouragement and love. I thank my sisters, Claudia, Diana, and Ana, for their advice and support in difficult times. I thank my nephews, José, Felipe, Santiago, Samuel, and my niece, Luciana, for their inspiration and motivation. I am grateful to my brothers-in-law, Iván and Andrés, for their camaraderie.

I thank my godmother Milta for her endless help since childhood and all my relatives who contributed somehow to this achievement.

I thank Daniela for her infinite understanding, patience, love, company, and support during these years.

I thank my friends Claudio, William, Diana, Felipe, Oscar, Augusto, Juan Pablo, Carlos, and Gabriela for the countless moments of happiness and fun that helped lighten the burdens. I thank my colleagues from ComLab, Fábio, Lailson, Kayol, Jonathan, Alaelson, Carlos, Thiago, Robson, Lucas, Humberto, Iliana, Igor, and Veruska for their kind encouragement and fellowship.

I am grateful to Professor Dalton for his rich academic and emotional advice.

I sincerely thank the State University of Campinas for all the resources offered during these years. I thank the Eindhoven University of Technology for hosting me during my research internship, especially Professor Chigo and my colleague Menno. I thank the NICT for the essential support to carry out my training stay. I give special thanks to Georg, Ben, Ruben, and Mr. Furukawa for their collaboration.

I give special thanks to Professor Hugo Figueroa for his support and advice.

I greatly appreciate each person who contributed to this magnificent achievement and motivated me to reach the goal.

Grants 2017/25537-8, 2018/25414-6, 2018/14026-5, 2015/24341-7, and 2015/24517-8, São Paulo Research Foundation (FAPESP).

Abstract

Coupled space division multiplexing (SDM) transmission is subject to random power coupling that demands multiple-input multiple-output (MIMO) equalizers to compensate for any crosstalk between multiple propagation paths. The multiplicity of transmission paths also introduces modal dispersion, an effect that also needs to be addressed at the receiver, increasing its complexity. Moreover, due to in-line components, SDM transmission experiences an imbalance of losses and gains among different transmission paths, a perturbation known as mode-dependent loss (MDL) and mode-dependent gain (MDG). Along with amplification noise, MDL and MDG reduce the channel capacity and represent a fundamental limit for the deployment of long-haul SDM systems. In SDM systems, channel parameter estimation is essential for system design, performance evaluation, and troubleshooting. Therefore, in this thesis, techniques for channel parameter estimation in the scope of SDM systems are investigated. We show that conventional methods for MDG and signal-to-noise ratio (SNR) estimation present critical performance limitations at certain operation regimes. One improved technique for MDG estimation using a correction factor, and one novel technique for MDG and SNR estimation based on multilayer perceptron artificial neural networks (ANNs) are proposed. The results show that the correction factor technique substantially improves the MDG estimation accuracy in a simulated 3-mode transmission over 2,500 km and in an experimental 3-mode transmission over fiber links of 32.5-m and 73-km length. Similarly, the results show that the ANN-based MDG and SNR estimator outperforms the conventional methods presenting a suitable performance over all the regimes of MDG and SNR evaluated in an experimental 3-mode transmission setup over a 73-km fiber link. In addition, the ANN-based MDG and SNR estimator presents consistent performance when applied to a case study of an experimental long-distance transmission of 6 spatial modes. We also evaluate three scanning-based methods for estimating the accumulated chromatic dispersion (CD) in a simulated 3-mode SDM transmission setup. The results show that scanning methods are very susceptible to crosstalk and that only the delay-tap sampling technique can be applied to SDM systems with very high accuracy, even for high crosstalk levels. Finally, as a lateral topic, the potential reduction of the MIMO equalizer complexity in an experimental 55-mode fiber transmission with weak mode-group coupling is studied. The results show that a 21.5% complexity reduction can be achieved with only a 4.9% data rate loss by selective finite impulse response (FIR) filter deactivation.

Keywords: space division multiplexing, multiple-input multiple-output, mode-dependent loss, mode-dependent gain, channel parameter estimation, digital signal processing, artificial neural network.

Resumo

A transmissão de sinais com multiplexação por divisão espacial (*space-division multiplexing* - SDM) acoplada está sujeita ao acoplamento aleatório de potência, requerendo o uso de equalizadores de múltiplas entradas e múltiplas saídas (*multiple-input multiple-output* - MIMO) para compensar qualquer crosstalk entre os diversos caminhos de propagação. A multiplicidade de caminhos de transmissão também introduz dispersão modal, efeito que precisa ser compensado no receptor, aumentando sua complexidade computacional. Além disso, devido aos componentes ópticos na linha, a transmissão SDM experimenta um desequilíbrio das perdas e ganhos entre os diferentes caminhos de transmissão, uma perturbação conhecida como perda dependente do modo (*mode-dependent loss* - MDL) e ganho dependente do modo (*mode-dependent gain* - MDG). Junto com o ruído de amplificação, a MDL e a MDG reduzem a capacidade do canal e representam um limite fundamental para a implantação de sistemas SDM de longa distância. Em sistemas SDM, a estimação de parâmetros de canal é essencial para o planejamento do sistema, avaliação de desempenho e solução de problemas. Portanto, nesta tese, técnicas de estimação de parâmetros de canal no âmbito de sistemas SDM são investigadas. Mostra-se que os métodos convencionais de estimação de MDG e da relação sinal a ruído (*signal-to-noise ratio* - SNR) apresentam limitações críticas de desempenho em determinados regimes de operação. Uma técnica melhorada para a estimação de MDG que utiliza um fator de correção analítico e uma nova técnica para a estimação de MDG e SNR baseada em redes neurais artificiais (*artificial neural networks* - ANNs) do tipo perceptron multicamadas são propostas. Os resultados mostram que a técnica de fator de correção melhora substancialmente a precisão da estimação de MDG em uma transmissão simulada de 3 modos ao longo de uma fibra de 2.500 km e em uma transmissão experimental de 3 modos sobre enlaces de fibra de 32,5 metros e 73 km. Da mesma forma, os resultados mostram que o estimador de MDG e SNR baseado em ANNs supera os métodos convencionais apresentando um desempenho adequado em todos os regimes de MDG e SNR avaliados em um setup de transmissão experimental de 3 modos sobre um enlace de fibra de 73 km. Adicionalmente, o estimador de MDG e SNR baseado em ANN apresenta um desempenho consistente quando aplicado a um caso de estudo de uma transmissão experimental de longa distância de 6 modos espaciais. Avaliam-se também três métodos baseados em varredura para a estimação da dispersão cromática acumulada (*chromatic dispersion* - CD) em um setup de transmissão SDM simulado de 3 modos. Os resultados mostram que os métodos de varredura são muito suscetíveis ao crosstalk e que apenas a técnica *delay tap sampling* pode ser aplicada a sistemas SDM com precisão satisfatória, mesmo para altos níveis de crosstalk. Finalmente, como tópico lateral, é estudada a redução potencial da complexidade do equalizador MIMO em uma transmissão experimental sobre uma fibra

de 55 modos com acoplamento fraco entre grupos modais. Os resultados mostram que uma redução de complexidade de 21,5% pode ser alcançada com uma perda de taxa de dados de apenas 4,9% por meio da desativação seletiva dos filtros de resposta ao impulso finita (*finite impulse response* - FIR).

Palavras chave: multiplexação por divisão espacial, múltiplas entradas e múltiplas saídas, perda dependente do modo, ganho dependente do modo, estimação de parâmetros de canal, processamento digital de sinais, rede neural artificial.

List of Figures

Figure 2.1 – Block diagram of an SDM/WDM transmission setup. Transmission of M_p spatial channels. Accounting by the polarization states, $2M_p$ orthogonal signals propagates through the fiber in each wavelength channel.	40
Figure 2.2 – quadrature amplitude modulation (QAM) digital constellations. (a) Square 4-QAM, 16-QAM, 64-QAM, and 256-QAM constellations. (b) Non-square 32-QAM constellation.	41
Figure 2.3 – Nyquist pulse with $T = 1$. (a) Impulse response. (b) Frequency response.	43
Figure 2.4 – Raised cosine filter with $T = 1$ for several values of roll-off factor. (a) Frequency response. (b) Impulse response.	43
Figure 2.5 – Atomic processes involved in laser light emission: absorption, spontaneous emission and stimulated emission.	45
Figure 2.6 – Mach-Zehnder modulator (a) Schematic diagram. (a) Output power as a function of the applied voltage.	46
Figure 2.7 – In-phase and Quadrature modulator (a) Schematic diagram. (a) Polarization multiplexing configuration. PBS and PBC stand for polarization beam splitter and polarization beam combiner, respectively.	47
Figure 2.8 – Illustrative example of a photonic lantern. Adapted from (RICHARDSON, 2016).	47
Figure 2.9 – Optical channel. (a) Cross section of an optical fiber. (b) Refractive index profile of a step-index fiber. (c) Refractive index profile of a graded-index fiber.	48
Figure 2.10–Modal map for a step-index fiber with linearly polarized modes.	53
Figure 2.11–Mode profiles of the first 15 LP modes.	54
Figure 2.12–Attenuation profile of a standard single-mode fiber (SSMF) as a function of the frequency bands (MELLO; BARBOSA, 2021).	55
Figure 2.13–Polarization mode dispersion. The transmitted pulse is broadened after propagation.	57
Figure 2.14–Dispersion map of SSMF. The total dispersion is the sum of material dispersion and waveguide dispersion.	59
Figure 2.15–ISI resulting from mode coupling and modal dispersion.	61
Figure 2.16–Erbium-doped fiber amplifier. (a) Architecture. (b) Energy levels diagram of the Erbium ions (Er^{3+}). Adapted from (RAMASWAMI <i>et al.</i> , 2010).	63

Figure 2.17–SDM amplification schemes. (a) Parallel SMF amplifiers. (b) Fully integrated SDM amplifier. (c) Core-pumping MC EDF amplifier. (d) Cladding-pumping MC EDF amplifier (JUNG <i>et al.</i> , 2020).	65
Figure 2.18–OSNR and SNR as a function of the length for $R_s = 30$ GBd, $P_{\text{Total}} = 0$ dBm, $\alpha = 0.2$ [dB/km], 150 spans of $L_s = 60$ km, and per-span amplifier with NF = 5 dB.	68
Figure 2.19–Theoretical curves of BER as a function of the SNR for QPSK, 16-QAM, and 64-QAM.	69
Figure 2.20–Fibers for SDM. (a) Bundle of single-mode fibers. (b) Multi-mode fiber. (c) Few-mode fiber. (d) Coupled multi-core fiber. (e) Uncoupled multi-core fiber. (f) Few-mode multi-core fiber.	70
Figure 2.21–Block diagram of a front-end with balanced detection for a single polarization system.	73
Figure 2.22–Block diagram of a front-end with balanced detection for a dual polarization system.	76
Figure 3.1 – DSP chain encompassing all the blocks required to compensate for the transmission impairments introduced by the SDM system.	78
Figure 3.2 – Multiple-input multiple-output model of an SDM system with $2M_p$ transmitters and $2M_p$ receivers. $s_j(t)$ is the transmitted signal by the j th transmitter, $r_i(t)$ is the received signal by the i th receiver, and \mathbf{H} represents the propagation channel.	79
Figure 3.3 – Constellations (a) 4-QAM without QI. (b) 4-QAM with QI. (c) 16-QAM without QI. (d) 16-QAM with QI.	81
Figure 3.4 – GSOP orthogonalization for QI imbalance compensation. From two non-orthogonal components of the received signal denoted by $I'[k]$ and $Q'[k]$, the GSOP results in a new pair of orthonormal components $I[k]$ and $Q[k]$.	82
Figure 3.5 – Block diagram of frequency recovery based on spectral analysis. M th-order power algorithm.	83
Figure 3.6 – 12×12 time-domain MIMO equalizer. Each vector $\mathbf{w}_{i,j}$ indicates the coefficients of the filter corresponding to input i and output j .	85
Figure 3.7 – 2×2 frequency-domain MIMO equalizer. S/P stands for serial to parallel. IFFT is the inverse fast Fourier transform (FFT). Adapted from (FARUK; KIKUCHI, 2011). In the scope of this thesis, the this structure was generalized to operate as a $2M_p \times 2M_p$ MIMO equalizer.	86

Figure 3.8 – Diagram of fully supervised adaptive equalization. \mathbf{R} , \mathbf{S} and $\hat{\mathbf{S}}$ are the received matrix, transmitted matrix and equalized matrix, respectively. \mathbf{W}_{MMSE} is the weight matrix of the MIMO equalizer. (a) Equalization independent of carrier phase recovery. (b) Equalization intertwined with a carrier phase recovery loop (MORI <i>et al.</i> , 2012).	88
Figure 3.9 – Complexity in terms of complex multiplications per output bit as a function of the equalizer length for different number of spatial modes and $M = 16$. (a) TDE. (b) FDE.	91
Figure 3.10–Constellation rotation due to Wiener phase noise for 10,000 and 30,000 symbol sequences.	92
Figure 3.11–Block diagram of the BPS algorithm.	93
Figure 3.12–Simulation setup of a coupled long-haul 3-mode transmission. The transmitter generates 16-QAM symbols at 30 GBd. At reception, TDE 6×6 MIMO equalization is carried out by 36 finite impulse response filters with 800 taps each, updated by a fully supervised least mean squares (LMS) algorithm.	94
Figure 3.13–MIMO equalizer convergence curves. (a) Normalized error as a function of the output symbol. (b) Amplitude of the output symbol as a function of the output symbol.	95
Figure 3.14–Impulse responses magnitude obtained from the 6×6 TDE MIMO after 5,000 km transmission.	96
Figure 3.15–BER as a function of the linewidth of the transmitter and LO lasers.	97
Figure 3.16–Performance curves. (a) BER vs SNR. (b) BER vs transmission distance.	97
Figure 3.17–Experimental long-haul 6-mode transmission setup with recirculating loop of 59 km. 12 spatial and polarization modes are supported, each one carry 15 wavelength-division multiplexing (WDM) channels centered around 1550 nm. Triangles represent erbium-doped fiber amplifiers (EDFAs) (WEERDENBURG <i>et al.</i> , 2018).	98
Figure 3.18–Magnitude average impulse response after 177 km (3 loops) and 590 km (10 loops) transmission got from the FDE MIMO.	99
Figure 3.19–Magnitude of the impulse responses after 177 km. Linear coupling between the LP_{01} mode and LP_{02} mode.	100
Figure 3.20–Performance curves of the experimental long-haul 6-mode transmission. (A) AIR per polarization vs launch power per mode. (b) BER vs launch power per mode.	101
Figure 3.21–(a) Averaged SNR computed after MIMO equalization as a function of the launch power per mode. (b) σ_{mdg} estimated by the conventional method as a function of the launch power per mode.	101

Figure 4.1 – In-line coupling and MDG components.	104
Figure 4.2 – Semi-analytical curves. (a) MDG capacity, C_{mdg} , as a function of σ_{mdg} . (b) Normalized capacity, C_{mdg}/C , as a function of σ_{mdg} . (c) Effective SNR loss, Δ_{mdg} , as a function of σ_{mdg} . The curves are generated using the multisection model of Section 4.2 for $2M_p = 6$	106
Figure 4.3 – Eigenvalues λ_i^2 as a function of the frequency bin for (a) Low MDG. (b) High MDG.	109
Figure 4.4 – Accumulated MDG as a function of the number of spans. The $\text{MDG}_{\text{pk-pk}}$ metric is shown at the left y-axis. The σ_{mdg} metric is shown at the right y-axis. Dashed lines show interpolated curves.	110
Figure 4.5 – (a) Eigenvalues estimated by digital signal processing (DSP), $\lambda_{i,\text{MMSE}}^2$, as a function of the actual eigenvalues λ_i^2 for different levels of SNR. (b) Distribution of the 12 eigenvalues of a 6 spatial modes channel at two different levels of MDG and SNR.	112
Figure 4.6 – Evolution of the maximum and minimum actual eigenvalues, λ_i^2 , and DSP-estimated eigenvalues, λ_{MMSE}^2 , and λ_{LMS}^2 , with the number of sections. (a) At low SNR = 10 dB. (b) At medium SNR = 17 dB. (c) At high SNR = 25 dB.	113
Figure 4.7 – (a) Semi-analytical estimation error in dB, computed as the difference between the actual MDG standard deviation, σ_{mdg} , and the σ_{mdg} estimated using $\mathbf{W}_{\text{MMSE}}^{-1}$ computed from \mathbf{H} . (b) Simulated MDG standard deviation σ_{mdg} estimated from the equalizer coefficients, $\mathbf{W}_{\text{MMSE}}^{-1}$, versus actual σ_{mdg} , at different SNRs.	114
Figure 4.8 – Simulation setup of coupled long-haul 6-mode transmission. The transmitter generates 16-QAM symbols at 30 GBd. At reception, 12×12 MIMO equalization is carried out by 144 finite impulse response filters with 100 taps each, updated by a fully supervised least mean squares (LMS) algorithm. MDG estimation is performed by DSP based on the MIMO MMSE transfer function.	115
Figure 4.9 – SNR estimation error in dB, computed as the difference between the actual SNR in dB and the SNR estimated using Eq. (4.24) in dB. . . .	117
Figure 5.1 – Correction factor technique. (a) Semi-analytical estimation error, computed as the difference in dB between the actual MDG standard deviation, σ_{mdg} in dB, and the σ_{mdg} estimated using $\mathbf{W}_{\text{MMSE}}^{-1}$ computed from \mathbf{H} , also in dB. (b) Simulated MDG standard deviation, σ_{mdg} , estimated from the equalizer coefficients, $\mathbf{W}_{\text{MMSE}}^{-1}$, versus actual σ_{mdg} , at different SNRs.	120

Figure 5.2 – Power transfer matrices of two photonic lanterns in back-to-back with a section of 32.5 meter MMF between them. (a) Experimental setup built at the High-Capacity Transmission Laboratory of the Eindhoven University of Technology. (b) Transmission with PL 2 at the transmitter and PL 1 at the receiver. (c) Transmission with PL 1 at the transmitter and PL 2 at the receiver.	121
Figure 5.3 – Experimental setup for MDG emulation in a 3-mode transmission system with polarization multiplexing. The launch powers of the 3 modes (LP ₀₁ , LP _{11a} and LP _{11b}) are independently controlled through VOAs before spatial multiplexing performed by a photonic lantern (PL). At the receiver, the signals are demultiplexed by a second PL, digitized and processed. MDG estimation is performed by DSP based on the MIMO equalizer transfer function.	122
Figure 5.4 – MDG versus attenuation ratio at different VOA configurations. (a) Peak to peak MDL/MDG. (b) σ_{mdg}	124
Figure 5.5 – MDG standard deviation σ_{mdg} estimated by DSP without noise loading, as a function of the launch powers in the LP ₀₁ and LP ₁₁ modes. (a) 32.5 m transmission with an intrinsic SNR = 38.5 dB. (b) 73 km transmission with an intrinsic SNR = 37.1 dB.	125
Figure 5.6 – Estimation error $\sigma_{\text{mdg}}^{\text{err}} = \sigma_{\text{mdg}} - \sigma_{\text{mdg}}^{\text{nl}}$, calculated as the difference in dB between the MDG standard deviation σ_{mdg} in dB estimated by DSP without noise loading, and $\sigma_{\text{mdg}}^{\text{nl}}$ in dB estimated by DSP with noise loading. In the figure, $\sigma_{\text{mdg}}^{\text{err}}$ is shown as a function of the power launched in the LP ₀₁ and LP ₁₁ modes for 32.5 m transmission. (a) Without correction at SNR = 17 dB. (b) Without correction at SNR = 12 dB. (c) Correction by the positive solution of Eq. (5.1) at SNR = 17 dB. (d) Correction by the positive solution of Eq. (5.1) at SNR = 12 dB.	126
Figure 5.7 – Estimation error $\sigma_{\text{mdg}}^{\text{err}} = \sigma_{\text{mdg}} - \sigma_{\text{mdg}}^{\text{nl}}$, calculated as the difference in dB between the MDG standard deviation σ_{mdg} in dB estimated by DSP without noise loading, and $\sigma_{\text{mdg}}^{\text{nl}}$ in dB estimated by DSP with noise loading. In the figure, $\sigma_{\text{mdg}}^{\text{err}}$ is shown as a function of the power launched in the LP ₀₁ and LP ₁₁ modes for 73 km transmission. (a) Without correction at SNR = 17 dB. (b) Without correction at SNR = 12 dB. (c) Correction by the positive solution of Eq. (5.1) at SNR = 17 dB. (d) Correction by the positive solution of Eq. (5.1) at SNR = 12 dB.	127

Figure 5.8 – Estimation error $\sigma_{\text{mdg}}^{\text{err}} = \sigma_{\text{mdg}} - \sigma_{\text{mdg}}^{\text{nl}}$, calculated as the difference in dB between the MDG standard deviation σ_{mdg} in dB estimated by DSP without noise loading, and $\sigma_{\text{mdg}}^{\text{nl}}$ in dB estimated by DSP with noise loading. In the figure, $\sigma_{\text{mdg}}^{\text{err}}$ is shown as a function of σ_{mdg} and the SNR. (a) 32.5 m transmission without correction. (b) 32.5 m transmission with correction by the positive solution of (5.1). (c) 73 km transmission without correction. (d) 73 km transmission with correction by the positive solution of (5.1).	128
Figure 5.9 – Schematic representation of MDG emulation. (a) at the transmitter side. (b) in-span MDG emulation.	129
Figure 5.10–Experimental setup for short-reach 3-mode transmission with polarization multiplexing (HOUT <i>et al.</i> , 2020). variable optical attenuators (VOAs) are used to control the σ_{mdg} of the link with in-span configuration. At the receiver, the signals are demultiplexed by a second PL, digitized and processed. MDG estimation is performed by DSP based on the MIMO equalizer transfer function.	129
Figure 5.11–MDG estimation error as a function of the actual MDG and the SNR. (a) Without correction factor. (b) With correction factor. The MDG is emulated at 33 km in the transmission fiber span.	130
Figure 6.1 – Architecture of a basic fully-connected MLP ANN.	133
Figure 6.2 – ANN-based MDG and SNR estimator. (a) The training set is generated by numerical multisection simulation and analytic formulas. (b) The validation set is generated by a short-reach 3-mode transmission setup and the case study data is generated by a long-haul 6-mode transmission setup. (c) Proposed ANN. The algorithm applies two separate networks for σ_{mdg} and SNR estimation.	134
Figure 6.3 – ANN loss, calculated as the mean squared error (MSE), as a function of the number of epochs. (a) σ_{mdg} estimation. (b) SNR estimation. The curves indicate no overfitting and a good generalization ability.	135
Figure 6.4 – Experimental short-reach 3-mode validation results. (a) Estimated σ_{mdg} as a function of the actual σ_{mdg} . (b) Estimated SNR as a function of the actual SNR. (c) σ_{mdg} estimation error in dB generated by the conventional method as a function of the actual σ_{mdg} and SNR. (d) SNR estimation error in dB generated by the conventional method as a function of the actual σ_{mdg} and SNR. (e) σ_{mdg} estimation error in dB generated by the ANN as a function of the actual σ_{mdg} and SNR. (f) SNR estimation error in dB generated by the ANN as a function of the actual σ_{mdg} and SNR.	137

Figure 6.5 – Experimental long-haul 6-mode case study. (a) Estimated σ_{mdg} as a function of the transmission distance. (b) Estimated SNR as a function of the transmission distance.	138
Figure 6.6 – (a) Averaged impulse response after 1,770 km (Top) and 4,130 km (Bottom). (b) Standard deviation of the averaged impulse response as a function of the transmission distance.	138
Figure 6.7 – (a) Estimated σ_{mdg} as a function of the transmission distance with conventional, correction factor, and ANN methods. (b) Estimated SNR as a function of the transmission distance with conventional and ANN methods.	140
Figure 7.1 – Block diagram of the simulated SDM transmission over a FMF with $2M_p$ orthogonal modes.	142
Figure 7.2 – Estimated CD for the 6 spatially multiplexed channels, for a link with CD of 2,200 ps/nm. (a) Godard’s error. (b) PAPR. (c) Delay-tap sampling. For the sake of clarity, only the estimates with a perceived error are labelled with their corresponding channel number.	144
Figure 7.3 – Estimation of the accumulated CD at different levels of linear XT and optical signal-to-noise ratio (OSNR)=21 dB. (a) Godard’s error. (b) PAPR. (c) Delay-tap sampling.	146
Figure 8.1 – Refractive index profile of a graded-index, 55-mode fiber and the corresponding mode-group (MG) structure.	147
Figure 8.2 – mode-group (MG)-averaged crosstalk matrices after 25.9 km transmission in a 55-mode fiber (RADEMACHER <i>et al.</i> , 2022). The dashed squares indicate the investigated MG selections employed for equalization to recover (a) MG #1 and (b) MG #5.	148
Figure 8.3 – Experimental setup for the 55-mode SDM transmission system (RADEMACHER <i>et al.</i> , 2022).	149
Figure 8.4 – (a) Mode-group (MG)-averaged, GMI-based data rate for different output MGs as a function of the number of input MGs, used for MIMO equalization. (b) Number of active filters for the 10 MGs as a function of the number of input MGs used for equalization.	151
Figure 8.5 – System GMI-based data rate as a function of the number of active filters.	151

List of Tables

Table 2.1 – Relation between LP modes and normalized frequency.	53
Table 4.1 – Model parameters employed for Fig. 4.4.	110
Table 5.1 – VOA attenuation for MDG emulation	124
Table 8.1 – Mode-groups employed for MIMO equalization to recover each desired mode-group. Part I.	150
Table 8.2 – Mode-groups employed for MIMO equalization to recover each desired mode-group. Part II.	150

List of Acronyms

ADC	Analog-to-digital converter
AIR	Achievable information rate
ANN	Artificial neural network
ASE	Amplified spontaneous emission
ASIC	Application-specific integrated circuit
AWGN	Additive white Gaussian noise
BER	Bit error rate
BPS	Blind phase search
BPSK	Binary phase shift keying
CC-MCF	Coupled-core multi-core fiber
CD	Chromatic dispersion
CNN	Convolutional neural network
CPE	Carrier phase estimation
CPR	Carrier phase recovery
CUT	Channel under test
DAC	Digital-to-analog converter
DCF	Dispersion compensating fibers
DD	Decision-directed
DD-LMS	Decision-directed least mean squares
DFB	Distributed feedback laser
DGD	differential group delay
DMD	Differential mode delay
DMGD	Differential mode group delay
DNN	Deep neural network
DSF	Dispersion-shifted fiber
DSP	Digital signal processing
ECL	External cavity laser
EDF	Erbium-doped fiber
EDFA	Erbium-doped fiber amplifier
FDE	Frequency domain equalizer
FEC	Forward error correction
FFT	Fast Fourier transform
FIR	Finite impulse response
FMF	Few-mode fiber
FM-MCF	Few-mode multi-core fiber
FPGA	Field-programmable gate array
FWM	Four wave mixing
GD	Group delay
GFF	Gain flattening filter
GMI	Generalized mutual information

GNSE	Generalized nonlinear Schrödinger equation
GSOP	Gram-Schmidt orthogonalization procedure
GVD	Group-velocity dispersion
IFFT	Inverse fast Fourier transform
IM	Intensity modulation
IL	Insertion loss
ISI	Intersymbol interference
ITU	International Telecommunications Union
IQM	In-phase and quadrature modulator
LASER	Light amplification by stimulated emission of radiation
LMS	Least mean square
LO	Local oscillator
LP	Linearly polarized
LS	Least-squares
LUT	Lookup table
MQAM	M-ary quadrature amplitude modulation
MCF	Multi-core fiber
MC-EDF	Multi-core Erbium-doped fiber
MDG	Mode-dependent gain
MDL	Mode-dependent loss
MDM	Mode-division multiplexing
MGD	Modal group delay
MG	Mode-group
MMF	Multi-mode fiber
MMSE	Minimum mean squared error
MSE	Mean squared error
MIMO	Multiple-input multiple-output
ML	Machine learning
MLP	Multilayer perceptron
MZM	Mach-Zehnder modulator
NA	Numerical aperture
NF	Noise figure
NN	Neural network
NRZ	Non-return-to-zero
TFB	Tapered fiber bundle
OEO	Optical-electrical-optical
OOK	On-off keying
OPM	Optical performance monitoring
OSA	Optical spectrum analyzer
OSNR	Optical signal-to-noise ratio
PAPR	Peak-to-average power ratio
PBC	Polarization beam combiner
PBS	Polarization beam splitter
PDG	Polarization-dependent gain
PD-CRX	Polarization diverse coherent receiver
PL	Photonic lantern
PLC	Planar lightwave circuits

PMD	Polarization mode dispersion
PSD	Power spectral density
PRBS	Pseudorandom bit sequence
QAM	Quadrature amplitude modulation
QI	Quadrature imbalance
QPSK	Quaternary phase-shift-keying
RRC	Root-raised-cosine
SDM	Space division multiplexing
SGD	steepest gradient descent
SINR	Signal-to-noise plus interference ratio
SNR	Signal-to-noise ratio
SPM	Self phase modulation
SSMF	Standard single-mode fiber
SMF	Standard single-mode fiber
SVD	Singular value decomposition
TDE	Time domain equalizer
TDM-SDM	Time-domain multiplexed space-division multiplexing
TE	Transverse electric
TM	Transverse Magnetic
ULH	Ultra-long-haul
VCSEL	Vertical-cavity surface-emitting laser
VOA	Variable optical attenuator
WDM	Wavelength division multiplexing
WSS	Wavelength selective switch
XPM	Cross phase modulation

List of Symbols

M	Modulation order
R_s	Symbol rate
T	Symbol period
W	Signal bandwidth
$\alpha_{roll-off}$	Excess bandwidth parameter
$E1$	Ground state of the atom
$E2$	Excited state of the atom
V_π	External tension for π radians delay
P_{out_mod}	Output power of the optical modulator
P_{in_mod}	Input power of the optical modulator
v_1, v_2	Voltages applied to the optical modulator
a	Fiber core radius
b	Fiber cladding radius
n_1	Fiber core refractive index
n_2	Fiber cladding refractive index
$\nabla \times$	Curl operator
$\nabla \cdot$	Divergence operator
\mathbf{E}	Electric field vector
\mathbf{H}	Magnetic field vector
\mathbf{D}	Electric flux density
\mathbf{B}	Magnetic flux density
\mathbf{J}	Surface current density
ρ	Volume density of free charges
\mathbf{P}	Induced electric polarization
\mathbf{M}	Induced magnetic polarization
χ	Linear susceptibility of the medium
ϵ_0	Permittivity of the vacuum
μ_0	Permeability of the vacuum
$\epsilon(\mathbf{r}, \omega)$	Frequency-dependent dielectric constant
n	Refractive index of the medium
k	Wave number
k_0	Wave number in vacuum
λ_0	Wavelength in vacuum
$\tilde{\mathbf{E}}$	Electric field vector in frequency domain
$\tilde{\mathbf{H}}$	Magnetic field vector in frequency domain
$\tilde{\chi}$	Linear susceptibility of the medium in frequency domain
r	Radial component
ϕ	Azimuthal component
z	Longitudinal component
J_l	Bessel function of the first kind
K_l	Modified Bessel function of the second kind
l	Number of oscillations in the azimuthal direction

E_l	Intensity of the electric field at the core-cladding interface
V	Normalized frequency
β	Propagation constant
b	Normalized propagation constant
γ	Fiber non-linear parameter
\bar{n}_2	Non-linear Kerr parameter
A_{eff}	Effective area of the fiber
α	Attenuation coefficient
z	Propagation distance
P_{av}	Signal average optical power
P_{in}	Power launched at the fiber input
P_{out}	Power launched at the fiber input
L_f	Fiber length
$\Delta\omega$	Spectral linewidth of a transmitted pulse
ω	Angular frequency
τ_{lm}	Group delay of the LP_{lm} mode
$v_{g,lm}$	Group velocity of the LP_{lm} mode
V	Vertical polarization
H	Horizontal polarization
T_d	Time delay
\bar{n}	Optical fiber effective index
c	Speed of light
ΔT	Time of pulse broadening
β_2	Group-velocity dispersion parameter
$\Delta\lambda$	Range of wavelengths emitted by the optical source
λ	Channel propagation wavelength
D	Fiber dispersion parameter
D_m	Material dispersion parameter
D_w	Waveguide dispersion parameter
\mathbf{J}_f	Jones formalism matrix
S_{sp}	Power spectral density of spontaneous-emission noise
ν	Optical frequency
n_{sp}	Spontaneous emission factor
h	Plank constant
G	Amplifier gain
N_1	Atomic populations for the ground state
N_2	Atomic populations for the excited state
P_{Total}	Total power of the signal in both polarization
B_{ref}	Reference bandwidth
SNR_{in}	Signal-to-noise ratio at the amplifier input
SNR_{out}	Signal-to-noise ratio at the amplifier output
NF	Noise figure
K	Number of spans
L_s	Span length
E_s	Total signal energy
$N_0/2$	Noise spectral density
erfc	Complementary error function

H_{coupler}	Transference function of a 3 dB coupler
E_r	Electrical field of the received signal
E_{Lo}	Electrical field of the local oscillator signal
I_p	Photo-current
R	Responsivity factor of a photo-detector
$P_{\text{in_pd}}$	Input power to photo-detector
η	Conversion efficiency of a photo-detector
q	Electron charge
i_Q	Current quadrature component
i_I	Current in-phase component
A_s	Optical signal amplitude
A_{Lo}	Local oscillator signal amplitude
ϕ_s	Optical signal phase
ω_o	Angular frequency of the optical carrier
ω_{Lo}	Angular frequency of the local oscillator signal
η_s	Complex Gaussian noise of the optical signal
η_{Lo}	Complex Gaussian noise of the local oscillator signal
$\Re(\cdot)$	Real part
$(\cdot)^*$	Complex conjugate
Z	Complex numbers set
ω_{IF}	Intermediate angular frequency
M_p	Number of propagation modes
\mathbf{H}	Channel transfer matrix
\mathbf{S}	Transmitter matrix
\mathbf{s}_j	Signal transmitted by the j th transmitter
\mathbf{R}	Received matrix
\mathbf{r}_i	Signal received by the i th receiver
$\hat{\mathbf{S}}'$	Equalized matrix
$\hat{\mathbf{S}}$	Estimated matrix
\mathbf{N}	Noise matrix
L	Length of the impulse response
$\mathbf{h}_{i,j}$	Element of \mathbf{H} in the (i, j) position
\mathbf{n}_i	Element of \mathbf{N} in the i position
$E[\cdot]$	Expected value operator
Δ_f	Frequency offset between transmitter laser and local oscillator laser
Δ_Φ	frequency offset-induced phase offset
T_{sa}	Time between samples
$\theta(k)$	Phase noise signal in discrete time
$(\cdot)^M$	M -th order power operation
T_{DSP}	Clock period of the DSP functions
\mathbf{W}	MIMO wieght matrix
$\mathbf{w}_{i,j}$	MIMO coefficients corresponding to input i and output j
S/P	Serial to parallel conversion
P/S	Parallel to serial conversion
N_{taps}	Number of taps of the MIMO equalizer filters
Σ	Summation operator
\mathbf{e}	Error signal for FDE gradient estimation

J	Cost function
\mathbf{W}_{MMSE}	Transfer matrix of a MIMO MMSE equalizer
μ_{step}	Equalizer updating step size
\mathbf{e}_{LMS}	Error vector of LMS algorithm
$(\cdot)^H$	Hermitian transpose operator
\mathbf{W}_{ini}	Initialization of \mathbf{W}
C_{TDE}	Complexity of the TDE equalizer
C_{FDE}	Complexity of the FDE equalizer
$\hat{\theta}$	Phase estimated by the CPR block
Δ_k, Δ_m	Gaussian random variables
Δ_ν	Sum of the transmitter laser linewidth and local oscillator laser linewidth
σ_Δ^2	Phase noise variance
$M(\varphi)$	Distance metric for BPS algorithm
φ	Test phase
N_B	Length of the summing window
UN	Unwrapping function
I	Number of test phase angles
$\text{argmin}(\cdot)$	Minimum argument
$\text{arg}(\cdot)$	Argument function
K	Number of fiber sections or spans (one section per span)
\mathbf{V}, \mathbf{U}	Random unitary matrix accounting for mode coupling
Λ	Diagonal matrix accounting for MDG and mode dispersion
Π	Product operator
$\text{diag}(\cdot)$	Diagonal of a matrix
C	Instantaneous theoretical capacity
C_{mdg}	Capacity of a MDG-impaired channel
Δ_{mdg}	Effective SNR loss
SNR_{mdg}	SNR degraded by the MDG
λ_i^2	Eigenvalues of the operator $\mathbf{H}\mathbf{H}^H$
ξ	Accumulated MDG standard deviation
σ_g	Per-amplifier MDG standard deviation
$\sigma_{g, \text{logpw}}$	Per-amplifier MDG standard deviation in log power units
$\sigma_{\tau, \text{per-span}}$	Group delay standard deviation per span
σ_{mdg}	Standard deviation of the overall MDG
$\hat{\sigma}_{\text{mdg}}$	Estimated standard deviation of the overall MDG
$\text{MDG}_{\text{pk-pk}}$	Peak-to-peak MDG
$\mathbf{W}_{\text{EQ}}^{-1}$	Inverse of the equalizer transfer function
\mathbf{I}	Identity matrix
$\mathbf{W}_{\text{MMSE}}^{-1}$	Inverse transfer matrix of a MIMO MMSE equalizer
$\lambda_{i, \text{MMSE}}^2$	Eigenvalues of the operator $\mathbf{W}_{\text{MMSE}}^{-1}(\mathbf{W}_{\text{MMSE}}^{-1})^H$
Λ_{H}	Diagonal matrix whose main diagonal has elements λ_i^2
\mathbf{Q}	Matrix whose columns are the eigenvectors of $\mathbf{H}\mathbf{H}^H$
\mathbf{W}_{LMS}	Transfer matrix of a MIMO equalizer updated by the LMS algorithm
$\mathbf{W}_{\text{LMS}}^{-1}$	Transfer matrix of a MIMO equalizer updated by the LMS algorithm
$\lambda_{i, \text{LMS}}^2$	Eigenvalues of the operator $\mathbf{W}_{\text{LMS}}^{-1}(\mathbf{W}_{\text{LMS}}^{-1})^H$
$[]_{i, i}$	i -th element in the main diagonal of a matrix
SNR_{imp}	Implementation penalty

$\sigma_{\text{mdg}}^{\text{err}}$	σ_{mdg} estimation error
$\sigma_{\text{mdg}}^{\text{nl}}$	σ_{mdg} estimated with noise loading
TX	Transmitter port of the photonic lantern
RX	Receiver port of the photonic lantern
$ \mathbf{H} ^2$	Intensity averaged impulse response
J_{Godard}	Cost function of the Godard's error algorithm
J_{PAPR}	Cost function of the PAPR algorithm
$J_{\text{Delay-tap}}$	Cost function of the delay-tap sampling algorithm
R_1, R_2	Normalization constants
$\max(\cdot)$	Maximum function
$\min(\cdot)$	Minimum function
XT	Crosstalk

List of Units

m	Meter
km	Kilometer
bit/s/Hz	Bits per second per Hertz
V	Volts
V/m	Volts per meter
A/m	Ampere per meter
C/m ²	Coulomb per meter squared
Wb/m ²	Weber per meter squared
C/m ³	Coulomb per meter cubed
A/m ²	Ampere per meter squared
W ⁻¹ m	Meter per Watt
m ² /W	Meter squared per Watt
Np/km	Neper per kilometer
dB/km	Decibel per kilometer
nm	Nanometer
μm	Micrometer
ps	Picoseconds
ns	Nanoseconds
ps/(km · nm)	Picosecond per kilometer per nanometer
ps / $\sqrt{\text{km}}$	Picosecond per square root of kilometer
b/s/Hz	Bits per second per Hertz
GBd	Gigabaud
dB	Decibel
dBm	Decibel-milliwatts
THz	Terahertz
GHz	Gigahertz
kHz	Kilohertz
Tb/s	Terabits per second
Gb/s	Gigabits per second
GSa/s	Giga-samples per second
dB/km	Decibel per kilometer
ps/km	Picosecond per kilometer
ps/nm	Picosecond per nanometer

List of Publications

- **Journals papers**

1. **Ospina, R. S.**, Hout M. V. D., Zacarias J. C., Lopez J. E., Astruc M. B., Correa A. A., Sillard P., Correa R., Okonkwo, C., and Mello, D. A. *Mode-dependent loss and gain estimation in SDM transmission based on MMSE equalizers*. Journal of Lightwave Technology, IEEE, v. 39, n. 7, p. 1968–1975, 2020.
2. **Ospina, R. S.**, Hout M. V. D., Heide S. V. D., Weerdenburg J. V., Ryf R., Fontaine N. K., Haoshuo C., Correa R., Okonkwo, C., and Mello, D. A. *MDG and SNR Estimation in SDM Transmission Based on Artificial Neural Networks*. Journal of Lightwave Technology, IEEE, v. 40, n. 15, p. 5021–5030, 2022.

- **Conference contributions**

1. **Ospina, R. S.**, dos Santos, L. F., Mello, D. A., and Ferreira, F. M. (2019, July). *Scanning-Based Chromatic Dispersion Estimation in Mode-Multiplexed Optical Systems*. In 2019 21st International Conference on Transparent Optical Networks (ICTON) (pp. 1-4). IEEE. *Invited*.
2. **Ospina, R. S.**, Okonkwo, C., and Mello, D. A. (2020, March). *DSP-based Mode-dependent Loss and Gain Estimation in Coupled SDM Transmission*. In Optical Fiber Communication Conference (OFC) (pp. W2A-47). Optical Society of America.
3. **Ospina, R. S.**, Hout M. V. D., Okonkwo, C., and Mello, D. A. (2020, November). *Mode-dependent Loss and Gain Emulation in Coupled SDM Transmission*. In 38th Brazilian Symposium on Telecommunications and Signal Processing (SBrT), Florianopolis, Brazil.
4. Hout M. V. D., **Ospina, R. S.**, Zacarias J. C., Lopez J. E., Astruc M. B., Correa A. A., Sillard P., Correa R., Okonkwo, C., and Mello, D. A. (2020). *Experimental validation of MDL emulation and estimation techniques for SDM transmission systems*. In European Conference in Optical Communication (ECOC) (pp. 1-4). IEEE.
5. **Ospina, R. S.**, Hout M. V. D., Heide S. V. D., Okonkwo, C., and Mello, D. A. (2021, June). *Neural-network-based MDG and Optical SNR Estimation in SDM Transmission*. In Optical Fiber Communication Conference (OFC). Optical Society of America.

6. Mello, D. A., Srinivas. H, Choutagunta K., **Ospina, R. S.**, and Kahn J. M. (2022, July). *Impact of Mode-Dependent Gain on the Capacity of Ultra-Long-Haul SDM Systems*. In Summer Topical Meeting Series. IEEE. *Invited*.
7. **Ospina, R. S.**, Rademacher G., Luís R. S., Puttnam B. J., Fontaine N. K., Mazur M., Chen H., Ryf R., Neilson D. T., Dahl D., Carpenter J., Sillard P., Achten F., Bigot M., Mello, D. A., and Furukawa H. (2023, March). *Experimental Investigation of Reduced Complexity MIMO Equalization in a 55-Mode Fiber SDM Transmission System*. In Optical Fiber Communication Conference (OFC). Optical Society of America.
8. Mello, D. A., **Ospina, R. S.**, Srinivas. H, Choutagunta K., Chou E. and Kahn J. M. (2023, March). *Impact and Mitigation of Mode-Dependent Gain in Ultra-Long-Haul SDM Systems*. In Optical Fiber Communication Conference (OFC). Optical Society of America. *Invited*.
9. **Ospina, R. S.**, Rademacher G., Luís R. S., Puttnam B. J., Furukawa H., Ryf R., Neilson D. T., and Mello, D. A. *MDG Estimation in SDM Transmission Systems Based on MIMO MMSE Equalization*. To appear in Signal Processing in Photonic Communications (SPPCom). *Invited*.

- **Scientific panel**

1. Invited talk on MDL/MDG estimation in SDM transmission during the Space-Division Multiplexing Workshop at the Asia Communications and Photonics Conference (ACP), Shanghai, China, 2021.
2. Invited talk on Digital Signal Processing for SDM transmission systems during the second Brazilian Webinar of Photonic Laboratories (SISFOTON), Brazil, 2022.

Over the manuscript, the scientific contributions achieved by the Ph.D. candidate as the first author are cited in the form (OSPINA *et al.*, year of publication, index).

Contents

1	INTRODUCTION	32
1.1	Thesis structure	36
1.2	Thesis contributions	37
2	SPACE-DIVISION MULTIPLEXING OPTICAL TRANSMISSION SYSTEMS	39
2.1	Pol-mux transmitter submodule (pol-mux TX)	40
2.1.1	Constellation mapping	41
2.1.2	Digital-to-analog conversion and pulse shaping	42
2.1.3	Optical modulation	44
2.2	Spatial multiplexers	47
2.3	Optical channel	48
2.3.1	Propagation modes in optical fibers	49
2.3.2	Pulse propagation	54
2.3.3	Attenuation	54
2.3.4	Group delay	56
2.3.5	Group velocity dispersion	57
2.3.6	Nonlinear impairments	59
2.3.7	Spatial channel interactions	60
2.3.8	Optical amplification	62
2.3.9	Fibers for space-division multiplexing	69
2.4	Receiver submodule (RX)	72
2.4.1	Front-end	72
2.5	Summary	76
3	DIGITAL SIGNAL PROCESSING FOR SDM TRANSMISSION SYSTEMS	78
3.1	Multiple-input multiple-output transmission model	79
3.2	Front-end impairment compensation	80
3.3	Frequency offset compensation	82
3.3.1	Frequency domain M -th order power algorithm	83
3.4	Static equalization	83
3.5	Dynamic MIMO equalization	84
3.5.1	Least mean square algorithm	87
3.5.2	Analysis of the computational complexity of dynamic equalization	90
3.6	Carrier phase recovery	91
3.6.1	Blind phase search (BPS)	92
3.6.2	Supervised CPR	94

3.7	Case study: simulation of a long-haul 3-mode SDM transmission link . . .	94
3.8	Case study: experimental long-haul 6-mode SDM transmission	98
3.8.1	Performance evaluation	100
3.9	Summary	102
4	FUNDAMENTALS OF MODE-DEPENDENT GAIN IN SDM SYSTEMS	103
4.1	Mode-dependent gain in SDM transmission systems	104
4.2	MDG simulation: Semi-analytical multisection model for strongly-coupled SDM transmission	107
4.3	DSP-based MDG estimation	109
4.3.1	Simulation results for long-haul transmission	114
4.4	Conventional method for optical SNR estimation	116
4.5	Receiver implementation penalty	117
4.6	Summary	117
5	CORRECTION FACTOR FOR DSP-BASED MDG ESTIMATION	119
5.1	MDG emulator for experimental laboratory setups	120
5.1.1	MDG emulation results	123
5.2	Experimental validation of the correction factor technique in a 3-mode transmission link	124
5.2.1	MDG estimation without noise loading	125
5.2.2	MDG estimation with noise loading	126
5.3	Summary	130
6	ARTIFICIAL NEURAL NETWORK-BASED MDG AND SNR ESTIMATION	132
6.1	Artificial Neural Networks	132
6.2	ANN-based Method for MDG and SNR estimation	133
6.3	Experimental short-reach transmission with known MDG and SNR	135
6.4	Experimental long-haul transmission with unknown MDG and SNR	136
6.5	Discussion	139
6.6	Summary	140
7	CHROMATIC DISPERSION ESTIMATION IN SDM TRANSMISSION	141
7.1	Scanning-based CD estimation techniques	141
7.1.1	Godard's error algorithm	142
7.1.2	Peak-to-average power ratio (PAPR) algorithm	143
7.1.3	Delay-tap sampling algorithm	143
7.2	Simulation setup and results	143
7.3	Summary	145
8	STUDY OF REDUCED COMPLEXITY MIMO EQUALIZATION	147
8.1	Experimental 55-mode transmission setup	148
8.2	Results and discussion	150

8.3 Summary	152
9 CONCLUSION	153
Bibliography	156

1 INTRODUCTION

Communication is an innate need of human beings. Since the beginning of civilizations, the exchange of information at a distance has evolved extraordinarily. Visual and sound signals were the first meaningful evidence of telecommunication between individuals despite being constrained by the short diversity of the messages and the mandatory line of sight. After a great leap forward, the appearance of the electric telegraph and the telephone alleviated both limitations, significantly boosting telecommunications. Nevertheless, the transmission of electrical signals through copper cables was subject to limited bandwidths and very high losses, demanding the integration of multiple repeater modules. It was not until the middle of the twentieth century that the invention of the semiconductor laser (MAIMAN *et al.*, 1960) and the optical fiber (KAO; HOCKHAM, 1966) allowed the transmission of optical waves at very high frequencies. Optical fibers provided higher bandwidths than copper cables and considerably increased the space between repeaters due to the reduced losses.

In the advent of optical fibers, multi-mode fibers (MMFs) were initially considered the most suitable medium for those new optical communication systems. However, due to modal dispersion and other constraints, single-mode fibers (SMFs) were preferred over MMFs for long-haul communication links. Aiming to increase the capacity-distance product, special SMFs were designed to work in the window of lowest attenuation around 1550 nm (MIYA *et al.*, 1979). Unfortunately, typical fibers at that time presented high dispersion over such operation bands. Therefore, new fibers called dispersion-shifted fibers (DSFs) were manufactured to have their minimum dispersion at the lowest attenuation window (ONISHI *et al.*, 1994), (BJARKLEV *et al.*, 1994). However, as a consequence of the undesirable non-linear effects enhanced by the DSFs small core area at high power levels, these fibers were not further contemplated for high-rate and long-distance transmission.

From the 1980s to the 2000s, intensity modulation (IM) at the transmitter side and a receiver employing direct detection (DD) based on a single photodetector were the basic technologies for communications systems over optical fibers. Nonetheless, the non-linear transformation of the optical signal into an electrical current carried out by the photodetector prevented the phase modulation of the optical carrier, limiting the system's spectral efficiency. Likewise, the non-linear photodetection process precluded the chromatic dispersion (CD) and polarization mode dispersion (PMD) compensation through electric linear filtering techniques.

Aiming to increase spectral efficiency and get longer transmission distances, optical systems with coherent detection were brought to light. Coherent detection schemes increase the sensitivity of the optical receiver, consequently admitting higher link losses. Additionally, with a coherent receiver, it is possible to modulate the phase of the optical carrier to employ efficient high-order modulation formats and increase spectral efficiency. Despite the evident advantages, the introduction of coherent detection was postponed due to the high complexity of the receiver architecture, and then, the attention was diverted to optical amplification (MEARS *et al.*, 1987) and wavelength-division multiplexing (WDM) technology.

Over the years, IM-DD optical communication systems with WDM faced a fast-growing demand for higher transmission rates that was hard to keep up. Increasing the transmission rate exponentially over the same network infrastructure was limited due to the high levels of resulting CD and PMD that could not be efficiently compensated at a low cost. Therefore, optical systems implementing coherent detection came back to the game (TAYLOR, 2004). In the 2000s, new technologies such as the receiver front-end, high-speed oscilloscopes, high-speed analog-to-digital converters (ADCs), and the appearance of digital signal processing (DSP) algorithms for impairment compensation made coherent optical systems a reality. With the advent of DSP, CD was compensated in the digital domain without the need to implement expensive physical compensation devices. Moreover, the PMD could be fully compensated by adaptive filtering. Currently, amplified coherent optical systems implementing WDM, high order modulation formats, polarization multiplexing, and DSP techniques for impairment compensation are the main alternative to transport the massive information traffic through optical networks. However, the sustained increment of data traffic resulting from the growing popularity of mobile devices and internet services will lead to capacity exhaustion of current optical networks (WINZER, 2014), (RICHARDSON, 2016).

Nearly two-thirds of the global population will have Internet access by 2023. There will be 5.3 billion total Internet users (66 % of the global population) by 2023, up from 3.9 billion (51 % of the global population) in 2018 (CISCO, 2020). Accounting for smartphones, tablets, computers, and smart TVs, among others, in 2023, the number of devices connected to internet networks is expected to be more than three times the global population (CISCO, 2020). With each of these connected devices contributing a vast amount of data, experts forecast an exponential growth of information traffic, making it necessary for the capacity of optical networks to scale accordingly.

Space division multiplexing (SDM) technology has been presented as the only solution capable of supporting such an overgrowth of data transmission demand. Besides the most straightforward approach of using multiple single-mode fibers in parallel as consid-

ered in (DOMINGUES *et al.*, 2017), (JATOBA-NETO *et al.*, 2018), spatial multiplexing can be done more efficiently using SDM fibers such as MMFs (RADEMACHER *et al.*, 2022) and multi-core fibers (MCFs) (LUIS *et al.*, 2022). MMFs support the propagation of multiple modes within a single core while MCFs present several cores sharing the same cladding. Other schemes include hybrid few-mode multi-core fibers (FM-MCFs) to provide the highest spatial multiplicity and MMFs with a limited number of modes called few-mode fibers (FMFs) aiming to relieve implementation complexity (SILLARD *et al.*, 2022), (RADEMACHER *et al.*, 2022). MCFs have spatial paths determined by a matrix of single-mode cores uniformly distributed in the fiber cross-section (SAITOH; MATSUO, 2016). This kind of fiber can be classified into two categories depending on the inter-core spacing. In weakly-coupled core MCFs, the spacing between cores is large enough to minimize inter-core interactions. Nonetheless, the random power coupling between neighboring cores leads to undesirable crosstalk. In strongly-coupled core MCFs, the inter-core distance is deliberately reduced to intensify the crosstalk. These fibers are commonly evaluated in the context of the transmission of so-called supermodes formed by the superposition of the field distribution in several strongly coupled modes (XIA *et al.*, 2013). As a consequence of high levels of crosstalk, multiple-input multiple-output (MIMO) equalizers are required to unravel the received signals in strongly-coupled core MCFs (RYF *et al.*, 2012), (RYF *et al.*, 2011b).

When the core radius or the core-cladding index difference become sufficiently large, an optical fiber can support multiple guided modes on a single core (HO *et al.*, 2013). Taking advantage of the orthogonality among guided modes, MMFs provide spatial multiplicity for data transmission. As in MCFs with coupled cores, any linear crosstalk between modes in MMFs should be handled by MIMO equalizers. A short channel impulse response is desirable to regulate the equalizer's computational complexity. Therefore, modal dispersion should be carefully managed during system design while residual CD leaked from previous DSP stages should be minimized.

The propagation coupling regime of MMFs has been shown to have a direct impact on the modal group delays (MGDs). In the strong coupling regime, the differential-mode delay (DMD) increases with the square root of the fiber length, while in the weak coupling regime, the DMD increases linearly with the fiber length (SHEMIRANI *et al.*, 2009). Then, MMFs operating under a strong coupling regime are an interesting alternative for reduced complexity MIMO equalizers.

Effects coming from modal dispersion and crosstalk are fully compensated by DSP without representing a fundamental limitation for SDM systems. On the other hand, SDM systems with coupled channels deployed at long distances will require multiple inline amplifiers to compensate for propagation losses. SDM amplifiers may present an unbalanced

gain profile over guided spatial modes, resulting in mode-dependent gain (MDG). Moreover, fiber bends, connectors, splices, and optical devices, such as multiplexers and demultiplexers, also introduce mode-dependent loss (MDL). MDL and MDG produce random variations in the powers of the signals propagating in different modes. These power variations may change over time and even affect the frequency components of each signal differently (HO *et al.*, 2013). As a consequence of the MDL and MDG, the MIMO system capacity becomes a random variable resulting in a possible decrement of the average capacity. Furthermore, at a given point in time, the instantaneous capacity may drop below a minimum threshold of the transmission rate, triggering a system outage (WINZER; FOSCHINI, 2011), (HO *et al.*, 2013), (MELLO *et al.*, 2019). Therefore, MDL and MDG, as well as the amplified spontaneous emission (ASE) noise, represent a fundamental limit for the deployment of high-capacity long-haul SDM systems.

In the scope of flexible optical communications systems, future SDM systems will also have to adapt to the transmission medium. Identifying the optical channel through parameter estimation is the first open challenge for potential system adaptation. In addition, the estimation of channel parameters is essential for performance evaluation and troubleshooting. Channel estimation has been deeply studied in single-mode coherent optical systems. In contrast, few works about channel parameter estimation in mode division multiplexing systems have been reported (HEI *et al.*, 2018), (SAIF *et al.*, 2019), (SAIF *et al.*, 2021). The few studies on channel parameter estimation in SDM systems focus mainly on optical signal-to-noise ratio (OSNR) estimation and modulation format identification, leaving many topics to be studied. Regarding MDL and MDG estimation, the works reporting SDM transmissions evaluate the MDL and MDG using a well-known method based on the transfer function of the MIMO equalizer (WEERDENBURG *et al.*, 2017), (RYF *et al.*, 2019), (SHIBAHARA *et al.*, 2020), (RADEMACHER *et al.*, 2020), (ARIKAWA *et al.*, 2021), (HUANG *et al.*, 2022). Such conventional DSP-based MDL/MDG estimation method is subject to approximations and has limited performance in specific system operating regimes that have yet to be studied. Concerning other channel parameters, the accumulated CD has been considered faithfully known at the reception in SDM experimental demonstrations. This assumption may lose validity in specific contexts, for example, in dynamically reconfigured systems, in which the actual length of the link may not be accurately known since the routing path varies with time. To the best of our knowledge, the estimation of the accumulated chromatic dispersion in SDM systems has not been studied and the proposed estimation methods found in the literature have been exclusively studied in single-mode systems.

To support both the adaptation of future SDM systems based on channel conditions and the performance assessment of SDM transmission, this thesis studies the estimation of

channel parameters in coupled SDM transmission using DSP-based techniques. The thesis is mainly focused on the estimation of the MDL/MDG and signal-to-noise ratio (SNR) using classical DSP methods and techniques enhanced by machine learning (ML) tools, particularly artificial neural networks (ANNs) of the kind multilayer perceptron (MLP). In addition, the thesis also addresses the estimation of the accumulated CD as a strategy to minimize the residual CD left over from the static equalizer mitigating an eventual increase of the MIMO equalizer complexity.

As a lateral topic, motivated by the need to implement computationally-efficient DSP algorithms for SDM systems, this thesis also studies the potential reduction of the complexity of MIMO equalizers required to separate the received signals in high-multiplicity SDM transmissions with weak coupling between mode-groups (MGs).

This thesis has resulted from the manipulation of data generated by Monte-Carlo simulations and experimental data of short and long-distance SDM transmission measured in partner laboratories such as the high-capacity transmission laboratory of the Eindhoven University of Technology (TUE), in The Netherlands, and the Photonics Laboratory of the National Institute of Information and Communications Technology (NICT), in Japan. The development of this thesis at the University of Campinas was sponsored by the *Fundação de Amparo à Pesquisa do Estado de São Paulo* (FAPESP) under grants 2017/25537-8, 2015/24341-7, and 2022/07488-8. Moreover, FAPESP fully supported the academic internship carried out at TUE under grant 2018/25414-6. FAPESP and NICT partially sponsored the 4-month academic internship in Japan.

The structure of the thesis and the contributions will be presented in the following sections.

1.1 Thesis structure

This thesis is composed of 9 chapters. Chapter 2 covers the main concepts of SDM technology and describes in detail the general components of an SDM/WDM transmission system. At the transmitter, constellation mapping, pulse-shaping, and optical modulation are presented. After transmitter description, the most widely employed spatial multiplexers are discussed. Later, the optical channel gathers the concepts of propagation modes over optical fibers and presents the linear and nonlinear effects that govern the propagation of light pulses. In addition, the main interactions between spatial channels in SDM transmission are studied. Optical amplification concepts and the fibers employed for SDM transmission are also introduced. On the receiver side, the optical-to-electrical conversion performed by the receiver front-end is mathematically explained. Chapter 3 presents the mathematical model of a MIMO communication system and describes the

DSP algorithms implemented in this thesis to compensate for the impairments introduced by the SDM optical channel. At the end of the chapter, the DSP algorithms are applied to two case studies. Chapter 4 describes the fundamentals of the MDG in SDM transmission systems, including its mathematical modeling and simulation through the semi-analytical multisection model for strongly-coupled SDM transmission. This chapter also presents the classical methods for MDG and SNR estimation in SDM transmission. The performance limitations of the conventional estimation methods under certain systems conditions are evidenced through simulations. Chapter 5 presents an improved DSP-based technique for MDG estimation in SDM systems using an analytical correction factor. The performance improvement provided by the proposed technique is evidenced through simulations and experiments. Chapter 6 presents a novel technique for MDG and SNR estimation in SDM systems based on ANNs. The method is validated using experimental data of a 3-mode transmission setup over a 73-km fiber link and applied to a case study of a long-haul 6-mode transmission setup. Chapter 7 studies the estimation of the accumulated CD in the scope of SDM transmission over FMFs. Three CD estimation techniques based on scanning procedures are applied to FMFs transmission setups using Monte-carlo simulation. As a lateral study, Chapter 8 presents the experimental investigation of the reduction of the MIMO equalizer computational complexity. The reduced complexity is studied in the scope of a 55-mode fiber transmission setup through the strategic deactivation of the filters that compose the MIMO equalizer based on the system crosstalk matrix. Finally, Chapter 9 concludes the thesis and introduces challenges for future work.

1.2 Thesis contributions

This thesis gathers the fundamental concepts of communication systems over optical fibers employing SDM. Transmitter components, transmission medium, and receiver are described in detail. Furthermore, this thesis presents the implementation of the DSP algorithms implemented to compensate for transmission impairments in SDM transmission setups, such as front-end imperfections, frequency offset, accumulated CD, modal dispersion, mode coupling, and phase noise. Using simulations, this thesis also compares the performance of two approaches for dynamic equalization and phase recovery, showing that under some operating conditions, phase recovery must be performed in a loop with the equalization to achieve equalizer convergence. Applying the implemented DSP chain on an experimental SDM setup, the presence of modal dispersion and mode coupling in long-haul experimental SDM transmission is evidenced. This thesis also contributes with the detailed description of the implementation of the semi-analytical multisection model

for strongly-coupled SDM transmission in MATLAB ¹, which is frequently used for the simulation of SDM systems with different levels of MDG. Further, during the development of this thesis, the limited accuracy of the conventional DSP-based MDL/MDG estimation method under particular system operating regimes is studied through simulations and experimental results. The results from simulated and experimental setups show that the conventional DSP-based estimation method underestimates the actual MDL/MDG at low levels of SNR and high levels of MDL/MDG, an expected scenario in long-haul SDM transmission systems. Once the performance limitations of the conventional DSP-based estimation method are evidenced, an improved technique for MDL/MDG estimation based on an analytical correction factor is proposed to remove the SNR dependence. Likewise, the influence of the MDL/MDG on the performance of the conventional SNR estimation method that employs the constellation of the electrical signals after DSP is studied through simulations. In addition, a novel technique for MDL/MDG and SNR estimation based on ANNs is proposed to improve the estimation accuracy and overcome the disadvantages of the conventional estimation methods. The proposed low-complexity ANN-based MDL/MDG and SNR estimation method employs information easily obtained after DSP from the MIMO equalizer and digital constellations. The neural network model is trained using semi-analytic data and can be used to estimate the MDL/MDG or SNR in experimental SDM systems regardless of the mode coupling regime. Besides MDL/MDG and SNR, in this thesis, the estimation of the accumulated CD in SDM transmission is studied as a strategy to minimize the residual CD left over from the static equalization that can potentially increase the MIMO computational complexity. In this context, three classical scanning-based techniques proposed for single-mode transmission are modified and applied to a simulated SDM transmission setup with coupled channels at different levels of modal dispersion, ASE noise, and mode coupling. Finally, this thesis performs the experimental investigation of the reduced complexity MIMO equalization in SDM transmissions by selective filter deactivation based on the system crosstalk matrix. Taking advantage of the weak coupling between MGs, a 21.5% MIMO complexity reduction is demonstrated with only a 4.9% data rate loss by selectively deactivating the finite impulse response (FIR) filters in an experimental graded-index 55-mode fiber transmission setup.

The development of this thesis has resulted in the publication list presented at the beginning of this manuscript.

¹ Note that, although the simulation model has been implemented in MATLAB in this thesis, its implementation can be extended to any programming language.

2 SPACE-DIVISION MULTIPLEXING OPTICAL TRANSMISSION SYSTEMS

In the current days, high-capacity coherent optical systems employing WDM, polarization multiplexing, and high-order modulation formats enable the transmission of massive data traffic through optical networks. Nevertheless, to sustain the exponential growth of the information traffic and preserve the low cost of transmission per bit in the medium and long term, the infrastructure of optical networks must implement a new disruptive technology (WINZER, 2014). In order to increase the capacity of optical systems in an energy-efficient way, maintaining the trend of reducing costs per transmitted bit, solutions based on SDM are being studied. SDM technology exploits parallel spatial paths, supporting the simultaneous transmission of independent signals. Therefore, in ideal conditions, the simultaneous transmission over M_p spatial propagation paths would raise the capacity by M_p times. However, in practice, the increment in capacity is lower as a consequence of certain impairments introduced by the SDM channel. As in single-mode digital coherent optical systems, in modern SDM systems, most channel impairments are compensated in the digital domain employing DSP algorithms. In SDM long-haul transmission with coupled channels, adaptive MIMO equalizers are required to compensate for any linear mixing between modes and unravel the transmitted signals (ARIK *et al.*, 2014), (RYF *et al.*, 2012b). The length of the filters that compose the MIMO equalizer depends directly on the modal dispersion and the level of residual CD leaked from the static equalization. Besides linear coupling, CD, and modal dispersion, phase noise effects, and frequency shifts are also present in SDM system and are compensated for by DSP. Transmission impairments compensated by DSP do not represent critical constraints for the performance of SDM systems. On the contrary, MDL and MDG generated in the fiber, amplifiers, and other in-line components introduce a non-unitary transformation on the signal that can not be trivially reversed by DSP. MDL and MDG decrease the average channel capacity, representing, along with the amplification noise, a fundamental limit for the deployment of future long-haul SDM systems.

Fig. 2.1 presents a general diagram of an SDM/WDM transmission system. The SDM transmitter comprises M_p identical blocks labeled as WDM transmitters (WDM TX). In each WDM transmitter, N_{ch} single-mode transmitters modulate optical carriers at different frequencies. The N_{ch} optical signals are multiplexed in wavelength by a WMUX. Since the M_p spatial channels are orthogonal, information can be sent over the same frequencies in all the M_p WDM transmitters. Within each polarization multi-

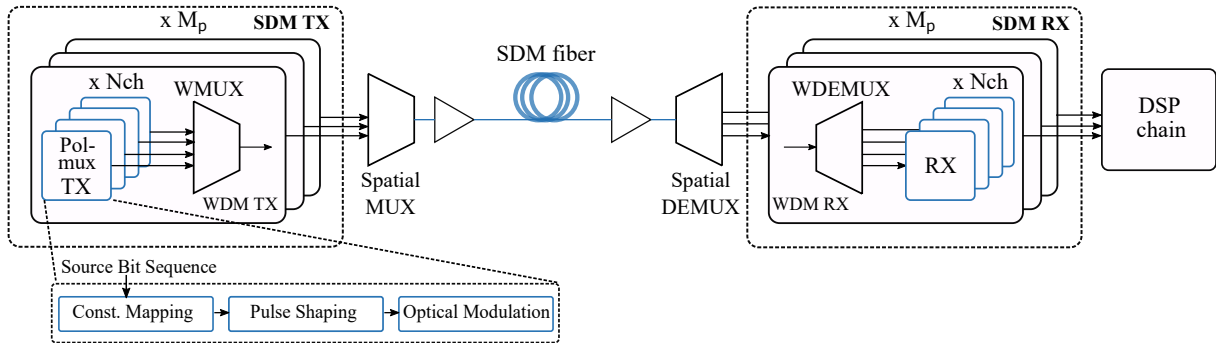


Figure 2.1 – Block diagram of an SDM/WDM transmission setup. Transmission of M_p spatial channels. Accounting by the polarization states, $2M_p$ orthogonal signals propagates through the fiber in each wavelength channel.

plexing single-mode transmitter submodule (pol-mux TX), several optoelectronic devices transform the information signal throughout three steps: constellation mapping, pulse shaping, and optical modulation. These processes are explained in detail in this chapter. The M_p optical signals with pol-mux coming from the M_p WDM transmitters, are spatially multiplexed and injected into the optical channel. Including polarization modes, $2M_p$ orthogonal signals propagate in each wavelength channel.

The optical channel is composed of amplifiers and other in-line devices. The main component of the optical channel is the optical fiber. The SDM fiber can be a MMF, FMF, MCF, or a FM-MCF. The fibers used for SDM transmission are described later in this chapter. At the receiver side, the detected signal is demultiplexed in space, and the resulting optical signals are passed to M_p identical blocks named WDM receivers. Within each WDM receiver, the signal is demultiplexed in wavelength, and then the N_{ch} channels are converted to the electrical domain by multiple single-mode receivers (RX). After conversion, the DSP chain processes the $2M_p$ electrical signals at the WDM channels of interest through a set of algorithms. The DSP module recovers the best possible version of the transmitted information by compensating for channel impairments. The DSP algorithms are described in Chapter 3. The components of an SDM communication system are described in the following sections.

2.1 Pol-mux transmitter submodule (pol-mux TX)

The SDM transmitter is composed of WDM transmitter blocks that generate M_p polarization multiplexed optical signals that are later multiplexed by the spatial multiplexer. Within each WDM transmitter, pol-mux single-mode transmitter submodules generate N_{ch} optical signals that are wavelength-multiplexed. In each pol-mux TX, an input bit sequence is mapped into a specific digital constellation defined by the modulation format. In this thesis, we do not address coded modulation concepts. The digital symbol

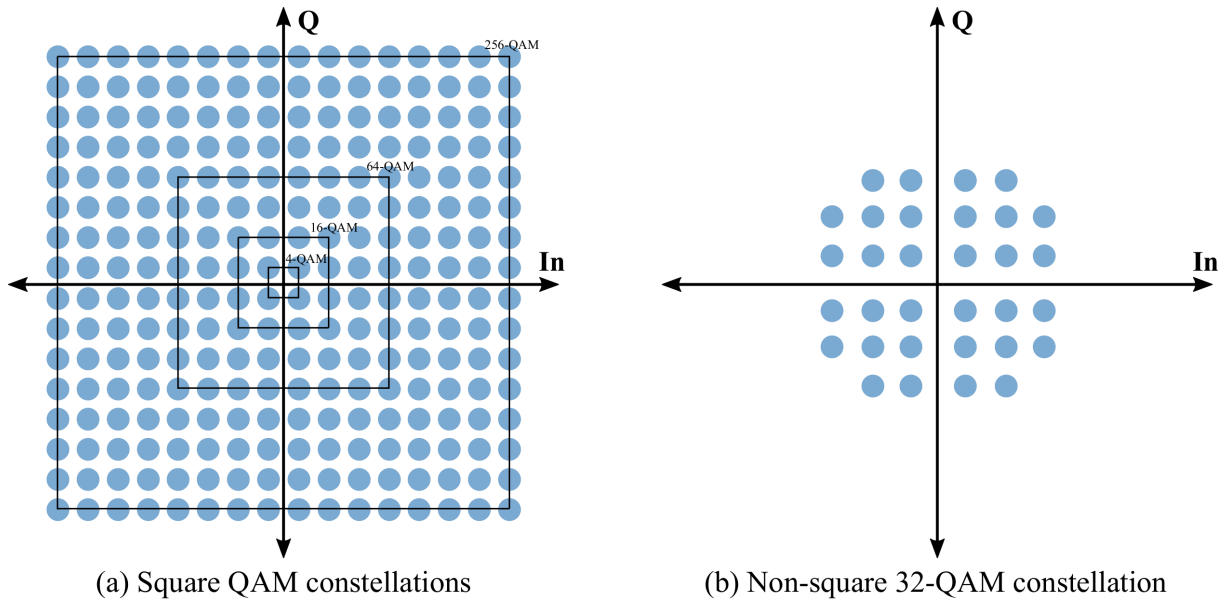


Figure 2.2 – QAM digital constellations. (a) Square 4-QAM, 16-QAM, 64-QAM, and 256-QAM constellations. (b) Non-square 32-QAM constellation.

sequence is passed through a pulse-shaping filter and then digital-to-analog converted. Later, the analog electric signal modulates an optical carrier coming from a continuous wave laser source. The modulated signals are finally multiplexed in wavelength by a WMUX and subsequently injected into the spatial multiplexer. The following sections describe the three main processes carried out by each transmitter submodule.

2.1.1 Constellation mapping

The available spectrum of the communication channels is limited. Therefore, the frequency bands for optical communication have to be efficiently used. Multilevel modulation formats are employed to optimize the available spectrum and increase the spectral efficiency by conveying several bits mapped to a single symbol. A robust digital modulation format frequently employed in coherent systems is the M -ary quadrature amplitude modulation (QAM) constellation, with M denoting the modulation order. In M -QAM constellations, the number of bits transmitted in each symbol is given by $k = \log_2 M$. As shown in (HAYKIN, 2001), symbols are mapped based on

$$s_i = \mathbf{A}_i + j\mathbf{B}_i \quad (2.1)$$

where $i = 1, 2, 3 \dots M$ points the location of the symbol within the constellation. In Eq. (2.1), j is the imaginary unit, and \mathbf{A} and \mathbf{B} are two vectors whose elements depend on the modulation scheme. Fig. 2.2 shows some examples of square and non-square QAM digital constellations.

The increment of the modulation format order increases the system spectral efficiency at the cost of reducing the distance among symbols or at the cost of increased

transmission power. The symbol distance reduction makes the system less robust to additive noise and phase perturbations. As a consequence of the lower noise tolerance of systems employing high-order constellations, higher levels of SNR are required for reliable communication. Usually, constellation mapping is performed by using the Gray coding scheme, which, when employed in high-order modulation formats, is susceptible to high levels of phase perturbations. Intense phase perturbations can cause cycle slips that result from significant rotations of the digital constellation (MEYR *et al.*, 1998). In square QAM constellations, the signal is invariant under a rotation of $2\pi/M$. Then, when random data is transmitted, the carrier synchronizer cannot distinguish between an angle θ and an angle θ plus an integer multiple of $2\pi/M$. This limitation produces catastrophic errors at reception as the symbols carry useful data information in their phases. An attractive mapping scheme known as differential encoding is employed to reduce the errors generated by very high phase noise levels. The working principle of the differential encoding is presented with details in (FATADIN *et al.*, 2010).

2.1.2 Digital-to-analog conversion and pulse shaping

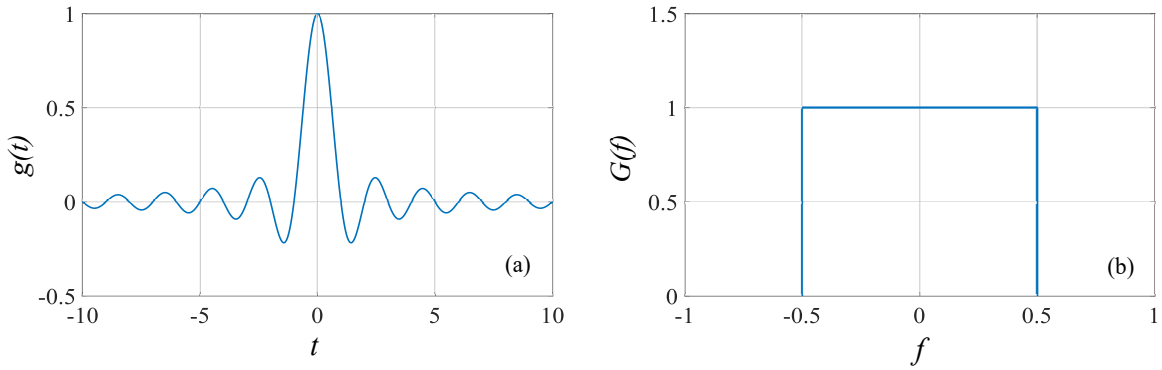
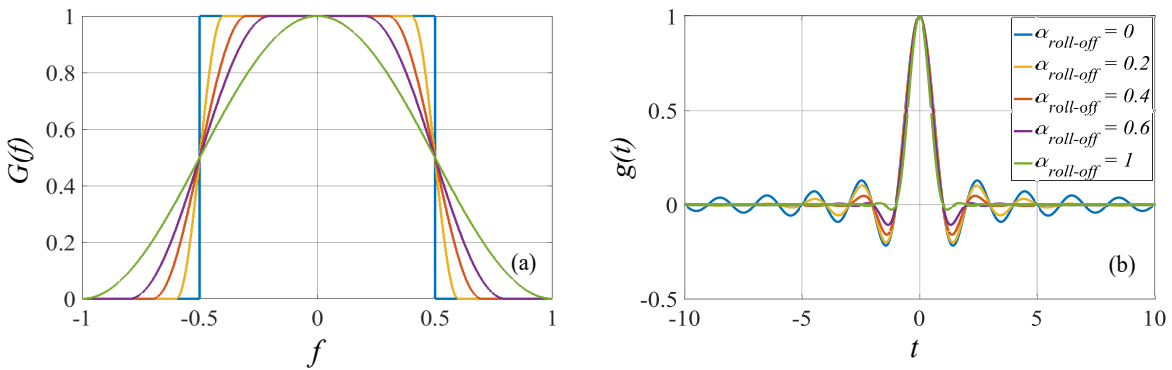
After constellation mapping, the digital symbol sequence is shaped by a pulse-shaping filter and subsequently converted into an analog electrical signal. The pulse-shaping filter prepares the electrical signal for electro-optical conversion and increases the spectral efficiency. The family of pulses known as Nyquist pulses provides high spectral efficiency. Nyquist pulse shaping prevents intersymbol interference during the modulation process while ensuring that the pulses do not occupy a frequency range much greater than the minimum required. Nyquist pulses are presented below.

2.1.2.1 Nyquist pulse shapes

The bandwidth required by a sequence of non-return-to-zero (NRZ) pulses that is transmitted at a symbol rate of R_s is approximately equal to $2R_s$. With a Nyquist pulse, on the contrary, a shaped sequence is ideally transmitted at a symbol rate of R_s over a bandwidth $W = R_s/2$. In general, according to Nyquist criterion, the symbol rate of a system with bandwidth W cannot exceed $2W$ symbols per second without intersymbol interference (ISI) (BARRY *et al.*, 2004). The restriction of a symbol rate to $2W$ symbols per second is the Nyquist rate. The impulse response of a Nyquist pulse with symbol period, T , and minimum transmission band, $1/2T$, is defined as

$$g(t) = \frac{\sin(\pi t/T)}{\pi t/T}, \quad (2.2)$$

which corresponds to a sinc function. The impulse response and the frequency response of a Nyquist pulse with $T = 1$ are shown in Fig. 2.3.

Figure 2.3 – Nyquist pulse with $T = 1$. (a) Impulse response. (b) Frequency response.Figure 2.4 – Raised cosine filter with $T = 1$ for several values of roll-off factor. (a) Frequency response. (b) Impulse response.

The ideal band-limited pulse that satisfies $W = R_s/2$ has an infinite duration, making its implementation impractical. Therefore, alternative pulse shapes are employed in practical implementations. This is the case of the widely used Nyquist raised cosine pulse, whose spectrum is given by

$$G(f) = \begin{cases} T, & \text{if } |f| \leq \frac{1-\alpha_{roll-off}}{2T} \\ T \cos^2 \left[\frac{\pi T}{2\alpha_{roll-off}} \left(|f| - \frac{1-\alpha_{roll-off}}{2T} \right) \right], & \text{if } \frac{1-\alpha_{roll-off}}{2T} < |f| < \frac{1+\alpha_{roll-off}}{2T} \\ 0, & \text{if } \frac{1+\alpha_{roll-off}}{2T} < |f| \end{cases} \quad (2.3)$$

where $\alpha_{roll-off}$ is the excess bandwidth parameter or commonly known as roll-off factor. The bandwidth of the raised cosine pulse can be controlled by the roll-off factor, resulting in an occupied bandwidth of $W = (R_s/2) \times (1 + \alpha_{roll-off})$. The minimum bandwidth Nyquist pulse is achieved for $\alpha_{roll-off} = 0$. In practical implementations, slightly higher roll-off factors are chosen, requiring a wider available bandwidth. Fig. 2.4a presents the frequency response of the raised cosine filter for several values of roll-off. The impulse response of a raised cosine filter is illustrated in Fig. 2.4b, and is defined as (HAYKIN, 2001)

$$g(t) = \left(\frac{\sin(\pi t/T)}{\pi t/T} \right) \left(\frac{\cos(\alpha_{roll-off} \pi t/T)}{1 - (2\alpha_{roll-off} t/T)^2} \right). \quad (2.4)$$

Raised cosine filters are commonly used in current communications systems. Generally, the most used configuration to avoid ISI consists in implementing a root-raised-cosine (RRC) filter at the transmitter and a RRC filter as a matched filter at the receiver to filter additive white gaussian noise (AWGN) (BARRY *et al.*, 2004). The RRC spectrum is obtained by taking the square root of $G(f)$ in Eq. (2.3).

2.1.3 Optical modulation

The waveform at the output of the RRC filter modulates a continuous wave coming from a laser source. The modulation process can be carried out directly on the laser source through a direct modulation scheme. Direct modulation is characterized by the interrupted operation of the optical source (on-off) based on the information signal. This operation principle makes direct modulation inexpensive and straightforward. Nonetheless, direct modulation is impaired by chirp that causes spectral broadening and limits the transmission rate.

On the other hand, externally-modulated laser sources are conveniently employed to circumvent large amounts of chirp experienced by the pulses during direct modulation (RAMASWAMI *et al.*, 2010) and minimize bandwidth limitations. In external modulation, the information signal modulates a continuously operated light source using an additional device. Although external modulation reduces the chirp of the pulse, the need for more components makes this approach more expensive and complex. The main components of an external modulator are described below.

2.1.3.1 Semiconductor lasers

The optical transmitter converts the electric input signal into an optical signal before launching it through the channel. The optical source that generates the light for modulation and transmission is a critical transmitter component. Currently, semiconductor lasers are often used as light sources in optical systems. Three processes govern the operating principle of a semiconductor laser: absorption, spontaneous emission, and stimulated emission. Fig. 2.5 illustrates the three atomic processes. Consider an atom and two energy levels, E1 and E2, known as ground state and excited state, respectively (DEMTRÖDER, 2005). When an incident photon from an external electromagnetic field has an energy equal to the energy difference between states E1 and E2, it is absorbed by the atom, which moves from E1 to E2. There are two types of light emission, stimulated emission and spontaneous emission. In spontaneous emission, an atom moves from E2 to E1 without any external radiation. During the transition from E2 to E1, the atom emits photons with random phases and directions, called non-coherent photons. In contrast, in the stimulated emission process, an incident photon triggers the emission of photons with

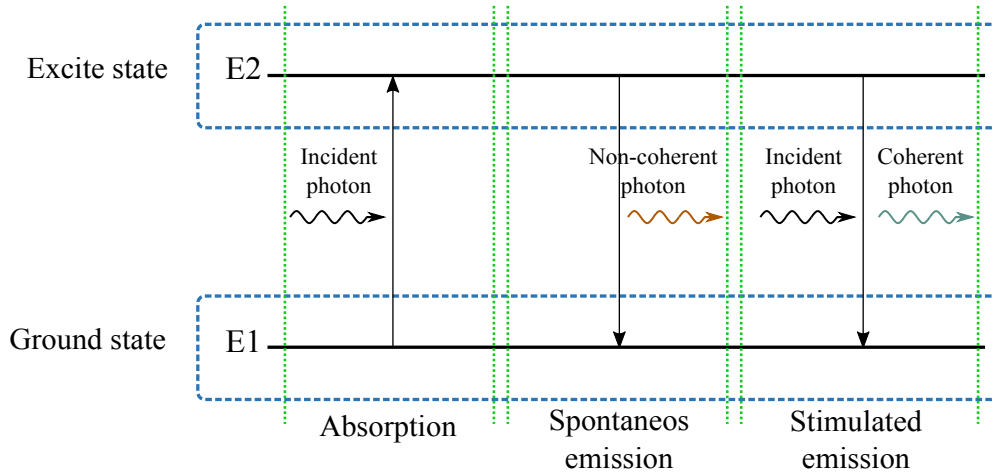


Figure 2.5 – Atomic processes involved in laser light emission: absorption, spontaneous emission and stimulated emission.

the same characteristics as the incident photon regarding energy, frequency, polarization, and propagation direction. The stimulated emission is the amplification principle of the laser devices, which receive their name from light amplification by stimulated emission of radiation (LASER).

The thermal equilibrium of a medium guarantees that the atomic density of the excited state is lower than the atomic density of the ground state. If there are no significant atoms at the highest energy level, the stimulated emission process is not dominant. Therefore, for the laser to work, it is necessary to pump energy into the semiconductor material so that the atomic density of the excited level is greater than the ground state, an effect known as population inversion (AGRAWAL, 2002). Although the stimulated emission leads to the generation of coherent light, non-coherent light is also generated by spontaneous emission during the laser operation process causing transmission impairments that must be accounted at reception.

Distributed feedback lasers (DFBs) (KOGELNIK; SHANK, 1972), (YEN *et al.*, 1973), (MROZIEWICZ *et al.*, 2017), external cavity lasers (ECLs) (FLEMING; MOORADIAN, 1981), and vertical-cavity surface-emitting lasers (VCSELs) (FAVRE *et al.*, 1986), (MOORADIAN, 1991), (TROPPEL *et al.*, 2004), (AGRAWAL, 2002), (RAMASWAMI *et al.*, 2010) are devices commonly used as light sources at the transmitter and local oscillator (LO).

2.1.3.2 External Mach-Zehnder modulator

The external Mach-Zehnder modulator (MZM) is an interferometric structure that performs intensity modulation using the principle of interference. The schematic of a MZM is depicted in Fig. 2.6a. The light entering the MZM is split into two paths. Each path comprises a phase modulator. The phase modulation in both paths depends on the

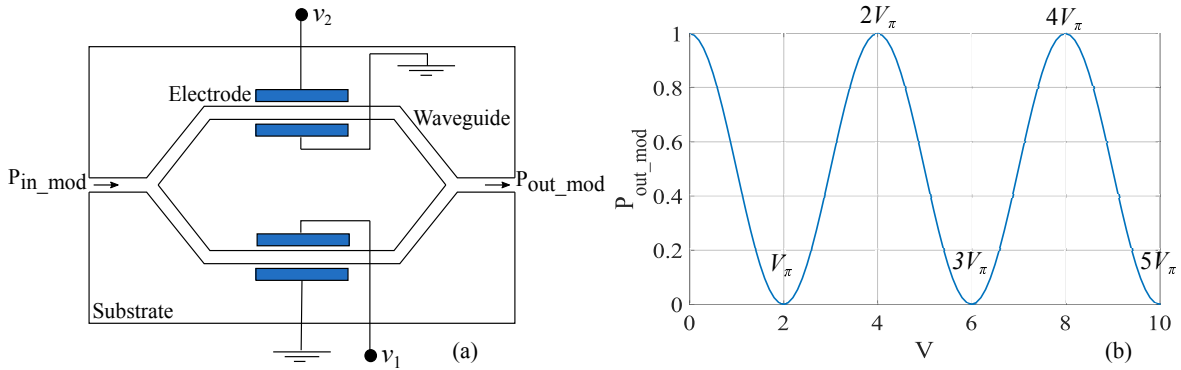


Figure 2.6 – Mach-Zehnder modulator (a) Schematic diagram. (a) Output power as a function of the applied voltage.

waveguide refractive index. Varying the refractive index by means of the application of an external voltage allows controlling the phase shift between paths in such a way that after recombining the two electric fields and depending on the relative phase delay between the two arms, the combination results in constructive or destructive interference. In practice, the driving voltage required to apply a π radians phase shift is denoted by V_π , which is equal for both phase modulators.

In the pull-push configuration, two voltages are applied such that $v_1 = -v_2 = V$, with V related to the output power as

$$P_{\text{out_mod}} = P_{\text{in_mod}} \cos^2 \left(\frac{\pi V}{2V_\pi} \right). \quad (2.5)$$

Note that for v_1 and v_2 that make V equal to $(2k + 1) \times V_\pi$ with $k \in 0, 1, 2, \dots$, the resulting interference between both arms is totally destructive and there is no output power. In contrast, when V is $(2k) \times V_\pi$ with $k = 0, 1, 2, \dots$, both arms interfere constructively and the output power is maximum. Fig. 2.6b shows the MZM output power as a function of V .

The MZM can modulate only the amplitude and polarity of the optical carrier. This functionality would be sufficient for on-off keying (OOK) and binary phase shift keying (BPSK) modulation formats. Nevertheless, for QAM constellations, both in-phase and quadrature components of the optical carrier have to be modulated. Therefore, for higher-order modulation formats, a different structure is designed from the combination of two MZMs. The in-phase and quadrature modulator (IQM) is shown in Fig. 2.7a. In an IQM, the input signal is equally divided between the in-phase (I) and quadrature (Q) arms. The signal through the quadrature arm passes through a phase modulator that introduces a $\pi/2$ radians phase shift so that the signal modulated in the MZM of arm Q is orthogonal to the signal modulated in the MZM of arm I. Finally, the signals are recombined at the output of the modulator.

In a polarization multiplexing system, the electro-optical conversion integrates two

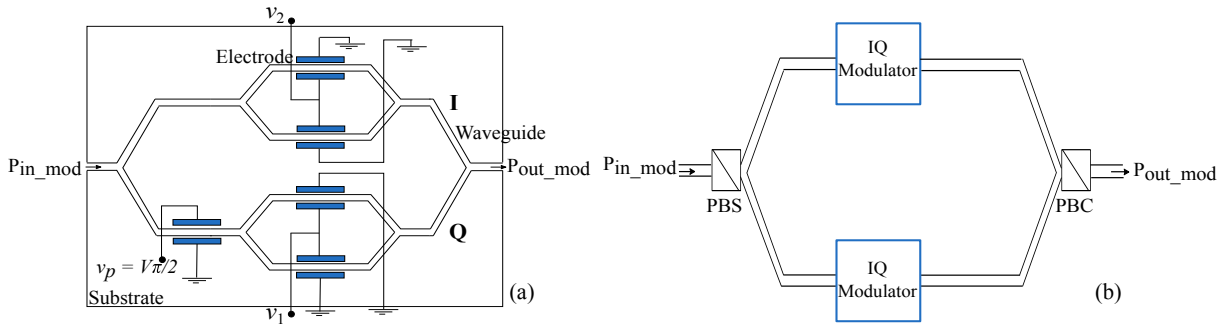


Figure 2.7 – In-phase and Quadrature modulator (a) Schematic diagram. (a) Polarization multiplexing configuration. PBS and PBC stand for polarization beam splitter and polarization beam combiner, respectively.

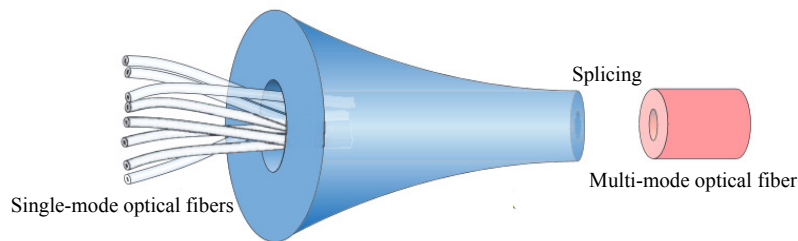


Figure 2.8 – Illustrative example of a photonic lantern. Adapted from (RICHARDSON, 2016).

IQM, as illustrated in Fig. 2.7b. At the input of the modulator, a polarization beam splitter (PBS) splits the input signal into two different arms, which are independently modulated by an IQM. After modulation, the output signals are again recombined through a polarization beam combiner (PBC).

2.2 Spatial multiplexers

The photonic lantern (PL) is one of the most common spatial multiplexers/demultiplexers employed in SDM setups due to its low footprint and low insertion losses that can be less than 1 dB in 3-mode multiplexers. The PL is composed of a bundle of single-mode fibers adiabatically tapered to form a single glass body that progressively reduces its cross-sectional dimension to form a MMF or FMF core. Fig. 2.8 shows an illustrative example of a PL. During the taper transition, light propagating through the single-mode cores evolves into a linear combination of the MMF/FMF modes at the lantern output (BIRKS *et al.*, 2015). Mode selectivity in PLs is achieved during the fabrication process, in which the use of different single-mode core diameters allows the selective excitation of a specific mode group (VELÁZQUEZ-BENÍTEZ *et al.*, 2018). As the number of modes increases, the design of the PL becomes more challenging in terms of geometry, losses, and MDL. The experimental demonstration in (VELÁZQUEZ-BENÍTEZ *et al.*, 2018) reports the multiplexing of up to 15 modes.

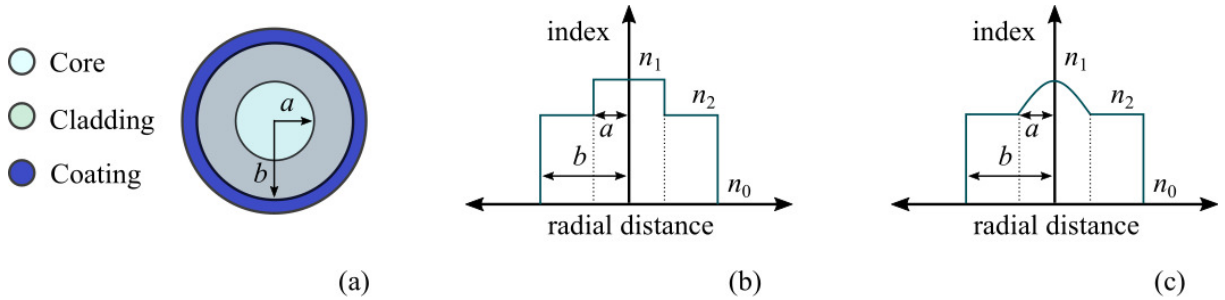


Figure 2.9 – Optical channel. (a) Cross section of an optical fiber. (b) Refractive index profile of a step-index fiber. (c) Refractive index profile of a graded-index fiber.

Phase plates based solutions (RYF *et al.*, 2011a) and spot launching (RYF *et al.*, 2012a) are also two promising approaches for mode multiplexing (FONTAINE *et al.*, 2022).

2.3 Optical channel

The optical fiber is a cylindrical dielectric waveguide that guides electromagnetic energy in light frequencies. An optical fiber is composed of three components as shown in Fig. 2.9a: core, cladding, and jacket. One of the most important characteristics of optical fibers is the refractive index profile that depends on the relation between the refractive index of the core, n_1 , and cladding, n_2 . If the boundary between core and cladding is abrupt, the fiber presents a step-index profile as depicted in Fig. 2.9b. In contrast, in Fig. 2.9c, a graded-index profile is illustrated, which is characterized by having a gradually decreasing refractive index for increasing radius.

Optical fibers are also classified based on the number of supported propagation modes. Under this criterion, optical fibers can be classified as SMF, MMF, and FMF. SMFs support the propagation of a single mode known as the fundamental mode. On the contrary, many modes can propagate through a MMF. High transmission multiplicity provided by MMFs can significantly increase channel capacity while requiring an increased transmitter and receiver complexity. FMFs support a reduced number of propagation modes to alleviate complexity constraints. Guaranteeing a certain number of supported modes requires special guidelines during manufacturing so that the optical fiber meets particular conditions. The following sections review the concept of propagation modes in optical fibers and the linear and non-linear impairments experienced by the signal during transmission. Besides, characteristics of the optical fibers manufactured for SDM transmission are presented.

2.3.1 Propagation modes in optical fibers

The study of the propagation modes in optical fibers can be performed by solving the wave equation.

2.3.1.1 Wave equation

Maxwell's equations govern the propagation of light in optical fibers. For this analysis, the optical fiber medium is assumed to be linear, isotropic, time-invariant, and free of charges (RAMASWAMI *et al.*, 2010). Under these assumptions, the four Maxwell's equations are defined as (AGRAWAL, 2002)

$$\nabla \times \mathbf{E} = -\frac{\partial \mathbf{B}}{\partial t} \quad (2.6)$$

$$\nabla \times \mathbf{H} = \frac{\partial \mathbf{D}}{\partial t} + \mathbf{J} \quad (2.7)$$

$$\nabla \cdot \mathbf{D} = \rho, \quad (2.8)$$

$$\nabla \cdot \mathbf{B} = 0, \quad (2.9)$$

where $\nabla \times$ and $\nabla \cdot$ represent the curl and divergence operators, respectively. \mathbf{E} (V/m) and \mathbf{H} (A/m) are the electric and magnetic field vectors, and \mathbf{D} (C/m²) and \mathbf{B} (Wb/m²) are the electric and magnetic flux densities, respectively. Assuming that the silica is a dielectric medium without free charges, the surface current density, \mathbf{J} (A/m²), and the volume density of free charges, ρ (C/m³), are equal to zero.

The flux densities are related to the field vectors via permittivity, ϵ_0 , and permeability, μ_0 , of the vacuum through the constitutive relations according to

$$\mathbf{D} = \epsilon_0 \mathbf{E} + \mathbf{P}, \quad (2.10)$$

$$\mathbf{B} = \mu_0 \mathbf{H} + \mathbf{M}, \quad (2.11)$$

where \mathbf{P} and \mathbf{M} are the induced electric and magnetic polarizations, respectively. As a consequence of the nonmagnetic nature of silica glass, $\mathbf{M} = 0$ in Eq. (2.11) for optical fibers.

Neglecting nonlinear effects in optical fibers, the relation between \mathbf{P} and \mathbf{E} can be expressed as

$$\mathbf{P}(\mathbf{r}, t) = \epsilon_0 \int_{-\infty}^{\infty} \chi(\mathbf{r}, t - t') \mathbf{E}(\mathbf{r}, t') dt', \quad (2.12)$$

where χ is the linear susceptibility of the medium and \mathbf{r} is the position vector.

Using the constitutive relations, Eq. (2.10) and Eq. (2.11), and the Maxwell's rotational equations, Eq. (2.6) and Eq. (2.7), the wave equation as a function of \mathbf{E} , can be obtained as (AGRAWAL, 2002)

$$\nabla \times (\nabla \times \mathbf{E}) = -\frac{1}{c^2} \frac{\partial^2 \mathbf{E}}{\partial t^2} - \mu_0 \frac{\partial^2 \mathbf{P}}{\partial t^2}, \quad (2.13)$$

where the speed of light in vacuum is given by $c = (\epsilon_0 \mu_0)^{-1/2}$.

Eq. (2.13) can be rewritten in the frequency domain as

$$\nabla \times (\nabla \times \tilde{\mathbf{E}}) = -\epsilon(\mathbf{r}, \omega) \left(\frac{\omega^2}{c^2} \right) \tilde{\mathbf{E}}, \quad (2.14)$$

where the frequency-dependent dielectric constant, $\epsilon(\mathbf{r}, \omega)$, is defined as a function of the Fourier transform of $\chi(\mathbf{r}, t)$ through

$$\epsilon(\mathbf{r}, \omega) = 1 + \tilde{\chi}(\mathbf{r}, \omega) \quad (2.15)$$

The frequency-dependent dielectric constant, $\epsilon(\mathbf{r}, \omega)$, is defined as

$$\epsilon(\mathbf{r}, \omega) = \left(n + \frac{j\alpha c}{2\omega} \right)^2, \quad (2.16)$$

where n is the refractive index of the medium and α is the absorption coefficient.

As silica fibers present low optical loss, α is assumed to be zero for deriving field profiles, then, the frequency-dependent dielectric constant is redefined as

$$\epsilon(\mathbf{r}, \omega) = n^2(\omega). \quad (2.17)$$

Replacing Eq. (2.17) in Eq. (2.14), the wave equation can be written as

$$\nabla \times (\nabla \times \tilde{\mathbf{E}}) = \frac{\omega^2}{c^2} n^2(\omega) \tilde{\mathbf{E}}. \quad (2.18)$$

Using the identity

$$\nabla \times (\nabla \times \tilde{\mathbf{E}}) \equiv \nabla(\nabla \cdot \tilde{\mathbf{E}}) - \nabla^2 \tilde{\mathbf{E}}, \quad (2.19)$$

and assuming that $\nabla \cdot \tilde{\mathbf{E}} = 0$ in a medium free of charges, the following wave equation, also known as Helmholtz equation for a homogeneous medium, is obtained (AGRAWAL, 2002)

$$\nabla^2 \tilde{\mathbf{E}} + n^2(\omega) \frac{\omega^2}{c^2} \tilde{\mathbf{E}} = 0. \quad (2.20)$$

A similar procedure can be performed to get the Helmholtz equation for the magnetic field, \mathbf{H} , given by

$$\nabla^2 \tilde{\mathbf{H}} + n^2(\omega) \frac{\omega^2}{c^2} \tilde{\mathbf{H}} = 0. \quad (2.21)$$

Introducing the wave number, $k = 2\pi/\lambda$, defined as

$$k = k_0 n = \omega \sqrt{\epsilon_0 \mu_0} n = \frac{\omega n}{c}, \quad (2.22)$$

where $k_0 = 2\pi/\lambda_0$ is the wave number in vacuum and λ_0 is the wavelength in vacuum. Then, the wave equations for the electrical and magnetic fields of Eq. (2.20) and Eq. (2.21) are also expressed by (AGRAWAL, 2002)

$$\nabla^2 \tilde{\mathbf{E}} + k^2 \tilde{\mathbf{E}} = 0, \quad (2.23)$$

and

$$\nabla^2 \tilde{\mathbf{H}} + k^2 \tilde{\mathbf{H}} = 0. \quad (2.24)$$

An optical mode is a specific solution of the wave equation that satisfies the appropriate boundary conditions and at the same time travels through an optical fiber with a spatial distribution that does not change with propagation. For the sake of simplicity, a step-index profile is assumed. Solving the wave equation for the full electromagnetic field provides the components $\tilde{E}_x, \tilde{E}_y, \tilde{E}_z, \tilde{H}_x, \tilde{H}_y, \tilde{H}_z$. Using the cylindrical system of coordinates and the method of separation of variables, each component can be expressed as the product of three independent functions. For example for \tilde{E}_x as

$$\tilde{E}_x(r, \phi, z) = R(r)\Phi(\phi)Z(z), \quad (2.25)$$

where r is the radial component, ϕ is the azimuthal component, and z is the longitudinal component. The longitudinal component has a solution of the form $Z = e^{j\beta z}$, where β is the modal propagation constant.

At a particular frequency component, ω , fields $\tilde{\mathbf{E}}$ and $\tilde{\mathbf{H}}$ are obtained through

$$\tilde{\mathbf{E}}(r, \phi, z) = \tilde{E}_x(r, \phi, z)\mathbf{x} + \tilde{E}_y(r, \phi, z)\mathbf{y} + \tilde{E}_z(r, \phi, z)\mathbf{z}, \quad (2.26)$$

and

$$\tilde{\mathbf{H}}(r, \phi, z) = \tilde{H}_x(r, \phi, z)\mathbf{x} + \tilde{H}_y(r, \phi, z)\mathbf{y} + \tilde{H}_z(r, \phi, z)\mathbf{z}, \quad (2.27)$$

where $\mathbf{x}, \mathbf{y}, \mathbf{z}$ are unit vectors pointing toward directions x, y and z .

Using the weakly guiding approximation that is often adopted for step-index profile fibers, in which the refractive index of the core and cladding are very close, the modes are considered linearly polarized (LP). For LP modes, the longitudinal field components \tilde{E}_z and \tilde{H}_z are negligible compared to their respective transverse components (GLOGE, 1971). Under the LP approximation, in the transverse section of the fiber, for $\tilde{E}_y = 0$, the signal is linearly polarized in the x direction, and for $\tilde{E}_x = 0$, the signal is linearly

polarized in the y direction. Then, for $\tilde{E}_x = 0$, $\tilde{E}_y(r, \phi)$ can be approximated by (GLOGE, 1971), (MELLO; BARBOSA, 2021)

$$\tilde{E}_y(r, \phi) = E_l \left[\begin{array}{c} J_l(ur/a)/J_l(u) \\ K_l(wr/a)/K_l(w) \end{array} \right] \cos(l\phi), \quad (2.28)$$

where J_l is the Bessel function of the first kind, K_l is the modified Bessel function of the second kind, l is the number of oscillations in the azimuthal direction, a is the fiber core radius, and E_l is the intensity of the electric field at the core-cladding interface. The upper expression corresponds to the field in the core and the lower expression to the field in the cladding. Other solutions are obtained using $\sin(l\phi)$ instead of $\cos(l\phi)$ in Eq. (2.28). Parameters u and w are constants related to core and cladding properties as

$$u = a\sqrt{(k_0n_1)^2 - \beta^2}, \quad (2.29)$$

and

$$w = a\sqrt{\beta^2 - (k_0n_2)^2}. \quad (2.30)$$

To find the propagation constant β for each mode, the boundary conditions of the tangential fields at the core-cladding interface are applied. Under the weakly guiding approximation, the boundary condition reduces to (GLOGE, 1971)

$$u \frac{J_{l-1}(u)}{J_l(u)} = -w \frac{K_{l-1}(w)}{K_l(w)}. \quad (2.31)$$

From the constants u and w , it is possible to obtain the normalized frequency of the modes, V , defined as

$$V = \sqrt{u^2 + w^2} = ak\sqrt{(n_1^2 - n_2^2)}. \quad (2.32)$$

For a given normalized frequency, V , Eq. (2.31) presents several solutions. These solutions correspond to the propagation constants of the modes supported by the fiber. The propagation LP modes are labeled with integers indices, l, m as LP_{lm} , where l denotes the number of sign changes of the amplitude along the azimuthal axis, and m is the number of sign changes in the radial direction which determines the index of the solution.

The normalized frequency is directly related to the number of modes supported by a step-index optical fiber. The higher the V , the larger the number of modes supported by the fiber. At $V \leq 2.405$, only the mode with $m = 0$ is accepted by the fiber. This cut-off frequency is known as the single-mode condition, and fibers of this type are called SMF.

A modal map is a helpful tool for visualizing the generation of modes with increasing frequencies. The modal map plots normalized propagation constants as a function of the normalized frequency. The normalized propagation constant, b , is defined as

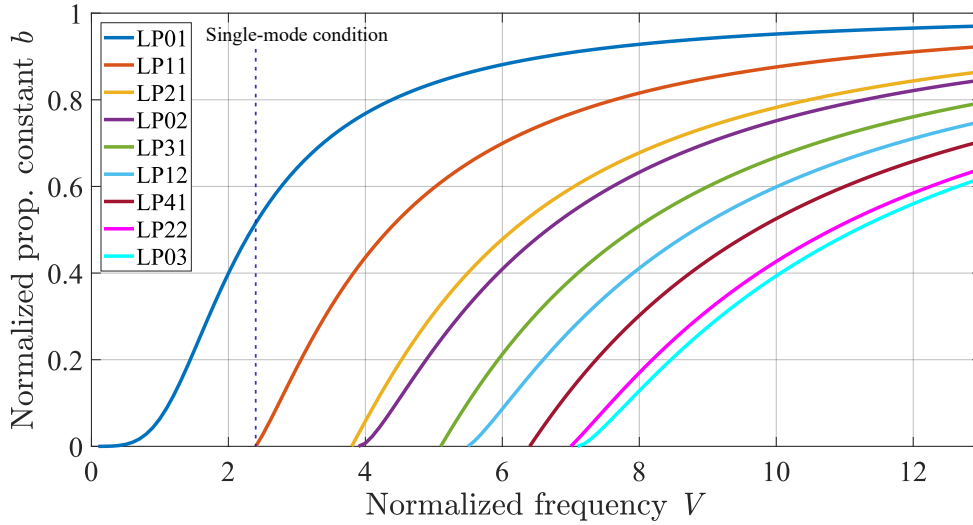


Figure 2.10 – Modal map for a step-index fiber with linearly polarized modes.

$$b(V) = 1 - (u^2 - V^2) \approx \frac{\beta/k - n_2}{n_1 - n_2}. \quad (2.33)$$

Fig. 2.10 shows the modal map for a weakly guiding step-index fiber with linearly polarized modes. The points where the curves intersect the $y = 0$ line indicate the cut-off frequency for each mode. The number of supported modes increases with the normalized frequency V . The relation between the first 10 LP_{tm} modes and the cut-off normalized frequency is depicted in Table 2.1. Ideally, degenerate modes share the same propagation constant and travel with the same group velocity through the fiber. The polarization orientations give the first grade of degeneracy. The second grade is the spatial degeneracy denoted with the sub-index “a” and “b”. Fig. 2.11 shows the mode field profiles of the first 15 LP modes computed by employing Eq. (2.28).

Group	LP mode	V cut-off	Degenerate modes
1	LP_{01}	-	2
2	LP_{11}	2.4	4
3	LP_{21}	3.8	4
	LP_{02}	3.9	2
4	LP_{31}	5.1	4
	LP_{12}	5.5	4
5	LP_{41}	6.4	4
	LP_{22}	7.0	4
	LP_{03}	7.1	2

Table 2.1 – Relation between LP modes and normalized frequency.

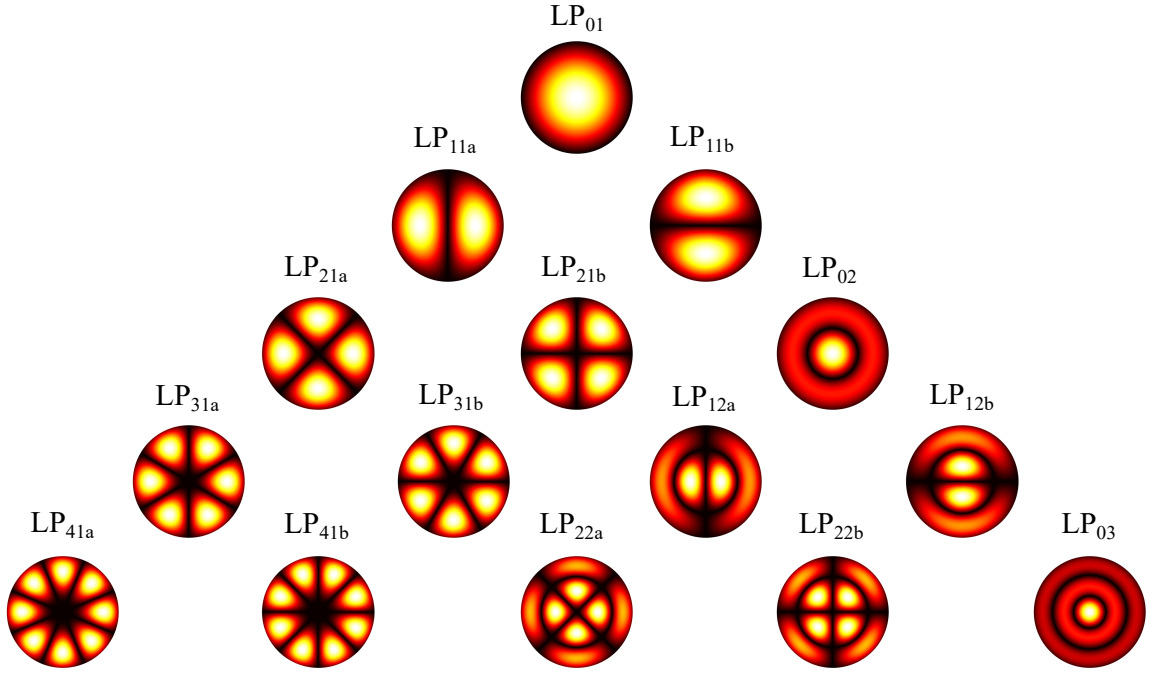


Figure 2.11 – Mode profiles of the first 15 LP modes.

2.3.2 Pulse propagation

Consider an optical fiber with electric field intensity, \mathbf{E} [V/m], propagation constant in z direction, β , and attenuation coefficient, α . Then, pulse propagation through the optical fiber can be described by the generalized nonlinear Schrödinger equation (GNSE) (AGRAWAL, 2011)

$$\frac{\partial \mathbf{E}}{\partial z} = -\frac{\alpha}{2} \mathbf{E} - \beta_1 \frac{\partial \mathbf{E}}{\partial t} - j \frac{\beta_2}{2} \frac{\partial^2 \mathbf{E}}{\partial t^2} + \frac{\beta_3}{6} \frac{\partial^3 \mathbf{E}}{\partial t^3} + j \gamma |\mathbf{E}|^2 \mathbf{E}, \quad (2.34)$$

where γ is the non-linear parameter of the fiber given in units [W^{-1}m]. The non-linear parameter is defined as a function of the non-linear Kerr parameter, \bar{n}_2 , with units [m^2/W], and the effective area of the fiber, A_{eff} , as

$$\gamma = \frac{\bar{n}_2 \omega}{c A_{eff}}. \quad (2.35)$$

On the right side of the GNSE in Eq. (2.34), we have, from left to right, the terms describing attenuation, group delay (GD), group-velocity dispersion (GVD), dispersion slope, and Kerr non-linearity. The physical effects related to the main components of Eq. (2.34) are described in the following sections.

2.3.3 Attenuation

As a consequence of fiber losses, the transmitted signal experiences attenuation. Attenuation is characterized by the reduction of the signal power with the distance. The attenuation is one of the most critical impairments experienced by the signal during

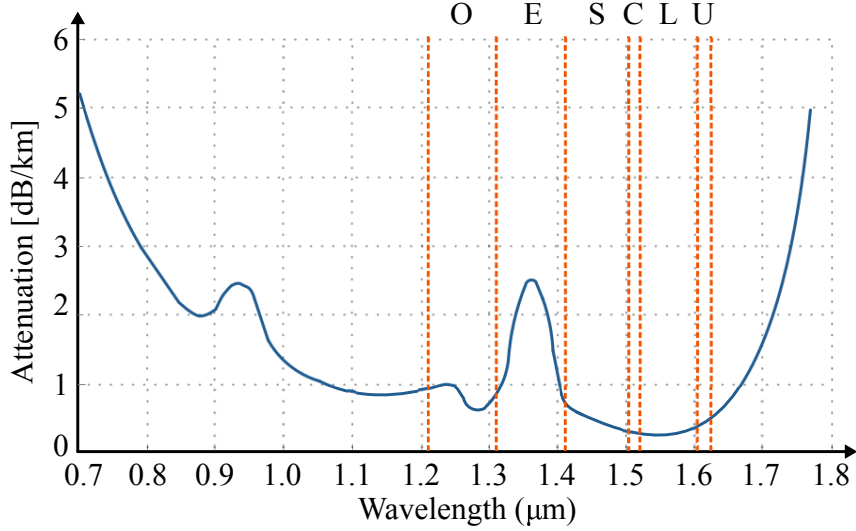


Figure 2.12 – Attenuation profile of a standard single-mode fiber (SSMF) as a function of the frequency bands (MELLO; BARBOSA, 2021).

propagation. This effect must be carefully studied as a design parameter for optical communication systems since it is directly related to the maximum achievable distance between the transmitter, intermediate amplifiers, and receiver. The sensitivity parameter of the receiver determines the minimum amount of power required at the receiver side for recovering the signal for a specific bit error rate (BER), limiting the link length. As a consequence of the attenuation, intermediate amplifiers are required to compensate for accumulated losses. Nevertheless, each amplification stage contributes to additional system costs (AGRAWAL, 2002) and noise.

To characterize the fiber losses, the attenuation coefficient α is defined in [Np/km] as (SALEH, 1991), (AGRAWAL, 2002)

$$\frac{dP_{av}}{dz} = -\alpha P_{av}, \quad (2.36)$$

where P_{av} is the signal average optical power and z the propagation distance. For an input launch power, P_{in} , through a fiber with length, L_f , the output power P_{out} is given by

$$P_{out} = P_{in} e^{-\alpha L_f}. \quad (2.37)$$

From Eq. (2.37), the attenuation coefficient in [dB/km] is

$$\alpha_{[dB/km]} = -\frac{10}{L_f} \log_{10} \frac{P_{out}}{P_{in}}. \quad (2.38)$$

Fiber losses result from the contribution of several phenomena; mainly absorption, Rayleigh scattering, and bending losses. Absorption losses are intrinsic to the fiber and come from the absorption of the fiber material and the impurities of the silica (KECK, 1985). Rayleigh scattering arises from the microscopic variations in the material density

that produce a fluctuation in the refractive index (BAGAD, 2007), (BORN; WOLF, 2013). Bends of the fiber, which are classified as macro bending (RENNER, 1992), (FAUSTINI; MARTINI, 1997) or micro bending (GARDNER, 1975), also contribute to the propagation losses. The combination of absorption and Rayleigh scattering gives rise to the attenuation profile of a SSMF. Fig. 2.12 shows the attenuation profile for the wavelength window between $0.7 \mu\text{m}$ and $1.8 \mu\text{m}$ in a SSMF. From the spectral range contained between 1100 nm and 1700 nm, the International Telecommunications Union (ITU) assigns six spectral bands, as illustrated in Fig. 2.12. The low attenuation over the regions from 1530 nm to 1565 nm and from 1565 nm to 1625 nm makes the C and L bands the most suitable bands for long-haul transmission (NAGAYAMA *et al.*, 2002).

2.3.4 Group delay

The mode LP_{lm} propagates through the optical fiber with propagation constant β_{lm} . Consider the Taylor expansion of the propagation constant for mode LP_{lm} around an angular frequency of interest, ω_0 , as

$$\beta_{lm}(\omega) = \beta_{lm}^{(0)} + \beta_{lm}^{(1)}(\omega - \omega_0) + \frac{\beta_{lm}^{(2)}}{2}(\omega - \omega_0)^2 + \frac{\beta_{lm}^{(3)}}{6}(\omega - \omega_0)^3 + \dots, \quad (2.39)$$

where

$$\beta_{lm}^{(i)}(\omega) = \left(\frac{d^i \beta_{lm}(\omega)}{d\omega^i} \right) \Bigg|_{\omega=\omega_0}. \quad (2.40)$$

The group velocity of the transmitted pulse over the mode LP_{lm} is given by

$$v_{g,lm} = \frac{1}{\beta_{lm}^{(1)}}. \quad (2.41)$$

The GD of the mode LP_{lm} after transmission over a fiber of length L_f is

$$\tau_{lm} = \frac{L_f}{v_{g,lm}}. \quad (2.42)$$

Under ideal conditions, in the absence of mode coupling, the differential group delay (DGD) between modes a and b is defined as

$$\text{DGD} = \tau_a - \tau_b. \quad (2.43)$$

In the scope of spatial propagation fields, the term DMD is more suitable to refer to the DGD between modes. DMD in SDM transmissions leads to pulse broadening increasing the time response of the channel. When several modes are excited in the optical fiber, the DMD is given by the difference between the fastest mode and the slowest mode.

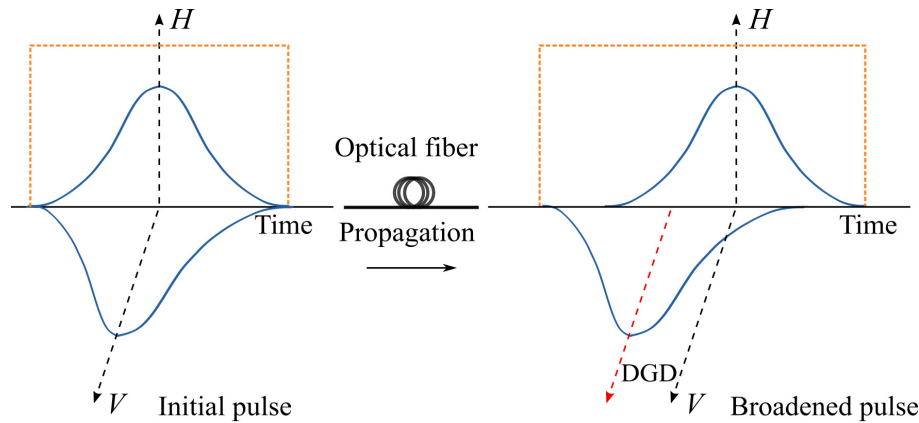


Figure 2.13 – Polarization mode dispersion. The transmitted pulse is broadened after propagation.

In single-mode optical fibers, DGD leads to a polarization effect known as PMD. In SMFs, the fundamental mode is composed of two orthogonally polarized components. These two polarization orientations are called vertical and horizontal polarizations, commonly labeled as V and H . Over ideal conditions, through a perfect optical fiber with circular symmetry and without imperfections, both polarizations propagate with identical group velocities receiving the name of degenerate modes. However, in practice, as a consequence of external stresses, fabrication irregularities, and installation processes, the fiber cross-section deviates from circular to elliptical, resulting in birefringence. In a birefringent fiber, orthogonal polarizations travel with different group velocities, giving rise to the concept of fast and slow axes. Consequently, one of the polarization orientations arrives earlier at the link end, generating a pulse broadening known as PMD (RASHLEIGH; ULRICH, 1978), (POOLE; WAGNER, 1986), (GALTAROSSA, 2005). Fig. 2.13 shows the pulse broadening after propagation generated by PMD.

Polarization dispersion and modal dispersion have a stochastic nature. Therefore, to compensate for both impairments, an adaptive equalizer whose coefficients are dynamically updated is employed to track the time-varying characteristics of the transmission channel.

2.3.5 Group velocity dispersion

The third component of the GNSE accounts for the difference between the group velocity of the distinct spectral components of the propagating pulse. In an optical fiber, the refractive index is wavelength-dependent. Therefore, as the light pulse is composed of different spectral components, groups of wavelengths propagate with different velocities, arriving at different times at the receiver. This phenomenon, known as group-velocity dispersion (GVD) or chromatic dispersion, generates pulse broadening. Chromatic dispersion is the result of the contribution of material dispersion and waveguide dispersion

(SHAPIRO, 1975), (SABRA, 1981), (CANTOR, 1983). Material dispersion results from the frequency dependence of the refractive index of the silica. On the other hand, waveguide dispersion takes place when the pulse energy does not propagate entirely in the core due to the geometric properties of the fiber (RAMASWAMI *et al.*, 2010).

To model the CD experienced by a propagation mode, consider the transmission of a pulse with spectral linewidth, $\Delta\omega$ over an optical fiber of length L_f . A specific spectral component at the frequency ω arrives at the end of the fiber after a time delay $T_d = L_f / v_g$, where v_g is the group velocity (AGRAWAL, 2002).

The propagation constant, β , can be related to the angular frequency, ω , speed of light, c , and effective index of the fiber, \bar{n} , as follows

$$\beta = \bar{n} \frac{\omega}{c}. \quad (2.44)$$

Then, the pulse broadening, ΔT , is found as

$$\begin{aligned} \Delta T &= \frac{dT_d}{d\omega} \Delta\omega \\ &= \frac{d}{d\omega} \left(\frac{L_f}{v_g} \right) \Delta\omega \\ &= L_f \frac{d^2\beta}{d\omega^2} \Delta\omega \\ &= L_f \beta_2 \Delta\omega, \end{aligned} \quad (2.45)$$

where $\beta_2 = d^2\beta/d\omega^2$ is known as the GVD parameter. Eq. (2.45) can be rewritten in terms of the bandwidth of the transmitted signal, $\Delta\lambda$, (AGRAWAL, 2002) as

$$\Delta T = \frac{d}{d\lambda} \left(\frac{L_f}{v_g} \right) \Delta\lambda = DL_f \Delta\lambda. \quad (2.46)$$

The dispersion parameter, D , that results of the contribution of material dispersion, D_m , and waveguide dispersion, D_w , is expressed in units of [ps/(km · nm)] as

$$D = D_m + D_w = -\frac{2\pi c}{\lambda^2} \beta_2 \quad \text{ps}/(\text{km} \cdot \text{nm}). \quad (2.47)$$

The dispersion map for SSMF is depicted in Fig. 2.14. The combination of both contributions results in $D = 0$ near 1330 nm, and approximately 17 [ps/(km · nm)] around 1550 nm (AINSLIE; DAY, 1986).

Dispersion compensating fibers (DCFs) are often used to mitigate CD (GRUNER-NIELSEN *et al.*, 2005). These special fibers are designed to have the opposite D parameter than the SSMF so that they can revert the dispersive effect experienced by the signal during transmission. Nevertheless, DCFs contribute to additional insertion losses. Nowadays, in coherent optical systems, CD is compensated for by digital signal processing.

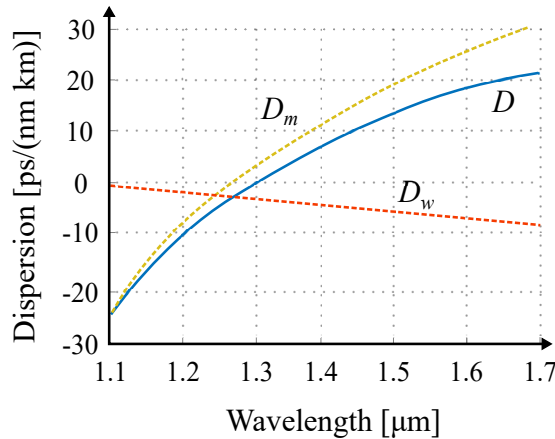


Figure 2.14 – Dispersion map of SSMF. The total dispersion is the sum of material dispersion and waveguide dispersion.

2.3.6 Nonlinear impairments

When light propagates over an optical fiber, the most considerable portion of the energy of the electromagnetic field is confined within the core. Due to the reduced core size, the spatial power density is relatively high, which leads the fiber to work in the nonlinear regime under some conditions. The strength of the nonlinear effects depends on the fiber length and on the signal power. As a consequence of the attenuation, most nonlinear perturbations occur in the first kilometers of the fiber, where the optical power is still very high. The signal is mainly disturbed by two nonlinear effects during propagation over a nonlinear fiber: inelastic light scattering and nonlinear phase modulation.

If the signal power is high enough to drive the fiber into the nonlinear regime, the nonlinear phase modulation will scale inversely to the effective area. Therefore, in MMFs whose effective areas are typically larger than SMFs, the distortion experienced by the signal due to the nonlinear phase noise is less for the same power intensity. Similarly, for the same level of nonlinear phase noise, the system can be operated at higher powers increasing the SNR and the SDM channel capacity. However, the transmission of multiple modes over MMFs can introduce additional nonlinear phase noise coming from the power contribution of the multiple modes.

2.3.6.1 Inelastic light scattering

Two examples of inelastic scattering are Brillouin scattering (BRILLOUIN, 1922) and Raman scattering (RAMAN, 1928). Because of these phenomena, the frequency of a propagating photon that interacts with the material molecular structure is shifted to a lower frequency. The difference in energy appears then in the form of a phonon. During Raman scattering, optical photons are generated, while acoustic phonons result from Brillouin scattering. Scattering processes cause a loss of power at the incident frequency.

At high power levels, the scattering becomes significant. As Brillouin scattering occurs only in the backward direction, it not only decreases the power in the incident frequency but can also cause damage to the transmitter. Raman scattering, in turn, takes place in both backward and forward directions. Although Raman crosstalk may affect the system performance, Raman scattering can be used to amplify an optical signal by transferring energy to it from a pump beam within a Raman amplifier (RAMASWAMI *et al.*, 2010).

2.3.6.2 Nonlinear phase modulation

Nonlinear phase modulation results from the nonlinear dependence of the refractive index with the optical power intensity, a phenomenon known as the Kerr effect (KERR, 1875), (DZIEDZIC *et al.*, 1981), (WEINBERGER, 2008). The Kerr effect gives rise to three types of nonlinear effects, self phase modulation (SPM), cross phase modulation (XPM) and four wave mixing (FWM). SPM is the dominant phase modulation effect in single-channel systems with high levels of CD, where the nonlinear phase noise intensity depends exclusively on the optical power of the current channel. On the other hand, XPM is significant in WDM systems since the phase modulation of a specific channel depends not only on the optical power in this channel, but also on the optical power in neighboring channels. Finally, FWM takes place in systems that transmit information on several frequencies and have a low local dispersion. FWM is characterized by the generation of a fourth frequency, ω_{ijk} , as a result of three co-propagating optical fields, with carrier frequencies ω_i, ω_j , and ω_k as

$$\omega_{ijk} = \omega_i + \omega_j - \omega_k, \quad k \neq i, j. \quad (2.48)$$

The new generated frequencies can cause interference with other existing signals (AGRAWAL, 2002), (RAMASWAMI *et al.*, 2010).

2.3.7 Spatial channel interactions

In an ideal SDM optical channel, modes propagate without any coupling. In practice, however, signals propagating over different modes are coupled by random or intentional perturbations, resulting in crosstalk. In SDM transmission, mode coupling can arise from manufacturing variations that cause non-circularity of the core, roughness at the core-cladding boundary, variations in the core radius, or index-profile variations in graded-index fibers. Mode coupling can also come from thermal mismatches between glasses of different compositions, micro-bending, macro-bending, or twists (HO; KAHN, 2014). In (HO; KAHN, 2013), the authors show that the coupling strength is inverse to the difference between propagation constants. Thereby, in theory, modes with nearly equal propagation constants strongly couple during transmission. In contrast, modes having highly unequal

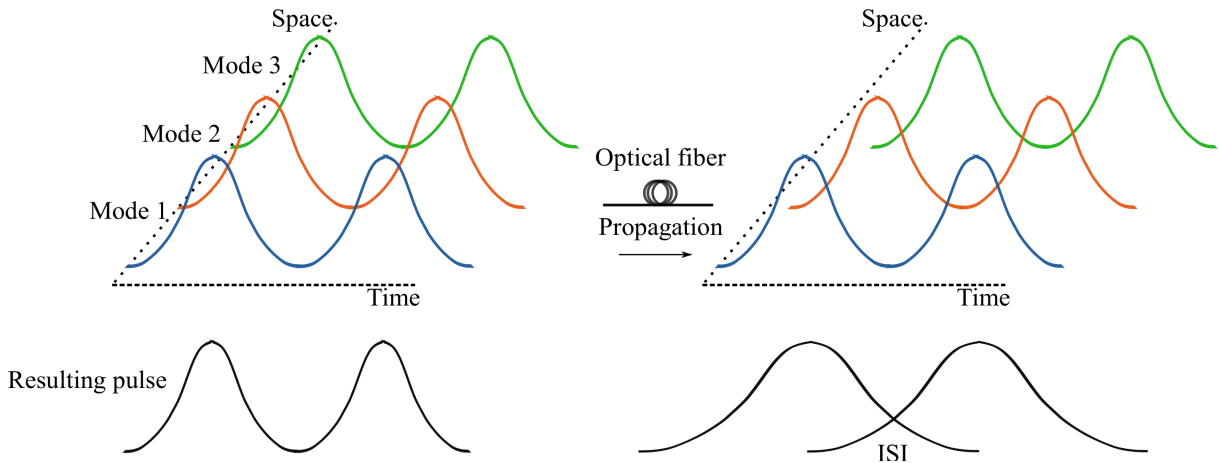


Figure 2.15 – ISI resulting from mode coupling and modal dispersion.

propagation constants experience weak coupling. High crosstalk levels in strongly-coupled transmission demand the deployment of MIMO equalization techniques to separate the independent transmitted signals.

Similarly to PMD in SMF, modal dispersion arises in SDM transmission as a consequence of the different group velocities of the propagation modes. Although PMD is also present in SDM transmission, the GD between modes is significantly greater than the GD between both polarization orientations of the same mode. In practice, even the spatial degenerate modes that, in theory, have the same propagation constant, travel with slightly different group velocities contributing to modal dispersion. The most significant contribution to modal dispersion comes from the propagation modes belonging to different modal groups¹. Mode coupling in the presence of modal dispersion causes ISI that is characterized by the transfer of energy among modes at different instants of time, as illustrated in Fig. 2.15. Notwithstanding, both ISI and pulse spread caused by mode coupling and modal dispersion are partially compensated for in the DSP stage without limiting the system performance.

In (SHEMIRANI *et al.*, 2009), Shemirani *et al.* show that, in the weak-coupling regime, the mode coupling has a negligible effect over the GD, resulting in a DMD that scales proportionally to the length of the fiber. On the contrary, in the strong-coupling regime, the GD is substantially influenced by mode coupling so that there is a reduction in the DMD that grows proportionally to the square root of the fiber length. In practical SDM transmission, in general, as the temporal memory of the MIMO equalizer is required to be long enough to accommodate the broadened channel impulse response, the complexity of the filters scales with the DMD. Therefore, strongly-coupled SDM transmissions are a highly attractive solution for reduced complexity receivers.

In addition to linear coupling and modal dispersion, SDM channels introduce other

¹ Note that the magnitude of the delay is typically nanoseconds.

significant impairments. Due to in-line components and the fiber itself, the guided modes may be subject to unequal attenuation and amplification levels. This effect is known as MDL and MDG. From this point, for convenience, the joint effect of MDL and MDG will be referred only as MDG. MDG reduces the instantaneous average channel capacity and, under some conditions, can generate system outages (HO; KAHN, 2011b). The combined effect of accumulated MDG and amplifier noise fundamentally limits the performance of high-capacity SDM systems to be deployed at long distances.

Unlike mode coupling and modal dispersion, MDG cannot be trivially compensated by DSP. Consequently, its effect must be handled at the component design level or, alternatively, during transmission. In (LOBATO *et al.*, 2012), Lobato *et al.* study how the induced mode coupling reduces the overall MDG, showing that, in a strongly-coupled SDM transmission, the MDG accumulates with the square root of the fiber length. Chapter 4 presents the MDG fundamentals, mathematical modeling, and simulation.

As the MDG limits the deployment of long-haul SDM transmission systems, the study of MDG estimation methods has become an important research topic in recent literature. The most widely used MDG estimation technique is based on DSP and employs the MIMO equalizer transfer matrix of coherent receivers. DSP-based methods for MDG estimation are presented in Chapters 4, 5, and 6.

2.3.8 Optical amplification

To compensate for the attenuation of the signal power in long-haul transmission, optical amplifiers should be inserted periodically over the link. Before optical amplification came to the landscape, the degradation of the signal power was overcome in the electrical domain. This approach requires expensive optical-electrical-optical (OEO) conversions to apply reamplification, as well as other processing steps on the data pulse as shaping and retiming (RAMASWAMI *et al.*, 2010). In addition, OEO conversion is not a cost-efficient technique for WDM systems as the conversion should be applied on each wavelength channel. A promising solution appeared with the erbium-doped fiber amplifier (EDFA) capable of amplifying multiple WDM channels simultaneously. An alternative amplification scheme based on stimulated RAMAN scattering was also proposed for WDM transmissions (BROMAGE, 2004), (NAMIKI *et al.*, 2006). The scope of this thesis is independent of the amplification scheme. Therefore, the optical amplification process is described here merely for EDFA amplifiers that are commonly employed in laboratory transmission setups and frequently adopted in commercial implementations. The working principle of amplifiers based on Erbium-doped fibers (EDFs) is presented below.

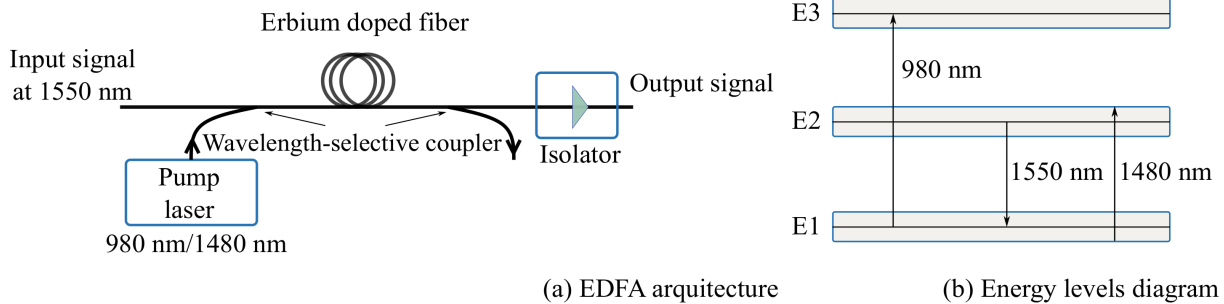


Figure 2.16 – Erbium-doped fiber amplifier. (a) Architecture. (b) Energy levels diagram of the Erbium ions (Er^{3+}). Adapted from (RAMASWAMI *et al.*, 2010).

2.3.8.1 Erbium doped fiber amplifiers

Among the optical amplifiers, the EDFA is the most widely used in optical communications systems. Originally, EDFAs were able to amplify all channels in the 35 nm wide spectrum of the C-band. However, currently, EDFAs that operate in the L band are also being commercialized. The active medium of the EDFAs is doped with Erbium ions (Er^{3+}), a chemical element that belongs to Rare Earths. Erbium ions are conveniently employed as a dopant since the difference between two of its energy levels corresponds to wavelengths close to 1550 nm, which is the lowest attenuation band in the fiber (see Fig. 2.12). The working principle of an EDFA, similar to semiconductor lasers, is based on population inversion and stimulated emission. Fig. 2.16 illustrates the architecture and the energy levels diagram of an EDFA. An EDFA consists of a segment of silica fiber whose core is doped with Erbium ions. The doped fiber is pumped using a pump signal from a laser, typically at a wavelength of 980 nm or 1480 nm. To combine the output of the pump laser with the input signal, the doped fiber is preceded by a wavelength-selective coupler. Another wavelength-selective coupler separates the amplified signal from any remaining pump signal power at the output. Usually, an isolator is used at the input and/or output of any amplifier to prevent reflections into the amplifier that can damage it (RAMASWAMI *et al.*, 2010). For the EDFA to work, two types of transitions are employed to obtain population inversion. The first type of transition occurs when the doped fiber is pumped with an optical laser at 980 nm making ionized atoms move from E1 to E3. Subsequently, ions fall from E3 to E2, releasing energy in the form of photons. On the contrary, when the doped fiber is pumped with an optical laser operating at 1480 nm, the Erbium ions move directly from E1 to E2. In the transition from E2 to E1, photons are released, driving the signal amplification. As the photon energy is inversely proportional to its wavelength, pumping at 1480 nm has a higher optical power conversion efficiency than pumping at 980 nm. However, 980 nm pumps are frequently preferred as they introduce less noise to the optical signal.

The optical signal is amplified during its propagation over the Erbium-doped fiber

by means of stimulated emission. Nevertheless, non-coherent photons are also amplified through spontaneous emission, giving rise to ASE noise covered in Section 2.3.8.3.

2.3.8.2 Optical amplifiers for SDM transmission setups

In single-mode optical systems, high-performance amplifiers present a balanced amplification profile over WDM channels so that each amplification stage guarantees a flat transmission spectrum. Furthermore, a flat gain profile over polarization modes is desirable to minimize polarization-dependent gain (PDG) (WYSOCKI; MAZURCZYK, 1996). Similarly, in SDM transmissions, SDM amplifiers are required to guarantee uniform amplification among all spatial channels to prevent any imbalance among modal gains. Amplifiers with a non-flat amplification profile over spatial paths contribute with MDG that reduces the transmission capacity. As MDG is a fundamental limit for SDM systems performance, designing SDM amplifiers with balanced amplification profiles is vital for deploying long-haul SDM systems.

EDFA amplifiers designed for SMFs are not compatible with MMFs and FMFs. However, the scientific community working on the amplification field for SDM technology is focusing its efforts on designing and manufacturing amplifiers compatible with SDM fibers based mainly on the operating principle of the EDFA (WADA *et al.*, 2016), (WAKAYAMA *et al.*, 2016), (JUNG *et al.*, 2018). One of the biggest challenges that constrain the SDM amplifiers design is the minimization of the MDG throughout various mitigation strategies (KANG *et al.*, 2014), (EZNAVEH *et al.*, 2017). Alternatively, in the literature, many works present experimental SDM demonstrations that employ multiple EDFAs to amplify the spatial channels separately. This amplification approach is widely used to reach long-distance SDM transmissions in laboratory environments. However, these setups do not align with the requirements of component sharing and device integration. Fig. 2.17a shows the parallel SMF amplifier architecture that has often been employed for SDM demonstrations. The parallel SMF amplifier architecture requires many duplicate optical components, electronics, and heat management units. The component multiplicity significantly increases the cost and energy consumption. In contrast, Fig. 2.17b shows a more cost-efficient amplification architecture for SDM transmission setups where multiple spatial channels share the same devices. The fully integrated SDM amplifier requires only two SDM fiber isolators, one gain flattening filter (GFF) and a single SDM EDF.

In the case of SDM systems on MCFs, two approaches are mainly used for SDM amplification: core-pumping (ABEDIN *et al.*, 2011), and cladding-pumping (ABEDIN *et al.*, 2014), (PUTTNAM *et al.*, 2019). Both techniques are viable options for realizing efficient amplifiers for transmission over MCFs. Core-pumping optical amplifiers can

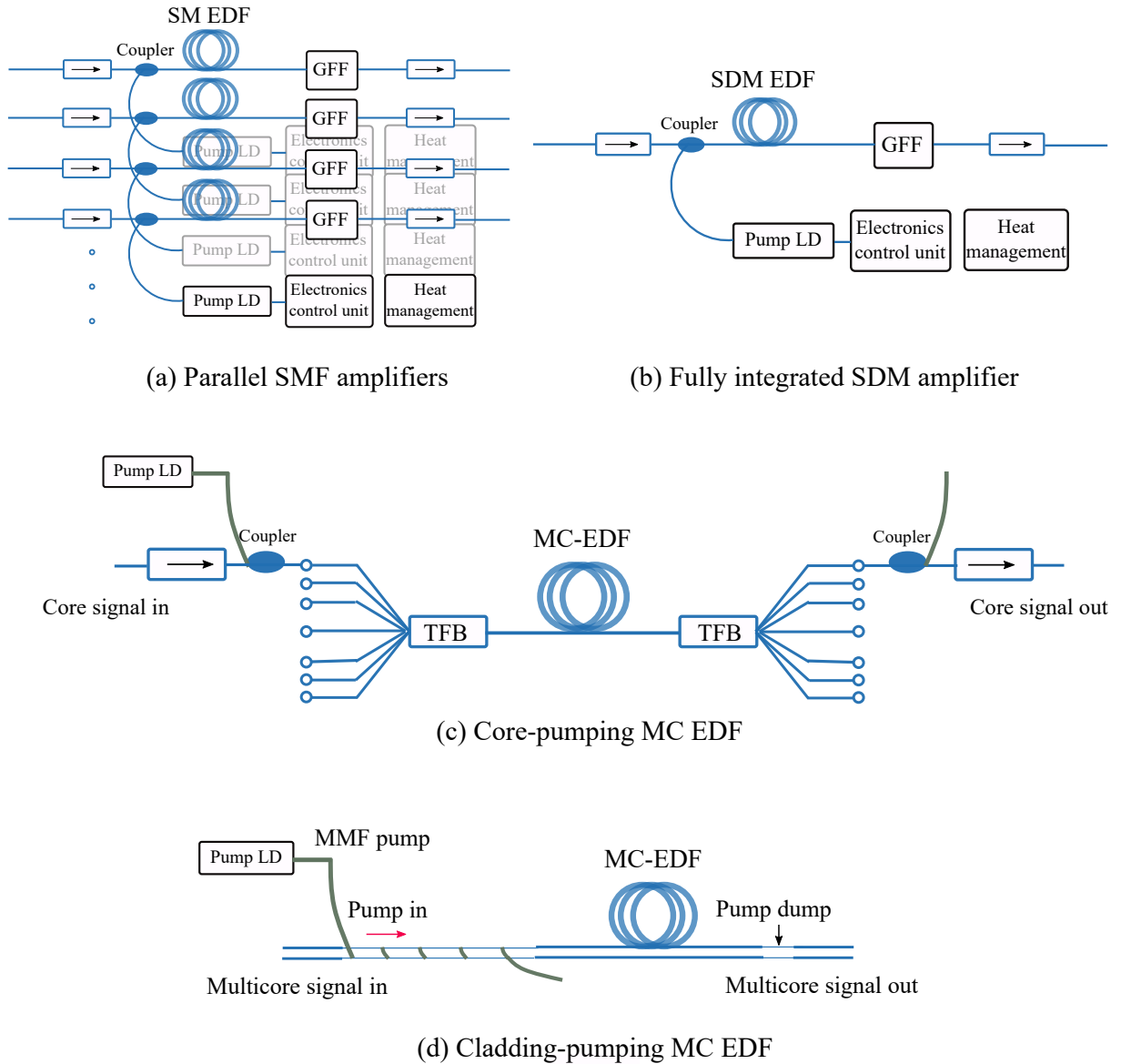


Figure 2.17 – SDM amplification schemes. (a) Parallel SMF amplifiers. (b) Fully integrated SDM amplifier. (c) Core-pumping MC EDF amplifier. (d) Cladding-pumping MC EDF amplifier (JUNG *et al.*, 2020).

achieve high-gain, low-noise figures and allow independent control of the individual gain of the cores. Cladding-pumping amplifiers can potentially reduce the cost and complexity of the amplifier by reducing the number of optical components and enabling the use of high-power, low-cost multimode pump laser diodes (JUNG *et al.*, 2020). In the core-pumping amplifier of Fig. 2.17c, coupling of light to the individual cores of the multi-core Erbium-doped fiber (MC-EDF) is done through two compact tapered fiber bundle (TFB) couplers manufactured by tapering a bundle of specially designed fibers to reach a core-to-core pitch at the tapered end matching the MC-EDF. One optical isolator at each extreme protects the devices from backward reflections. A cladding-pumping MC amplifier that employs side-pumping is shown in Fig. 2.17d. In this case, the side-coupling of pump

radiation is performed using a tapered multimode fiber. A short section of the gain fiber near the input end is stripped of its low-index coating, and the exposed area is disposed into optical contact with the tapered multimode pump fiber (ABEDIN *et al.*, 2014). The cladding-pumping approach is more efficient as it amplifies all the cores with the same pump radiation. However, this strategy can lead to high values of MDG by privileging the outer cores of the MCF.

2.3.8.3 Amplified spontaneous emission

Stimulated emission is the physical principle behind signal amplification in amplified optical systems. The photons generated through stimulated emission not only have the same energy as the incident photons but also the same direction of propagation, phase, and polarization (AGRAWAL, 2002), (RAMASWAMI *et al.*, 2010), (DEMTRÖDER, 2005). Therefore, the amplification process results from the contribution of the new photons that add constructively to the incident field. On the other hand, in spontaneous emission, photons are emitted in random directions, polarizations, and phases (RAMASWAMI *et al.*, 2010). Consequently, amplified spontaneous emission appears as noise at the output of the amplifier and becomes a source of degradation of the system performance.

The power spectral density (PSD) of spontaneous emission induced noise, $S_{sp}(\nu)$, is nearly constant in the signal bandwidth. Therefore, the ASE noise can be modeled as AWGN. From (AGRAWAL, 2002), $S_{sp}(\nu)$ is given by

$$S_{sp}(\nu) = (G - 1) n_{sp} h\nu, \quad (2.49)$$

where h is Planck's constant, ν is the optical frequency, G is the amplifier gain, and n_{sp} is the spontaneous emission factor, defined as

$$n_{sp} = \frac{N_2}{N_2 - N_1}, \quad (2.50)$$

where N_1 and N_2 are the atomic populations of the ground and excited states (E1 and E2, E3), respectively.

In optical systems, ASE noise accumulates over the link due to several amplification stages that progressively degrade the signal quality. In the presence of ASE noise, the OSNR is an important metric for system characterization. Under the assumption of balanced and spatially white noise, for each spatial transmission mode, including both orthogonal polarization orientations, the OSNR is related to the ASE PSD (AGRAWAL, 2002) according to

$$\text{OSNR} = \frac{P_{\text{Total}}}{2 S_{sp} B_{ref}}, \quad (2.51)$$

where P_{Total} is the total power of the signal considering two polarization orientations, and B_{ref} is the reference bandwidth, whose typical value is 12.5 GHz, corresponding to

a 0.1 nm resolution bandwidth of optical spectrum analyzers at 1550 nm. The “2” in the denominator makes references to two polarization orientations.

For a system with polarization multiplexing and assuming Nyquist pulse shaping, the SNR is obtained from the OSNR (ESSIAMBRE *et al.*, 2010a), (ESSIAMBRE; TKACH, 2012) through

$$\text{SNR} = \frac{B_{ref}}{R_s} \text{OSNR}. \quad (2.52)$$

The total amount of noise added by an optical amplifier is quantified by the noise figure (NF), which is defined as the ratio between the SNR at the input and output of the amplifier, as

$$\text{NF} = \frac{\text{SNR}_{in}}{\text{SNR}_{out}}, \quad (2.53)$$

where, the higher the SNR_{out} , the higher the gain of the amplifier. In optical systems, amplifiers with low noise figure are desired. In analogy with electronic amplifiers, the noise figure of an optical amplifier describes the degradation of the SNR during the amplification resulting from diverse noise contributions. However, amplification processes in the optical domain are impaired by different electrical and optical noise sources, making it difficult to define the noise figure of optical amplifiers accurately. Therefore, the noise figure of optical amplifiers is usually determined considering the electric SNR at an ideal hypothetical receiver accounting for shot noise only at the device input and the beat of ASE noise with the signal at the output.

The OSNR can be expressed as a function of the number of spans, K , noise figure, NF, attenuation coefficient, α , and span length, L_s , as

$$\text{OSNR} = \frac{P_{\text{Total}}}{\text{NF } K (e^{\alpha L_s} - 1) h\nu B_{ref}}. \quad (2.54)$$

Fig. 2.18 shows the OSNR and SNR as a function of the link length for a system with dual-polarization, $R_s = 30$ GBd, $P_{\text{Total}} = 0$ dBm, $\alpha = 0.2$ [dB/km], 150 spans with $L_s = 60$ km, and per-span amplifier with $\text{NF} = 5$ dB.

Optical amplifiers are classified into three types. The booster amplifier is located just after the transmitter. This kind of amplifier aims to provide very high power levels to the optical signal that will be launched through the optical fiber. In-line amplifiers are periodically distributed over the fiber to compensate for the accumulated loss of a fiber segment. Finally, the pre-amplifier is positioned immediately before the optical receiver to increase the received signal power to a level higher than the receiver sensitivity.

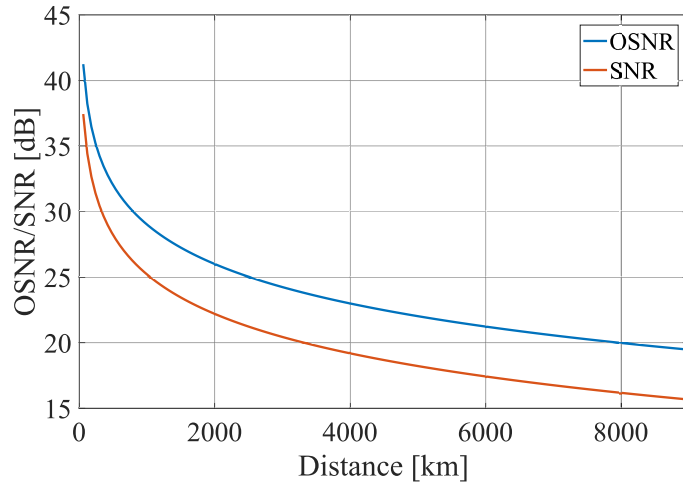


Figure 2.18 – OSNR and SNR as a function of the length for $R_s = 30$ GBd, $P_{\text{Total}} = 0$ dBm, $\alpha = 0.2$ [dB/km], 150 spans of $L_s = 60$ km, and per-span amplifier with $NF = 5$ dB.

2.3.8.4 System performance metrics

The most popular metric to evaluate the performance of a communications system is the BER. The BER is computed for each propagation mode by the ratio between the number of bits detected with error and the total amount of transmitted bits. The relation between BER and OSNR gives clear insights regarding the robustness of the system against different sources of degradation. Let us define SNR as a function of the total signal energy, E_s , and the noise PSD, N_0 , (HAYKIN, 2001)

$$\text{SNR} = \frac{E_s}{N_0}. \quad (2.55)$$

According to (BARRY *et al.*, 2004) and assuming Gray mapping, a theoretical relationship amidst BER and SNR can be obtained using the following expressions

for QPSK

$$\text{BER} = \frac{1}{2} \text{erfc} \sqrt{\frac{\text{SNR}}{\log_2(M)}}, \quad (2.56)$$

for 16-QAM

$$\text{BER} = \frac{3}{8} \text{erfc} \sqrt{(6 \times 15) \frac{\text{SNR}}{\log_2(M)}}, \quad (2.57)$$

and for 64-QAM

$$\text{BER} = \frac{2}{\log_2(M)} \times \left(1 - \frac{1}{\log_2(M)}\right) \text{erfc} \sqrt{\frac{3 \text{SNR}}{2 \log_2(M) - 2}}, \quad (2.58)$$

where erfc denotes the complementary error function. Fig. 2.19 shows the theoretical curves of BER versus the SNR for QPSK, 16-QAM, and 64-QAM.

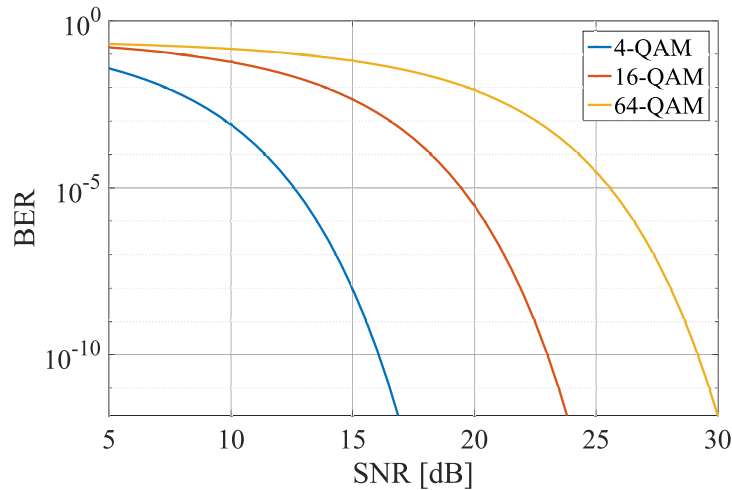


Figure 2.19 – Theoretical curves of BER as a function of the SNR for QPSK, 16-QAM, and 64-QAM.

The BER has become the standard performance evaluation metric in the communications field. Nevertheless, in particular transmission scenarios, the BER is not the most appropriate metric to evaluate the system performance, for instance, in coded modulation systems (MELLO; BARBOSA, 2021). In contrast, the achievable information rate (AIR) metric has been demonstrated to be a more suitable performance indicator for coded optical systems allowing fair comparisons among constellations, DSP algorithms, decoding, and nonlinearity compensation techniques (ALVARADO *et al.*, 2018). AIR indicates a limit on the amount of information bits that can be reliably transferred through a channel with arbitrarily low error probability. The AIR metric depends on the modulation format and is widely employed in systems that implement forward error correction (FEC) codes. As AIRs are achieved under ideal FEC schemes, in practical implementations, AIRs provide a pre-FEC performance indicator to ensure an arbitrarily low BER post FEC based on pre-calculated gaps related to specific FEC implementations (MELLO; BARBOSA, 2021).

2.3.9 Fibers for space-division multiplexing

Nowadays, long-haul optical transmission is carried out over SMF, taking advantage of the low implementation costs and the low attenuation profile over a wide band. Over these SMFs, high-order modulation formats and multiplexing techniques in frequency, polarization, and time are employed to maximize the channel capacity. However, for SDM transmission, special fibers must be manufactured. With the appearance of new optical fibers for SDM, the low cost per bit will remain only if integration at the component level is achieved, such as transmitters, lasers, and amplifiers.

The most direct and obvious approach for spatial multiplexing is to use an array

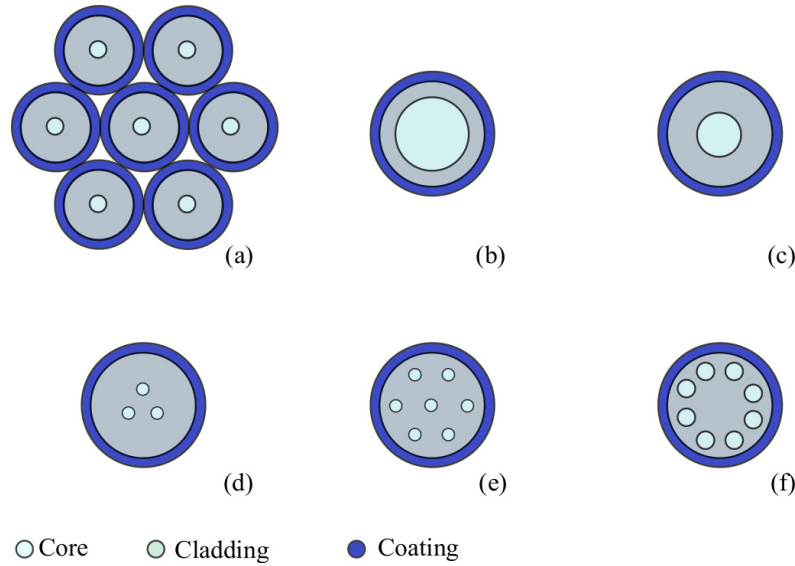


Figure 2.20 – Fibers for SDM. (a) Bundle of single-mode fibers. (b) Multi-mode fiber. (c) Few-mode fiber. (d) Coupled multi-core fiber. (e) Uncoupled multi-core fiber. (f) Few-mode multi-core fiber.

of several single-core fibers in parallel as depicted in Fig. 2.20a (DOMINGUES *et al.*, 2017), (JATOBA-NETO *et al.*, 2018). The bundle approach offers significant advantages in terms of ease of practical system implementation. However, it offers only limited scope for increased spatial densities and associated device integration (RICHARDSON, 2016). Therefore, new fibers exclusively for spatial multiplexing are being designed. The most common types of fibers for SDM are presented below.

2.3.9.1 Multi-mode fibers and few-mode fibers

The core of a MMF has a radius considerably larger than a SMF, as illustrated in Fig. 2.20b. The independent and orthogonal paths are mainly confined and guided within the core, giving rise to the concept of mode-division multiplexing (MDM) over MMFs. During transmission over MMFs, the orthogonal signals experience power transfer, resulting in randomly coupled signals. Random coupling causes crosstalk that demands MIMO equalization techniques at the receiver to unravel the signals. In particular scenarios, MIMO equalization is required at both the transmitter and receiver to guarantee the link performance (WEERDENBURG *et al.*, 2018). Conventional MMFs with core/cladding diameters of $50/125 \mu\text{m}$ and $62.5/125 \mu\text{m}$ can support more than 100 modes and accumulate huge delays in long links, despite being carefully engineered for small differential mode group delays (DMGDs). Regarding the complexity of the MIMO equalizer, managing the linear crosstalk and pulse broadening caused by modal dispersion of hundreds of modes propagating over long-haul links can be challenging or unfeasible. Therefore, MMFs are commonly used for short communications systems such as data centers and in-building networks.

To face the challenges found in MMFs, recent advances have led to the development of new fibers called FMFs, designed to support a limited number of modes (see Fig. 2.20c). FMFs typically support 3, 6, 10, or 15 LP modes and present low DMGD (GRÜNER-NIELSEN *et al.*, 2012), (MORI *et al.*, 2013), (SILLARD *et al.*, 2016b), (RADEMACHER *et al.*, 2017). The number of modes supported by a FMF is a parameter for design and manufacturing. For a given number of desired modes, the corresponding V value is chosen. Subsequently, the fiber properties are optimized to achieve the V parameter according to Eq. (2.32). To minimize the DMGD, the refractive index profile is carefully designed. In addition, the DMGD is often optimized by combining multiple fiber spools with positive and negative modal dispersion values, a technique similar to chromatic dispersion compensation with DCFs (RANDEL *et al.*, 2012b).

In addition to mode coupling and modal dispersion, the transmission over MMFs and FMFs is impaired by differential modal loss or gain as a consequence of the mode-dependent performance of the various in-line components as fibers, amplifiers, multiplexers, and demultiplexers. This particular impairment is not compensated for by DSP but should be handled in the component design stage.

2.3.9.2 Coupled and uncoupled multi-core fibers

MCFs present multiple cores in a single cladding as depicted in Fig. 2.20d,e. Each distinguishable path then propagates over a particular core. The uncoupled MCFs are designed with sufficient spacing between cores so that the inter-core crosstalk is substantially reduced. The level of inter-core crosstalk is controlled by the inter-core distance and the core design to obtain a particular difference between propagation constants of neighboring cores. In addition, the incorporation of trench or holes around the cores to better confine the light is another typical approach to reduce the inter-core crosstalk.

Many cores result in large cladding diameters fibers that are susceptible to fracture. For example, diameters greater than $\sim 250\mu\text{m}$ are considered impractical, imposing a rigid limit on the number of cores that can be incorporated in MCFs for long-haul transmission (RICHARDSON, 2016). The most common uncoupled MCF has a hexagonal arrangement of seven cores. In this configuration, the central core has the highest level of crosstalk as it has six nearest neighbors, whereas the outer cores have only three nearest neighbors.

On the other hand, a coupled MCF is manufactured by decreasing the inter-core spacing. Light in the coupled cores propagates in the so-called super modes behaving similar to MMFs. High crosstalk is achieved by designing the cores to have close propagation constants. MIMO equalization techniques are required to unravel the mixed signals. Experiments over coupled and uncoupled MCFs have been reported in (RYF *et al.*, 2011), (SASAKI *et al.*, 2017), (SAKAMOTO *et al.*, 2017), (RYF *et al.*, 2019), (RADEMACHER

et al., 2020).

2.3.9.3 Few-mode multi-core fibers

The highest spatial multiplicity is reached by combining the multi-mode and multi-core approaches. FM-MCFs support multiple cores in a single cladding, and simultaneously, each core supports multiple modes as depicted in Fig. 2.20f. Therefore, a total of *number of cores* \times *number of modes* spatial channels are supported. In a FM-MCF, inter-mode and inter-core effects should be considered. Independent MIMO equalizers can be employed to unravel the signals over each core if the inter-core crosstalk is low enough to be negligible. 10.16 peta-bit/s transmission over a FM-MCF has been demonstrated in (SOMA *et al.*, 2017).

2.4 Receiver submodule (RX)

The detected optical signal is demultiplexed at the receiver side by a spatial DEMUX. The M_p spatial signals are then forwarded to WDM receivers. In the WDM receiver, each spatial signal is demultiplexed in wavelength, and the N_{ch} WDM channels are converted back from the optical to the electrical domain by the receiver front-end. The front-end of the receiver submodules that perform the optoelectrical conversion is described below.

2.4.1 Front-end

Coherent detection schemes are based on the interference between the received optical signal and a continuous wave local oscillator (LO). The front-end implements a LO laser and a photo-detector arrangement to obtain two electric signals that correspond to the in-phase and quadrature components of the received signal. The resulting analog electrical signal is further converted to the digital domain and processed for recovering the transmitted information. The structure of an optical front-end is depicted in Fig. 2.21. The LO generates a reference signal to be coherently mixed with the received signal. Optical coherent receivers are classified as homodyne, heterodyne, or intradyne, depending on the degree of similarity between the nominal central frequencies of the transmitter laser and the LO laser. In a homodyne receiver, for example, the central frequencies of the transmitter and LO lasers are nominally identical. In contrast, in a heterodyne receiver, the central frequencies differ significantly. Practical implementations of these two types of coherent receivers are not straightforward due to the high complexity and cost. In contrast, the intradyne receiver compensates for the disadvantages of complexity, cost, sensitivity, and bandwidth requirements of homodyne and heterodyne receivers. In an in-

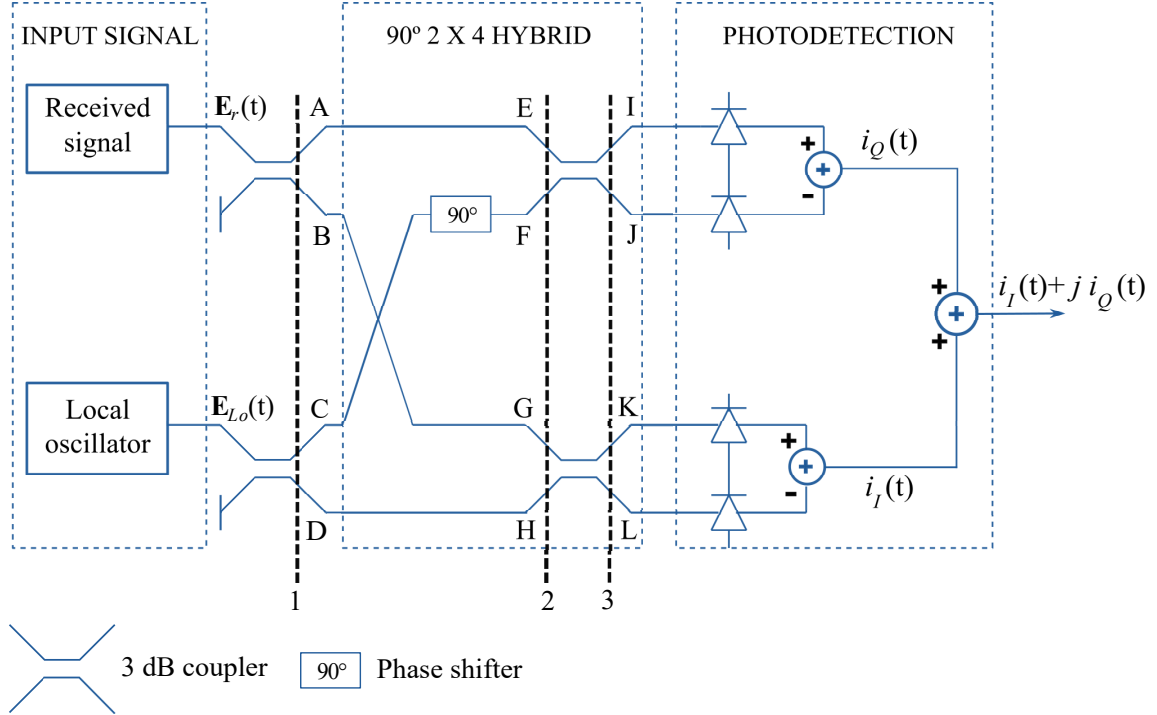


Figure 2.21 – Block diagram of a front-end with balanced detection for a single polarization system.

tradyn receiver, the central frequencies of the transmitter and LO lasers are not precisely the same but very similar, resulting in a slight offset that is compensated for by advanced algorithms in the DSP stage (LEVEN *et al.*, 2007).

The $90^\circ 2 \times 4$ hybrid performs the linear combination between the received signal and the reference signal coming from the LO. The $90^\circ 2 \times 4$ hybrid is composed of four 3 dB couplers and one 90° phase shifter. The working principle of the hybrid is primarily based on the transfer function of a 3 dB coupler. According to (AGRAWAL, 2002), the transfer function of a 3 dB coupler, H_{coupler} , is given by

$$H_{\text{coupler}} = \frac{1}{\sqrt{2}} \begin{bmatrix} 1 & 1 \\ 1 & -1 \end{bmatrix}. \quad (2.59)$$

Based on H_{coupler} , the fields at boundary **1** in Fig. 2.21 are expressed as

$$\mathbf{E}_A(t) = \frac{1}{\sqrt{2}} \mathbf{E}_r(t), \quad (2.60)$$

$$\mathbf{E}_B(t) = \frac{1}{\sqrt{2}} \mathbf{E}_r(t), \quad (2.61)$$

$$\mathbf{E}_C(t) = \frac{1}{\sqrt{2}} \mathbf{E}_{Lo}(t), \quad (2.62)$$

$$\mathbf{E}_D(t) = \frac{1}{\sqrt{2}} \mathbf{E}_{Lo}(t), \quad (2.63)$$

where $\mathbf{E}_r(t)$ and $\mathbf{E}_{Lo}(t)$ are the fields of the received signal and LO, respectively.

At boundary **2**, due to the 90° phase shifter, the fields become

$$\mathbf{E}_E(t) = \frac{1}{\sqrt{2}}\mathbf{E}_r(t), \quad (2.64)$$

$$\mathbf{E}_F(t) = \frac{1}{\sqrt{2}}\mathbf{E}_{Lo}(t)e^{j\frac{\pi}{2}}, \quad (2.65)$$

$$\mathbf{E}_G(t) = \frac{1}{\sqrt{2}}\mathbf{E}_r(t), \quad (2.66)$$

$$\mathbf{E}_H(t) = \frac{1}{\sqrt{2}}\mathbf{E}_{Lo}(t). \quad (2.67)$$

Finally, after the last two 3 dB couplers, the fields at boundary **3** are described by

$$\mathbf{E}_I(t) = \frac{1}{2}\mathbf{E}_r(t) + \frac{1}{2}\mathbf{E}_{Lo}(t)e^{j\frac{\pi}{2}}, \quad (2.68)$$

$$\mathbf{E}_J(t) = \frac{1}{2}\mathbf{E}_r(t) - \frac{1}{2}\mathbf{E}_{Lo}(t)e^{j\frac{\pi}{2}}, \quad (2.69)$$

$$\mathbf{E}_K(t) = \frac{1}{2}\mathbf{E}_r(t) + \frac{1}{2}\mathbf{E}_{Lo}(t), \quad (2.70)$$

$$\mathbf{E}_L(t) = \frac{1}{2}\mathbf{E}_r(t) - \frac{1}{2}\mathbf{E}_{Lo}(t). \quad (2.71)$$

From Eq. (2.68) to Eq. (2.71), the transfer function of a $90^\circ 2 \times 4$ hybrid can be summarized as

$$\begin{bmatrix} \mathbf{E}_I(t) \\ \mathbf{E}_J(t) \\ \mathbf{E}_K(t) \\ \mathbf{E}_L(t) \end{bmatrix} = \frac{1}{2} \begin{bmatrix} 1 & e^{j\frac{\pi}{2}} \\ 1 & -e^{j\frac{\pi}{2}} \\ 1 & 1 \\ 1 & -1 \end{bmatrix} \begin{bmatrix} \mathbf{E}_r(t) \\ \mathbf{E}_{Lo}(t) \end{bmatrix}. \quad (2.72)$$

After the $90^\circ 2 \times 4$ hybrid, the signal mixing is carried out by a non-linear transformation performed by the photo-detection stage. The photo-detection block comprises two pairs of balanced photo-detectors that execute the optical-electrical conversion.

For an input power, $P_{\text{in_pd}}$, a photo-detector generates a current, I_p , that is given by (AGRAWAL, 2002)

$$I_p = R P_{\text{in_pd}}, \quad (2.73)$$

where R is known as responsivity factor. The responsivity of a photo-detector is an indicator of its conversion efficiency, η , and can be derived as

$$\eta = \frac{\text{Electron generation rate}}{\text{Photon incidence rate}} = \frac{I_p / q}{P_{\text{in_pd}} / h\nu}, \quad (2.74)$$

where q is the electron charge. From Eq. (2.73) and Eq. (2.74), the responsivity factor, R , is expressed as

$$R = \frac{\eta q}{h\nu}. \quad (2.75)$$

From Eq. (2.68) to Eq. (2.71) and Eq. (2.73), the photo-currents that correspond to in-phase and quadrature components of the detected electrical signal are found as

$$\begin{aligned}
i_Q(t) &= R |\mathbf{E}_I(t)|^2 - R |\mathbf{E}_J(t)|^2 \\
&= R \left| \frac{1}{2} \mathbf{E}_r(t) + \frac{1}{2} \mathbf{E}_{Lo}(t) e^{j\frac{\pi}{2}} \right|^2 - R \left| \frac{1}{2} \mathbf{E}_r(t) - \frac{1}{2} \mathbf{E}_{Lo}(t) e^{j\frac{\pi}{2}} \right|^2 \\
&= R \left| \frac{1}{2} \mathbf{E}_r(t) + \frac{1}{2} \mathbf{E}_{Lo}(t) e^{j\frac{\pi}{2}} \right|^2 - R \left| \frac{1}{2} \mathbf{E}_r(t) + \frac{1}{2} \mathbf{E}_{Lo}(t) e^{j\frac{3\pi}{2}} \right|^2,
\end{aligned} \tag{2.76}$$

and

$$\begin{aligned}
i_I(t) &= R |\mathbf{E}_K(t)|^2 - R |\mathbf{E}_L(t)|^2 \\
&= R \left| \frac{1}{2} \mathbf{E}_r(t) + \frac{1}{2} \mathbf{E}_{Lo}(t) \right|^2 - R \left| \frac{1}{2} \mathbf{E}_r(t) - \frac{1}{2} \mathbf{E}_{Lo}(t) \right|^2 \\
&= R \left| \frac{1}{2} \mathbf{E}_r(t) + \frac{1}{2} \mathbf{E}_{Lo}(t) \right|^2 - R \left| \frac{1}{2} \mathbf{E}_r(t) + \frac{1}{2} \mathbf{E}_{Lo}(t) e^{j\pi} \right|^2.
\end{aligned} \tag{2.77}$$

The electric fields of the received and local oscillator signal can be defined as (HO, 2005)

$$\mathbf{E}_r(t) = [A_s(t) e^{j\phi_s(t)} + \eta_s(t)] e^{j\omega_o t}, \tag{2.78}$$

and

$$\mathbf{E}_{Lo}(t) = [A_{Lo} + \eta_{Lo}(t)] e^{j\omega_{Lo} t}, \tag{2.79}$$

where A_s and A_{Lo} are the amplitudes of the received signal and LO signal, respectively. Note that the amplitude of the optical signal is variant over time, while the amplitude of the LO signal is constant. ϕ_s is the optical signal phase, and ω_o and ω_{Lo} are the angular frequencies of the optical carrier and the local oscillator, respectively. η_s is the complex additive Gaussian noise of the optical signal, and η_{Lo} is the local oscillator noise.

Using the following relationship

$$|a + b|^2 = |a|^2 + |b|^2 + 2 \Re \{ a b^* \}, \quad a, b \in Z, \tag{2.80}$$

the photo-currents of Eq. (2.76) and Eq. (2.77) are redefined as

$$i_Q(t) = R A_{Lo} A_s(t) \sin(\omega_{IF} + \phi_s) + R \Re \left\{ [A_{Lo} \eta_s(t) + A_s(t) \eta_{Lo}(t) e^{j\phi_s(t)}] e^{j(\omega_{IF} + \frac{\pi}{2})} \right\}, \tag{2.81}$$

and

$$i_I(t) = R A_{Lo} A_s(t) \cos(\omega_{IF} + \phi_s) + R \Re \left\{ [A_{Lo} \eta_s(t) + A_s(t) \eta_{Lo}(t) e^{j\phi_s(t)}] e^{j\omega_{IF}} \right\}, \tag{2.82}$$

where ω_{IF} is the intermediate frequency corresponding to the difference between the angular frequencies of the carrier signal and LO as

$$\omega_{IF} = \omega_o - \omega_{Lo}. \tag{2.83}$$

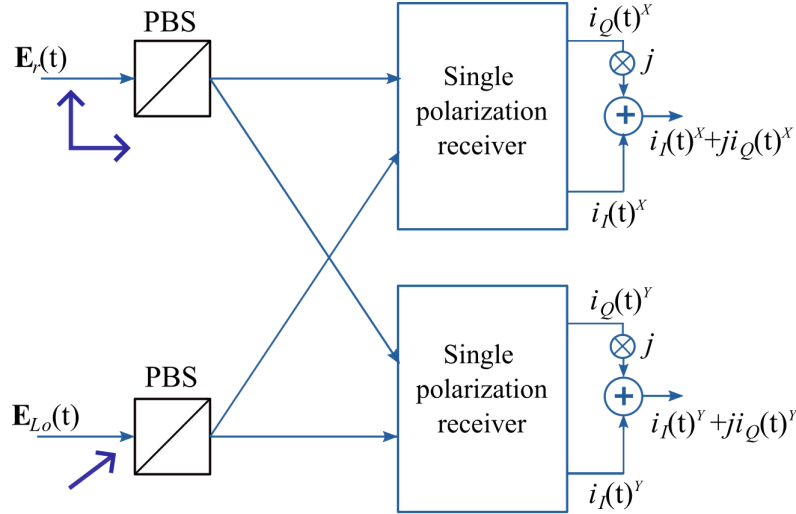


Figure 2.22 – Block diagram of a front-end with balanced detection for a dual polarization system.

If homodyne coherent detection is considered, the intermediate frequency, ω_{IF} , becomes zero, and the photo-currents can be expressed through equations (HO, 2005)

$$i_Q(t) = R A_{Lo} A_s(t) \sin(\phi_s) + R \Re \left\{ [A_{Lo} \eta_s(t) + A_s(t) \eta_{Lo}(t) e^{j\phi_s(t)}] e^{j\frac{\pi}{2}} \right\}, \quad (2.84)$$

$$i_I(t) = R A_{Lo} A_s(t) \cos(\phi_s) + R \Re \left\{ [A_{Lo} \eta_s(t) + A_s(t) \eta_{Lo}(t) e^{j\phi_s(t)}] \right\}. \quad (2.85)$$

Once the front-end has carried out the optical to electrical conversion, the electrical signal is digitized for later being processed in the DSP stage.

For a polarization-multiplexed system, the receiver has to be properly designed to correctly recover the in-phase and quadrature components of the horizontal and vertical polarization signals. A dual-polarization coherent receiver comprises two $90^\circ 2 \times 4$ hybrids, and four pairs of balanced photo-detectors as illustrated in Fig. 2.22. Moreover, a couple of PBS are required to split both the optical signal and local oscillator signal into two orthogonally polarized branches. \mathbf{E}_r is decomposed into V and H components in the first PBS. In the second PBS, \mathbf{E}_{Lo} , which is linearly polarized at 45° with respect to the PBS reference, is also split into its V and H components.

2.5 Summary

This chapter describes in detail the general components of an SDM/WDM transmission system. At transmitter block, constellation mapping, pulse-shaping, and optical modulation are explained. Later, the most widely employed spatial multiplexers are discussed. In the optical channel, the wave equation is solved to explain the propagation of modes over optical fibers. Subsequently, the GNSE that governs the pulse propagation

through an optical channel is presented. The linear and nonlinear effects experienced by the optical signal during transmission are also described. Moreover, the main interactions between spatial channels in SDM transmissions are studied. Optical amplification concepts and the fibers for SDM transmission are also introduced. On the receiver side, the front-end of the coherent receiver is described in detail for one-polarization and dual-polarization transmission systems, along with the mathematical process that describes the optical to electrical conversion of the received signal.

3 DIGITAL SIGNAL PROCESSING FOR SDM TRANSMISSION SYSTEMS

DSP algorithms are employed in coherent optical systems to compensate for the transmission impairments experienced by the signals during propagation through the optical channel. The chain of DSP algorithms implemented to compensate for channel impairments in SDM transmission systems is depicted in Fig. 3.1.

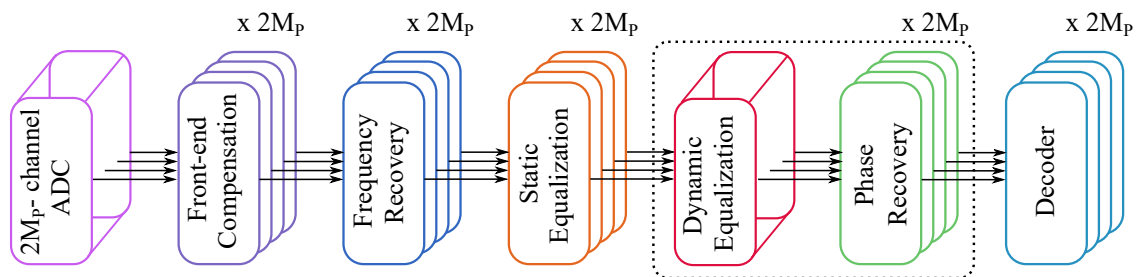


Figure 3.1 – DSP chain encompassing all the blocks required to compensate for the transmission impairments introduced by the SDM system.

The ADC with $2M_p$ - channels re-samples the received signals at two samples per symbol and delivers the $2M_p$ sequences to the DSP chain. The front-end compensation block aims to compensate for the orthogonality loss between the in-phase and quadrature components resulting from receiver imperfections. Note that one block is required for each received signal to be processed independently. Next, the frequency recovery blocks compensate for the frequency offset coming from the difference between the operating frequencies of the transmitter and LO lasers. Later, the CD is removed from the signals by static equalization. If the accumulated CD is unknown at the receiver, CD estimation techniques are required. The DSP chain also comprises a dynamic MIMO equalizer and a carrier phase recovery block. If the algorithm employed to update the adaptive equalizer is based exclusively on the signal modulus, dynamic equalization and phase recovery are implemented as two independent blocks. On the other hand, for adaptive algorithms based on both amplitude and phase, dynamic equalization and phase recovery should be implemented jointly within a loop (MORI *et al.*, 2012). In this thesis, both approaches are evaluated. After DSP, the $2M_p$ signals are independently decoded.

This chapter presents the mathematical model of a multiple-input multiple-output transmission system. Afterward, the chapter describes the algorithms employed in each module of Fig. 3.1. In particular, we focus on the algorithms implemented in this work to compensate for channel impairments in SDM transmissions.

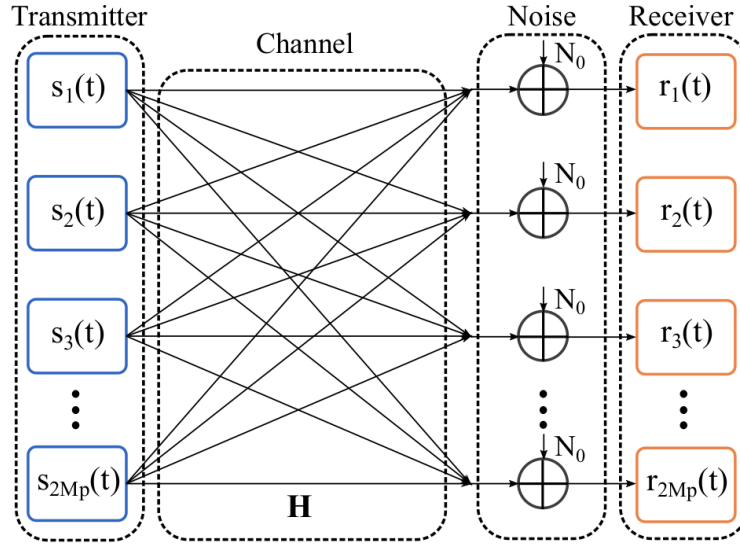


Figure 3.2 – Multiple-input multiple-output model of an SDM system with $2M_p$ transmitters and $2M_p$ receivers. $s_j(t)$ is the transmitted signal by the j th transmitter, $r_i(t)$ is the received signal by the i th receiver, and \mathbf{H} represents the propagation channel.

3.1 Multiple-input multiple-output transmission model

Neglecting any nonlinear effect, and assuming a linear operation regime, Fig. 3.2 shows the model of a multiple-input multiple-output transmission system with $2M_p$ transmitters and $2M_p$ receivers. Note that, in the scope of SDM optical systems, the number “2” comes from the two polarization orientations and M_p denotes the number of supported spatial paths. In a linear coupled MIMO transmission, the $2M_p$ receivers detect a noisy linear combination of the $2M_p$ transmitted signals. Since a spatially white noise is presumed (HO; KAHN, 2011b), the noisy sources are modeled as AWGN with the same power spectral density, N_0 , for all the paths.

The generalized $2M_p \times 2M_p$ MIMO transmission model can be described by

$$\mathbf{R} = \mathbf{H}\mathbf{S} + \mathbf{N}, \quad (3.1)$$

where the channel transfer matrix, \mathbf{H} , is expressed as

$$\mathbf{H} = \begin{bmatrix} \mathbf{h}_{1,1} & \mathbf{h}_{1,2} & \mathbf{h}_{1,3} & \cdots & \mathbf{h}_{1,2M_p} \\ \mathbf{h}_{2,1} & \mathbf{h}_{2,2} & \mathbf{h}_{2,3} & \cdots & \mathbf{h}_{2,2M_p} \\ \mathbf{h}_{3,1} & \mathbf{h}_{3,2} & \mathbf{h}_{3,3} & \cdots & \mathbf{h}_{3,2M_p} \\ \vdots & \vdots & \vdots & \ddots & \vdots \\ \mathbf{h}_{2M_p,1} & \mathbf{h}_{2M_p,2} & \mathbf{h}_{2M_p,3} & \cdots & \mathbf{h}_{2M_p,2M_p} \end{bmatrix}. \quad (3.2)$$

The elements $\mathbf{h}_{i,j}$ of \mathbf{H} denote the impulse response coefficients from transmitter j to receiver i . If L is the length of the impulse response of each element of \mathbf{H} , $\mathbf{h}_{i,j}$ can be

represented as

$$\mathbf{h}_{i,j}[k] = [h_{i,j}[k] \quad h_{i,j}[k-1] \quad h_{i,j}[k-2] \quad \cdots \quad h_{i,j}[k-L+1]]. \quad (3.3)$$

The transmitted matrix, \mathbf{S} , and received matrix, \mathbf{R} , consist of $2M_p$ sequences of L symbols as

$$\mathbf{S} = [\mathbf{s}_1[k] \quad \mathbf{s}_2[k] \quad \mathbf{s}_3[k] \quad \cdots \quad \mathbf{s}_{2M_p}[k]]^T, \quad (3.4)$$

$$\mathbf{R} = [\mathbf{r}_1[k] \quad \mathbf{r}_2[k] \quad \mathbf{r}_3[k] \quad \cdots \quad \mathbf{r}_{2M_p}[k]]^T, \quad (3.5)$$

where the L -length symbols sequences, $\mathbf{s}_j[k]$, and $\mathbf{r}_i[k]$, are expressed as

$$\mathbf{s}_j[k] = [s_j[k] \quad s_j[k-1] \quad s_j[k-2] \quad \cdots \quad s_j[k-L+1]], \quad (3.6)$$

$$\mathbf{r}_i[k] = [r_i[k] \quad r_i[k-1] \quad r_i[k-2] \quad \cdots \quad r_i[k-L+1]]. \quad (3.7)$$

The AWGN matrix, \mathbf{N} , consists of $2M_p$ noisy sequences that are added to the linear combination of the transmitted signals. The noise matrix, \mathbf{N} , and each component, $\mathbf{n}_i[k]$, are given by

$$\mathbf{N} = [\mathbf{n}_1[k] \quad \mathbf{n}_2[k] \quad \mathbf{n}_3[k] \quad \cdots \quad \mathbf{n}_{2M_p}[k]]^T, \quad (3.8)$$

$$\mathbf{n}_i[k] = [n_i[k] \quad n_i[k-1] \quad n_i[k-2] \quad \cdots \quad n_i[k-L+1]]. \quad (3.9)$$

3.2 Front-end impairment compensation

In coherent receivers, imperfections on hybrids, phase shifters, or photo-detectors can induce the loss of orthogonality between the in-phase and quadrature components of the signal, a phenomenon known as quadrature imbalance (QI). If not compensated, the QI effect can significantly degrade the system performance, mainly for high-order modulation formats. Fig. 3.3 shows the 4-QAM and 16-QAM constellations without and with QI.

The QI compensation is commonly done by using the Gram-Schmidt orthogonalization procedure (GSOP) that allows recovering the orthogonality between two vectors. In the DSP chain implemented for SDM systems, the GSOP is separately applied over each received signal to compensate for QI. From (FATADIN *et al.*, 2008), given two non-orthogonal components of the received signal denoted by $I'[k]$ and $Q'[k]$, the GSOP results in a new pair of orthonormal components $I[k]$ and $Q[k]$. The GSOP is performed through a set of steps. First, let us define $\rho_g = E[I[k]Q[k]]$ and \bar{P}_I and \bar{P}_Q as the average power of the respective component given by

$$\bar{P}_I = E[I^2[k]], \quad (3.10)$$

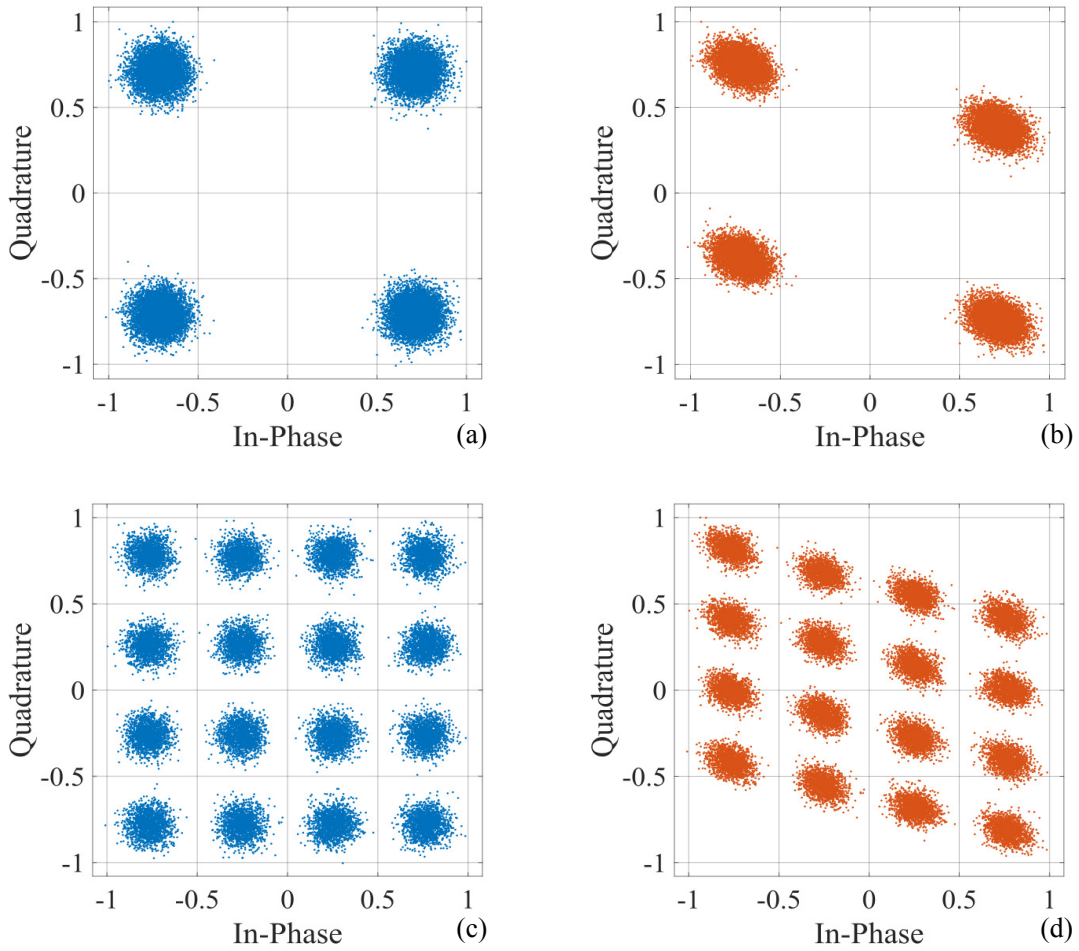


Figure 3.3 – Constellations (a) 4-QAM without QI. (b) 4-QAM with QI. (c) 16-QAM without QI. (d) 16-QAM with QI.

$$\bar{P}_Q = E[Q^2[k]], \quad (3.11)$$

then, $I[k]$ is calculated from $I'[k]$ as

$$I[k] = \frac{I'[k]}{\sqrt{\bar{P}_I}}, \quad (3.12)$$

and later, an intermediate variable $Q^o[k]$ is obtained using $Q'[k]$ and $I'[k]$

$$Q^o[k] = Q'[k] - \frac{\rho_g I'[k]}{\bar{P}_I}, \quad (3.13)$$

finally, $Q[k]$ is given by

$$Q[k] = \frac{Q^o[k]}{\sqrt{\bar{P}_Q}}, \quad (3.14)$$

The Gram-Schmidt orthogonalization method generates a new vector that is orthogonal to a particular vector. This process makes the two vectors orthogonal as shown in Fig. 3.4. After GSOP, the constellations initially with QI recover their characteristic shape without any distortions introduced by the optical front-end imperfections.

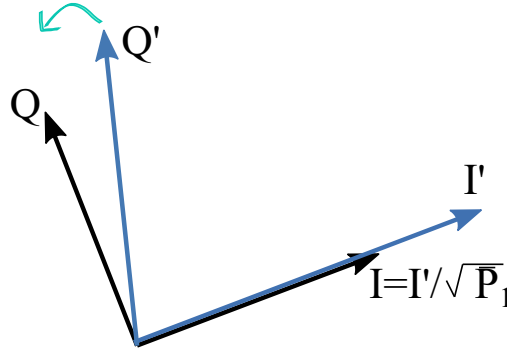


Figure 3.4 – GSOP orthogonalization for QI imbalance compensation. From two non-orthogonal components of the received signal denoted by $I'[k]$ and $Q'[k]$, the GSOP results in a new pair of orthonormal components $I[k]$ and $Q[k]$.

3.3 Frequency offset compensation

In an intradyne coherent receiver, in which the operating frequencies of the transmitter and LO lasers are similar but not identical, a perturbation in the phase of the received signal is generated as a consequence of the frequency offset, Δ_f , between them. The beating between two optical signals whose central frequencies are different results in a signal that oscillates in an intermediate frequency (SELMİ *et al.*, 2009), (HOFFMANN *et al.*, 2008). The received signal in the presence of phase and frequency offset is expressed as (FARUK; SAVORY, 2017), (HOFFMANN *et al.*, 2008)

$$r[k] = s[k]e^{j(\theta[k]+k\Delta_\Phi)} + n[k], \quad (3.15)$$

where $s[k]$ is the transmitted signal, $\theta[k]$ is the phase noise and $n[k]$ is the AWGN. The parameter Δ_Φ is the frequency offset-induced phase offset between the instants k and $k + 1$, given by

$$\Delta_\Phi = 2\pi\Delta_f T_{\text{sa}}, \quad (3.16)$$

where Δ_f is the difference between the central frequencies of the transmitter and LO lasers, and T_{sa} is the time between samples.

The objective of the frequency estimator is to identify the frequency offset that produces the phase shift experienced by the received symbols. Frequency recovery techniques can be widely classified as blind and training-aided methods. An interesting description of training-aided approaches is found in (FARUK; SAVORY, 2017). A widely used blind method implemented for frequency offset estimation is called the M th-order power algorithm (FARUK; SAVORY, 2017). In the SDM receiver, the M th-order power algorithm is independently applied over each one of the $2M_p$ received signals.

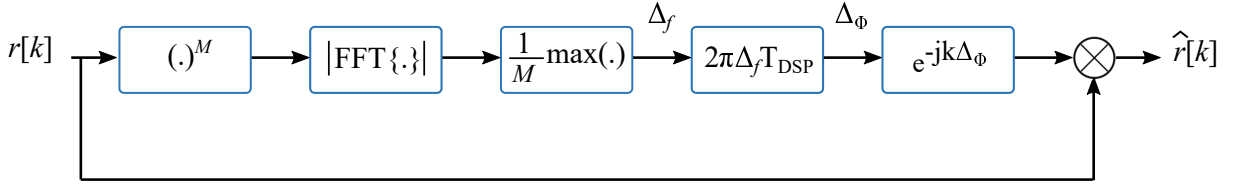


Figure 3.5 – Block diagram of frequency recovery based on spectral analysis. M th-order power algorithm.

3.3.1 Frequency domain M -th order power algorithm

The M th-order power algorithm is based on spectral analysis. The working principle is to detect the frequency corresponding to the peak of the fast Fourier transform (FFT) of the received signal raised to the 4th power. The technique was initially proposed for quaternary phase-shift-keying (QPSK) and 4-QAM but it can be extended for M -QAM with $M > 4$. Since the spectrum of the 4th-order power of the signal exhibits a peak at 4 times the frequency offset, the value of Δ_f can be estimated directly from the spectrum (FARUK; SAVORY, 2017). Fig. 3.5 shows the step-by-step of the M th-order power algorithm.

The M th-order power is applied to remove the phase modulation information of the transmitted signal. The frequency offset, Δ_f , is given by the index position of the peak of the FFT operation divided by M . The parameter T_{DSP} is the clock period of the DSP functions (FERREIRA, 2017) that can match the time between samples, T_{sa} . FFT-based methods can achieve reliable frequency offset estimation but the implementation complexity is high, especially for higher-order QAM formats (ZHOU, 2014), (PFAU *et al.*, 2009).

3.4 Static equalization

As CD is practically time invariant (SALEH, 1991), it is usually compensated for by a static equalizer (XU *et al.*, 2010). The dispersion compensating filter is given by the all-pass filter $1/G(z, \omega)$, where $G(z, \omega)$ is given by (SAVORY, 2008), (KUSCHNEROV *et al.*, 2009b):

$$G(z, \omega) = \exp\left(-j \frac{D\lambda^2}{4\pi c} \omega^2 z\right), \quad (3.17)$$

where ω is the angular frequency, D is the fiber dispersion parameter given in [ps/(km · nm)], λ is the channel propagation wavelength, c is the speed of light, and z is the propagation distance. The static equalizer can be implemented in the time or frequency domains (KUSCHNEROV *et al.*, 2009b). Since static equalization in the frequency domain presents less computational complexity for incremental dispersion values, this approach is preferred over equalization in the time domain. The DSP block that processes the $2M_p$ -mode SDM

transmission encompasses $2M_p$ frequency-domain static equalizers to independently compensate for the accumulated CD over each path. High residual CD leaked from this block results in an increased complexity of the MIMO equalizer implemented in the next stage.

3.5 Dynamic MIMO equalization

In the absence of nonlinear effects, the SDM transmission can be represented by a linear MIMO model with $2M_p$ transmitters and $2M_p$ receivers, as shown in Section 3.1. As a consequence of linear coupling and amplified spontaneous emission noise, the $2M_p$ receivers detect a noisy linear combination of the $2M_p$ transmitted signals. The linearly coupled signals can be unraveled through adaptive MIMO equalizers, which are dynamically updated to reverse the time-varying effects of the SDM link. As MIMO equalizers also compensate for residual CD and modal dispersion, their complexity increases with the broadening of the impulse response.

In the equalization block, the MIMO weight matrix, \mathbf{W} , multiplies the noisy received matrix, \mathbf{R} , to generate an estimate of the transmitted matrix, $\hat{\mathbf{S}}$, as

$$\hat{\mathbf{S}} = \mathbf{W} \mathbf{R} = \mathbf{W} (\mathbf{H} \mathbf{S} + \mathbf{N}). \quad (3.18)$$

During the equalization, the matrix \mathbf{W} is dynamically updated using an iterative procedure. MIMO equalization can be performed in time or frequency domains. Fig. 3.6 shows the block diagram of the time domain equalizer (TDE) MIMO implemented for adaptive equalization of a 6-mode transmission with polarization multiplexing. The equalizer receives 12 signals at the input and delivers 12 unraveled signals at the output that later go into the carrier phase recovery stage. The equalizer is a structure of 12×12 FIR filters that operate on twice-oversampled input sequences. Each one of the 144 filters has a length of N_{taps} taps, with N_{taps} high enough to accommodate the complete broadened channel impulse response coming from modal dispersion and residual CD.

Each of the 12 signals at the output of the TDE MIMO equalizer are computed through

$$\hat{s}_q = \sum_{i=1}^{12} \mathbf{w}_{i,q} r_i, \quad \text{with } q \in (1, 2, 3, \dots, 12). \quad (3.19)$$

For large delay spreads, a frequency domain equalizer (FDE) considerably reduces the implementation complexity compared to TDE, while preserving performance (SHIBAHARA *et al.*, 2016), (HAYKIN, 1996). Fig. 3.7 shows the structure of the 2×2 FDE MIMO proposed in (FARUK; KIKUCHI, 2011). The authors demonstrate that the m -th output of a MIMO equalizer can be represented as combinations of convolutions of odd and even sub-equalizers spaced at the symbol rate. Therefore, instead of updating the

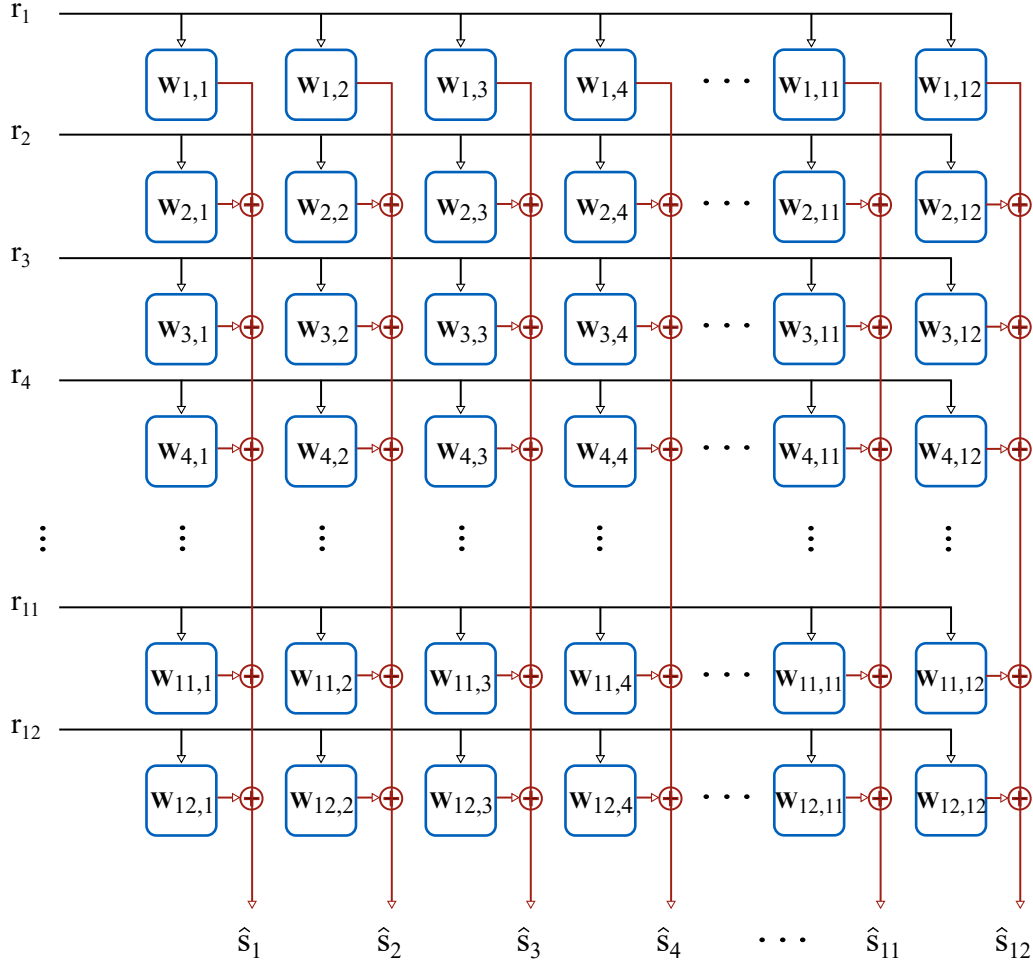


Figure 3.6 – 12×12 time-domain MIMO equalizer. Each vector $\mathbf{w}_{i,j}$ indicates the coefficients of the filter corresponding to input i and output j .

coefficients of the conventional $T/2$ spaced filters every two samples followed by a down-sampling step, the MIMO based on sub-equalizers can operate by updating the filters spaced at T , sample to sample without any need of down-sampling the output sequences. The equalizer proposed in (FARUK; KIKUCHI, 2011) is configured in a butterfly structure encompassing 8 FIR filters to separately equalize the odd and even samples of 2 channels.

In the FDE equalizer, both input signals, r_1 and r_2 , are split into two sequences containing odd and even samples. The serial to parallel converters transform the sequences to data blocks, $r_1^{e,o}[k]$ and $r_2^{e,o}[k]$, at the input of the FFT. Each block represents a column vector of length $N = N_{\text{taps}}/2$. For the implementation of linear convolution in the frequency-domain, 50% factor overlap-save is employed (SHYNK *et al.*, 1992). With this overlap factor, the sequences at the sub-equalizers input, $R_1^{e,o}[k]$ and $R_2^{e,o}[k]$, are composed by N samples of the current block and N samples from the previous block as

$$R_{1,2}^{e,o}[k] = \mathbf{FFT} [r_{1,2}^{e,o}[kN - N], \dots, r_{1,2}^{e,o}[kN + N - 1]]^T. \quad (3.20)$$

The N tap-weights of all sub-equalizers are padded with N zeros, and then, $2N$ -

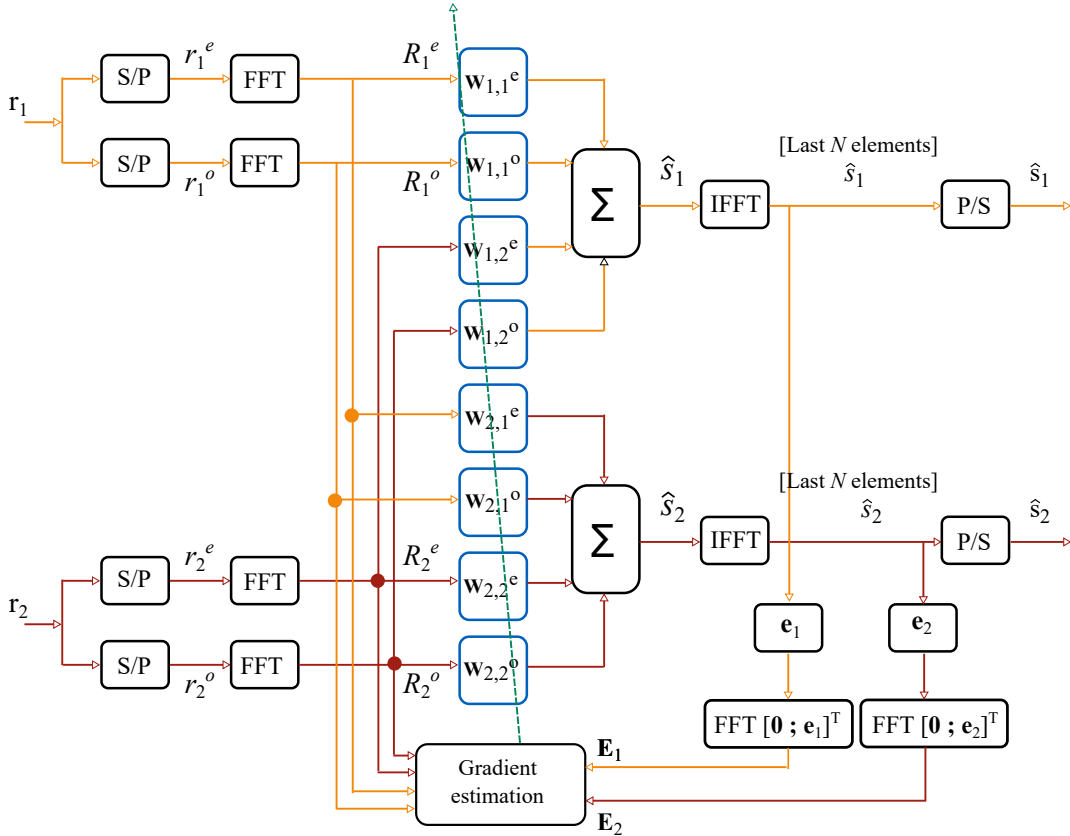


Figure 3.7 – 2×2 frequency-domain MIMO equalizer. S/P stands for serial to parallel. IFFT is the inverse FFT. Adapted from (FARUK; KIKUCHI, 2011). In the scope of this thesis, this structure was generalized to operate as a $2M_p \times 2M_p$ MIMO equalizer.

point FFTs are applied to generate FFT-coefficient vectors of the zero-padded tap-weight vectors, $\mathbf{w}_{p,q}^{e,o}[k]$, given by

$$\mathbf{W}_{p,q}^{e,o}[k] = \mathbf{FFT} [\mathbf{w}_{p,q}^{e,o}[k]; \mathbf{O}_N]^T, \quad (3.21)$$

where p and $q \in (1, 2)$.

The data blocks at the output of the sub-equalizers are computed as

$$\hat{S}_1[k] = \mathbf{W}_{1,1}^e[k] \otimes R_1^e[k] + \mathbf{W}_{1,1}^o[k] \otimes R_1^o[k] + \mathbf{W}_{1,2}^e[k] \otimes R_2^e[k] + \mathbf{W}_{1,2}^o[k] \otimes R_2^o[k], \quad (3.22)$$

and

$$\hat{S}_2[k] = \mathbf{W}_{2,1}^e[k] \otimes R_1^e[k] + \mathbf{W}_{2,1}^o[k] \otimes R_1^o[k] + \mathbf{W}_{2,2}^e[k] \otimes R_2^e[k] + \mathbf{W}_{2,2}^o[k] \otimes R_2^o[k]. \quad (3.23)$$

By employing the inverse fast Fourier transform (IFFT), the output N -length data blocks in the time-domain are given by

$$\hat{s}_{1,2}[k] = \text{last } N \text{ elements of } \mathbf{IFFT} [\hat{S}_{1,2}[k]], \quad (3.24)$$

where the first N elements are discarded due to the circular convolution.

Before gradient estimation, the N -length error column vector, $\mathbf{e}_{1,2}[k]$, is computed in the time-domain based on the adaptive algorithm criterion. Then, the error vector is padded with N zeros and passed to the frequency-domain as

$$\mathbf{E}_{1,2}[k] = \mathbf{FFT} [\mathbf{O}_N; \mathbf{e}_{1,2}[k]]^T, \quad (3.25)$$

where $\mathbf{E}_{1,2}[k]$ is a $2N$ -length column vector.

The gradient vectors, $\nabla_{p,q}^{e,o}$, are then computed by applying the overlap-save method as

$$\nabla_{p,q}^{e,o}[k] = \text{first } N \text{ elements of } \mathbf{IFFT} [\mathbf{E}_p \otimes \text{conj}(R_q^{e,o}[k])]^T. \quad (3.26)$$

Finally, gradient vectors are zero-padded and tap weights are updated in the frequency domain by using the gradient descent algorithm as

$$\mathbf{W}_{p,q}^{e,o}[k+1] = \mathbf{W}_{p,q}^{e,o}[k] + \mu_{\text{step}} \mathbf{FFT} [\nabla_{p,q}^{e,o}[k]; \mathbf{O}_N]^T, \quad (3.27)$$

where μ_{step} is the algorithm learning rate or also known as step size parameter.

The parallel to serial converters transform the equalized data blocks to the output signals, $\hat{\mathbf{s}}_1$ and $\hat{\mathbf{s}}_2$.

In the scope of this thesis, the 2×2 frequency-domain MIMO equalizer was expanded to a $2M_p \times 2M_p$ structure. For example, with $2M_p = 12$, a structure of 288 FIR filters (144 for even samples and 144 for odd samples) is required.

In this thesis, the cost function of the least mean square (LMS) algorithm is employed to update the coefficients of the equalizer filters for both TDE and FDE. The description of the LMS algorithm is presented below.

3.5.1 Least mean square algorithm

For a MIMO equalizer updated by the LMS algorithm, Eq. (3.18) can be rewritten as

$$\hat{\mathbf{S}} = \mathbf{W}_{\text{MMSE}} \mathbf{R} = \mathbf{W}_{\text{MMSE}} (\mathbf{H}\mathbf{S} + \mathbf{N}), \quad (3.28)$$

where the sub-index refers to the minimum mean square error (MMSE) criterion that defines the cost function to be optimized. The LMS algorithm is based on the steepest gradient descent (SGD) concept that is an optimization algorithm for finding a local minimum of a cost function with a gradient descent (WIDROW; HOFF, 1960), (SAYED, 2011). The LMS is a data-aided algorithm that employs the transmitted signal as desired sequence during the training stage. The usage of a training sequence ensures the convergence to the global minimum, and hence the weight matrix, \mathbf{W}_{MMSE} , can be arbitrarily initialized. In the LMS algorithm, the training sequence is independent of receiver side

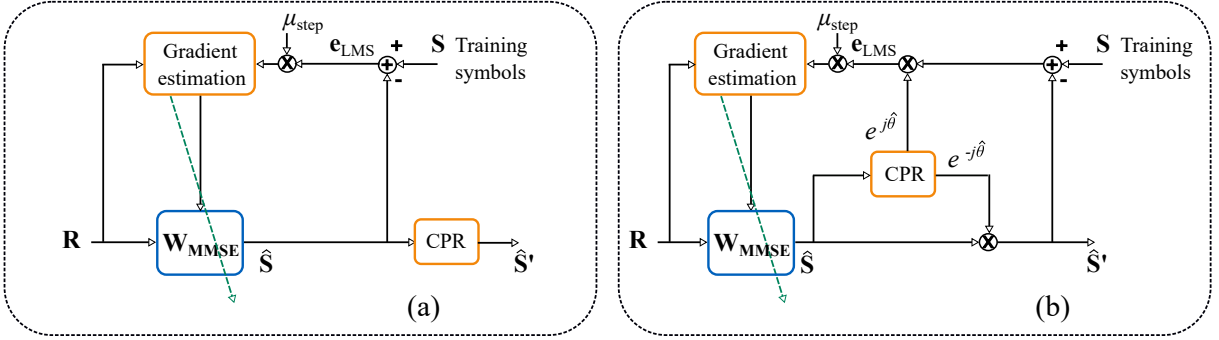


Figure 3.8 – Diagram of fully supervised adaptive equalization. \mathbf{R} , \mathbf{S} and $\hat{\mathbf{S}}$ are the received matrix, transmitted matrix and equalized matrix, respectively. \mathbf{W}_{MMSE} is the weight matrix of the MIMO equalizer. (a) Equalization independent of carrier phase recovery. (b) Equalization intertwined with a carrier phase recovery loop (MORI *et al.*, 2012).

symbol estimation, unlike the decision-directed least mean squares (DD-LMS) algorithm, which uses the detected symbol as a reference for error signal computation (UDEN, 2014). The LMS for complex signals is a low-complexity algorithm, simple and easy to implement. For a received matrix at the k^{th} instant, $\mathbf{R}[k]$, the TDE MIMO equalizer coefficients are updated at each iteration, according to the following equation

$$\mathbf{W}_{\text{MMSE}}[k+1] = \mathbf{W}_{\text{MMSE}}[k] + \mu_{\text{step}} \mathbf{e}_{\text{LMS}}[k] \mathbf{R}[k]^H, \quad (3.29)$$

where μ_{step} is the learning rate, and $\mathbf{e}_{\text{LMS}}[k]$ is the error of the LMS algorithm at the k^{th} instant given by

$$\mathbf{e}_{\text{LMS}}[k] = \mathbf{S}[k] - \hat{\mathbf{S}}[k], \quad (3.30)$$

where $\mathbf{S}[k]$ is the training matrix and $\hat{\mathbf{S}}[k]$ is the matrix after equalization at the k^{th} instant.

The block diagram of the equalization scheme based on the LMS algorithm is depicted in Fig. 3.8a. At each iteration, the received matrix, \mathbf{R} , multiplies the MIMO weight matrix, \mathbf{W}_{MMSE} , to generate the equalized matrix, $\hat{\mathbf{S}}$. As the equalization scheme is assumed to be fully supervised, the error matrix, \mathbf{e}_{LMS} , is computed by subtracting the equalized matrix, $\hat{\mathbf{S}}$, from the transmitted matrix, \mathbf{S} . Next, the error matrix is multiplied by the learning rate parameter, μ_{step} , and finally, in the gradient estimation block, $\mu_{\text{step}} \mathbf{e}_{\text{LMS}}$ is used to update \mathbf{W}_{MMSE} according to Eq. (3.29). After equalization, the equalized matrix goes through the carrier phase recovery (CPR) block for phase noise compensation that is described in the next section.

Algorithm 1 describes the adaptive equalization process based on the supervised LMS algorithm.

In coupled SDM transmission, high levels of phase noise can hinder the convergence of the adaptive algorithm. Therefore, the LMS algorithm is often implemented intertwined

Algorithm 1: LMS algorithm**Input :**

Samples per symbol: sps
 Training matrix: \mathbf{R}
 Received matrix: \mathbf{S}
 Step size: μ_{step}
 Number of taps: N_{taps}
 Initialization: \mathbf{W}_{ini}

Output:

Equalized matrix: $\hat{\mathbf{S}}$

```

1  $\mathbf{W} = \mathbf{W}_{\text{ini}}$ ;
2 for  $i \leftarrow 1 : \text{sps} : \text{length}(\mathbf{R}) - N_{\text{taps}}$  do
3   buffer =  $i : 1 : i + N_{\text{taps}} - 1$ ;
4    $\hat{\mathbf{S}}[i] = \mathbf{W}\mathbf{R}[\text{buffer}]$ ;
5    $\mathbf{e}_{\text{LMS}}[i] = \mathbf{S}[i] - \hat{\mathbf{S}}[i]$ ;
6    $\mathbf{W} = \mathbf{W} + \mu_{\text{step}} \mathbf{e}_{\text{LMS}}[i] \mathbf{R}[\text{buffer}]^H$ ;
7 end

```

Algorithm 2: LMS algorithm intertwined with a carrier phase recovery loop**Input :**

Samples per symbol: sps
 Training matrix: \mathbf{R}
 Received matrix: \mathbf{S}
 Step size: μ_{step}
 Number of taps: N_{taps}
 Initialization: \mathbf{W}_{ini}

Output:

Equalized matrix after CPR: $\hat{\mathbf{S}}'$

```

1  $\mathbf{W} = \mathbf{W}_{\text{ini}}$ ;
2 for  $i \leftarrow 1 : \text{sps} : \text{length}(\mathbf{R}) - N_{\text{taps}}$  do
3   buffer =  $i : 1 : i + N_{\text{taps}} - 1$ ;
4    $\hat{\mathbf{S}}[i] = \mathbf{W}\mathbf{R}[\text{buffer}]$ ;
5    $\hat{\theta}[i] = \text{CPR}(\hat{\mathbf{S}}[i])$ ;
6    $\mathbf{e}_{\text{LMS}}[i] = e^{j\hat{\theta}[i]} (\mathbf{S}[i] - \hat{\mathbf{S}}[i]e^{-j\hat{\theta}[i]})$ ;
7    $\hat{\mathbf{S}}'[i] = \hat{\mathbf{S}}[i]e^{-j\hat{\theta}[i]}$ ;
8    $\mathbf{W} = \mathbf{W} + \mu_{\text{step}} \mathbf{e}_{\text{LMS}}[i] \mathbf{R}[\text{buffer}]^H$ ;
9 end

```

with a carrier phase recovery loop (MORI *et al.*, 2012) as shown in Fig. 3.8b. Algorithm 2 describes the LMS algorithm working in a loop with the CPR block. In this case, the received matrix, \mathbf{R} , multiplies the MIMO weight matrix, \mathbf{W}_{MMSE} , to generate the equalized matrix, $\hat{\mathbf{S}}$. The equalized matrix, $\hat{\mathbf{S}}$, passes through the CPR block that provides an estimate of the transmitted matrix, $\hat{\mathbf{S}}'$, and an estimate of the phase, $\hat{\theta}$. The error matrix is then computed as $\mathbf{e}_{\text{LMS}} = e^{j\hat{\theta}} (\mathbf{S} - \hat{\mathbf{S}}e^{-j\hat{\theta}})$. Next, the error matrix is rotated by the estimated phase, θ , and then multiplied by the learning rate parameter, μ_{step} . Finally, in the gradient estimation block, $\mu_{\text{step}}\mathbf{e}_{\text{LMS}}$ is used to update \mathbf{W}_{MMSE} according to Eq. (3.29).

For MIMO equalization in the frequency-domain performed by a FDE, Algorithm 1

and Algorithm 2 implement direct and inverse FFTs along with zero padding techniques as illustrated in Fig. 3.7 and described from Eq. (3.20) to Eq. (3.27).

3.5.2 Analysis of the computational complexity of dynamic equalization

Regarding power consumption and chip space for implementation of DSP algorithm in application-specific integrated circuits (ASICs) or field-programmable gate arrays (FPGAs), the cost for a multiplier is considered much higher than for an adder (TESSIER; BURLESON, 2001). Therefore, the computational complexity of the TDE and FDE is commonly evaluated in terms of the required number of complex multiplications per output bit.

Assume a general butterfly-structured $2M_p \times 2M_p$ TDE equalizer composed of $(2M_p)^2$ FIR filters of N_{taps} length working in loop-mode with the CPR algorithm as shown in Fig. 3.8b. To obtain one symbol at each of the $2M_p$ output ports of the TDE, three main stages of computational operations are performed: signal filtering, FIRs tap updating, and error-value calculation. Filtering, updating, and error computation requires $N_{\text{taps}}(2M_p)^2$, $N_{\text{taps}}(2M_p)^2$, and $2(2M_p)$ complex multiplications to get one symbol at each output port, respectively. As one output symbol generates $\log_2 M$ bits, where M is the modulation format order, the complexity of the TDE equalizer in terms of total number of complex multiplications per output bit is given by

$$\begin{aligned} C_{TDE} &= \frac{N_{\text{taps}}(2M_p)^2 + N_{\text{taps}}(2M_p)^2 + 2(2M_p)}{(2M_p) \log_2 M}, \\ &= \frac{2N_{\text{taps}}(2M_p) + 2}{\log_2 M}. \end{aligned} \quad (3.31)$$

On the other hand, to obtain a block of $N_{\text{taps}}/2$ symbols at each output port of a $2M_p \times 2M_p$ FDE equalizer operating in loop-mode with the CPR stage, $2N_{\text{taps}}(2M_p)^2$, $2N_{\text{taps}}(2M_p)^2$, and $N_{\text{taps}}(2M_p)$ complex multiplications are required for filtering, filter updating, and error computation, respectively. Moreover, additional complex multiplications are needed for FFT/IFFT processes. $2(2M_p)$ FFTs are required for inputs, $2M_p$ IFFTs are required for outputs, $2M_p$ FFTs are required for error computation, $2(2M_p)^2$ IFFTs are needed for gradient estimation, and finally, $2(2M_p)^2$ FFTs are needed for filter updating. For FFT implementation, the use of the classical radix-2 algorithm is assumed, which requires $(k \log_2 k)/2$ multiplications to execute FFT of k complex numbers. Summing up the individual contributions, the complexity of the FDE equalizer in terms of total number of complex multiplications per output bit is given by

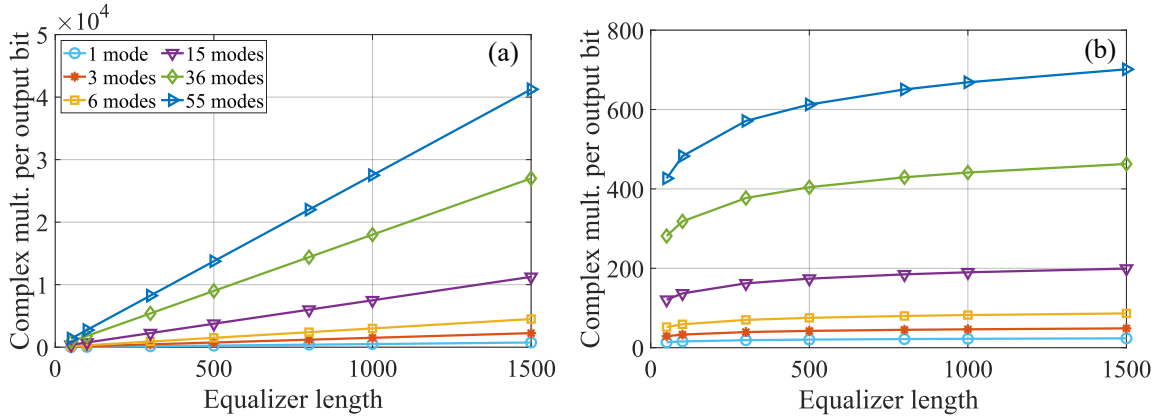


Figure 3.9 – Complexity in terms of complex multiplications per output bit as a function of the equalizer length for different number of spatial modes and $M = 16$. (a) TDE. (b) FDE.

$$\begin{aligned}
 C_{FDE} &= \frac{2N_{\text{taps}}(2M_p)^2 + 2N_{\text{taps}}(2M_p)^2 + N_{\text{taps}}(2M_p) + 2(2M_p)(2M_p + 1)(N_{\text{taps}} \log_2 N_{\text{taps}})}{(N_{\text{taps}}/2)(2M_p) \log_2 M}, \\
 &= \frac{8(2M_p) + 4(2M_p + 1) \log_2 N_{\text{taps}} + 2}{\log_2 M}.
 \end{aligned} \tag{3.32}$$

Fig. 3.9 shows the complexity for TDE and FDE equalizers as a function of the equalizer length for different number of spatial modes and $M = 16$. Note that the Y axis of both figures presents a different scale. From Fig. 3.9, the computational complexity increases linearly for the TDE equalizer. The FDE equalizer requires significantly fewer multiplications per output bit than the TDE equalizer for a given equalizer length and number of spatial modes.

3.6 Carrier phase recovery

Ideally, the laser is designed for generating light in a single frequency. In practice, however, lasers emit light in a wide band of frequencies, giving rise to what is known as phase noise. Phase noise on the received signal causes a random rotation in the constellation, which leads to a total loss of reference for the quadrature and in-phase components. Phase noise can be modeled as a Wiener process, where the phase perturbation experienced by the k^{th} symbol (PFAU *et al.*, 2009) is given by

$$\theta[k] = \theta[k - 1] + \Delta[k] = \sum_{m=0}^{k-1} \Delta[m], \tag{3.33}$$

where $\Delta[k]$ and $\Delta[m]$ are Gaussian random variables with zero mean and variance

$$\sigma_{\Delta}^2 = 2\pi\Delta_{\nu}T_{\text{sa}}, \tag{3.34}$$

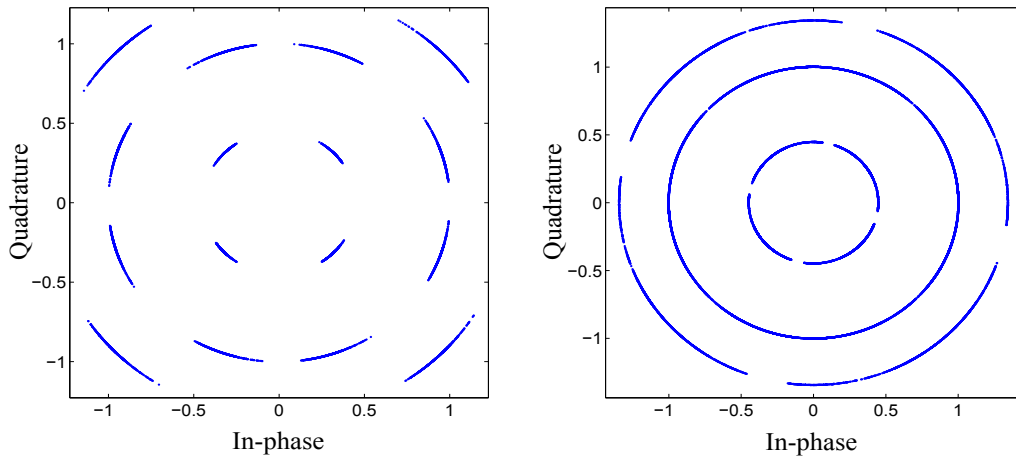


Figure 3.10 – Constellation rotation due to Wiener phase noise for 10,000 and 30,000 symbol sequences.

where Δ_ν is the sum of the transmitter and LO laser linewidths, and T_{sa} is the time between samples. In consequence, the higher the product $\Delta_\nu T_{sa}$, the higher the phase noise intensity. Eq. (3.33) and Eq. (3.34) show the laser linewidth-induced phase noise in the k^{th} instant as the result of the addition of k independent and identically distributed increments. Fig. 3.10 reflects the random rotation of two 16-QAM constellations with different lengths.

In the DSP block, the phase recovery stage aims to identify the phase perturbation experienced by the samples due to the Wiener phase noise and subsequently compensate for it. The most widely used algorithm for phase noise compensation in high-order QAM constellations is known as blind phase search (BPS).

3.6.1 Blind phase search (BPS)

Depending on the modulation format, phase recovery can be carried out by different methods. For higher-order QAM signals, BPS represents an accurate technique that demands high complexity of implementation but offers a very high performance (PFAU, 2009). Fig. 3.11 illustrates the block diagram of the BPS algorithm.

After dynamic equalization, the sample of the received signal at the k^{th} instant is still contaminated with phase noise and additive noise. For phase noise estimation, a distance metric, $M[\varphi, k]$, is defined as

$$M[\varphi, k] = \sum_{n=k-\text{ceil}(N_B/2)+1}^{k+\text{floor}(N_B/2)} |\hat{s}[n]e^{j\varphi} - \text{decision}[\hat{s}[n]e^{j\varphi}]|^2, \quad (3.35)$$

where $\text{decision}[\cdot]$ refers to symbol decision process according to the QAM constellation, φ represents the test phase defined between $[-\pi/4 \pi/4)$ due to the $\pi/2$ rotational symmetry of the QAM constellations, and N_B is an integer denoting the length of the summing

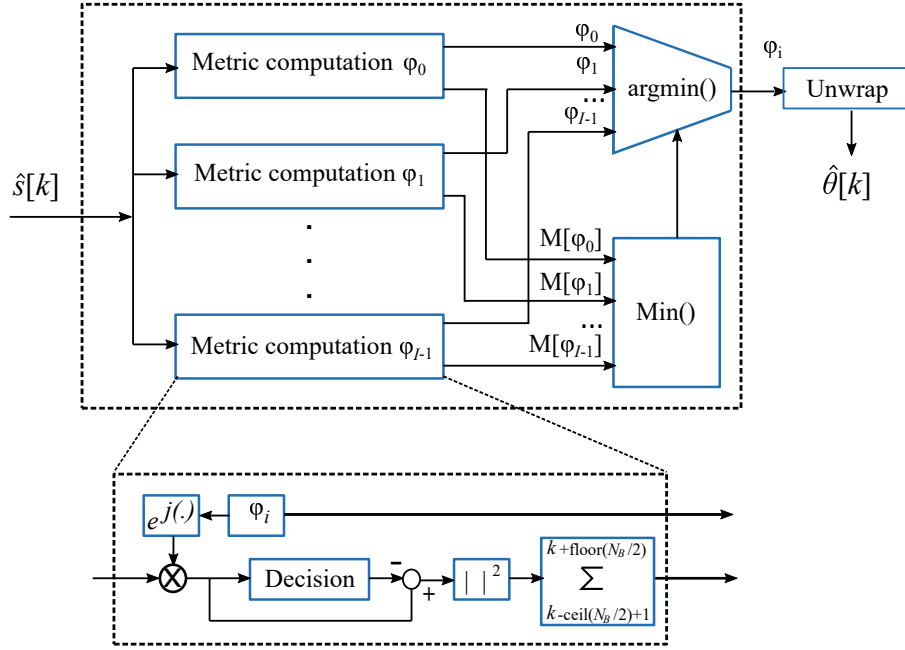


Figure 3.11 – Block diagram of the BPS algorithm.

window within which the squared Euclidean distances are summed up to filter out the additive noise. Based on the distance metric, the BPS algorithm finds the phase angle with the minimum $M[\varphi, k]$ as

$$\hat{\theta}[k] = \operatorname{argmin}_{\varphi \in [-\pi/4, \pi/4)} M[\varphi, k], \quad (3.36)$$

where $\hat{\theta}[k]$ is the phase estimate for the k^{th} symbol and $\operatorname{argmin}_{\varphi}(A)$ searches for phase φ that minimizes A . An additional step called phase unwrapping is carried out to overcome discontinuities in the phase estimation. The estimated phase after unwrapping is given by

$$UN[\hat{\theta}[k]] = \hat{\theta}[k] + \left(\frac{1}{2} + \frac{\hat{\theta}[k-1] - \hat{\theta}[k]}{2\pi/M} \right) \frac{2\pi}{M}, \quad (3.37)$$

where $UN[\cdot]$ stands for unwrapping operation.

In practice, it is unfeasible to solve the minimization problem of Eq. (3.36) over a continuous phase range. Hence, it is necessary to discretize the test phases interval into a finite set of equidistant phase angles as follows

$$\varphi_i = \frac{i\pi}{2I} - \frac{\pi}{4}, \quad \text{where } i = 0, 1, \dots, I-1, \quad (3.38)$$

where i is the index of the discrete phase angle and I is the total number of phase angles that defines the test phase resolution (LI *et al.*, 2011). The computational complexity of the algorithm depends on the number of test phases, I . In order to decrease computational efforts, low-complexity phase recovery algorithms based on BPS have been proposed. For instance, in (ZHOU, 2014), a scheme called multistage hybrid blind phase search and maximum likelihood algorithm is presented. Likewise, a common approach for reducing the operational and computational cost is the two-stage BPS algorithm initially proposed in (PFAU *et al.*, 2009).

3.6.2 Supervised CPR

Based on the transmitted matrix, \mathbf{S} , the matrix of phases denoted by $\hat{\theta}$, of the equalized matrix, $\hat{\mathbf{S}}$, can be estimated in a supervised way as

$$\hat{\theta}[k] = \arg \left[\sum_{i=1}^{N_B} \hat{\mathbf{S}}[k-i] \mathbf{S}^*[k-i] \right], \quad (3.39)$$

where $|\cdot|^*$ corresponds to the conjugate operator. As the supervised CPR technique employs the arg operator, phase unwrapping should be applied after Eq. (3.39).

The following sections apply the DSP algorithms previously described to a simulated 3-mode SDM transmission and an experimental 6-mode SDM transmission. Both setups implement polarization multiplexing.

3.7 Case study: simulation of a long-haul 3-mode SDM transmission link

The simulation setup of a coupled long-haul transmission link with $2M_p = 6$ propagation modes is depicted in Fig. 3.12. $2M_p = 6$ accounts for three spatial modes, each one with two polarization orientations. At the transmitter, 6 independent binary sequences are mapped into 560,000 16-QAM symbols at 30 GBd. The complex constellations are fed into RRC shaping filters with a 0.01 roll-off factor, generating an output signal at 8 samples/symbol. The shaped signals are then sent to I/Q MZM models for electro-optical conversion. Phase noise intensity is controlled by setting the linewidth of the transmitter and LO lasers that are used for optical modulation and demodulation modeling. The 6 optical signals are then launched into the transmission fiber model with strong mode coupling. The SDM channel is modeled using the multisection scheme presented in (HO; KAHN, 2011b) and described in detail in Section 4.2. The channel consists of 1,000 frequency bins spread over 240 GHz (note that the simulation bandwidth is 30 GHz times 8 samples per symbol, yielding 240 GHz). The resolution of the channel in the frequency domain is adjusted by replicating channel matrices between simulated frequency bins. The

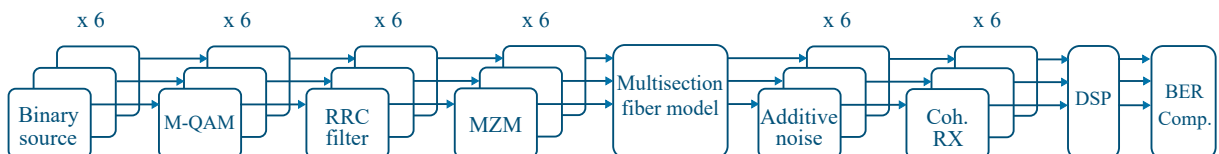


Figure 3.12 – Simulation setup of a coupled long-haul 3-mode transmission. The transmitter generates 16-QAM symbols at 30 GBd. At reception, TDE 6×6 MIMO equalization is carried out by 36 finite impulse response filters with 800 taps each, updated by a fully supervised least mean squares (LMS) algorithm.

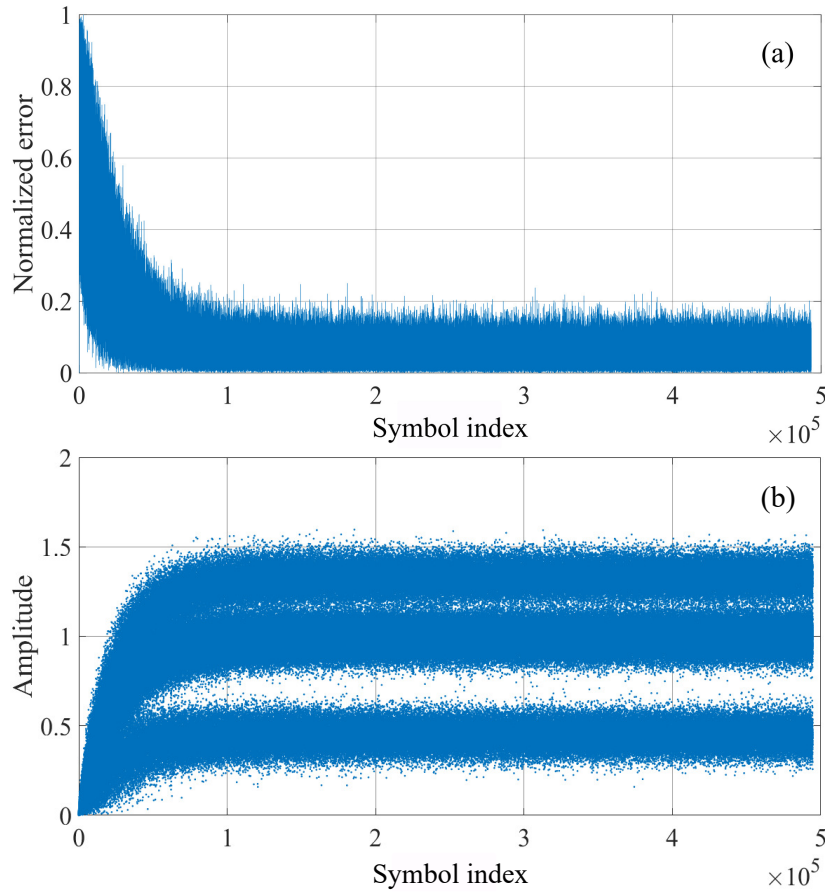


Figure 3.13 – MIMO equalizer convergence curves. (a) Normalized error as a function of the output symbol. (b) Amplitude of the output symbol as a function of the output symbol.

group delay standard deviation is set to $3.1 \text{ ps}/\sqrt{\text{km}}$ (HAYASHI *et al.*, 2017). The overall MDG of the link is controlled by a per-amplifier MDG standard deviation. Nonlinear transmission effects are not simulated. AWGN noise is added to the optical signals under the assumption of balanced and spatially white noise. After propagation, the received signals are converted from the optical to the electrical domain by the receiver front-end model, where frequency offset is injected by adding a difference between the central frequencies of the transmitter and LO lasers. The electric signals are down-sampled at two samples per symbol and fed into the DSP block. Frequency offset compensation, static equalization, dynamic MIMO equalization, and phase recovery are performed, followed by BER computation. In the dynamic equalizer, TDE 6×6 MIMO equalization is performed by 36 FIR filters with 800 taps each, updated by a fully supervised LMS algorithm with a learning rate of 2×10^{-5} . The number of taps, learning rate, as well as other hyper-parameters were optimized to guarantee filter convergence.

Fig. 3.13 shows the convergence curves of the TDE MIMO for the simulated 6-mode long-haul transmission over 5,000 km in the absence of frequency offset, phase noise, and MDG. The SNR is set up at 23 dB. In Fig. 3.13a, the normalized error signal decreases with

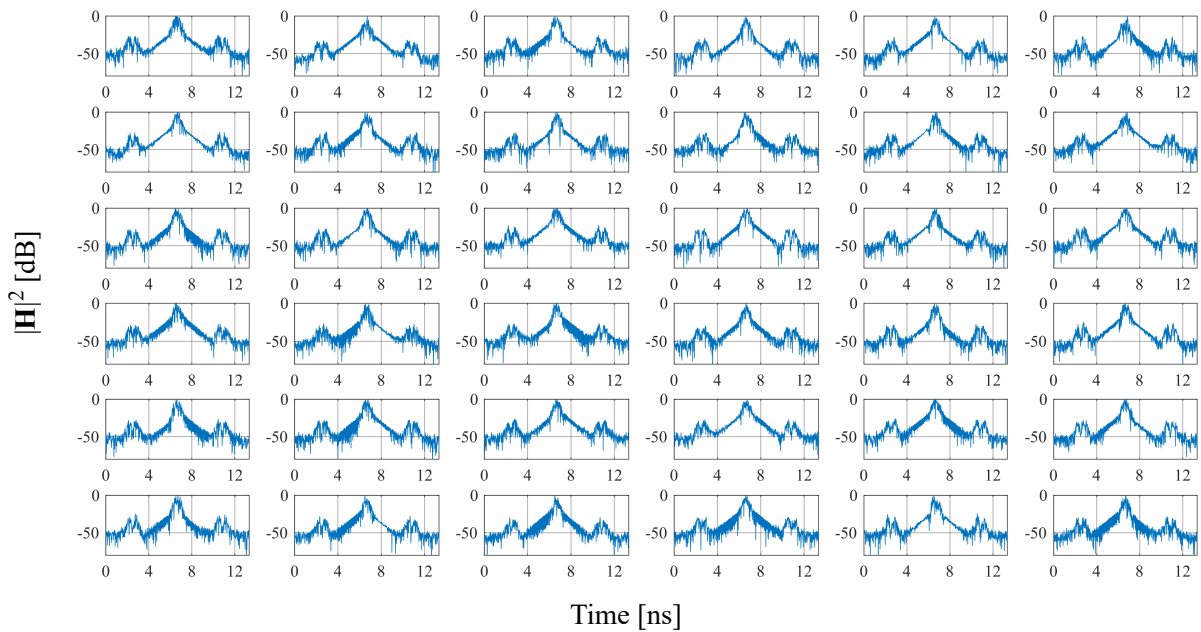


Figure 3.14 – Impulse responses magnitude obtained from the 6×6 TDE MIMO after 5,000 km transmission.

the increment of the number of output symbols, exhibiting a clear convergence of the LMS algorithm at around 100,000 symbols. After convergence, the normalized error remains below 0.2 until the end of the equalization process. Fig. 3.13b shows the evolution of the amplitude of the output symbol during convergence. After 50,000 symbols, the amplitudes start moving towards 3 distinct regions. From 100,000 symbols, once the algorithm has converged, the amplitudes remain oscillating around 3 well-defined values that correspond to the rings of the normalized 16-QAM constellation.

The impulse response magnitude of the 36 filters that compose the MIMO equalizer after 495,000 output symbols are depicted in Fig. 3.14. Filters outside the main diagonal reflect the influence of neighboring modes on a particular propagation mode. Therefore, the impulse responses outside the main diagonal reveal the presence of mode coupling and modal dispersion, while the impulse response of the filters over the diagonal exhibits only the power contribution from a mode to itself.

A simulation transmission over 1,000 km is done to evaluate the performance of both CPR approaches: independent CPR after equalization and CPR intertwined with the MIMO equalizer (see Fig. 3.8). For this transmission setup, the SNR is set up at 22 dB, and no MDG is considered. Fig. 3.15 shows the BER as a function of the linewidth of the transmitter and LO lasers for three different approaches, no CPR, CPR performed by the BPS algorithm after equalization, and supervised CPR in a loop with the MIMO equalizer. For both BPS and supervised CPR, the length of the averaging window, N_B , is 100 samples. The BPS algorithm evaluates $I = 16$ phase angles. In coupled SDM transmission, the transmitted signals experience high crosstalk levels, arriving significantly mixed to

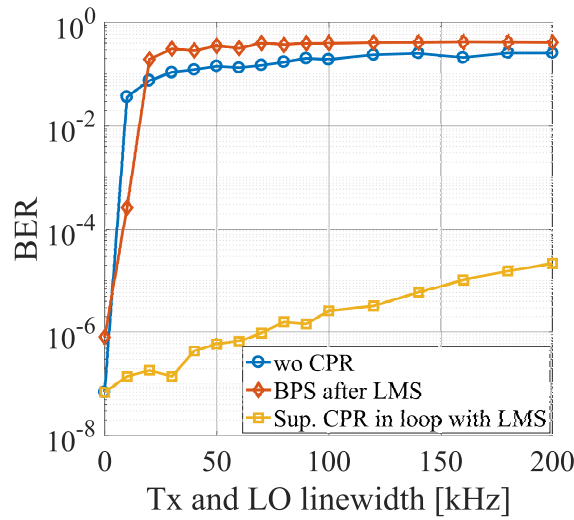


Figure 3.15 – BER as a function of the linewidth of the transmitter and LO lasers.

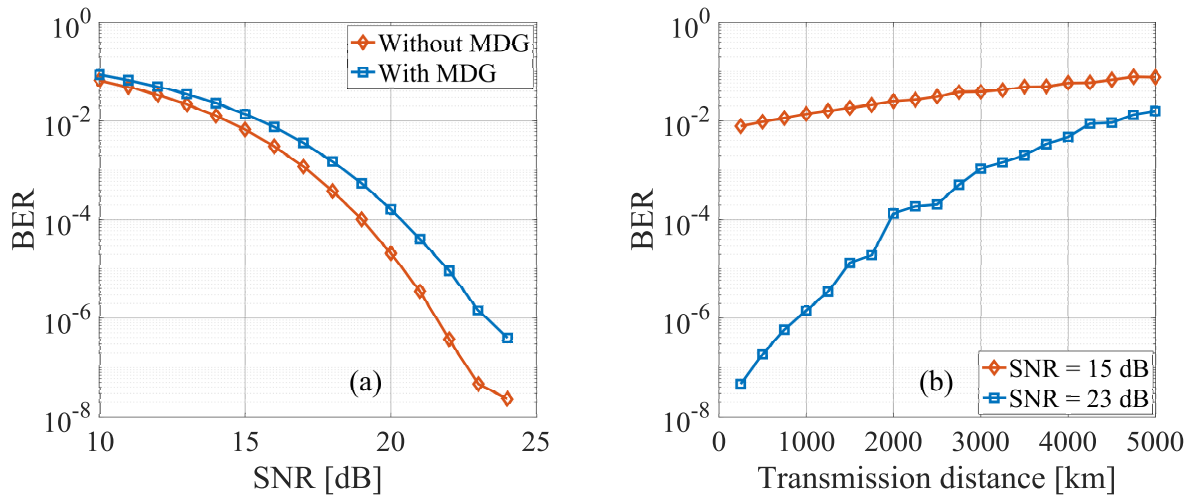


Figure 3.16 – Performance curves. (a) BER vs SNR. (b) BER vs transmission distance.

the DSP module. Consequently, the presence of phase noise coming from the linewidth of the lasers can inhibit the convergence of the LMS adaptive algorithm. Thus, as the MIMO equalizer fails to converge due to phase noise, both approaches, no CPR and CPR after equalization, lead to high error rates. The supervised CPR intertwined with the LMS adaptive algorithm presents the highest performance since the convergence of the algorithm is not affected by phases mismatches. Even though MIMO convergence is achieved in this case, the BER slowly increases with the increment of the linewidth of the transmitter and LO due to residual phase noise.

Fig. 3.16a shows the BER as a function of the SNR for an SDM transmission link over 1,000 km without and with MDG. The linewidth of the transmitter and LO lasers is fixed at 50 kHz. The equalization stage is intertwined with a supervised CPR block. At a fixed SNR, the BER is higher in the presence of MDG. For example, with MDG, an SNR of 20.3 dB is required to obtain a certain $\text{BER} = 10\text{e-}4$. On the contrary, in the absence

of MDG, an SNR of 19 dB is needed to obtain the same BER.

The BER as a function of the transmission distance is depicted in Fig. 3.16b for two different values of SNR. The MDG of the system accumulates with the transmission distance. Then, for a given SNR, the BER increments with distance as a consequence of the growing MDG.

3.8 Case study: experimental long-haul 6-mode SDM transmission

The experimental setup employed for a 138-Tb/s long-haul SDM transmission is depicted in Fig. 3.17. The long-haul experiments were performed at the Nokia Bell Labs by a partner researcher (WEERDENBURG *et al.*, 2018). The transmission setup generates 15 WDM channels transmitted over 4 LP spatial modes (LP₀₁, LP₁₁, LP₂₁, and LP₀₂). Including polarization and degenerate modes (LP_{11a}, LP_{11b}, LP_{21a}, and LP_{21b}) the setup supports 12 propagation modes. The 15-channel comb is generated using five DFBs and one phase-modulated MZM. Odd and even channels are separately modulated using IQ-modulators. The modulators are driven by two digital-to-analog converters (DACs) running at 60 GS/s, which produce 16-QAM symbol sequences. Polarization-multiplexing is generated by splitting, delaying by 50 ns, and combining the transmitted signals. The channel under test (CUT) is generated separately using a similar scheme and added to the comb using a wavelength selective switch (WSS). To decorrelate the spatial tributaries, delays of 98 ns are applied at the transmitter side. In the absence of long-distance FMFs, the multiplexed signals are transmitted through a recirculating loop that allows reusing the same fiber segment several times. Six conventional single-mode recirculating loops are combined with PLs and a 59 km long 6-mode FMF to create the SDM channel. In this setup, EDFAs, GFFs, and variable optical attenuators (VOAs) are used to compensate for losses and different gains among spectral and spatial channels that can come from

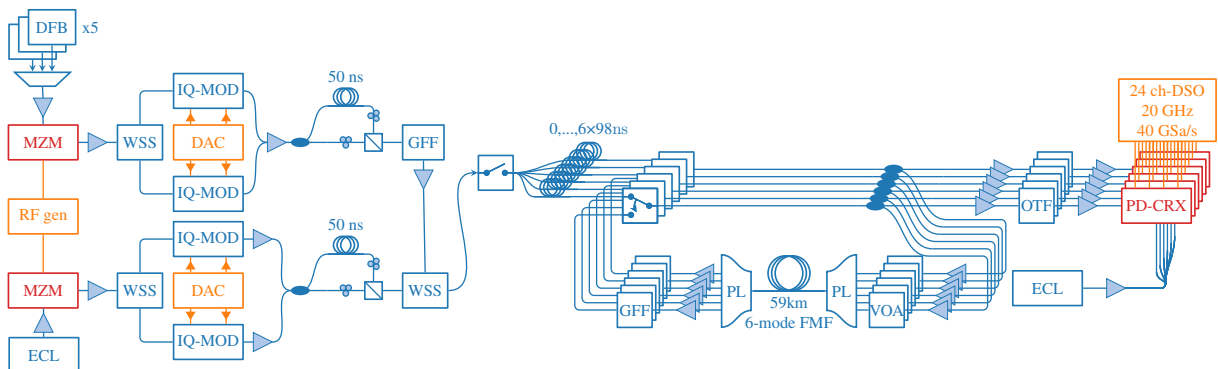


Figure 3.17 – Experimental long-haul 6-mode transmission setup with recirculating loop of 59 km. 12 spatial and polarization modes are supported, each one carry 15 WDM channels centered around 1550 nm. Triangles represent EDFAs (WEERDENBURG *et al.*, 2018).

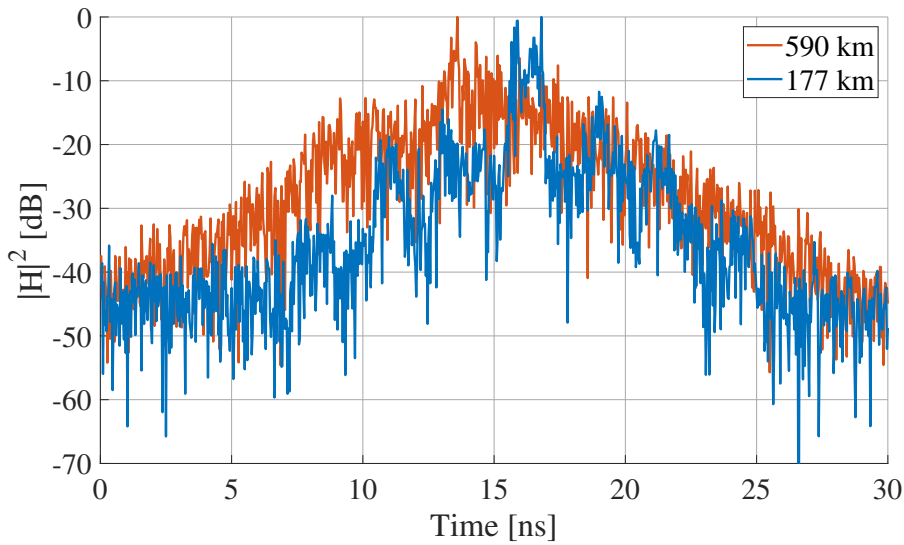


Figure 3.18 – Magnitude average impulse response after 177 km (3 loops) and 590 km (10 loops) transmission got from the FDE MIMO.

the recirculating loop. At the output of the loop, signals are amplified and forwarded to a coherent receiver array called polarization diverse coherent receiver (PD-CRX). The coherent receivers implement 10 kHz linewidth ECLs as LOs. After coherent reception, the 12 signals are converted to the digital domain by a 20 GHz bandwidth, 24 channels real-time oscilloscope operating at 40 GS/s. Then, the digital sequences are re-sampled to two samples per symbol and passed through an offline DSP chain for impairments compensation. The DSP chain employed to process the SDM experimental data consists of front-end compensation, frequency-offset compensation, static equalization, dynamic equalization, and phase recovery. The last two stages are implemented within a loop so that the phase mismatches do not affect the convergence of the LMS algorithm. The FMF used in the experiments presents a dispersion parameter approximately of 18 ps/(km · nm) averaged over all the modes. As the transmission distance is also known, no CD estimation techniques are needed.

The 59-km FMF segment used in the experiments was designed by splicing 4 fiber spools with positive and negative modal dispersion to obtain an accumulated modal dispersion of 0.35 ns. Assuming the worst scenario in which dispersion grows linearly with distance, as in the case of weakly-coupled transmission (HO; KAHN, 2011c), (ANTONELLI *et al.*, 2015), the accumulated modal dispersion after 177 km (3 loops) and 590 km (10 loops) is 1.05 ns and 3.5 ns, respectively. Fig. 3.18 shows the intensity average impulse response obtained from the FDE MIMO after 177 km and 590 km transmission. In Fig. 3.18, the intensity average impulse response broadens with the transmission distance in such a way that the orange curve (590 km) reflects a higher modal dispersion than the blue curve (177 km). In the experiments, within the MIMO, 288 1800-tap filters were required

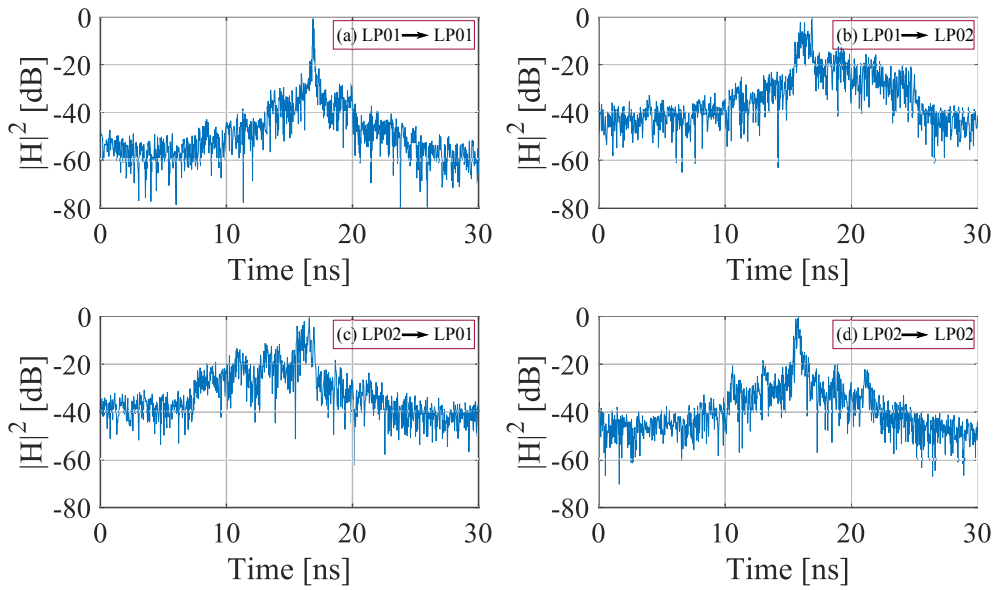


Figure 3.19 – Magnitude of the impulse responses after 177 km. Linear coupling between the LP_{01} mode and LP_{02} mode.

to equalize and separate the 12 received signals. Shorter filter lengths exhibited noticeable penalties. We believe that, in addition to fiber dispersion, such long filters also compensate for implementation issues.

In the presence of modal dispersion and linear mode coupling, the received signals experience interference due to the transfer of power between symbols of different modes at different time instants. The interference between spatial paths can be observed from the SDM channel impulse response. Fig. 3.19 shows the coupling impulse responses between LP_{01} and LP_{02} modes after 177 km. Fig. 3.19a,d illustrate the power transfer from LP_{01} to LP_{01} , and from LP_{02} to LP_{02} , respectively. In this case, the impulse responses represent the transfer of power from a propagation mode to itself in such a way that the curves exhibit a unique sharp peak, indicating low modal dispersion. On the contrary, Fig. 3.19b,c exhibit several peaks that result as a consequence of the contribution of energy of neighboring modes detected with different delays (HO *et al.*, 2013).

3.8.1 Performance evaluation

SDM transmission is subject to nonlinearities and, therefore, the signal launch power cannot be indefinitely increased. Hence, there exists an optimal launch power that maximizes the system performance. Fig. 3.20a,b show the AIR and BER as a function of the launch power per mode after different transmission distances, respectively. Both AIR and BER metrics are computed from the decoded bit sequences at the output of the DSP block and then averaged through the 12 channels. These curves were generated us-

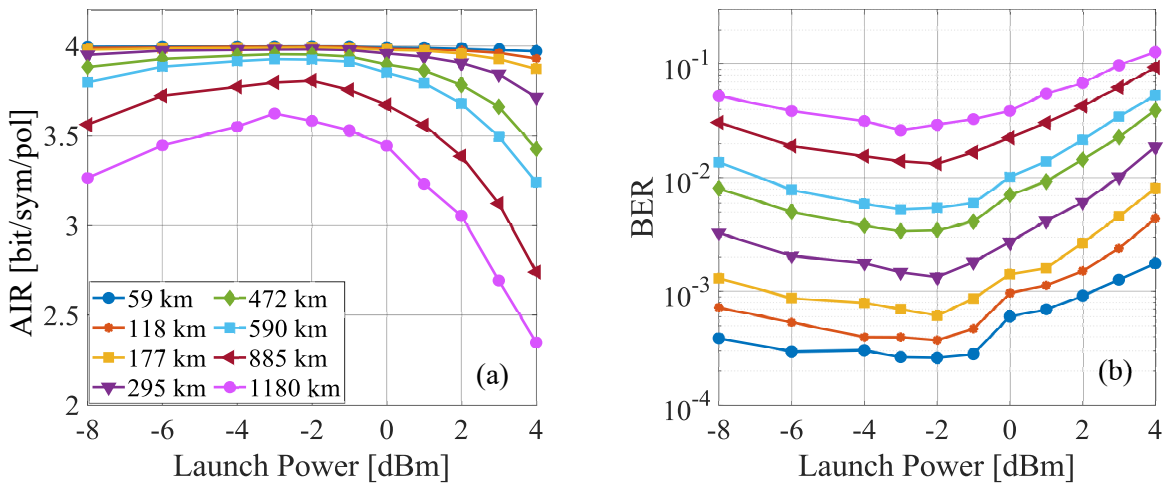


Figure 3.20 – Performance curves of the experimental long-haul 6-mode transmission. (A) AIR per polarization vs launch power per mode. (b) BER vs launch power per mode.

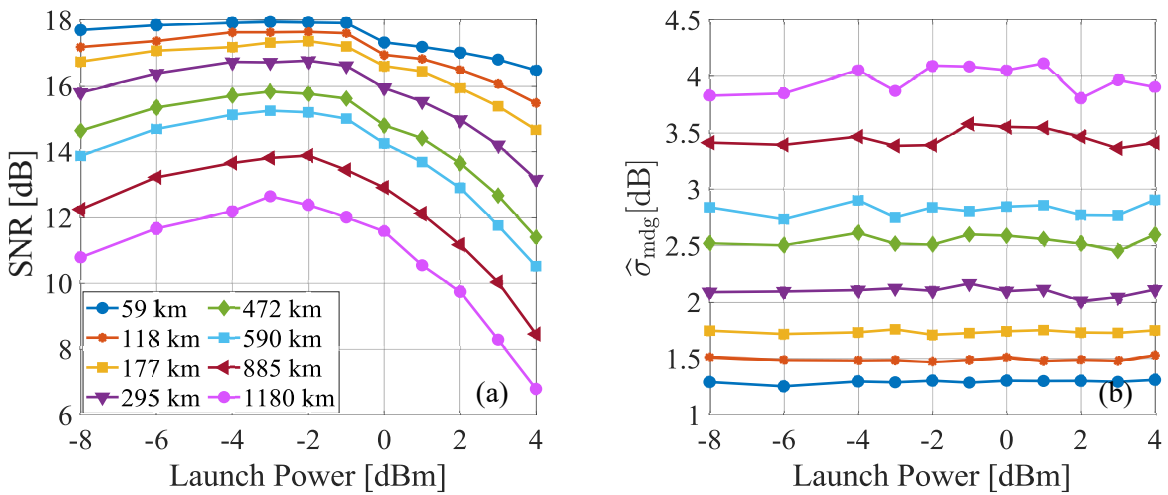


Figure 3.21 – (a) Averaged SNR computed after MIMO equalization as a function of the launch power per mode. (b) σ_{mdg} estimated by the conventional method as a function of the launch power per mode.

ing a frequency-domain MIMO equalizer. Moreover, the time-domain MIMO equalizer presented the same performance and higher computational complexity. In the linear operation regime, the performance of the 12-mode transmission increases as the launch power increases until reaching the optimal power of around -2 dBm. At launch powers higher than -2 dBm, the fiber starts operating on the nonlinear regime, and the system performance progressively decreases with the power. In order to increase the channel capacity from the SNR increment, nonlinearities compensation techniques can be integrated into the DSP chain in such a way that the optimal launch power becomes higher.

In Fig. 3.21a, the SNR averaged over the 12 propagation modes computed after MIMO equalizer is depicted as a function of the launch power per mode. The SNR of

each constellation is estimated using the least-squares (LS) channel estimation technique (WAUTELET *et al.*, 2007), (DAS; RAO, 2012). In the linear regime, the electrical SNR computed after equalization increases with the launch power until it reaches -2 dBm. This behavior remains for all evaluated transmission distances. Once the launch power is high enough to bring the fiber to the non-linear regime, the nonlinearities behave like additional noise, decreasing the total SNR. On the other hand, Fig. 3.21b shows the MDG versus the launch power per mode. σ_{mdg} is estimated through the conventional method that will be studied in detail in Chapter 4. From Fig. 3.21b, the MDG is approximately constant over the launch power range, being independent of the fiber operation regime.

3.9 Summary

This chapter presents the model of a MIMO system and describes the impairments experienced by the transmitted signals during the propagation over the SDM channel along with the DSP algorithms implemented in this thesis to compensate for them. The DSP chain is composed of 5 sub-blocks. The front-end compensation block aims to remove the QI coming from the receiver imperfections. The frequency recovery block compensates for the frequency offset induced by the different operating frequencies of the transmitter and local oscillator lasers. Assuming that both the dispersion parameter of the fiber and the link length are known, a static equalizer compensates for the accumulated CD without any need for CD estimation techniques. Once the CD has been removed, a dynamic MIMO equalizer either in the time or frequency domain unravels the received signals and removes the linear crosstalk. Finally, the CPR block is implemented during or after equalization to compensate for phase noise. Regarding dynamic MIMO equalization, the equalization process performed by the TDE and FDE is described in detail. Moreover, the LMS adaptive algorithm used to update the coefficients of the MIMO filters is studied. In addition, in this chapter, the DSP algorithms are applied to a simulation long-haul 3-mode transmission system and an experimental long-haul 6-mode transmission setup. System performance evaluation is done using metrics such as AIR and BER over different transmission conditions.

4 FUNDAMENTALS OF MODE-DEPENDENT GAIN IN SDM SYSTEMS

The MDG generated in optical amplifiers and other in-line components introduces a non-unitary transformation into the signal that cannot be trivially compensated for by DSP, resulting in a fundamental limitation for SDM transmission systems. The random power variations of guided modes induced by MDG turn the channel capacity into a random variable, reducing the average capacity and generating outages. The impact of MDG on the channel capacity of coupled SDM transmission has been widely investigated. In (HO; KAHN, 2011b), Ho *et al.* present a statistical characterization of MDL and quantify its effect on the channel capacity in strongly coupled SDM systems. In (WINZER; FOSCHINI, 2011), Winzer *et al.* discuss the MDL-induced capacity reduction in SDM channels and provide closed-form expressions for the system outage performance. In (MELLO *et al.*, 2019), Mello *et al.* review analytical expressions for channel capacity in MDG-impaired SDM systems. Moreover, they study the effect of frequency diversity on the MDG-induced outage probability and quantify the maximum tolerable per-amplifier MDG for a certain average capacity metric in ultra-long-haul (ULH) systems. In the literature, the MDG is presented as one of the main limitations for the deployment of SDM transmission systems. Thus, the study of this impairment and its estimation is essential for system evaluation and monitoring.

Besides MDG, amplification noise also constrains the link transmission rate and distance, turning into another fundamental limitation for SDM systems. Therefore, assessing both the accumulated MDG and the optical SNR at the receiver is essential for performance evaluation and troubleshooting. In the recent literature, MDG has been estimated by DSP using the transfer function of the MIMO equalizer implemented in coherent receivers. DSP-based estimation of MDG by coherent receivers yields a two-fold benefit namely: assessing the link performance and estimating a lower bound on the per-amplifier MDG performance. In (WEERDENBURG *et al.*, 2018), Van Weerdenburg *et al.* present the evolution with distance of the MDL estimated from a 12×12 LMS MIMO equalizer in a 138-Tb/s 6-mode transmission. In (WEERDENBURG *et al.*, 2017), the same authors discuss the DSP-based MDL estimation over 120 wavelength channels throughout the C-band in a 650 km 6-mode transmission. In (RADEMACHER *et al.*, 2017), Rademacher *et al.* use the coefficients of a 6×6 MIMO equalizer to estimate the MDL at different modal launch powers in a 3-mode transmission. Also, recently in (RADEMACHER *et al.*, 2020b), Rademacher *et al.* estimate the MDL in a 38-core-3-mode transmission by employing a 6

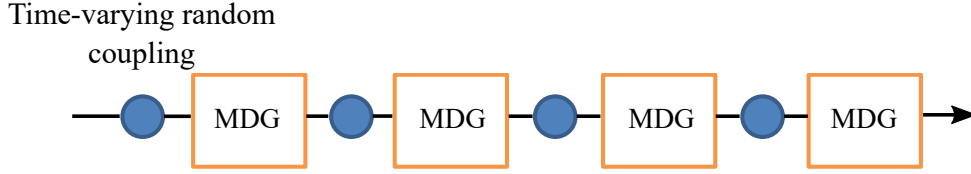


Figure 4.1 – In-line coupling and MDG components.

$\times 6$ MIMO equalizer to process each core. Although the conventional DSP-based MDG estimation method is widely used in the literature, it can lead to considerable estimation errors.

To assess the detrimental effect caused by the ASE noise, estimating the optical SNR in coupled SDM receivers is not trivial. In single-mode transmission, PDG is not a limiting effect, and the optical SNR can be estimated from the electrical SNR by a simple direct equation (ESSIAMBRE *et al.*, 2010b). In coupled SDM transmission, however, the electrical SNR may be strongly affected by MDG. In this case, estimating the optical SNR directly from the electrical SNR would underestimate the actual value.

This chapter presents the fundamentals of MDG. Firstly, the mathematical modeling of MDG in SDM transmission systems is described. The MDG-induced capacity reduction and effective SNR loss in MDG-impaired SDM transmission systems are evaluated. Moreover, this chapter describes the semi-analytical multisection model for strongly-coupled SDM transmission and its implementation in MATLAB. The multisection model is frequently used in the thesis to simulate coupled SDM channels with different levels of MDG. This chapter also presents the conventional DSP-based methods used to estimate MDG and SNR in coupled SDM transmission and evidences their performance limitations through semi-analytical and simulation results.

4.1 Mode-dependent gain in SDM transmission systems

During propagation, guided paths experience different losses and gains, giving rise to MDL and MDG, commonly called only MDG as a general impairment. The imbalance between the modal gains results from the non-flat profile of amplifiers, splices, switches, routers, and other in-line components. A linear SDM link can be modeled as a set of elements in cascade as shown in Fig. 4.1. The SDM link is composed of several time-varying random coupling elements and MDG elements. Propagating signals are randomly coupled between network blocks through coupling elements that vary over time. The MDG elements, however, are deterministic and remain constant. Omitting the frequency dependence for simplicity, any linear SDM component supporting $2M_p$ modes can be represented by a $2M_p \times 2M_p$ transfer matrix as

$$\mathbf{H}(\mathbf{k}) = \mathbf{V}^{(\mathbf{k})} \mathbf{\Lambda}^{(\mathbf{k})0.5} \mathbf{U}^{(\mathbf{k})H} \quad (4.1)$$

where \mathbf{V} and \mathbf{U} are unitary matrices accounting for random coupling at the input and output of the element, respectively, and $\mathbf{\Lambda}^{(k)}$ is a diagonal matrix with non-negative real values given by

$$\mathbf{\Lambda}^{(k)} = \text{diag} [e^{g_1(k)}, e^{g_2(k)}, e^{g_3(k)}, \dots, e^{g_{2M_p}(k)}], \quad (4.2)$$

where $g_1(k), g_2(k), g_3(k), \dots, g_{2M_p}(k)$ are the modal gains of the k -th MDG element measured in log-power-gain units, and $\text{diag}(\cdot)$ represents a square matrix formed by placing a vector on the main diagonal of a $2M_p \times 2M_p$ matrix of zeros. The total transfer matrix of the SDM link, \mathbf{H} , is then obtained as the product of the transfer matrices of the K elements as

$$\begin{aligned} \mathbf{H} &= \prod_{k=1}^K \mathbf{H}^{(k)} \\ &= \prod_{k=1}^K \mathbf{V}^{(k)} \mathbf{\Lambda}^{(k)0.5} \mathbf{U}^{(k)H}. \end{aligned} \quad (4.3)$$

The operator, $\mathbf{H}\mathbf{H}^H$, can be expressed by its eigendecomposition as

$$\mathbf{H}\mathbf{H}^H = \mathbf{Q}\mathbf{\Lambda}\mathbf{Q}^{-1}, \quad (4.4)$$

where $\mathbf{\Lambda}$ is a diagonal matrix whose main diagonal contains the eigenvalues of $\mathbf{H}\mathbf{H}^H$, λ_i^2 , and \mathbf{Q} is a matrix whose columns are the eigenvectors of $\mathbf{H}\mathbf{H}^H$. For an MDG-free SDM transmission link, all the λ_i^2 are equal to one. In the presence of MDG, the λ_i^2 are different from one representing the optical field power gains associated with the propagation paths. The imbalance between the optical field power gains of the propagation modes decreases the average capacity of the system.

In the absence of MDG, the instantaneous theoretical capacity in [b/s/Hz] of an ideal SDM channel with $2M_p$ independent modes is given by (MELLO *et al.*, 2019)

$$C = 2M_p \log_2 \left(1 + \frac{\text{SNR}}{2M_p} \right), \quad (4.5)$$

where the SNR is the ratio between the total signal power including all the modes and the noise power per mode. For an MDG-impaired SDM channel, the MDG capacity, C_{mdg} , is computed as (MELLO *et al.*, 2019)

$$C_{\text{mdg}} = \sum_{i=1}^{2M_p} \log_2 \left(1 + \frac{\text{SNR}}{2M_p} \lambda_i^2 \right), \quad (4.6)$$

where the eigenvalues, λ_i^2 , of $\mathbf{H}\mathbf{H}^H$, account for the MDG of the channel with transfer matrix, \mathbf{H} . Fig. 4.2a,b show the MDG capacity, C_{mdg} , computed through Eq. (4.6), and the normalized capacity, C_{mdg}/C , as a function of σ_{mdg} for $2M_p = 6$ and $\text{SNR}/2M_p = 22$ dB and 7 dB. The eigenvalues, λ_i^2 , are obtained from matrices \mathbf{H} with different levels of

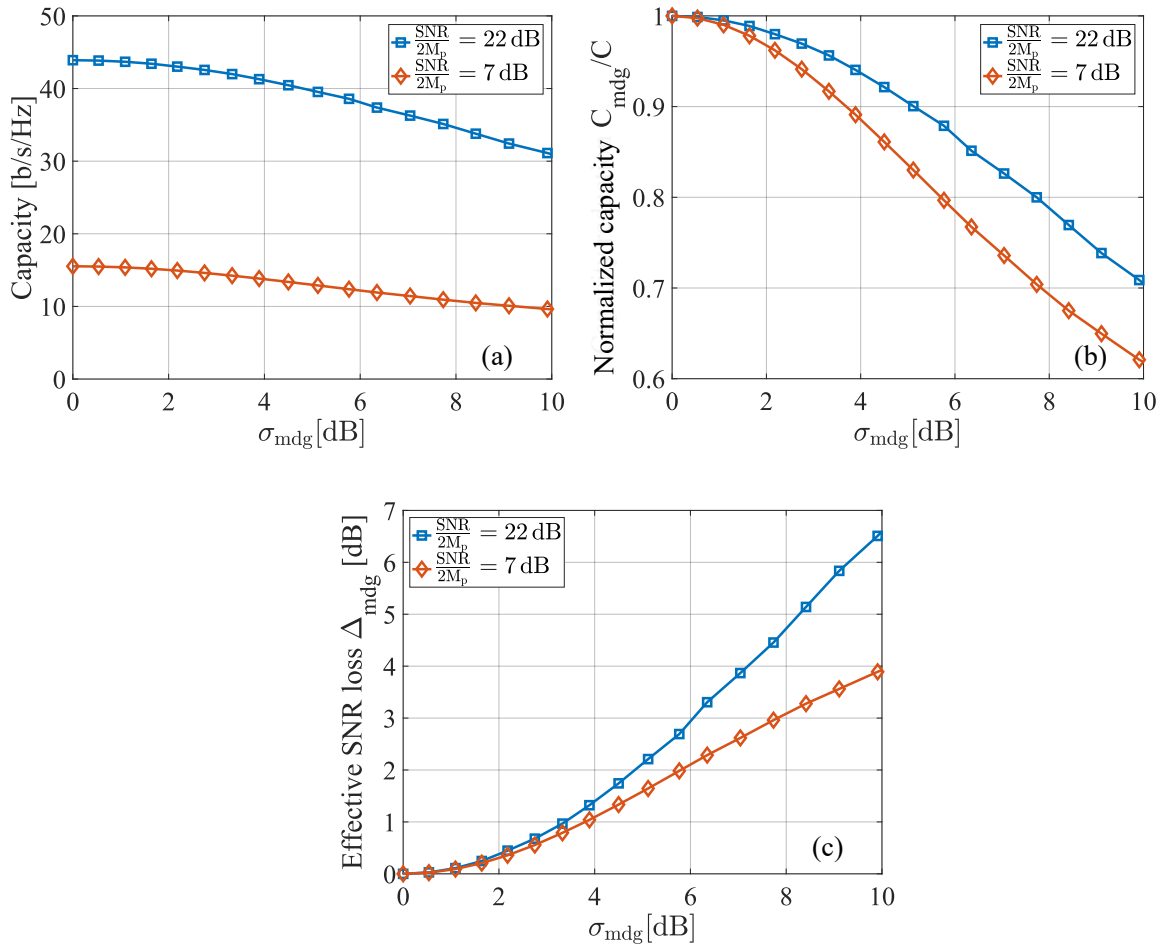


Figure 4.2 – Semi-analytical curves. (a) MDG capacity, C_{mdg} , as a function of σ_{mdg} . (b) Normalized capacity, C_{mdg}/C , as a function of σ_{mdg} . (c) Effective SNR loss, Δ_{mdg} , as a function of σ_{mdg} . The curves are generated using the multisection model of Section 4.2 for $2M_p = 6$.

MDG simulated employing the multisection model described in Section 4.2. Each point is the average of 40 matrix realizations.

The impact of the MDG on the performance of a SDM system can also be assessed by the effective SNR loss metric, Δ_{mdg} , given by

$$\Delta_{\text{mdg}} = 10\log_{10}(\text{SNR}) - 10\log_{10}(\text{SNR}_{\text{mdg}}), \quad (4.7)$$

that represents the decrease of the reference SNR that produces the same loss of capacity as the MDG causes. The SNR_{mdg} is the equivalent SNR of a system degraded by MDG defined as

$$\text{SNR}_{\text{mdg}} = 2M_p \left(2^{C_{\text{mdg}}/2M_p} - 1 \right). \quad (4.8)$$

The effective SNR loss is depicted in Fig. 4.2c as a function of σ_{mdg} for $2M_p = 6$ and $\text{SNR}/2M_p = 22$ dB and 7 dB. From Fig. 4.2, in a 6-mode transmission, a $\sigma_{\text{mdg}} = 8$ dB induces a capacity reduction of 21.5 % and 31 % for $\text{SNR}/2M_p = 22$ dB and 7 dB,

respectively. Employing the SNR loss metric, a $\sigma_{\text{mdg}} = 8$ dB introduces an effective SNR loss of 4.6 dB and 3.1 dB for $\text{SNR}/2M_p = 22$ dB and 7 dB, respectively.

4.2 MDG simulation: Semi-analytical multisection model for strongly-coupled SDM transmission

Usually, semi-analytical models are employed to study SDM systems in numerical and simulation contexts (HO; KAHN, 2011b), (FERREIRA *et al.*, 2012). In this section, the multisection model for strongly-coupled SDM transmission proposed in (HO; KAHN, 2011b) is described.

The multisection model for strongly-coupled SDM transmission (HO; KAHN, 2011b) splits the fiber link into K sections. At an angular frequency ω , the transfer matrix of the k^{th} section, $\mathbf{H}^{(k)}(\omega)$, can be modeled as the product of $3 \times 2M_p \times 2M_p$ matrices, with $2M_p$ being the number of orthogonal modes (spatial and polarization modes)

$$\mathbf{H}^{(k)}(\omega) = \mathbf{V}^{(k)} \mathbf{\Lambda}^{(k)}(\omega) \mathbf{U}^{(k)H}, \quad \text{with } k = 1, \dots, K, \quad (4.9)$$

where $(\cdot)^H$ denotes the Hermitian transpose operator. The random unitary matrices \mathbf{V} and \mathbf{U} are frequency-independent and describe mode coupling at the input and output of the section, respectively. The diagonal matrix $\mathbf{\Lambda}^{(k)}(\omega)$, accounting for MDG and mode dispersion, is given by

$$\mathbf{\Lambda}^{(k)}(\omega) = \text{diag} \left[e^{\frac{1}{2}g_1^{(k)} - j\omega\tau_1^{(k)}}, e^{\frac{1}{2}g_2^{(k)} - j\omega\tau_2^{(k)}}, \dots, e^{\frac{1}{2}g_{2M_p}^{(k)} - j\omega\tau_{2M_p}^{(k)}} \right], \quad (4.10)$$

where

$$\mathbf{g}^{(k)} = \left(g_1^{(k)}, g_2^{(k)}, \dots, g_{2M_p}^{(k)} \right), \quad (4.11)$$

and

$$\boldsymbol{\tau}^{(k)} = \left(\tau_1^{(k)}, \tau_2^{(k)}, \dots, \tau_{2M_p}^{(k)} \right), \quad (4.12)$$

are the uncoupled log-power gains and the uncoupled modal groups delays, respectively. The overall transfer matrix $\mathbf{H}(\omega)$ of a fiber of K sections is given by

$$\mathbf{H}(\omega) = \prod_{k=1}^K \mathbf{H}^{(k)}(\omega). \quad (4.13)$$

The transfer matrix $\mathbf{H}(\omega)$ can be also expressed, after singular-value decomposition, as the product of three matrices

$$\mathbf{H}(\omega) = \mathbf{V}(\omega) \mathbf{\Lambda}(\omega) \mathbf{U}^H(\omega), \quad (4.14)$$

where \mathbf{V} and \mathbf{U} are unitary matrices, and $\mathbf{\Lambda}$ is a diagonal matrix that characterizes the system MDG.

In this thesis, the multisection model is implemented in MATLAB assuming one section per fiber span, following the steps below:

1. Define the number of modes $2M_p$, the number of fiber spans K , the span length L_s (in km), the group delay standard deviation σ_τ (in ps/ $\sqrt{\text{km}}$), and the target accumulated MDG standard deviation ξ (in dB).
2. From ξ , compute the per-amplifier MDG standard deviation, σ_g , in log-power units, $\sigma_{g, \text{logpw}}$.
3. Compute the uncoupled log-power gains vector of Eq. (4.11) as $[\text{ones}(1, M_p) - \text{ones}(1, M_p)] \times \sigma_{g, \text{logpw}}$ (HO; KAHN, 2011b).
4. Compute the group delay standard deviation per span through $\sigma_{\tau, \text{per-span}} = \sigma_\tau \times \sqrt{L_s}$.
5. Compute the uncoupled modal groups delays vector of Eq. (4.12) as $\mathbf{GD} \times \sigma_{\tau, \text{per-span}}$, where \mathbf{GD} is a Gaussian distributed vector that sums to zero.
6. For each span, generate two frequency-independent random unitary matrices $\mathbf{V}^{(k)}$ and $\mathbf{U}^{(k)}$ to describe mode coupling at the input and output.
7. At each frequency, ω , and for each k^{th} span, generate the diagonal matrix $\mathbf{\Lambda}^{(k)}(\omega)$ using the uncoupled log-power gains and the uncoupled modal groups delays, obtained in steps 3 and 5, respectively.
8. At each frequency, ω , and each k^{th} span, multiply the three matrices, $\mathbf{V}^{(k)}$, $\mathbf{\Lambda}^{(k)}(\omega)$, and $\mathbf{U}^{(k)}$ to generate $\mathbf{H}^{(k)}(\omega)$.
9. For each frequency, ω , multiply the K matrices $\mathbf{H}^{(k)}(\omega)$ to generate the overall transfer matrix $\mathbf{H}(\omega)$.
10. Normalize $\mathbf{H}(\omega)$ by the square root of the mean of the overall coupled modal power gains at all frequencies, to ensure equal input and output powers.

The overall coupled modal gains in log-power units are given by the logarithm of the eigenvalues λ_i^2 of the operator $\mathbf{H}(\omega)\mathbf{H}^H(\omega)$. These eigenvalues, λ_i^2 , describe the power distribution of the propagation modes. For low levels of MDG, the set of λ_i^2 is confined around one. In contrast, as the MDG increases, the eigenvalues spread and move away from one. Fig. 4.3 shows the λ_i^2 as a function of the frequency bin for a 3-mode transmission with polarization multiplexing at two levels of MDG, with $K = 50$ and span length, $L_s = 50$ km. In the multisection model, 1,000 frequency bins are used to represent $\mathbf{H}(\omega)$.

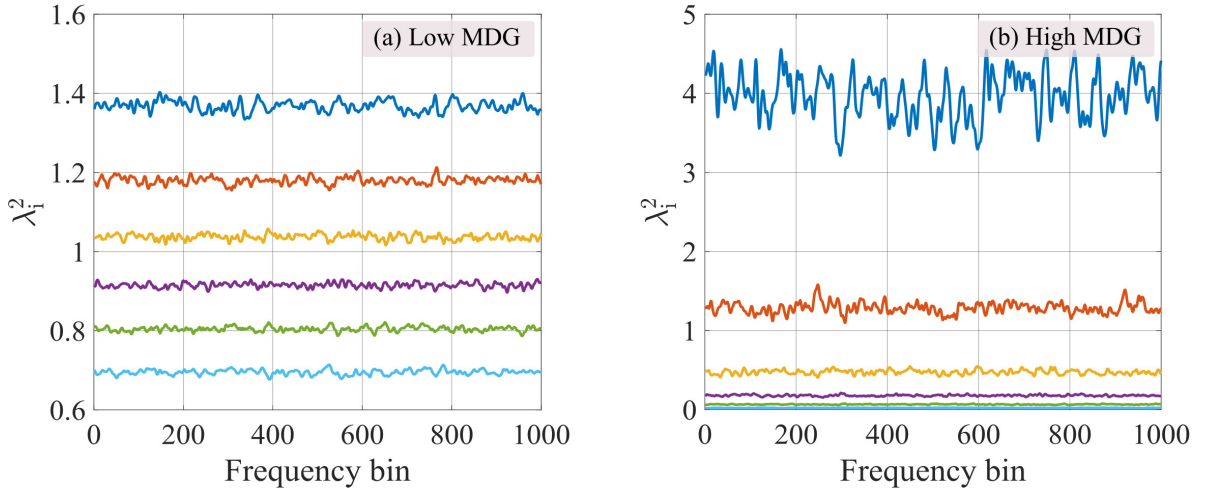


Figure 4.3 – Eigenvalues λ_i^2 as a function of the frequency bin for (a) Low MDG. (b) High MDG.

As will be defined later in Section 4.3, there are two main metrics to quantify the overall MDG in SDM systems: the standard deviation of the overall MDG denoted by σ_{mdg} and the peak-to-peak MDG denoted by $\text{MDG}_{\text{pk-pk}}$ (WINZER; FOSCHINI, 2011). The overall MDG is controlled through the MDG standard deviation per span, σ_g , that is employed to define the uncoupled gains vector per span of Eq. (4.11). The accumulated MDG standard deviation, ξ , increases with the square-root of K as $\xi = \sigma_g \sqrt{K}$. The standard deviation of the overall MDG, σ_{mdg} , and the accumulated MDG standard deviation, ξ , are related as

$$\sigma_{\text{mdg}} = \xi \sqrt{1 + \frac{\xi^2}{12 (1 - (2M_p)^{-2})}}. \quad (4.15)$$

Fig. 4.4 shows the peak-to-peak MDG and the overall σ_{mdg} in dB units computed from $\mathbf{H}(\omega)$ as a function of the number of spans in a 3-mode system with polarization multiplexing, $\sigma_g = 0.55$ dB, span length of 50 km, and group delay standard deviation of $3.1 \text{ ps}/\sqrt{\text{km}}$ (HAYASHI *et al.*, 2017). Fig. 4.4 also shows σ_{mdg} obtained from Eq. (4.15). The model parameters are summarized in Table 4.1.

4.3 DSP-based MDG estimation

The MDG of a link with transfer matrix $\mathbf{H}(\omega)$ can be computed from the eigenvalues λ_i^2 of the operator $\mathbf{H}(\omega)\mathbf{H}^H(\omega)$, where $(\cdot)^H$ is the Hermitian transpose operator (HO; KAHN, 2011b), (WINZER; FOSCHINI, 2011). As mentioned in the previous section, the accumulated MDG can be quantified by two metrics. The first one is the peak-to-peak MDG, $\text{MDG}_{\text{pk-pk}}$, given by the subtraction of the largest and the lowest eigenvalues in dB following

$$\text{MDG}_{\text{pk-pk}} = 10\log_{10}(\lambda_i^{\max})^2 - 10\log_{10}(\lambda_i^{\min})^2. \quad (4.16)$$

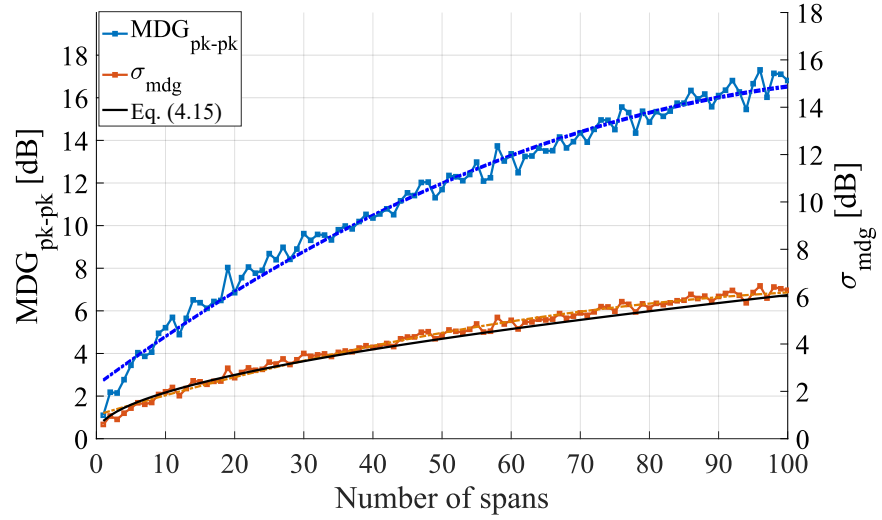


Figure 4.4 – Accumulated MDG as a function of the number of spans. The $\text{MDG}_{\text{pk-pk}}$ metric is shown at the left y-axis. The σ_{mdg} metric is shown at the right y-axis. Dashed lines show interpolated curves.

Table 4.1 – Model parameters employed for Fig. 4.4.

Parameter	Value
$2M_p$, number of orthogonal modes	6
K , number of spans	From 0 to 100
Span length	50 km
λ_i^2 , eigenvalues of $\mathbf{H}(\omega)\mathbf{H}^H(\omega)$	Variable
σ_g , MDG standard deviation per span	0.55 dB
ξ , MDG accumulated standard deviation	Variable
σ_{mdg} , standard deviation of the overall MDG	Variable
σ_τ , group delay standard deviation	3.1 ps/ $\sqrt{\text{km}}$
Symbol rate	25 GBd

The second metric is the standard deviation of the overall MDG, σ_{mdg} , computed as the standard deviation of the eigenvalues in logarithmic scale as

$$\sigma_{\text{mdg}} = \text{std}(\log(\lambda_i^2)). \quad (4.17)$$

An interesting advantage of the standard deviation metric is that, in long-haul links with strong mode coupling, it allows to estimate the impact of MDG on capacity using analytic formulas (HO; KAHN, 2011b), (MELLO *et al.*, 2019). Therefore, in this thesis, the standard deviation metric is mainly used.

In DSP-based MDG estimation, \mathbf{H} is unknown and needs to be estimated from the data. Classic channel estimation in narrowband and subcarrier transmission systems uses

the LS or the linear MMSE algorithms¹ (BEEK *et al.*, 1995). These techniques transmit pilot sequences and estimate \mathbf{H} based on block operations on the transmit and receive signals. Both methods have their limitations, as the LS algorithm is severely impaired by noise, and the MMSE strategy required previous knowledge of the channel covariance matrix and the noise variance (EDFORS *et al.*, 1998). Employing these classic channel estimation algorithms in SDM optical transmission systems is not straightforward due to the severe conditions of phase noise and frequency drift generated in semiconductor lasers typically used in fiber optic communications.

Alternatively, the inverse of the equalizer transfer function, $\mathbf{W}_{\text{EQ}}^{-1}$, is conventionally used as an estimate of \mathbf{H} (WEERDENBURG *et al.*, 2018), (RADEMACHER *et al.*, 2017), (RADEMACHER *et al.*, 2020b). MIMO receivers are usually implemented by MMSE equalizers, whose transfer function can be expressed as (KIM *et al.*, 2008), (MCKAY *et al.*, 2009)

$$\mathbf{W}_{\text{MMSE}} = \left(\frac{\mathbf{I}}{\text{SNR}} + \mathbf{H}^H \mathbf{H} \right)^{-1} \mathbf{H}^H, \quad (4.18)$$

where SNR is calculated in the optical domain using the signal bandwidth as reference noise bandwidth. In the conventional DSP-based MDG estimation method, the standard deviation of the overall MDG, σ_{mdg} , is then computed from the eigenvalues, $\lambda_{i,\text{MMSE}}^2$, of the operator the $\mathbf{W}_{\text{MMSE}}^{-1}(\mathbf{W}_{\text{MMSE}}^{-1})^H$ as

$$\hat{\sigma}_{\text{mdg}} = \text{std}(\log(\lambda_{i,\text{MMSE}}^2)). \quad (4.19)$$

As optical communications systems are typically wideband, a narrowband per-frequency \mathbf{W}_{MMSE} is calculated through the Fourier transform of the equalizer impulse response.

From Eq. (4.18), the operator $\mathbf{W}_{\text{MMSE}}^{-1}(\mathbf{W}_{\text{MMSE}}^{-1})^H$ is given by

$$\mathbf{W}_{\text{MMSE}}^{-1}(\mathbf{W}_{\text{MMSE}}^{-1})^H = \frac{(\mathbf{H}\mathbf{H}^H)^{-1}}{\text{SNR}^2} + \frac{2\mathbf{I}}{\text{SNR}} + \mathbf{H}\mathbf{H}^H. \quad (4.20)$$

The relationship between the actual eigenvalues, λ_i^2 , and the eigenvalues obtained by DSP, $\lambda_{i,\text{MMSE}}^2$, can be obtained from the eigendecomposition of $\mathbf{W}_{\text{MMSE}}^{-1}(\mathbf{W}_{\text{MMSE}}^{-1})^H$, as

$$\mathbf{W}_{\text{MMSE}}^{-1}(\mathbf{W}_{\text{MMSE}}^{-1})^H = \mathbf{Q} \left[\frac{\mathbf{\Lambda}_H^{-1}}{\text{SNR}^2} + \frac{2\mathbf{I}}{\text{SNR}} + \mathbf{\Lambda}_H \right] \mathbf{Q}^{-1}, \quad (4.21)$$

where $\mathbf{\Lambda}_H$ is a diagonal matrix whose main diagonal has elements λ_i^2 , and \mathbf{Q} is a matrix whose columns are the eigenvectors of $\mathbf{H}\mathbf{H}^H$. From Eq. (4.21), the original eigenvalues

¹ Please note the distinction between MMSE channel estimation and MMSE equalization.

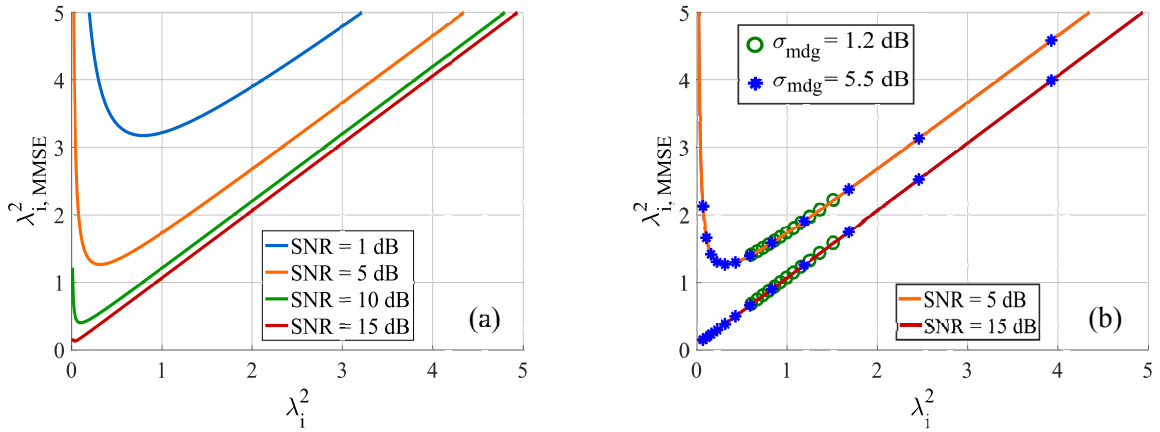


Figure 4.5 – (a) Eigenvalues estimated by DSP, $\lambda_{i,MMSE}^2$, as a function of the actual eigenvalues λ_i^2 for different levels of SNR. (b) Distribution of the 12 eigenvalues of a 6 spatial modes channel at two different levels of MDG and SNR.

λ_i^2 , and the eigenvalues obtained by DSP, $\lambda_{i,MMSE}^2$, are related by (OSPINA *et al.*, 2020b)

$$\lambda_{i,MMSE}^2 = \left[\frac{(\lambda_i^2)^{-1}}{\text{SNR}^2} + \frac{2}{\text{SNR}} + \lambda_i^2 \right], \quad (4.22)$$

Fig. 4.5a shows $\lambda_{i,MMSE}^2$ as a function of λ_i^2 for different levels of SNR. At high SNR, the first term in Eq. (4.22) tends to zero, and λ_i^2 and $\lambda_{i,MMSE}^2$ are linearly related with linear coefficient $2/\text{SNR}$. As the SNR decreases, lower values of λ_i^2 start to raise, breaking the linear relation, further impairing the estimation process. Fig. 4.5b illustrates the same effect, indicating by markers the eigenvalues obtained by different realizations of MDG and SNR in a system with 6 spatial modes (12 spatial and polarization modes). At SNR = 15 dB, the eigenvalues are positioned on the $x = y$ curve, and the conventional estimation process is successful. At SNR = 5 dB and $\sigma_{mdg} = 1.2$ dB, the estimated eigenvalues are simply displaced by $2/\text{SNR}$. If the SNR is known, this displacement can be corrected. At SNR = 5 dB and $\sigma_{mdg} = 5.5$ dB, the eigenvalues λ_i^2 in blue asterisks disperse and the lower estimated eigenvalues raise because of the nonlinear term. In this condition, the estimation accuracy of the standard DSP-based method is strongly affected.

Eq. (4.22) and Fig. 4.5 indicate that the accuracy of the conventional method that estimates σ_{mdg} based on the DSP-estimated eigenvalues, $\lambda_{i,MMSE}^2$, is clearly affected by the optical SNR (OSPINA *et al.*, 2020b). In coupled SDM transmission, the MMSE equalizer is usually implemented by means of semi-supervised or supervised adaptive schemes, such as the well-known LMS algorithm intertwined with a phase recovery loop (MORI *et al.*, 2012). The results of this section are obtained by a fully-supervised LMS algorithm. Although the LMS algorithm reaches the MMSE for mild channel conditions, it can suffer from implementation issues in extreme channel conditions, such as in pathological levels of MDG.

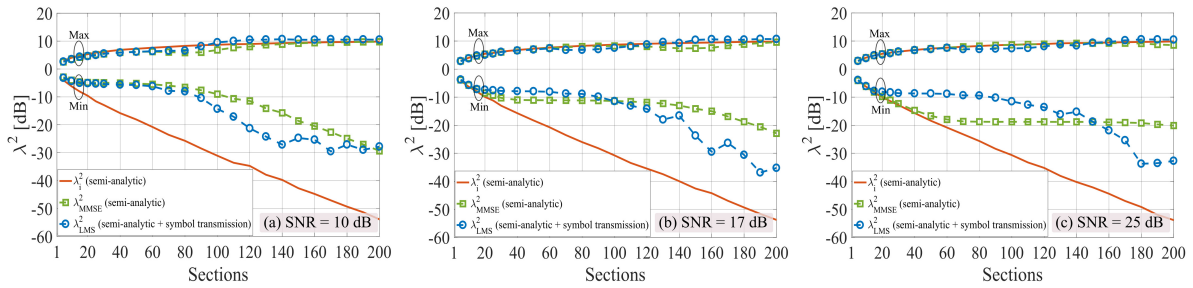


Figure 4.6 – Evolution of the maximum and minimum actual eigenvalues, λ_i^2 , and DSP-estimated eigenvalues, λ_{MMSE}^2 , and λ_{LMS}^2 , with the number of sections. (a) At low SNR = 10 dB. (b) At medium SNR = 17 dB. (c) At high SNR = 25 dB.

Fig. 4.6 shows the maximum and minimum eigenvalues for coupled SDM transmission, for three different SNR values. For each transmission distance, matrices \mathbf{H} are generated using the semi-analytical multisection model described in Section 4.2. The model simulates the coupled transmission of $2M_p = 12$ spatial and polarization modes over 50-km fiber spans. The per-amplifier MDG standard deviation, σ_g , is set to 1 dB. Eigenvalues λ_i^2 are calculated directly from \mathbf{H} . Eigenvalues $\lambda_{i,MMSE}^2$ are computed by inverting \mathbf{W}_{MMSE} calculated in Eq. (4.18). Eigenvalues $\lambda_{i,LMS}^2$ are obtained by Monte-Carlo simulation of a complete coupled SDM transmission system. The transmitter generates 12 independent sequences of 460,000 16-QAM symbols at 30 GBd. The complex signals are shaped by RRC filters and converted to the optical domain by a MZM model. The simulated channel consists of 1,000 frequency bins spread over 240 GHz (note that the simulation bandwidth is 30 GHz times 8 samples per symbol, yielding 240 GHz). The resolution of the channel in frequency domain is adjusted by replicating channel matrices between simulated frequency bins. The modal dispersion per span is 21.9 ps, corresponding to 50-km of a fiber with group delay standard deviation of $3.1 \text{ ps}/\sqrt{\text{km}}$ (HAYASHI *et al.*, 2017). Additive white Gaussian noise is added with equal power to all received channel streams to set the desired receiver SNR. At the receiver, the signals are converted to the electric domain by a coherent receiver front-end model. The electrical signals are then filtered, digitized, and processed by the DSP chain, including a fully-supervised LMS algorithm. The detailed description of the simulation setup has been already presented in Section 3.7.

In Figs. 4.6(a)-(c), three regimes of $\lambda_{i,MMSE}^2$ can be identified. In the first regime, the absolute values of both maximum and minimum $\lambda_{i,MMSE}^2$ simultaneously increase, tracking the actual eigenvalues λ_i^2 . In the second regime, both maximum and minimum $\lambda_{i,MMSE}^2$ remain approximately constant, leading the minimum $\lambda_{i,MMSE}^2$ to deviate considerably from λ_i^2 . In the third regime, the absolute value of the minimum $\lambda_{i,MMSE}^2$ increases again. The LMS MIMO equalizer results in a maximum $\lambda_{i,LMS}^2$ that tracks the maximum λ_i^2 and $\lambda_{i,MMSE}^2$ with high accuracy over the entire link. On the other hand, the minimum $\lambda_{i,LMS}^2$ diverges from the minimum $\lambda_{i,MMSE}^2$ for high values of accumulated MDG.

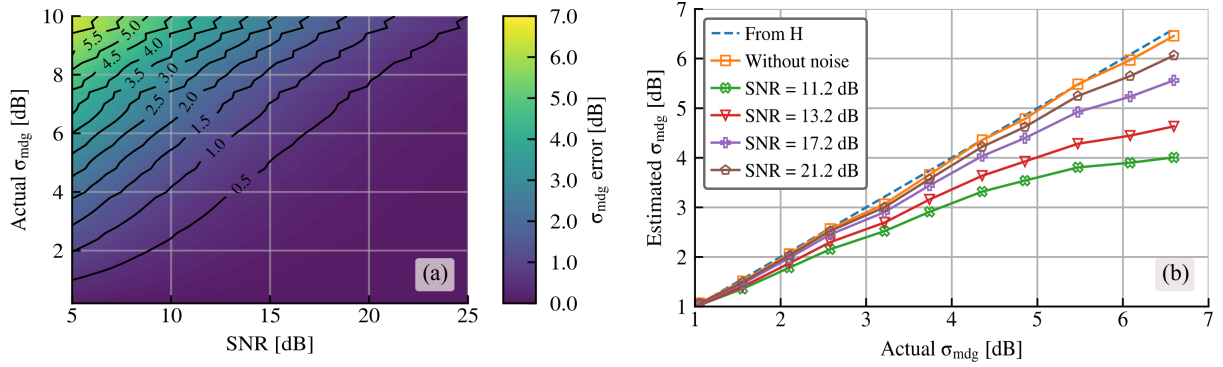


Figure 4.7 – (a) Semi-analytical estimation error in dB, computed as the difference between the actual MDG standard deviation, σ_{mdg} , and the σ_{mdg} estimated using $\mathbf{W}_{\text{MMSE}}^{-1}$ computed from \mathbf{H} . (b) Simulated MDG standard deviation σ_{mdg} estimated from the equalizer coefficients, $\mathbf{W}_{\text{MMSE}}^{-1}$, versus actual σ_{mdg} , at different SNRs.

The results in Fig. 4.6 indicate that eigenvalues derived directly from the equalizer coefficients, such as $\lambda_{i,\text{LMS}}^2$, track the actual eigenvalues λ_i^2 only over low-MDG links. For long distances and high MDG, conventional estimation methods largely underestimate the link MDG.

4.3.1 Simulation results for long-haul transmission

The performance of the DSP-based MDG estimation method in a simulated long-haul SDM transmission is evaluated. We implement in Matlab the multisection model presented in Section 4.2. The channel model consists of 12×12 matrices \mathbf{H} , simulating a linear strongly coupled pol-mux 6-mode transmission of 100 50-km spans, yielding a total length of 5,000 km. The group delay standard deviation is set to $3.1 \text{ ps}/\sqrt{\text{km}}$ (RYF *et al.*, 2019), (HAYASHI *et al.*, 2017). The MDG of the link is controlled by a per-amplifier MDG standard deviation, σ_g . Matrices \mathbf{H} are represented by 1,000 frequency bins over a bandwidth of 240 GHz to capture the effect of frequency diversity (HO; KAHN, 2011a). The MDG standard deviation σ_{mdg} is estimated in dB using $\mathbf{W}_{\text{MMSE}}^{-1}$ computed from \mathbf{H} through Eq. (4.18). The total MDG is calculated by averaging over the 1,000 frequency bins. Fig. 4.7a shows the contour plot of the estimation error in dB for a wide range of SNRs and MDG standard deviations σ_{mdg} . The estimation error is computed as the difference between the actual and estimated σ_{mdg} in dB. Therefore, a positive estimation error implies the underestimation of the actual σ_{mdg} . In Fig. 4.7a, the estimation error obtained with the conventional method for MDG estimation achieves up to 6 dB for $\sigma_{\text{mdg}} > 9$ dB across the low SNR region. At an SNR = 10 dB, an error higher than 1 dB is observed for $\sigma_{\text{mdg}} > 4$ dB. Even at a higher SNR = 15 dB, the estimation error exceeds 1.5 dB for $\sigma_{\text{mdg}} > 8$ dB. The contour plot in Fig. 4.7a makes evident the SNR impact on the estimation accuracy.

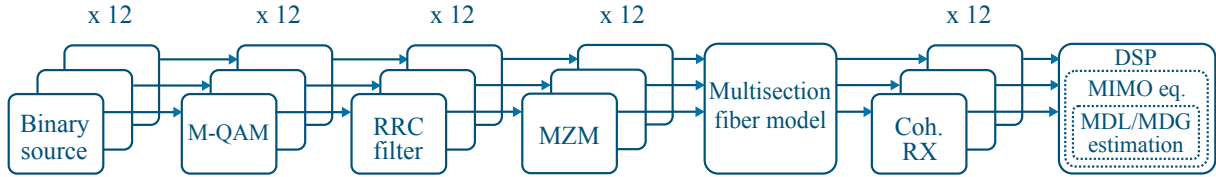


Figure 4.8 – Simulation setup of coupled long-haul 6-mode transmission. The transmitter generates 16-QAM symbols at 30 GBd. At reception, 12×12 MIMO equalization is carried out by 144 finite impulse response filters with 100 taps each, updated by a fully supervised least mean squares (LMS) algorithm. MDG estimation is performed by DSP based on the MIMO MMSE transfer function.

We further simulate a coupled long-haul transmission link with $2M_p = 12$ spatial modes and polarization multiplexing, as depicted in the simulation setup of Fig. 4.8. At the transmitter, $2M_p$ independent binary sequences are mapped into 400,000 16-QAM symbols at 30 GBd. The complex constellations are fed into RRC shaping filters with 0.01 roll-off factor, generating an output signal at 8 samples/symbol. The shaped signals are then sent to I/Q MZM models for electro-optical conversion. The $2M_p$ optical signals are then launched into the transmission fiber model with strong mode coupling. The fiber is modeled using the multisection scheme for 100 spans and 5,000 km total length. The channel consists of 1,000 frequency bins spread over 240 GHz (note that the simulation bandwidth is 30 GHz times 8 samples per symbol, yielding 240 GHz). The resolution of the channel in frequency domain is adjusted by replicating channel matrices between simulated frequency bins. The group delay standard deviation is set to $3.1 \text{ ps}/\sqrt{\text{km}}$ (HAYASHI *et al.*, 2017). The MDG of the link is controlled by the per-amplifier MDG standard deviation, σ_g . Nonlinear transmission effects are not simulated. After propagation, the received signals are converted from the optical to the electrical domain by the receiver front-end model. No phase noise has been considered for the simulations. The electric signals are down-sampled to two samples per symbol and fed into the MIMO equalizer for source separation and equalization. 12×12 MIMO equalization is carried out by 144 finite impulse response filters with 100 taps each, updated by a fully supervised LMS algorithm. The MDG standard deviation σ_{mdg} is computed at each frequency of the MIMO transfer function and averaged across the signal band. Fig. 4.7b shows σ_{mdg} estimated by the coefficients of the MMSE equalizer as a function of the actual value. In absence of noise, σ_{mdg} estimated from the equalizer coefficients tracks the actual σ_{mdg} with negligible error. As the SNR decreases, the estimation error increases for higher values of σ_{mdg} , underestimating the actual MDG.

Alternatively to the classical DSP-based method for MDG estimation that employs the inverse of the MIMO transfer function, the MDG can be estimated from the transfer matrix of the MIMO equalizer operated in reverse mode, in which the received signal is

used as a training sequence, and the transmitted signal is applied to the input of the MIMO equalizer (RADEMACHER *et al.*, 2020a). Although reverse equalization can achieve outstanding performance in an extensive range of MDG and SNR values (MELLO *et al.*, 2022), its applicability is limited in practical scenarios, as it requires the implementation of an equalizer used only for MDG estimation.

4.4 Conventional method for optical SNR estimation

Estimating the optical SNR is also not trivial in coupled SDM systems affected by MDG. In systems with coherent detection, the optical SNR can be estimated from the so-called electrical SNR. In systems with MMSE equalization, the electrical SNR in stream i is actually a signal-to-noise plus interference ratio (SINR) (MCKAY *et al.*, 2009)

$$\text{SINR}_i = \frac{1}{\left[(\mathbf{I} + \text{SNR} \mathbf{H}^H \mathbf{H})^{-1} \right]_{i,i}} - 1, \quad (4.23)$$

where $[\]_{i,i}$ indicates the i -th element in the main diagonal. The optical SNR is then estimated as

$$\widehat{\text{SNR}} = \frac{1}{2M_p} \sum_{i=1}^{2M_p} \text{SINR}_i. \quad (4.24)$$

In single-mode transmission with low PDG, \mathbf{H} is approximately unitary, such that, in Eq. (4.23) and Eq. (4.24), $\widehat{\text{SNR}} \approx \text{SNR}$. Therefore, $\widehat{\text{SNR}}$ is usually obtained from SINR_i , which is calculated using the LS method (WAUTELET *et al.*, 2007), (DAS; RAO, 2012). In MDG-impaired SDM systems, however, \mathbf{H} is non-unitary, turning $\widehat{\text{SNR}}$ dependent on \mathbf{H} . In this case, estimating the SNR from the SINR_i would underestimate the actual value since within the equalizer, the MDG is interpreted as additional noise. Any extra noise introduced into the receiver is more evident at high SNR values. Fig. 4.9 shows the SNR estimation error in dB as a function of the actual σ_{mdg} and SNR for a pol-mux 6-mode transmission system. The SNR is estimated semi-analytically through Eq. (4.24) where SINR_i is computed using Eq. (4.23). Channel matrices, \mathbf{H} , are simulated using the semi-analytical multisection model with the same fiber parameters of Section 4.3.1. From Fig. 4.9, in MDG-impaired SDM systems, the performance of the conventional SNR estimation method is highly affected by the MDG and SNR regimes. The SNR estimation error increases for high levels of MDG and high values of SNR, achieving up to 7 dB for the maximum MDG and SNR evaluated. Removing the influence of the MDG on the conventional SNR estimation is not straightforward. Therefore, the conventional method that estimates the SNR from the SINR through Eq. (4.24) would present critical estimation errors for long-distance SDM systems that accumulate high levels of MDG.

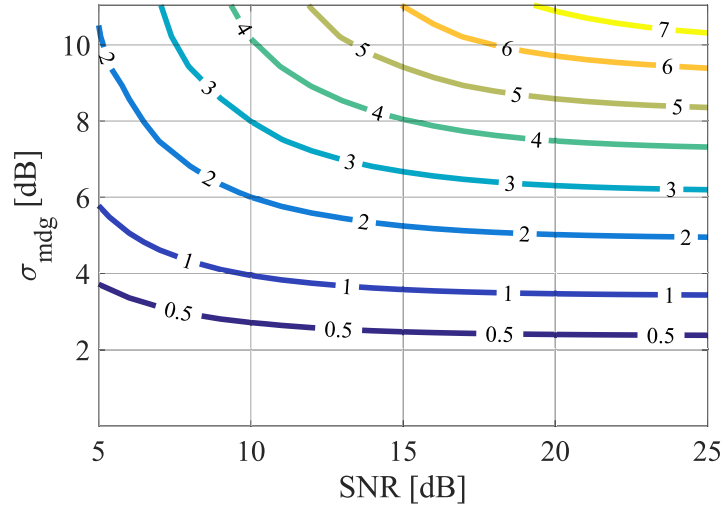


Figure 4.9 – SNR estimation error in dB, computed as the difference between the actual SNR in dB and the SNR estimated using Eq. (4.24) in dB.

4.5 Receiver implementation penalty

Another issue that may be taken into account in Eqs. (4.18), (4.19) and (4.22) to (4.24) is the fact that receiver implementation imperfections also affect the interplay of noise and MDG. These receiver imperfections can be modeled as a contribution added to the optical noise. In this case, the SNR can be redefined as SNR' , expressed as

$$\text{SNR}' = \left(\frac{1}{\text{SNR}} + \frac{1}{\text{SNR}_{\text{imp}}} \right)^{-1}, \quad (4.25)$$

where SNR_{imp} is an implementation penalty computed as the average SINR_i estimated from the equalized data streams in back-to-back, i.e., without any MDG and optical noise.

To improve the accuracy of the conventional SNR estimation technique that employs the LS method, the implementation penalty contribution can be removed. In this case, the estimated SNR is redefined as

$$\widehat{\text{SNR}} = \left(\frac{1}{\frac{1}{2M_p} \sum_{i=1}^{2M_p} \text{SINR}_i} - \frac{1}{\text{SNR}_{\text{imp}}} \right)^{-1}. \quad (4.26)$$

4.6 Summary

Coupled SDM transmission is a promising alternative for future high-capacity optical interconnection. Nevertheless, the increase in capacity provided by coupled SDM systems is fundamentally limited by MDG and ASE noise. Therefore, monitoring MDG and SNR is essential for accurate performance evaluation and troubleshooting. This chapter gathers fundamental concepts of MDG and presents its mathematical modeling. Two metrics to quantify the impact of the MDG on the system performance are introduced: capacity reduction and effective SNR loss. In addition, this chapter explains the multisection

model for strongly-coupled SDM transmission used in this dissertation to simulate SDM channels with different levels of MDG and provides a set of steps for its implementation in MATLAB. This chapter also presents the conventional MDG estimation method based on the transfer matrix of MIMO equalizers that optimize the MMSE criterion. The results show that the conventional MDG estimation method underestimates the actual value at high levels of MDG and low SNRs. The performance limitation of the conventional MDG estimation method is demonstrated with semi-analytical data and validated by Monte-Carlo simulation of waveforms launched into a coupled transmission model and received by an LMS dynamic equalizer. Similarly, the results of this chapter show that estimating the optical SNR is not a trivial task in SDM systems due to the strong influence of the MDG on the SINR. The limited performance of the conventional SNR estimation method in MDG-impaired SDM systems is evidenced using semi-analytical results. Finally, the inherent implementation imperfections in experimental setups are modeled as additional optical noise. To improve the accuracy of the conventional SNR estimation technique that employs the LS channel estimation method, the implementation penalty contribution was removed from the estimated SNR by introducing a new parameter known as SNR_{imp} .

5 CORRECTION FACTOR FOR DSP-BASED MDG ESTIMATION

Chapter 4 presents the conventional methods for MDG and SNR estimation in coupled SDM transmission. The results show that the conventional DSP-based MDG estimation method presents performance limitations in certain conditions of MDG and SNR. In this chapter, an improved DSP-based technique for MDG estimation based on a correction factor is proposed and validated using semi-analytical, simulation, and experimental data. The semi-analytical and simulation data used in this chapter are generated based on the multisection model for strongly-coupled SDM transmission presented in Section 4.2. The experimental traces with different MDG levels are obtained using the MDG emulator for experimental laboratory setups described in Section 5.1. The experimental data were measured at the High-Capacity Transmission Laboratory of the Eindhoven University of Technology, The Netherlands. The correction factor method for MDG estimation is described below.

In Section 4.3, it was shown that, as adaptive MIMO equalizers typically use the MMSE criterion (FARUK; SAVORY, 2017), the MDG estimation accuracy of the conventional method is affected by the channel SNR. The semi-analytical and simulation results indicate that the MDG accumulated over long links is underestimated mainly for high levels of MDG and low values of SNR. Using the analytical transfer function of MMSE equalizers and assuming a known SNR, a correction factor for the DSP-based eigenvalues can be obtained to remove the SNR dependence and improve the MDG estimation accuracy.

If the SNR is known, Eq. (4.22) can be inverted to recover λ_i^2 from $\lambda_{i,\text{MMSE}}^2$, resulting in a quadratic equation with two roots

$$\lambda_i^2 = \frac{[\text{SNR}^2 \lambda_{i,\text{MMSE}}^2 - 2 \text{SNR}] \pm \sqrt{[\text{SNR}^2 \lambda_{i,\text{MMSE}}^2 - 2 \text{SNR}]^2 - 4 \text{SNR}^2}}{2 \text{SNR}^2}. \quad (5.1)$$

The highest solution of Eq. (5.1) recovers λ_i^2 for high and moderate values of SNR and low and moderate values of MDG. Such positive solution is adopted as a correction factor applied over the DSP eigenvalues, $\lambda_{i,\text{MMSE}}^2$, to enhance the MDG estimation process.

The expression for the MMSE equalizer in Eq. (4.18) and the correction of the estimated eigenvalues by Eq. (5.1) apply to any coupled system represented by a transfer matrix \mathbf{H} , irrespective if it operates in the regimes of weak or strong mode coupling. In this thesis, we evaluate a long-haul transmission system with strong-mode coupling

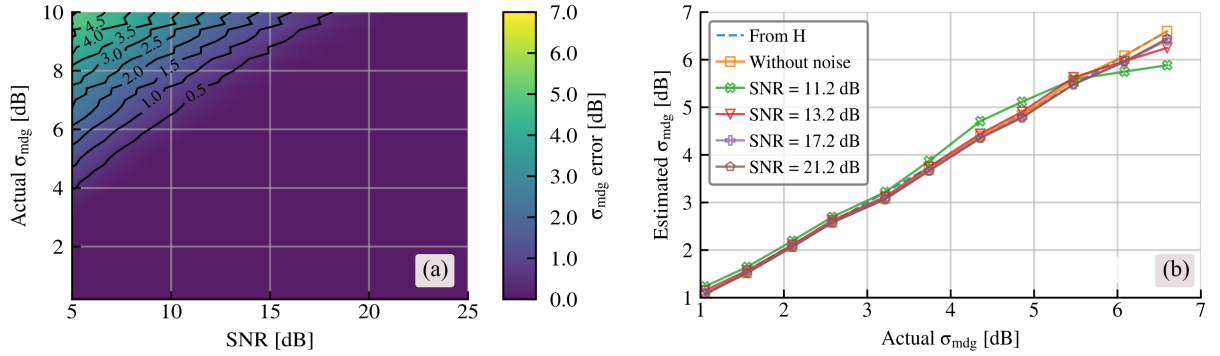


Figure 5.1 – Correction factor technique. (a) Semi-analytical estimation error, computed as the difference in dB between the actual MDG standard deviation, σ_{mdg} in dB, and the σ_{mdg} estimated using $\mathbf{W}_{\text{MMSE}}^{-1}$ computed from \mathbf{H} , also in dB. (b) Simulated MDG standard deviation, σ_{mdg} , estimated from the equalizer coefficients, $\mathbf{W}_{\text{MMSE}}^{-1}$, versus actual σ_{mdg} , at different SNRs.

through simulations, and a short-reach transmission system with weak mode coupling through experiments.

Fig. 5.1 shows the curves obtained with semi-analytical and simulated data for the same system configuration of Section 4.3.1 after using the correction factor technique to correct the MMSE eigenvalues. In comparison to Fig. 4.7, in Fig. 5.1a, the correction of the DSP-estimated eigenvalues by the positive solution of Eq. (5.1) enhances the estimation process. Here, in the low SNR regime, the maximum error is 4.5 dB for $\sigma_{\text{mdg}} > 9$ dB. At an SNR = 10 dB, an error higher than 1 dB is achieved only for $\sigma_{\text{mdg}} > 7$ dB. For SNR ≥ 19 dB, the correction factor provides an estimation error below 0.5 dB over the entire range of evaluated σ_{mdg} . In the case of the simulated system, Fig. 5.1b shows that DSP-based MDG estimation can be significantly improved using the positive correction factor derived in Eq. (5.1), resulting in a small residual error in the investigated range of σ_{mdg} , even for the lowest SNR evaluated for which, only a maximum estimation error of 0.5 dB is obtained at the highest σ_{mdg} .

5.1 MDG emulator for experimental laboratory setups

As the achievable channel capacity and transmission distance in SDM systems are fundamentally constrained by MDG, complex laboratory setups become an essential tool for studying the MDG impact on the system performance and the MDG estimation methods. Frequently, in a smaller-scale experimental setup, long-haul SDM fibers, multiple multi-mode amplifiers, and recirculating loops are not available, then the accumulated MDG should be artificially introduced. In (MIZUNO *et al.*, 2015), Mizuno *et al.* emulate different levels of MDL by using attenuators and mode multiplexers based on planar light-wave circuits (PLCs). However, mode multiplexers based on PLs are currently regarded

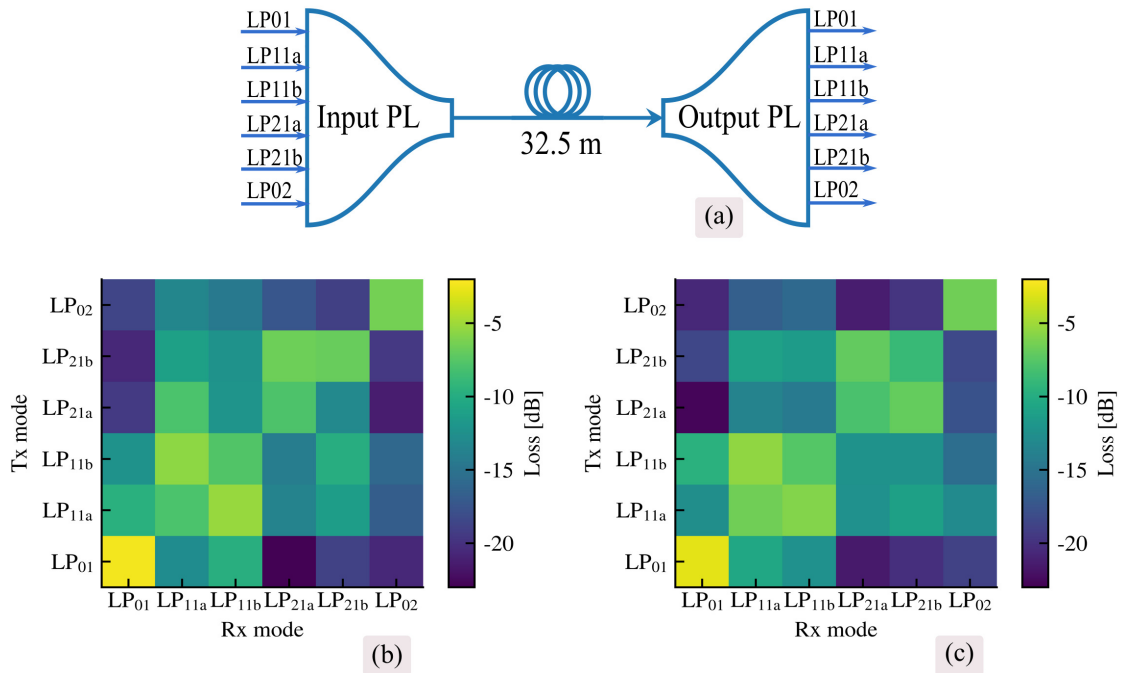


Figure 5.2 – Power transfer matrices of two photonic lanterns in back-to-back with a section of 32.5 meter MMF between them. (a) Experimental setup built at the High-Capacity Transmission Laboratory of the Eindhoven University of Technology. (b) Transmission with PL 2 at the transmitter and PL 1 at the receiver. (c) Transmission with PL 1 at the transmitter and PL 2 at the receiver.

as the most promising solution for mode multiplexing. Therefore, MDG emulation must be aligned with the potential integration of these devices in practical SDM systems.

In this section, an MDG emulator based on variable optical attenuators (VOAs) and mode-multiplexers and demultiplexers based on photonic lanterns is experimentally evaluated. The MDG emulator is implemented to introduce accumulated MDG in a short-reach 3-mode (32.5 meters) fiber link. The results assess MDG emulation at different VOA configurations and demonstrate the capacity of the emulator to provide a wide range of MDG as a function of the difference among mode launch powers.

MDG can be emulated by selective attenuation using VOAs preceding spatial multiplexing. Spatial mode multiplexers and demultiplexers play a critical role in SDM systems. Depending on the component type and design, these devices can have large insertion loss, strong power coupling, and high MDL. PLs are low-loss passive optical waveguides that efficiently convert multi-mode light into multiple single-mode signals, or vice-versa (VELÁZQUEZ-BENÍTEZ *et al.*, 2018).

Fig. 5.2b,c show the transfer matrices of two 6-mode PLs in back-to-back configuration, with a section of 32.5 meter MMF between them, as shown in Fig. 5.2a. Fig. 5.2b corresponds to the transfer function in which the signals are transmitted in PL 2 and

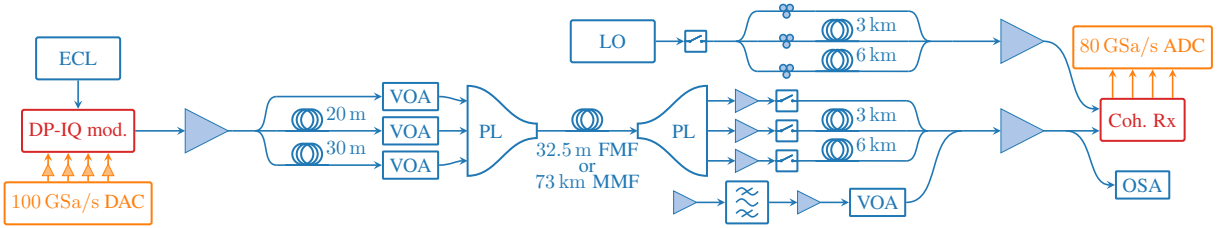


Figure 5.3 – Experimental setup for MDG emulation in a 3-mode transmission system with polarization multiplexing. The launch powers of the 3 modes (LP_{01} , LP_{11a} and LP_{11b}) are independently controlled through VOAs before spatial multiplexing performed by a photonic lantern (PL). At the receiver, the signals are demultiplexed by a second PL, digitized and processed. MDG estimation is performed by DSP based on the MIMO equalizer transfer function.

received in PL 1. In Fig. 5.2c, the signals are transmitted in PL 1 and received in PL 2. The color bar indicates the power transmission from the TX port located in the vertical axis to the RX port located in the horizontal axis. The measurement process is performed by launching a signal with a known power at each port of the input PL and measuring the output power at all ports of the output PL in the configuration depicted in Fig. 5.2a. The power transmission is given by the ratio between the output power and the input power. From Fig. 5.2b,c, both PLs have similar performance. For LP_{01} and LP_{02} , most of the power launched at the input port is received at the corresponding port at the output PL, indicating low mode coupling. In the case of mode groups with degenerated modes “a” and “b”, such as LP_{11} and LP_{21} , although high levels of mode coupling exist between LP_{11a} and LP_{11b} , and LP_{21a} and LP_{21b} , the largest portion of energy remains within the same mode group as expected. In general, modes within the same mode group or with similar propagation constants experience strong mode coupling, while low mode coupling is experienced by modes whose propagation constants are highly unequal (HO *et al.*, 2013).

The experimental setup evaluated for MDG emulation based on VOAs and PLs is depicted in Fig. 5.3. The transmitter generates polarization-multiplexed 16-QAM symbols at a transmission rate of 25 GBd. Pulse shaping at the transmitter is done using a RRC filter with 0.01 roll-off factor. The pulse-shaped signal is converted to the analog domain by a 100 GS/s DAC followed by RF-amplifiers. The analog signal modulates the output of an ECL operating at a frequency of 193.4 THz with a linewidth of 80 kHz using a dual-polarization in-phase and quadrature modulator. After optical modulation, the signal is amplified by an EDFA, split and delayed by 0 m, 20 m and 30 m to generate three decorrelated data streams that are passed through VOAs and then multiplexed by a mode-selective PL (VELÁZQUEZ-BENÍTEZ *et al.*, 2018). The VOAs allow the independent control of the launch powers in the 3 spatial modes LP_{01} , LP_{11a} and LP_{11b} to deliberately introduce MDG into the system. The output of the PL is an FMF that

supports 4 LP mode groups. At the receiver side, a second PL is used as mode demultiplexer. Splicing the FMF pigtailed of the two photonic lanterns results in a 32.5 m link. The receiver employs a time-domain multiplexed space-division multiplexing (TDM-SDM) receiver (UDEN *et al.*, 2014b) that delays two flows by 3 km and 6 km of SSMF to reduce the required amount of the coherent receivers. After the TDM-SDM stage, a noise loading stage composed of two EDFAs, a WSS and a VOA is placed to vary the OSNR at the coherent receiver input. This noise-loading setup places a 250 GHz wide noise-band around the 193.4 THz carrier. The average OSNR is measured by an optical spectrum analyzer (OSA) after the last amplification stage. The SNR at the receiver input is computed as $\text{SNR} = \text{OSNR} (T_s \times 12.5 \text{ GHz})$ where $T_s = 40 \text{ ps}$ is the symbol time (ESSIAMBRE *et al.*, 2010b). The noisy signal is amplified and converted from the optical to the electrical domain by the receiver front-end that integrates a second ECL as LO. The TDM electric signals are fed into 80 GSa/s ADC to be digitized. In the DSP block, the TDM streams are parallelized and down-sampled to two samples per symbol. The signal is matched-filtered by a RRC filter, and, finally, data-aided equalization is applied. In order to compensate for transmission effects including coupling from higher order modes, 6×6 MIMO equalization (processing 3 spatial modes, with 2 polarization modes each) is carried out using a widely linear complex-valued adaptive equalizer with 72 FIR filters with 1001 taps each, updated by a fully supervised LMS algorithm (SILVA; ZIBAR, 2016).

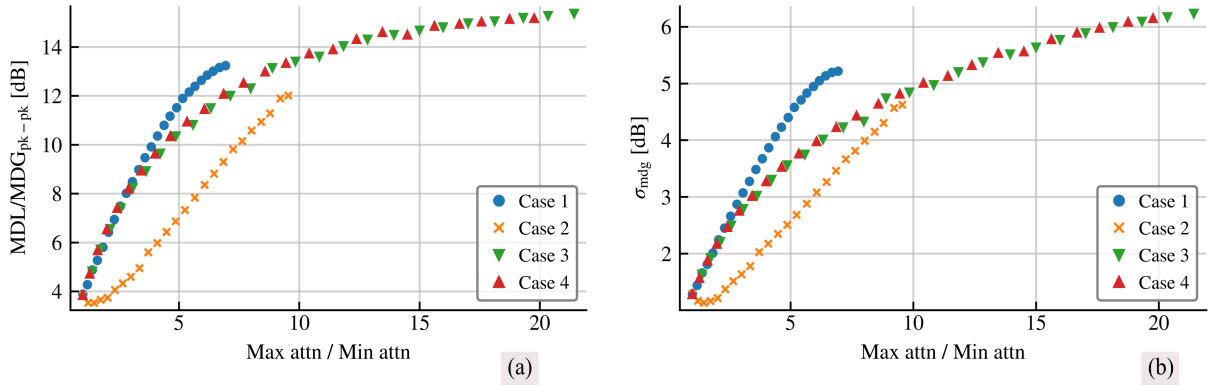
5.1.1 MDG emulation results

The experimental emulation of MDG is carried out by attenuating the single-mode signals at the input of the multiplexer PL. At 0 dB attenuation, the launch powers are 0.55 dBm, -0.15 dBm and -0.15 dBm for LP_{01} , LP_{11a} and LP_{11b} , respectively. The system has an inherent $\text{MDG}_{\text{pk-pk}} = 3.9 \text{ dB}$ and $\sigma_{\text{mdg}} = 1.3 \text{ dB}$ coming from the different launch powers, imperfections of the optical splitters and different insertion losses of the VOAs. In order to keep the total launch power constant at -4.9 dBm , the 3 VOAs are initialized in 5 dB attenuation to attenuate or de-attenuate the signals according to the configurations defined in Table 5.1. In case 1, the LP_{11b} mode is gradually attenuated, while the attenuation of the LP_{01} mode decreases in such a way that the total launch power is constant. For case 2, the LP_{01} mode is attenuated instead of the LP_{11b} mode. In cases 3 and 4, the LP_{11a} and LP_{11b} modes are simultaneously attenuated, while the attenuation over the LP_{01} mode decreases.

The induced MDG is estimated after DSP from the MIMO transfer function and averaged over 5 iterations. Fig. 5.4 shows $\text{MDG}_{\text{pk-pk}}$ and σ_{mdg} as a function of the ratio between the maximum and minimum attenuation for the four cases of Table 5.1. From Fig. 5.4, the MDG emulation is effectively achieved by means of the different attenuation

Table 5.1 – VOA attenuation for MDG emulation

Case	Attenuation sweep		
	LP ₀₁	LP _{11a}	LP _{11b}
1	Decreases	Constant at 5 dB	5 dB to 17 dB
2	5 dB to 17 dB	Constant at 5 dB	Decreases
3	Decreases	5 dB to 17 dB	6 dB to 18 dB
4	Decreases	5 dB to 17 dB	5 dB to 17 dB

Figure 5.4 – MDG versus attenuation ratio at different VOA configurations. (a) Peak to peak MDL/MDG. (b) σ_{mdg} .

scenarios described in Table 5.1. For the four attenuation scenarios, in general, the higher the ratio between attenuations, the higher the induced MDG. In case 2, at low attenuation ratios, the induced MDG decreases slightly before turning into an increasing curve. Such behavior comes from the fact that, in this configuration, the strongest mode, LP₀₁, is more attenuated than modes LP_{11a} and LP_{11b}. Then, at some attenuation settings, the induced MDG counteracts the inherent system MDG. Using cases 3 and 4, MDG_{pk-pk} and σ_{mdg} achieve values higher than 15 dB and 6 dB, respectively, as a consequence of the simultaneous attenuation of both LP_{11a} and LP_{11b} modes. From these results, MDG emulation can be carried out by the independent attenuation of the single-mode signals before spatial multiplexing (OSPINA *et al.*, 2020a).

5.2 Experimental validation of the correction factor technique in a 3-mode transmission link

Once the MDG emulation based on VOAs and PLs was validated in Section 5.1.1, the emulation approach is employed to validate the correction factor technique in the experimental 3-mode transmission setup of Fig. 5.3. Two fiber lengths are validated, 32.5 m and 73 km. The experimental setup for both link distances is the same as described in

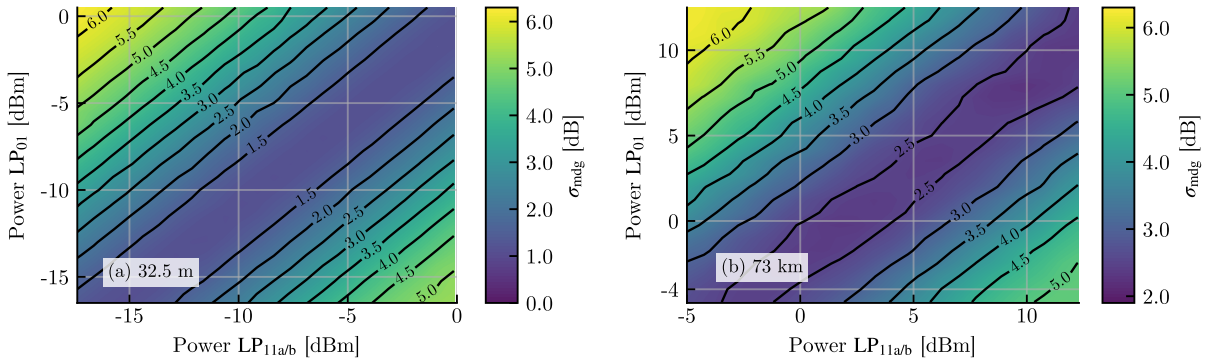


Figure 5.5 – MDG standard deviation σ_{mdg} estimated by DSP without noise loading, as a function of the launch powers in the LP₀₁ and LP₁₁ modes. (a) 32.5 m transmission with an intrinsic SNR = 38.5 dB. (b) 73 km transmission with an intrinsic SNR = 37.1 dB.

Section 5.1.1. The longer link results by fusion splicing the FMF pigtailed to a 73 km fiber link consisting of 16 spools of 50 μm core diameter graded-index MMF (SILLARD *et al.*, 2016a) with lengths varying from 1.2 km to 8.9 km. Note that a 50 μm core diameter multi-mode fiber supporting up to 36 spatial modes is employed. This fiber allows the scaling to more spatial modes with respect to FMFs tailored to a specific number of modes. At the receiver, in the case of 73 km transmission, after down-sample conversion, the dispersion is digitally compensated and frequency offset is estimated and compensated for.

5.2.1 MDG estimation without noise loading

The three VOAs employed to vary the input power for the LP₀₁, LP_{11a}, and LP_{11b} ports of the PL provide an attenuation range from 0 dB to 25 dB for an applied voltage between 0 V and 5 V. Since the relation between the applied voltage and the resulting attenuation is not linear, each individual VOA is calibrated by scanning the applied voltage and measuring the attenuation. This data is used to generate a lookup table (LUT), which is interpolated to achieve an arbitrary attenuation.

Using the three VOAs to experimentally emulate MDG, we generate a wide range of MDG values by attenuating independently the LP₀₁ mode, and jointly the degenerate modes LP_{11a} and LP_{11b}, which receive identical attenuation. Figs. 5.5a and 5.5b show the σ_{mdg} estimated by DSP as a function of the launch powers in the LP₀₁ and LP₁₁ modes achieved by sweeping the attenuation from 0 dB to 17 dB in the 3 VOAs for 32.5 m and 73 km transmission, respectively. In the absence of noise loading, the SNR obtained from the OSNR measured optically by the OSA is 38.5 dB for transmission over 32.5 m and 37.1 dB for transmission over 73 km. From the contour plot in Fig. 5.5a, σ_{mdg} increases from the middle of the grid towards the top left corner and the bottom right corner, where the difference between the launch powers is maximized. On the contrary,

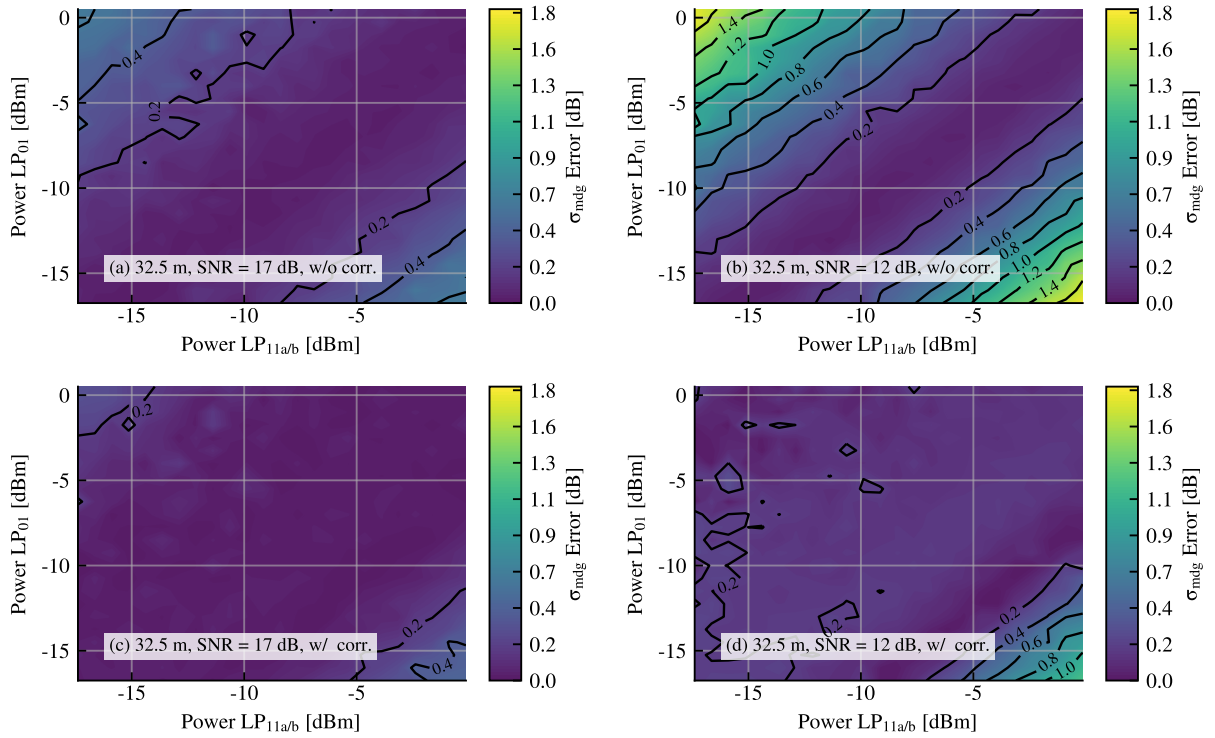


Figure 5.6 – Estimation error $\sigma_{\text{mdg}}^{\text{err}} = \sigma_{\text{mdg}} - \sigma_{\text{mdg}}^{\text{nl}}$, calculated as the difference in dB between the MDG standard deviation σ_{mdg} in dB estimated by DSP without noise loading, and $\sigma_{\text{mdg}}^{\text{nl}}$ in dB estimated by DSP with noise loading. In the figure, $\sigma_{\text{mdg}}^{\text{err}}$ is shown as a function of the power launched in the LP₀₁ and LP₁₁ modes for 32.5 m transmission. (a) Without correction at SNR = 17 dB. (b) Without correction at SNR = 12 dB. (c) Correction by the positive solution of Eq. (5.1) at SNR = 17 dB. (d) Correction by the positive solution of Eq. (5.1) at SNR = 12 dB.

the region encompassing the diagonal between the bottom left corner and the top right corner presents low σ_{mdg} as a consequence of the high similarity between the launch powers. In Fig. 5.5b, for 73 km transmission, σ_{mdg} also increases in the direction in which the difference between the launch powers is maximized, achieving up to 6.3 dB. Over the region where the launch powers are similar, σ_{mdg} remains low around 2 dB.

5.2.2 MDG estimation with noise loading

The influence of noise on MDG estimation is analyzed by loading noise to the optical transmission setup and calculating the estimation error $\sigma_{\text{mdg}}^{\text{err}}$, defined as the difference in dB between σ_{mdg} in dB, estimated in the setup without noise loading, and $\sigma_{\text{mdg}}^{\text{nl}}$ in dB, estimated with noise loading ($\sigma_{\text{mdg}}^{\text{err}} = \sigma_{\text{mdg}} - \sigma_{\text{mdg}}^{\text{nl}}$).

Figs. 5.6a and 5.6b show $\sigma_{\text{mdg}}^{\text{err}}$ for the 32.5 m transmission link, at SNR = 17 dB and SNR = 12 dB. As expected from the results in Section 4.3.1, $\sigma_{\text{mdg}}^{\text{err}}$ for SNR = 17 dB (up to 0.6 dB) is significantly lower than for SNR = 12 dB (up to 1.8 dB). The estimation

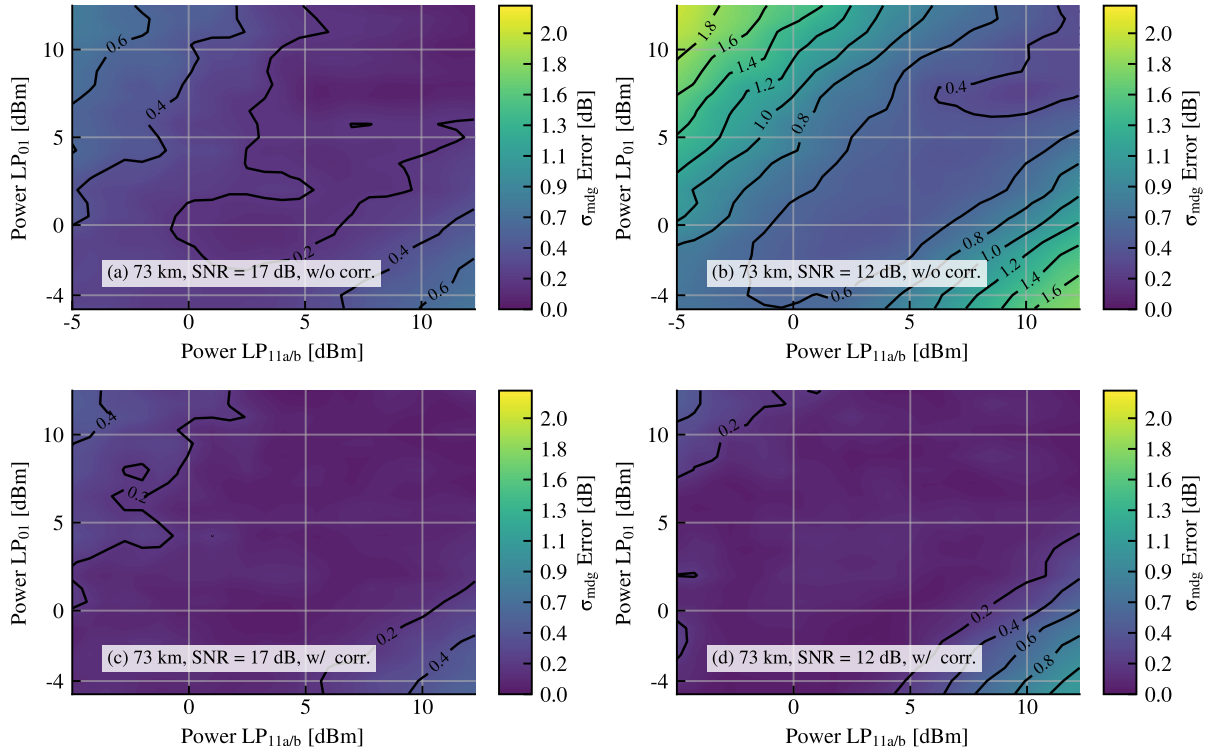


Figure 5.7 – Estimation error $\sigma_{\text{mdg}}^{\text{err}} = \sigma_{\text{mdg}} - \sigma_{\text{mdg}}^{\text{nl}}$, calculated as the difference in dB between the MDG standard deviation σ_{mdg} in dB estimated by DSP without noise loading, and $\sigma_{\text{mdg}}^{\text{nl}}$ in dB estimated by DSP with noise loading. In the figure, $\sigma_{\text{mdg}}^{\text{err}}$ is shown as a function of the power launched in the LP₀₁ and LP₁₁ modes for 73 km transmission. (a) Without correction at SNR = 17 dB. (b) Without correction at SNR = 12 dB. (c) Correction by the positive solution of Eq. (5.1) at SNR = 17 dB. (d) Correction by the positive solution of Eq. (5.1) at SNR = 12 dB.

error after correction is shown in Figs. 5.6c and 5.6d for SNR = 17 dB and SNR = 12 dB. The correction factor given by the positive solution of Eq. (5.1) significantly enhances the estimation process over most of the grid, remaining only a small residual error in the high MDG regime for both SNRs.

The effect of noise on $\sigma_{\text{mdg}}^{\text{err}}$ for 73 km transmission is presented in Figs. 5.7a and 5.7b. The estimation error at SNR = 17 dB achieves up to 0.7 dB, while the estimation error at SNR = 12 dB reaches up to 2.2 dB. The estimation error after correction is shown in Figs. 5.7c and 5.7d for SNR = 17 dB and SNR = 12 dB, respectively. As observed in the 32.5 m link, the correction factor significantly reduces the estimation error, remaining only a small residual error in the high MDG regime for both SNRs.

Next, we sweep both the attenuation of the VOAs and the noise power at the receiver input. Figs. 5.8a and 5.8b show $\sigma_{\text{mdg}}^{\text{err}}$ as a function of σ_{mdg} and SNR without and with correction of the DSP-estimated eigenvalues for 32.5 m transmission. In Fig. 5.8a, without

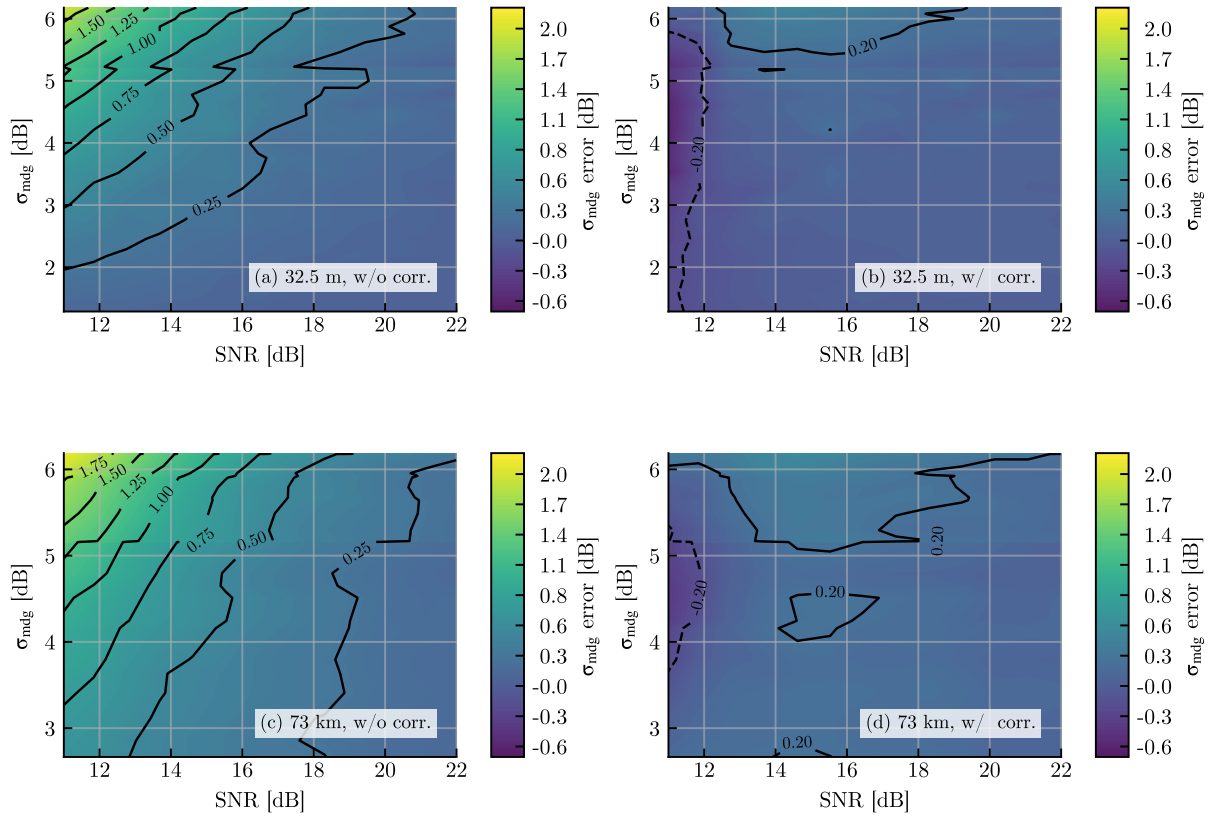


Figure 5.8 – Estimation error $\sigma_{\text{mdg}}^{\text{err}} = \sigma_{\text{mdg}} - \sigma_{\text{mdg}}^{\text{nl}}$, calculated as the difference in dB between the MDG standard deviation σ_{mdg} in dB estimated by DSP without noise loading, and $\sigma_{\text{mdg}}^{\text{nl}}$ in dB estimated by DSP with noise loading. In the figure, $\sigma_{\text{mdg}}^{\text{err}}$ is shown as a function of σ_{mdg} and the SNR. (a) 32.5 m transmission without correction. (b) 32.5 m transmission with correction by the positive solution of (5.1). (c) 73 km transmission without correction. (d) 73 km transmission with correction by the positive solution of (5.1).

correction, the estimation error achieves up to 1.8 dB for $\sigma_{\text{mdg}} > 6$ dB and $\text{SNR} < 12$ dB. At an $\text{SNR} = 12$ dB, the estimation error varies from 0.25 dB to 1.7 dB across the range $2 \text{ dB} < \sigma_{\text{mdg}} < 6$ dB. As the SNR increases, the estimation error decreases progressively. At an $\text{SNR} > 20.5$ dB, the estimation error is less than 0.25 dB for all ranges of σ_{mdg} . The correction factor applied over the DSP-estimated eigenvalues enhances the estimation across all ranges of σ_{mdg} and SNR evaluated in Fig. 5.8b. Here, a residual error of 0.2 dB is achieved for the high MDG regime. For $\text{SNR} < 12$ dB, the residual error is negative as a consequence of the over-correction of the eigenvalues, resulting in an estimated σ_{mdg} higher than the actual σ_{mdg} . The results for 73 km transmission are shown in Figs. 5.8c and 5.8d. In Fig. 5.8c, without correction, the estimation error achieves up to 2 dB for $\sigma_{\text{mdg}} > 6$ dB and $\text{SNR} < 12$ dB. At an $\text{SNR} = 12$ dB, the estimation error varies from 0.75 dB to 1.75 dB across the range $3.5 \text{ dB} < \sigma_{\text{mdg}} < 6$ dB. An estimation error less than 0.25 dB for all values of σ_{mdg} is obtained for SNR values higher than 22 dB. The correction

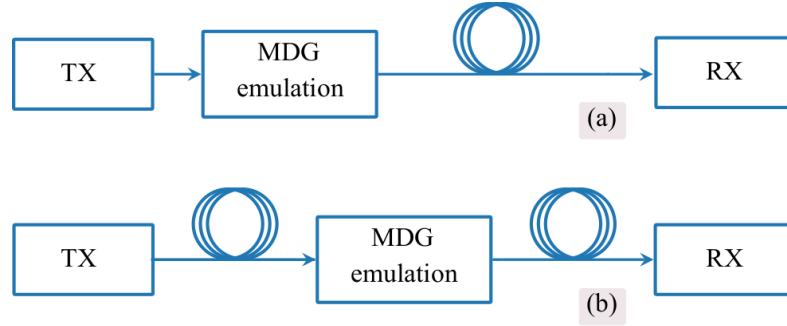


Figure 5.9 – Schematic representation of MDG emulation. (a) at the transmitter side. (b) in-span MDG emulation.

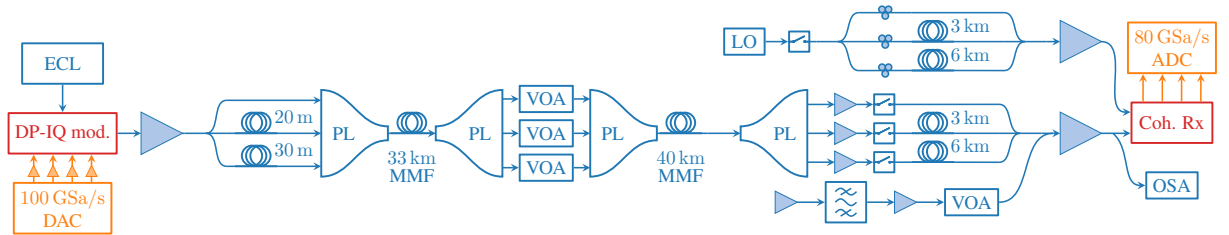


Figure 5.10 – Experimental setup for short-reach 3-mode transmission with polarization multiplexing (HOUT *et al.*, 2020). VOAs are used to control the σ_{mdg} of the link with in-span configuration. At the receiver, the signals are demultiplexed by a second PL, digitized and processed. MDG estimation is performed by DSP based on the MIMO equalizer transfer function.

factor significantly reduces the estimation error, as shown in Fig. 5.8d. In this case, only a residual error of 0.2 dB is observed in certain regions of the grid. For $\text{SNR} < 12$ dB and $3.7 \text{ dB} < \sigma_{\text{mdg}} < 5.2$ dB, there is a negative residual error of -0.2 dB as a consequence of over-correction (OSPINA *et al.*, 2020).

MDG emulation by varying individual mode powers can be done by placing an MDG emulator stage directly after the transmitter, an approach that was employed in the previous results. (see Fig. 5.9a). Alternatively, the deliberate insertion of MDG can be done in-span configuration (see Fig. 5.9b). Compared to the MDG emulation at the transmitter side, in the in-span configuration, the modal powers are varied after the modes have mixed and a certain degree of coupling has been achieved. Therefore, in-span configuration enables a more approximate emulation of the MDG introduced by SDM components such as multi-mode amplifiers, optical switches, spatial (de)multiplexers, and MMF.

The experimental setup of a 3-mode transmission with in-span MDG emulation is depicted in Fig. 5.10. The configuration of the transmitter and receiver of the experimental setup in Fig. 5.10 is the same as in the experimental setup of Fig. 5.3. The essential difference is the optical link that starts from the first PL. The output of the PL is connected to a $50\mu\text{m}$ core diameter graded-index MMF of 73 km (SILLARD *et al.*, 2016a).

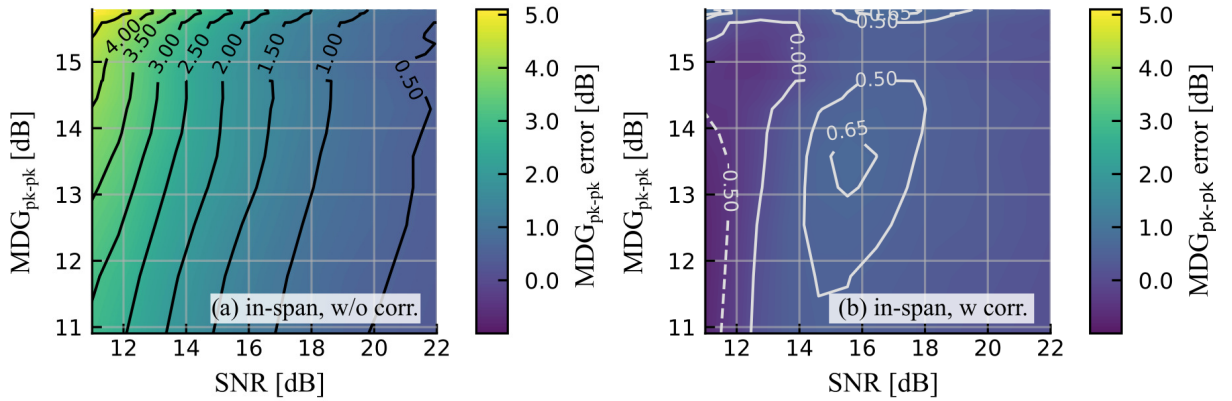


Figure 5.11 – MDG estimation error as a function of the actual MDG and the SNR. (a) Without correction factor. (b) With correction factor. The MDG is emulated at 33 km in the transmission fiber span.

The deployed multi-mode fiber supports up to 36 spatial modes, so that transmission can be eventually scaled to more spatial modes. To control the overall MDG, two photonic lanterns and three VOAs are placed after the first 33 km fiber segment. The three VOAs allow to sweep the MDG of the link by modifying the power in the three spatial modes. After MDG emulation, the signals are transmitted over the remaining 40 km of fiber. At the receive side, a fourth PL is used as mode de-multiplexer.

The correction factor technique for MDG estimation is also validated by sweeping the MDG and SNR in the in-span MDG emulation setup. In addition, the metric $\text{MDG}_{\text{pk-pk}}$ is employed to validate the performance of the correction factor technique over both MDG metrics. The estimated $\text{MDG}_{\text{pk-pk}}$ without noise loading is assumed to be the actual system MDG. Then, the MDG estimation error is defined as the difference between the $\text{MDG}_{\text{pk-pk}}$ estimated without noise loading for which $\text{SNR} = 35.4$, and the $\text{MDG}_{\text{pk-pk}}$ estimated with noise loading. Fig. 5.11a,b show the MDG estimation error without and with correction factor, respectively. From Fig. 5.11a, the MDG estimation error increases for low SNR and high MDG, a behavior expected from previous results. A maximum error of 5 dB is observed, indicating a critical underestimation of the system MDG. In Fig. 5.11b, with correction factor, the MDG error is reduced to below 0.65 dB. For SNR below 14 dB, a small negative MDG estimation error is seen resulting from the overestimation of the MDG (HOUT *et al.*, 2020).

5.3 Summary

In SDM systems with coupled channels, the achievable channel capacity and transmission distance are fundamentally constrained by ASE and MDG. In these systems, accurate MDG is mandatory for an adequate link assessment and troubleshooting. In this

chapter, an improved technique called correction factor is proposed to overcome the performance limitations of the conventional DSP-based MDG estimation method. Using the transfer function of a MIMO equalizer based on the MMSE criterion, a correction factor for the DSP-based eigenvalues is obtained. The correction factor improves the estimation process in moderate levels of MDG and SNR. The method is validated by Monte-Carlo simulation of a 6-mode long-haul coupled transmission processed by a 12×12 dynamic equalizer. Moreover, the technique is experimentally validated in a 3-mode transmission link using the coefficients of a 6×6 dynamic equalizer for both 32.5 m and 73 km transmission. The simulations and experiments confirm the applicability of the method in practical transmission scenarios.

6 ARTIFICIAL NEURAL NETWORK-BASED MDG AND SNR ESTIMATION

Currently, ML techniques are being extensively investigated for optical performance monitoring in both single-mode (SAIF *et al.*, 2020) and mode-multiplexed systems (SAIF *et al.*, 2021). In this chapter, an ANN-based solution to estimate both MDG and optical SNR in coupled SDM transmission is proposed. The ANN-based estimator is validated in an experimental short-haul 73 km 3-mode FMF link with controlled MDG and optical SNR. In addition, the ANN estimator is applied in a case study of an experimental long-haul 6-mode transmission setup with unknown MDG and SNR.

6.1 Artificial Neural Networks

Inspired by the biological structure of the neural cells in human brains, an ANN is a collection of neurons that are connected to each other in a communication network, through which the structure is able to carry out highly complex computations (SHALEV-SHWARTZ; BEN-DAVID, 2014), (SAIF *et al.*, 2020). In ANNs, layers of neurons are connected in a cascade arrangement, and information propagates through the network experiencing several transformations in order to produce output data. There are many types of ANNs, which are based on the same concept but have different structures. Fig. 6.1 shows a basic fully-connected ANN architecture of the kind MLP that is composed of three layers of neurons: an input layer (x), one hidden layer (z), and an output layer (y). The input layer receives an input vector that is transferred to all neurons of the hidden layer. After transformations applied by the hidden layer, the information is passed to the output layer. Each neuron is modeled as a non-linear activation function whose inputs (coming from proceeding layers) are multiplied by weights (\mathbf{w}_k) and shifted by bias coefficients (b_k), giving to the ANN algorithm non-linear properties and making it possible to learn any function. In the training stage and assuming supervised learning, the weights and bias coefficients are optimized to minimize the error between the obtained output and the target. During training, the information travels in the forward direction. Subsequently, if the weights updating approach is based on the backpropagation paradigm, the error moves in the backward direction so that the ANN model can be updated in each iteration. In each neuron, the output is computed as

$$Z_k = f \left(\sum_{i=1}^n w_i x_i + b_k \right), \quad (6.1)$$

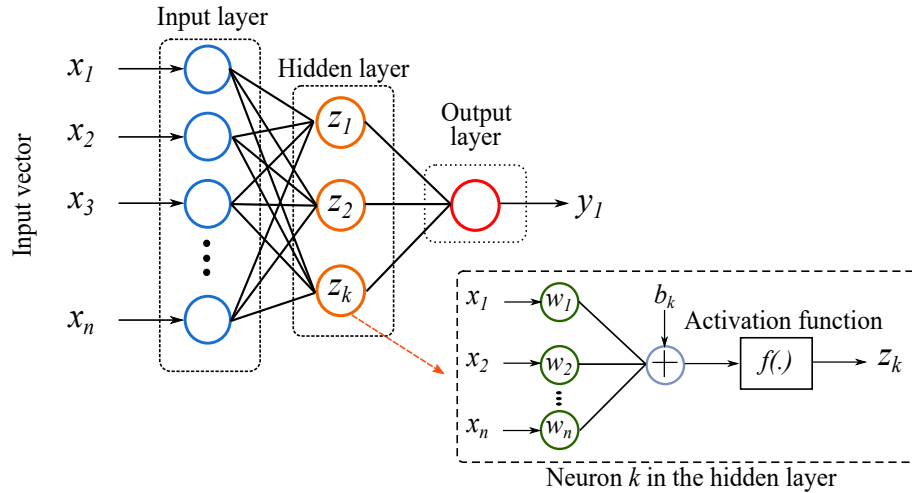


Figure 6.1 – Architecture of a basic fully-connected MLP ANN.

where $f(\cdot)$ represents the activation function. The most widely used activation functions are ReLu, logistic, and hyperbolic tangent. In practice, ANN hyperparameters such as number of layers, number of neurons, learning rate, and activation function should be optimized to get the highest accuracy.

The operating principle of ANNs can be extended to more complex architectures such as the deep neural networks (DNNs) and convolutional neural networks (CNNs) (SAIF *et al.*, 2020). In literature, these different types of neural networks (NNs) are being widely used in optical communications systems mainly for optical performance monitoring (OPM) (CHO *et al.*, 2020). The most common applications of NNs in optical systems are OSNR estimation (KHAN *et al.*, 2017), modulation format identification (KHAN *et al.*, 2016), (SAIF *et al.*, 2019), soft failure identification (LUN *et al.*, 2020), and fiber nonlinearities mitigation (HáGER; PFISTER, 2018).

Particularly in SDM systems, NNs have been employed to monitor OSNR, CD and mode coupling (SAIF *et al.*, 2021). Section 6.2 presents a novel ANN-based method proposed in this thesis for MDG and SNR estimation in SDM systems (OSPINA *et al.*, 2022).

6.2 ANN-based Method for MDG and SNR estimation

To circumvent the limitations of conventional estimation methods at certain MDG and SNR regimes, a MLP ANN-based method to estimate σ_{mdg} and SNR from features extracted after DSP is proposed (OSPINA *et al.*, 2021). The ANN aims to extract the non-trivial relationships between the MDG and the optical SNR that cannot be unraveled by classical DSP techniques. The block diagram of the proposed solution is depicted in Fig. 6.2. Firstly, the ANN of inset (c) is trained with semi-analytical data from inset

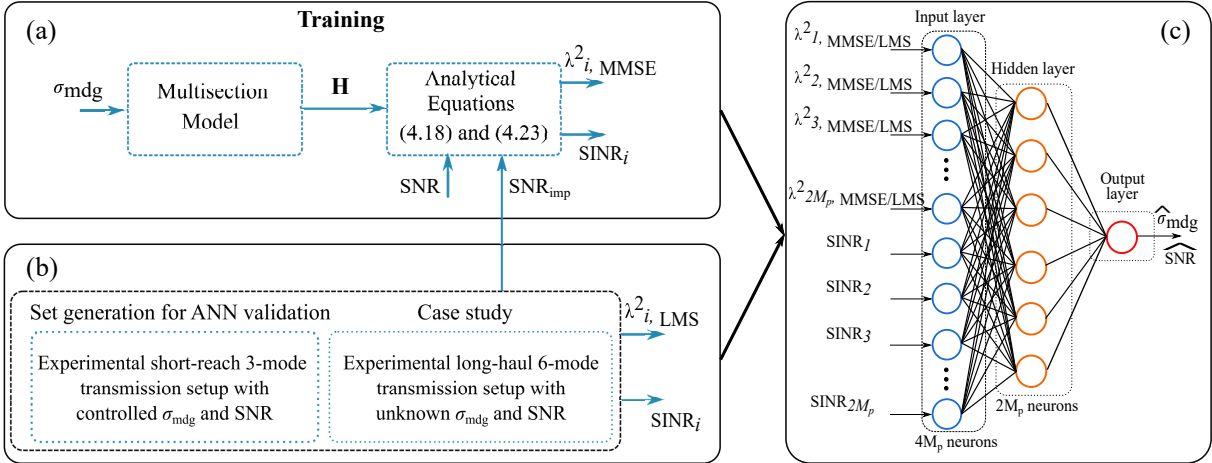


Figure 6.2 – ANN-based MDG and SNR estimator. (a) The training set is generated by numerical multisection simulation and analytic formulas. (b) The validation set is generated by a short-reach 3-mode transmission setup and the case study data is generated by a long-haul 6-mode transmission setup. (c) Proposed ANN. The algorithm applies two separate networks for σ_{mdg} and SNR estimation.

(a), generated by numerical multisection simulation and analytic formulas (Eq. (4.18) and Eq. (4.23)). Once the ANN is trained with semi-analytic data, the resulting model is applied to experimental setups for MDG and SNR estimation. The construction of the training dataset is described below.

The training dataset is generated according to Fig. 6.2(a). Using the multisection model, $2M_p \times 2M_p$ matrices \mathbf{H} are generated to simulate an M_p -mode transmission with polarization multiplexing over a link with $K = 50$ spans of 50 km each, yielding a total length of 2,500 km. The total link length was arbitrarily selected to represent a strongly-coupled SDM transmission. The overall MDG of \mathbf{H} is controlled by the per-amplifier MDG standard deviation, σ_g . The MDG of the simulated 2,500 km-FMF link is adjusted to result in $0.2 \text{ dB} < \sigma_{\text{mdg}} < 7.9 \text{ dB}$ ¹. As the actual σ_{mdg} parameter is known, the σ_{mdg} range is defined based on the minimum and maximum expected σ_{mdg} to be estimated. The modal dispersion per span obeys to a group delay standard deviation of 3.1 ps/ $\sqrt{\text{km}}$ (HAYASHI *et al.*, 2017).

For each \mathbf{H} , the SNR is swept from 10 dB to 25 dB to generate $2M_p$ $\lambda_{i,\text{MMSE}}^2$ values and $2M_p$ SINR_i values using Eqs. (4.18) and (4.23) for a total of 9,610 samples. Input SNR_{imp} , is a parameter measured experimentally in the transmission setup where the technique is being applied as indicated in Section 4.5². The labelled set of $\lambda_{i,\text{MMSE}}^2$ and

¹ Note that, according to (MELLO *et al.*, 2019), $\sigma_{\text{mdg}} > 7 \text{ dB}$ is sufficient to reduce the channel capacity below 80% with respect to a system without MDG. Therefore, we expect this range to cover most practical applications.

² It is worth clarifying that the ANN-based estimator must be retrained for different values of SNR_{imp} depending on the experimental setup where it is going to be applied. Furthermore, the number of propagation modes that defines the structure of the ANN also depends on the experimental setup.

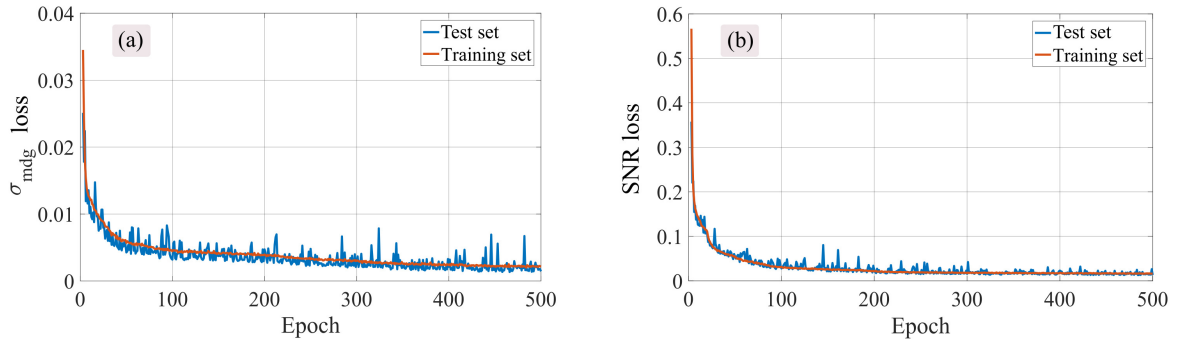


Figure 6.3 – ANN loss, calculated as the mean squared error (MSE), as a function of the number of epochs. (a) σ_{mdg} estimation. (b) SNR estimation. The curves indicate no overfitting and a good generalization ability.

SINR_i is fed into the ANN shown in Fig. 6.2(c) as input training features. The ANN receives $2M_p \lambda_{i,\text{MMSE}}^2$ values and $2M_p \text{SINR}_i$ values, and provides an estimate of σ_{mdg} or SNR. A hidden layer with $2M_p$ neurons, and an output layer with 1 neuron, learn the relation between the input features and the output. The ANN is trained using the Adam optimizer (KINGMA; BA, 2014) using batches of 5 samples. The number of hidden layers, the number of neurons, batch size, and other hyper-parameters were optimized based on an accuracy criterion.

Figs. 6.3a and 6.3b show the ANN convergence curves for MDG and SNR estimation, respectively, considering $2M_p = 6$. The ANN loss, calculated as the MSE, is depicted as a function of the number of epochs. Both training and test sample sets are evaluated comprising 8,649 and 970 samples, respectively. The results indicate a substantial reduction in the MSE after 100 epochs, and still a small improvement up to 500 epochs for σ_{mdg} estimation. Therefore, we use 500 epochs for training. The loss of the test set tracks the loss of the training set for the entire figure. We expect, therefore, no overfitting and a good ANN ability to generalize over unseen samples. After training, the ANN-based method is validated using data captured from a short-reach experimental setup with controlled parameters, and tested in a case study of a long-haul experimental link.

6.3 Experimental short-reach transmission with known MDG and SNR

The ANN-based estimator is validated using the short-reach 73-km 3-mode transmission setup with in-span MDG emulation depicted in Fig. 5.10 and described in Section 5.1 and Section 5.2.2. After DSP, the eigenvalues $\lambda_{i,\text{LMS}}^2$ are computed at each frequency of \mathbf{W}_{LMS} and averaged across the signal band. The SINR_i is computed from each of the 6 equalized data streams using a single-coefficient LS estimator (WAUTELET *et al.*, 2007).

The implementation penalty is computed in back-to-back as $\text{SNR}_{\text{imp}} = 18.8$ dB. The ANN in Fig. 6.2c is fed with 9,610 analytical labelled samples generated using Eqs. (4.18) and (4.23) as indicated in Fig. 6.2a. In a first stage, 8,649 samples are used for model training and the remainder 970 samples for model testing. After training, model validation is performed by 520 experimental samples generated by the short-reach 3-mode transmission setup. Using the VOAs located in middle of the span, σ_{mdg} is varied from 4.5 dB to 6.5 dB. At the receiver, the noise loading stage sweeps the SNR from 11 dB to 22 dB.

The validation results of the conventional and ANN-based estimators in a short-reach transmission setup are depicted in Fig. 6.4. Figs. 6.4a and 6.4b compare the actual value indicated by the dashed red curve and the estimated σ_{mdg} and SNR parameters generated by the conventional and ANN-based methods. The estimated values track the actual values within a small deviation over the entire range of parameters evaluated, resulting in a MSE of 0.11 for σ_{mdg} and 0.53 for SNR, both computed in dB.

Figs. 6.4c and 6.4d show the estimation error provided by the conventional methods in dB, computed as the difference between the actual value and the estimated value. The conventional method provides a σ_{mdg} estimation error up to 2 dB at high MDG and low SNR. In the case of SNR, the estimation error achieves up to 8 dB at high levels of MDG and high SNR. Figs. 6.4e and 6.4f show the estimation error in decibels for σ_{mdg} and SNR, respectively, for the ANN solution. The ANN estimator provides a highest residual σ_{mdg} estimation error of 0.6 dB in the region of high MDG, exhibiting a low dependence on the evaluated SNR. On most of the grid, the σ_{mdg} estimation error is lower than 0.3 dB. For the SNR, an estimation error higher than 1.4 dB is observed at high values of σ_{mdg} and SNR. Over most of the evaluated range, the SNR estimation error is lower than 0.8 dB.

In (OSPINA *et al.*, 2021), the ANN-based MDG and SNR estimator is also validated in a 3-mode transmission setup with back-to-back configuration.

6.4 Experimental long-haul transmission with unknown MDG and SNR

We also apply the ANN-based estimator to the long-haul 6-mode transmission with polarization multiplexing setup and depicted in Fig. 3.17 and described in Section 3.8. After equalization, the eigenvalues $\lambda_{i,\text{LMS}}^2$ are computed at each frequency of \mathbf{W}_{LMS} , and averaged across the signal band. The SINR_i is computed for each of the 12 equalized data streams. The implementation penalty is computed in back-to-back as $\text{SNR}_{\text{imp}} = 18.6$ dB. As the parameters σ_{mdg} and SNR are unknown, the simulated link used to generate the

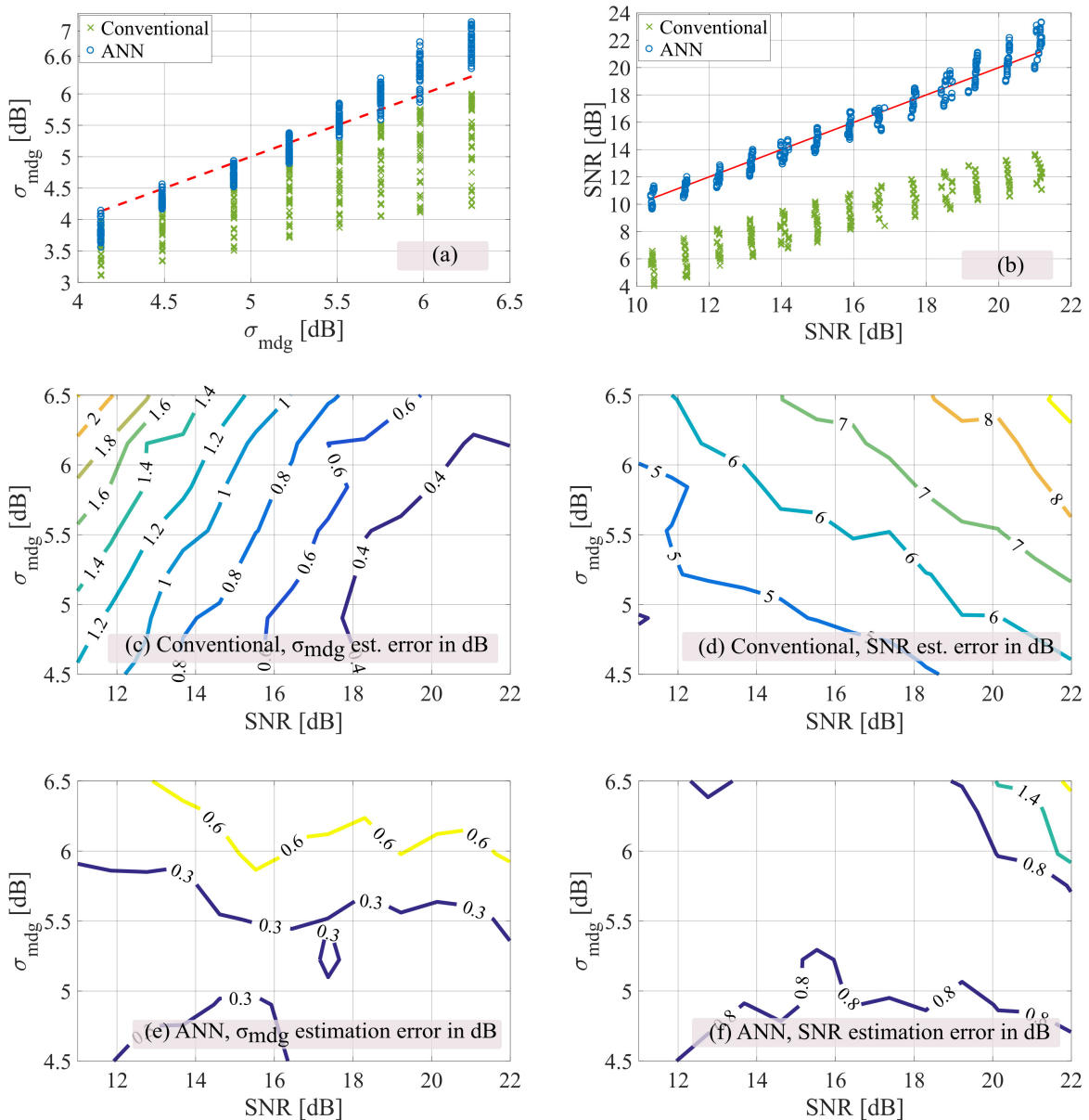


Figure 6.4 – Experimental short-reach 3-mode validation results. (a) Estimated σ_{mdg} as a function of the actual σ_{mdg} . (b) Estimated SNR as a function of the actual SNR. (c) σ_{mdg} estimation error in dB generated by the conventional method as a function of the actual σ_{mdg} and SNR. (d) SNR estimation error in dB generated by the conventional method as a function of the actual σ_{mdg} and SNR. (e) σ_{mdg} estimation error in dB generated by the ANN as a function of the actual σ_{mdg} and SNR. (f) SNR estimation error in dB generated by the ANN as a function of the actual σ_{mdg} and SNR.

training set is adjusted to present $0.5 \text{ dB} < \sigma_{\text{mdg}} < 23.9 \text{ dB}$ and $10 \text{ dB} < \text{SNR} < 25 \text{ dB}$, expecting that the minimum and maximum values to be estimated are close to or within these intervals. After ANN training by 46,035 labelled samples, the ANN-based method is applied to experimental traces corresponding to transmission distances between 59 km and 5,900 km.

Fig. 6.5 shows σ_{mdg} and SNR estimated in the long-haul case study. Fig. 6.5a shows

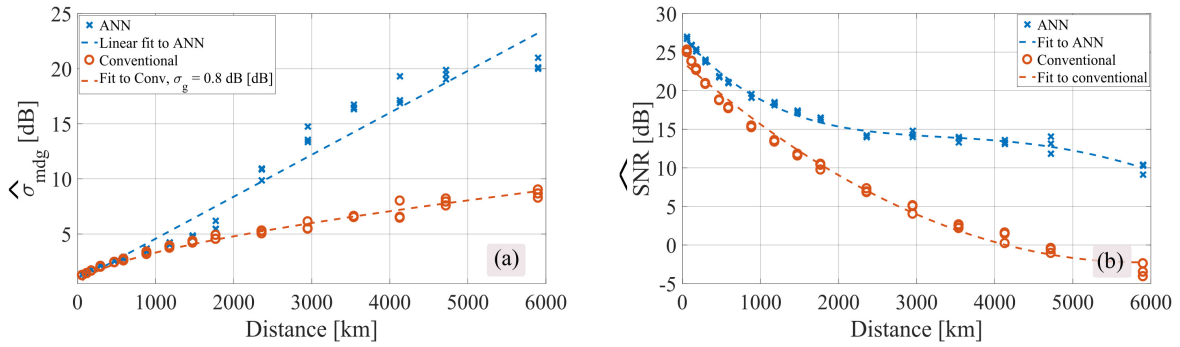


Figure 6.5 – Experimental long-haul 6-mode case study. (a) Estimated σ_{mdg} as a function of the transmission distance. (b) Estimated SNR as a function of the transmission distance.

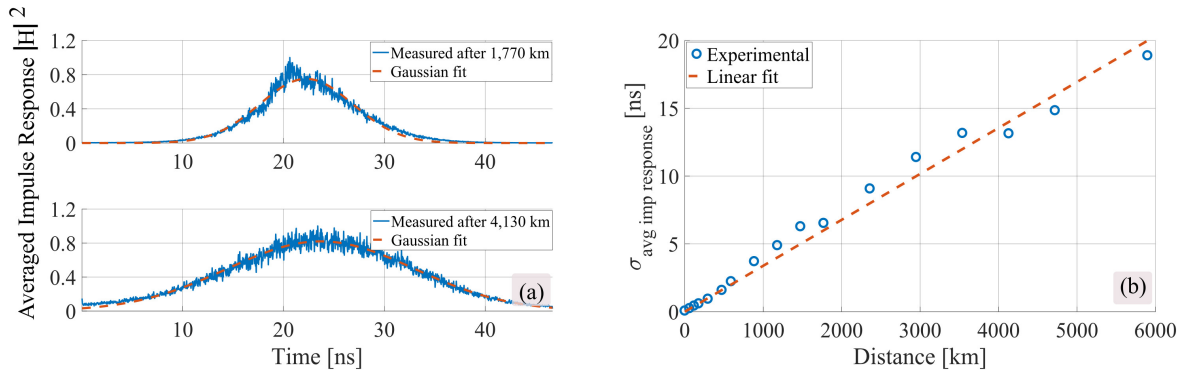


Figure 6.6 – (a) Averaged impulse response after 1,770 km (Top) and 4,130 km (Bottom). (b) Standard deviation of the averaged impulse response as a function of the transmission distance.

the estimated σ_{mdg} as a function of the transmission distance. The orange circles correspond to σ_{mdg} estimated by the conventional method. The dashed orange line fits the experimental data to Eq. (4.15) with a per-span MDG of $\sigma_g = 0.8$ dB. The ANN-based estimates are shown by the blue crosses, indicating a large deviation with respect to the conventional method. The approximately linear increase of the σ_{mdg} estimated by the ANN suggests a possible weakly-coupled SDM transmission (LOBATO *et al.*, 2012). Fig. 6.5b shows the estimated SNR as a function of the transmission distance. As expected, the conventional technique results are substantially lower than those obtained by the ANN-based method. As the conventional method neglects the detrimental effects of MDG, it tends to underestimate the actual SNR. The dashed curves are polynomial fitting functions indicating the trend of the SNR with the transmission distance.

To further investigate the weak coupling hypothesis, we also evaluate the channel delay spread. In general, weakly-coupled transmission leads to a linear increase of the channel delay spread (HO; KAHN, 2011c), (ANTONELLI *et al.*, 2015). Fig. 6.6a shows the averaged impulse response computed as the average of the 144 intensity matrices obtained from the MIMO equalizer after 1,770 km and 4,130 km. The dashed red curve is a Gaussian fit whose standard deviation provides a metric for evaluating the total delay

spread. Fig. 6.6b shows the standard deviation of the averaged impulse response as a function of the transmission distance. The approximately linear increase in the equalizer impulse response corroborates the hypothesis of weak coupling (HO; KAHN, 2011c).

6.5 Discussion

In Section 6.4, we observed considerable differences between ANN-based and conventional estimation methods for σ_{mdg} and SNR in long-haul transmission. We conjectured that the very high values of MDG estimated by the ANN appeared because of a potential linear accumulation of MDG in the recirculation loop. To further understand the problem we attempt in this section to reproduce by simulation the results observed in Section 6.4.

The simulated transmitter generates 12 16-QAM symbol sequences at 30 GBd. The sequences are processed by RRC shaping filters and converted to the optical domain by an MZM model. The channel model generates 12×12 channel transfer matrices \mathbf{H} using the analytical multisection model presented in (HO; KAHN, 2011b). The per-span MDG σ_g is set to 1.5 dB. The transmission distance is varied from 1 to 100 59-km spans, yielding σ_{mdg} from 0.5 dB to 22 dB. Such high MDG would severely impair the transmission capacity (according to (MELLO *et al.*, 2019), effective SNR losses higher than 1 dB are expected for $\sigma_{\text{mdg}} > 3\text{-}4$ dB). The SNR after the first span is set to 26.83 dB, and then decreased considering noise accumulation generated by amplifiers with 9-dB noise figure. The received sequence is fed into a coherent receiver model. The digital signals are processed by a DSP chain composed of an static equalizer and a 12×12 MIMO equalizer updated by the fully-supervised LMS algorithm.

Three σ_{mdg} estimation methods are evaluated. The LMS-based conventional method transmits symbols over the channel matrix \mathbf{H} . At the receiver, the transfer matrix of the dynamic LMS MIMO equalizer is used to estimate the eigenvalues $\lambda_{i,\text{LMS}}^2$ and σ_{mdg} . The LMS-based correction factor methods applies the correction factor proposed and validated in Chapter 5 to the DSP-estimated eigenvalues before estimating σ_{mdg} (OSPINA *et al.*, 2020b), (HOUT *et al.*, 2020), (OSPINA *et al.*, 2020). The ANN estimator uses the same structure and training data as in the long-haul case study in Section 6.4. The results are shown in Fig. 6.7a. The solid black line corresponds to the actual σ_{mdg} estimated from \mathbf{H} . The LMS-based conventional method provides accurate estimates with an estimation error less than 0.5 dB up to $\sigma_{\text{mdg}} = 4.5$ dB. After this point, the method starts to significantly underestimate the MDG, reaching two plateaus. The LMS-based technique with correction factor slightly improves the estimation quality. The correction factor provides a low correction capability at the beginning of the link because the SNR is relatively high. At the end of the link, the accumulated MDG is so high that the equalizer coefficients

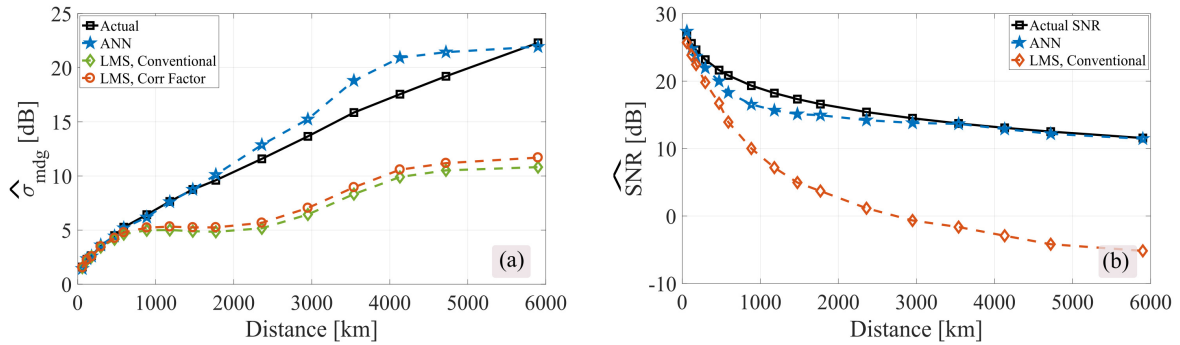


Figure 6.7 – (a) Estimated σ_{mdg} as a function of the transmission distance with conventional, correction factor, and ANN methods. (b) Estimated SNR as a function of the transmission distance with conventional and ANN methods.

diverge from the MMSE coefficients. The estimates provided by the ANN-based estimator accurately track the actual MDG up to $\sigma_{\text{mdg}} = 10$ dB. For $\sigma_{\text{mdg}} > 10$ dB, the ANN estimator slightly overestimates σ_{mdg} . Although the two plateaus are not observed in the experimental data, we believe the trends are fairly reproduced.

We also estimate the SNR using the conventional (after LMS equalization) and ANN-based methods. The results are shown in Fig. 6.7b. As expected, the SNR is underestimated by the conventional method because of the strong MDG added to the link. The ANN-based method offers more accurate estimates, also in reasonable agreement with the experimental results in Section 6.4. Finally, it should be noted that the entire simulation and experimental study was carried out under the assumption of balanced and spatially white noise. This assumption should hold in real-life long-haul links, which are in fact the systems that suffer most from MDG (HO; KAHN, 2011b). The effectiveness of the ANN in scenarios with noise correlation or SNR imbalances is left for a further study.

6.6 Summary

High accuracy MDG and SNR estimation is mandatory for an adequate performance evaluation and troubleshooting in long-haul SDM systems. This chapter presents a novel ANN-based method proposed to estimate MDG and SNR in SDM systems with coupled channels based on features extracted after DSP. The proposed method is validated in an experimental short-reach 73-km 3-mode transmission setup with polarization multiplexing. After validation, the ANN-based method is applied to a case study consisting of an experimental long-haul 6-mode transmission link with polarization multiplexing. The results suggest that the ANN-based method can largely exceed the performance provided by conventional methods in scenarios of high accumulated MDG, as in long-haul links with weak mode coupling.

7 CHROMATIC DISPERSION ESTIMATION IN SDM TRANSMISSION

Optical transmission over SDM channels experience several impairments that are compensated for by DSP after coherent reception. As the combined effect of inter-modal crosstalk and modal dispersion demands MIMO equalizers, a main point of concern in practical coherent optical systems with SDM is the complexity of the equalizer filters, which is strongly dependent on the channel delay spread caused by modal dispersion. Such complexity also increases if high levels of residual CD are left over from the static equalization. Therefore, the accumulated CD at the end of the link has to be accurately estimated and compensated for previously to the dynamic MIMO equalizer. Currently, the estimation of the accumulated CD in single-mode systems can be carried out through one of the several techniques explored in the literature (KUSCHNEROV *et al.*, 2009a), (XIE, 2013), (WANG *et al.*, 2011). In particular, scanning-based techniques successfully estimate the accumulated CD in single-mode systems (SORIANO *et al.*, 2011). However, their performance in SDM systems has not been evaluated. This chapter evaluates the performance of three scanning-based estimation techniques developed for single-mode systems in the scope of SDM transmission over FMFs. The techniques under evaluation are: Godard's error (KUSCHNEROV *et al.*, 2009a), peak-to-average power ratio (PAPR) (XIE, 2013) and delay-tap sampling (WANG *et al.*, 2011). The performance of the algorithms is evaluated under several conditions of linear crosstalk and OSNR. Section 7.1 presents the architecture of the simulated FMF system and the description of the scanning-based CD estimation techniques.

7.1 Scanning-based CD estimation techniques

The scanning-based CD estimation techniques are applied to an SDM transmission link over a FMF supporting M_p spatial modes. In the setup, each spatial mode supports two polarization orientations, for a total of $2M_p$ orthogonal modes, as indicated in Fig. 7.1. At the transmitter, $2M_p$ independent sources generate binary sequences that later are mapped into M-QAM alphabets. The $2M_p$ complex constellations are fed into RRC shaping filters. Then, the shaped signals pass through DAC and next by I/Q MZM models for electro-optical conversion. Finally, the $2M_p$ optical signals are multiplexed in space and polarization and launched into the FMF. After propagation, the received signals are first demultiplexed and then converted from the optical to the electrical domain

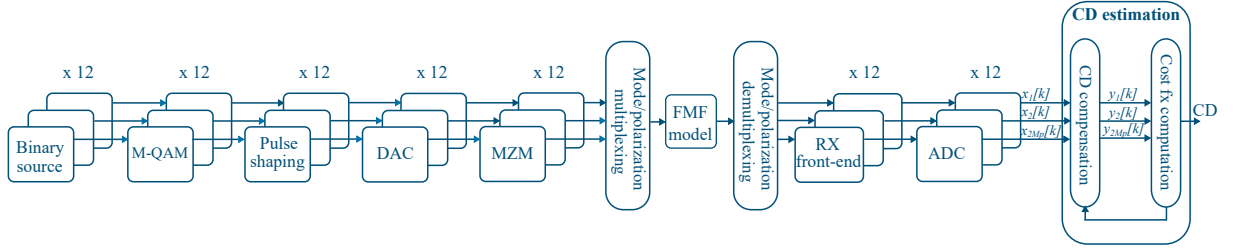


Figure 7.1 – Block diagram of the simulated SDM transmission over a FMF with $2M_p$ orthogonal modes.

by the receiver front-end. The electrical signals are fed into an ADC to be sampled at two samples per symbol. After ADCs, the CD estimator block receives $2M_p$ sequences denoted as $x_i[k]$ with $i = 1, 2, \dots, 2M_p$, which are equalized by a bank of static filters that compensate for the accumulated CD sweeping the CD values within a scanning range wide enough. A fine search can be carried out after a coarse search to improve accuracy, and the total complexity depends on the step size employed in both stages. The scanning-based algorithm searches for the filter that minimizes a cost function related to the equalized signal (SORIANO *et al.*, 2011). Once the best-matching filter is found, the algorithm assumes the associated accumulated CD as the most accurate estimate. The algorithms are applied over the $2M_p$ signals at the static equalizer output based on the approaches proposed in (KUSCHNEROV *et al.*, 2009a), (XIE, 2013), (WANG *et al.*, 2011). Firstly, the $2M_p$ signals pass through $2M_p$ identical and independent static equalizers for CD compensation. Next, all equalized signals are used to adjust the filter transfer function based on the minimization of the estimation criterion. The evaluated estimation criteria are described below.

7.1.1 Godard's error algorithm

After static equalization of the $2M_p$ sequences, $x_i[k]$, the resulting signal vectors, $y_i[k]$, are added to introduce an averaging effect as

$$y_T[k] = \sum_{i=1}^{2M_p} y_i[k], \quad (7.1)$$

next, the algorithm calculates the deviation of the power of the resulting signal, $y_T[k]$, with respect to a constant, R , as

$$J_{Godard}(CD) = \sum_{k=1}^{\text{length}(y_T)/2} \left(\left| |y_T[2k-1]|^2 - R_1 \right| + \left| |y_T[2k]|^2 - R_2 \right| \right), \quad (7.2)$$

where k is the temporal index and R_1, R_2 are normalization constants (GODARD, 1980). For Godard's error algorithm the best-matching filter minimizes the J_{Godard} cost function.

7.1.2 Peak-to-average power ratio (PAPR) algorithm

Similar to Godard's error estimator, before applying the PAPR criterion, the $2M_p$ signals at the output of the static equalizers are added according to (7.1). As remarked in (XIE, 2013), low fiber dispersion is associated with a reduced PAPR, defined as

$$J_{PAPR}(CD) = \max(|y_T[k]|^2) / \min(|y_T[k]|^2), \quad (7.3)$$

then, the PAPR algorithm estimates the accumulated CD by finding the filter than minimizes the J_{PAPR} function in Eq. (7.3).

7.1.3 Delay-tap sampling algorithm

The delay-tap sampling estimator uses a cost function related to the power variations between neighbouring symbols. The algorithm evaluates the remaining dispersion in the equalized signal through a dispersion parameter computed through

$$J_{Delay-tap}(CD) = \frac{1}{2M_p} \sum_{i=1}^{2M_p} \text{std}(d_i[k]), \quad (7.4)$$

where std is the standard deviation operator. The dispersion sequences, $d_i[k]$, are computed from the signals after static equalization as

$$d_i[k] = \frac{(|P_i[2k] - P_i[2k - 1]|)}{\sqrt{2}}, \quad \text{for } i = 1, 2, 3, \dots, 2M_p, \quad (7.5)$$

where $P_i[k]$ is the power of $y_i[k]$.

7.2 Simulation setup and results

The optical channel employed for simulations introduces mode coupling by applying random fluctuations of the core center position according to the semi-analytical model for linear SDM transmission proposed in (FERREIRA *et al.*, 2012). We simulate $M_p = 6$ spatial modes (LP₀₁, LP₀₂, LP_{11a}, LP_{11b}, LP_{21a}, LP_{21b}), each with two orthogonal polarizations. At the transmitter, 12 sequences carrying 50,000 16-QAM symbols are generated at 32 GBd. The transmission setup implements RRC shaping pulses with a 513-coefficient filter and 0.01 roll-off factor. The shaped signals are multiplexed in polarization comprising 256 Gb/s per propagation mode. The operating wavelength is 1550 nm. In addition to mode coupling, the optical channel introduces modal dispersion and CD. Three levels of crosstalk are evaluated: -inf dB/km, -30 dB/km, and -20 dB/km. The group delay vector is (-1.12, -11.26, -2.53, -2.53, 8.73, 8.73) ps/km. The fiber dispersion parameter is adjusted at 22 ps/(km · nm) for all modes, while the fiber length is varied from 100 km to 600 km. After the receiver front-end, the signal is demultiplexed in mode and polarization. Later,

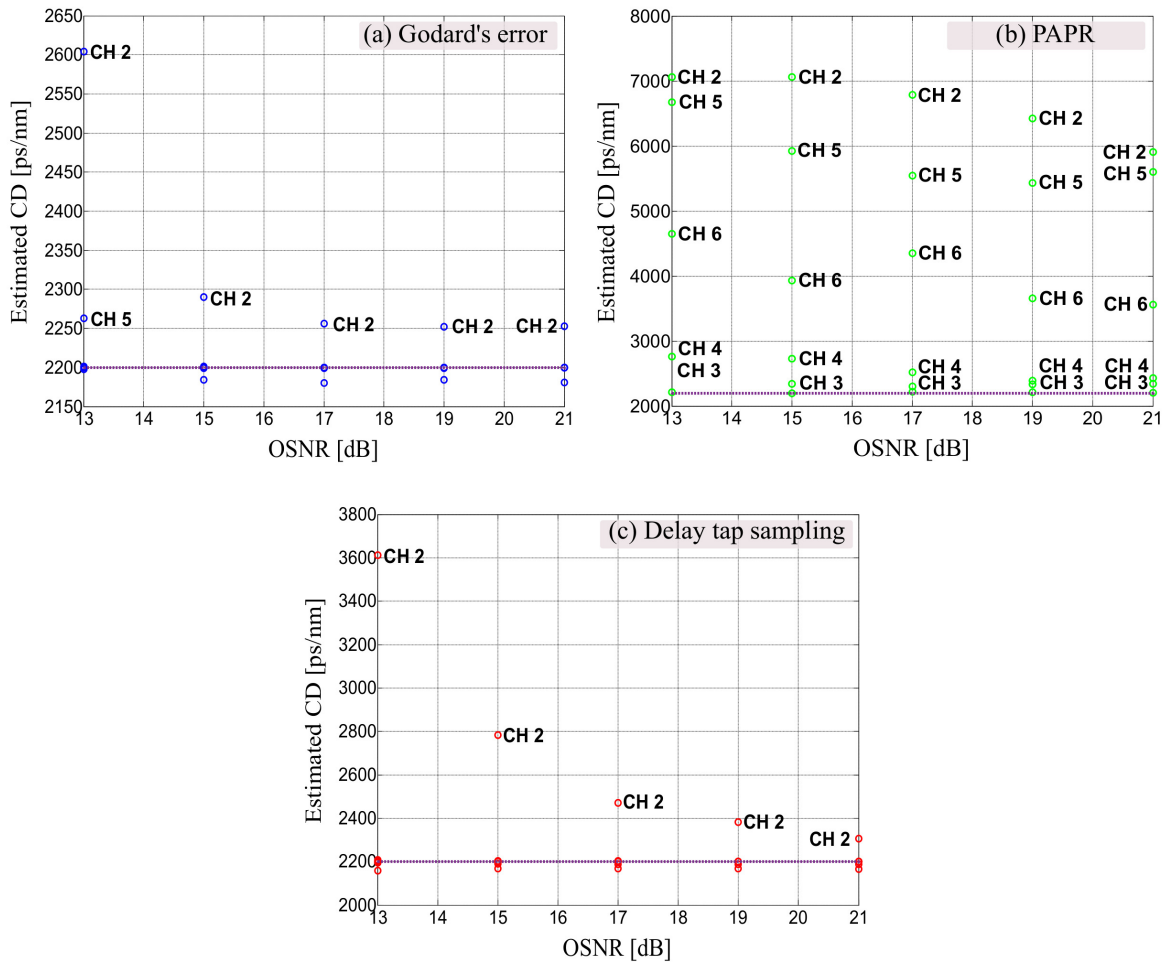


Figure 7.2 – Estimated CD for the 6 spatially multiplexed channels, for a link with CD of 2,200 ps/nm. (a) Godard's error. (b) PAPR. (c) Delay-tap sampling. For the sake of clarity, only the estimates with a perceived error are labelled with their corresponding channel number.

the 12 electrical flows are digitized at 2 samples per symbol. The CD estimation methods are applied to sequences of 100,000 samples. CD equalization is carried out through a static FDE (SAVORY, 2008).

In preliminary experiments, the CD estimation is performed by applying the methods described in Section 7.1 separately to each of the 6 spatial channels. For each spatial channel, the orthogonal polarizations are fed into two static FDE for CD compensation, and later the cost functions are computed from the resulting signals. Then, the algorithms search for the best-matching filter that minimizes the sum of the two cost functions. Fig. 7.2 shows the CD estimates after transmission over the FMF for: DMD = 20 ps/km, crosstalk XT = -20 dB/km and accumulated CD = 2,200 ps/nm. The scanning range was defined from 660 ps/nm to 15,400 ps/nm in steps of 110 ps/nm. The horizontal purple line shows the actual accumulated CD. The three figures present six circles vertically located at different OSNRs indicating the estimated CD value from each of the 6 spatial channels. Note that, for the sake of clarity, only the estimates with a perceived error are labelled

with their corresponding channel number. In addition, note that the Y axis presents a different scale for each figure.

Fig. 7.2 shows high variability in the estimation performance according to the channel number. The low estimation accuracy for channels 2, 5, and 6 can be attributed to a higher power transfer towards these modes. On the other hand, the estimation accuracy increases significantly with the OSNR for Godard's error and delay-tap sampling. For the PAPR method, however, the estimation performance is low for most channels regardless of the OSNR. This can be explained by the fact that even moderate levels of crosstalk already affect the PAPR of the signal significantly. The divergence among the estimates obtained from different spatial channels could severely hamper the CD compensation algorithm, leaving over high levels of residual CD to the dynamic MIMO equalizer.

In an attempt to improve the algorithms accuracy by removing the estimation dependence on the selected channel, we also applied the estimators simultaneously to the 12 sequences, as described in Section 7.1. New estimates were obtained after FMF transmission with $DMD = 20$ ps/km and $OSNR = 21$ dB, which corresponds to a pre-FEC BER = 10^{-3} at crosstalk $XT = -30$ dB/km (SANTOS *et al.*, 2017). The dispersion parameter of the fiber was set at $D = 22$ ps/(km · nm) and the link length was varied from 100 km to 600 km in steps of 100 km. Fig. 7.3 shows the actual CD versus the estimated CD under different levels of crosstalk for the three evaluated techniques. Fig. 7.3a shows that the Godard's error method is able to successfully estimate the accumulated CD at $XT = -\infty$ and $XT = -30$ dB/km. At $XT = -20$ dB/km, the estimates deviate from the actual values mainly for the extreme values of accumulated chromatic dispersion. Fig. 7.3b shows that the PAPR is critically degraded by crosstalk. However, even in absence of crosstalk ($XT = -\infty$), the technique presents low estimation performance. The poor performance of the PAPR algorithm can be explained by the fact that the resulting mixed signals exhibit a high PAPR anyway, even after CD compensation. Fig. 7.3c shows that the delay-tap sampling technique is able to accurately estimate the accumulated CD even for the highest XT evaluated. Therefore, the dispersion parameter estimated after averaging the standard deviation of the 12 dispersion sequences (see Eq. (7.4)) accurately reveals the zero-dispersion state, even in the presence of mode and polarization effects.

7.3 Summary

As the complexity of the MIMO equalizer depends on modal dispersion and residual CD, the accumulated CD should be accurately estimated and compensated for during static equalization. This chapter evaluates the performance of three scanning-based techniques for CD estimation in the scope of SDM optical systems. The results show that

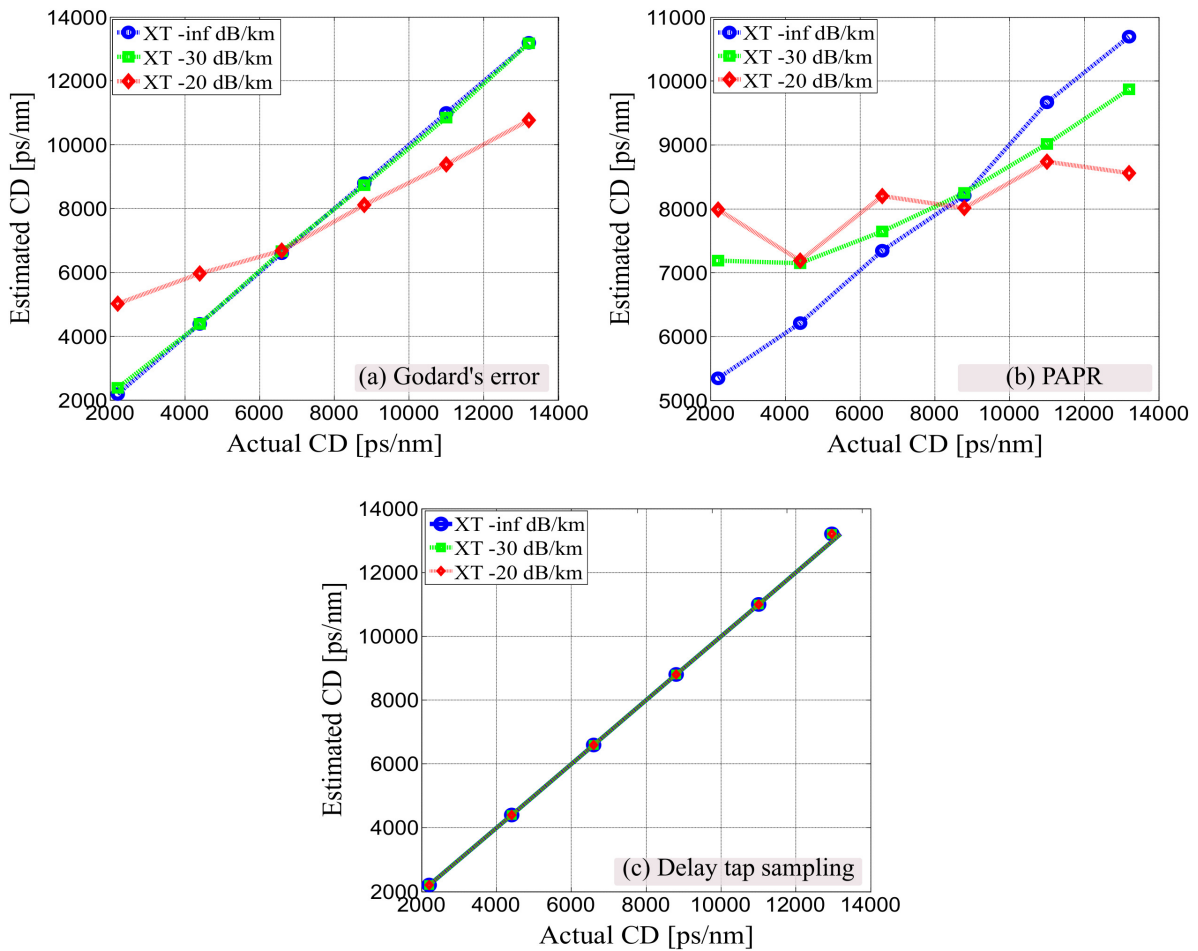


Figure 7.3 – Estimation of the accumulated CD at different levels of linear XT and OSNR=21 dB. (a) Godard's error. (b) PAPR. (c) Delay-tap sampling.

estimating the accumulated CD using individual spatial channels may provide inaccurate estimates, yielding higher errors for increasing levels of crosstalk and ASE noise. Therefore, an alternative approach to estimate the accumulated CD in SDM systems using a combination of all received signals is evaluated. The results show that methods based on the signal PAPR are severely affected by mode mixing. Similarly, the Godard's error method leads to accurate estimates of CD only for crosstalk levels lower than XT = -30 dB/km. On the other hand, the delay-tap sampling method is able to estimate the accumulated CD between 2,200 ps/nm and 13,200 ps/nm, even in the worst scenario of crosstalk evaluated (OSPINA *et al.*, 2019).

8 STUDY OF REDUCED COMPLEXITY MIMO EQUALIZATION

Coupled SDM transmission over MCFs and MMFs requires MIMO equalizers to compensate for channel coupling, introduced by non-ideal devices and fiber propagation (OSPINA *et al.*, 2020). MIMO DSP is often implemented with FIR filters (SAVORY, 2008). The complexity of MIMO equalizers depends on the number of coupled channels and the required length of FIR filters, determined by the total channel delay spread (INAN *et al.*, 2012), (RANDEL *et al.*, 2012a), (SANTOS *et al.*, 2019). MIMO equalization in high-mode-count SDM transmission can become very complex even for short-distance transmission with low delay spread.

The M_p -mode transmission with strong coupling between all modes requires a $2M_p \times 2M_p$ MIMO equalizer with $(2M_p)^2$ FIR filters to receive the $2M_p$ -transmitted signals including spatial and polarization orientations. MMFs typically have a structure, where a number of modes are arranged into MGs, as indicated in Fig. 8.1. Modes within the same MG experience strong coupling, while coupling between modes belonging to different MGs can be orders of magnitude lower. This is indicated by the MG-averaged crosstalk matrices, shown in Fig. 8.2a,b after 25.9 km transmission in a graded-index 55-mode fiber (RADEMACHER *et al.*, 2022). The prominent diagonal in the crosstalk matrix indicates a mode-group selective transmission regime, in which the signal power is concentrated around the main diagonal with decreasing coupling levels to MGs further away from the

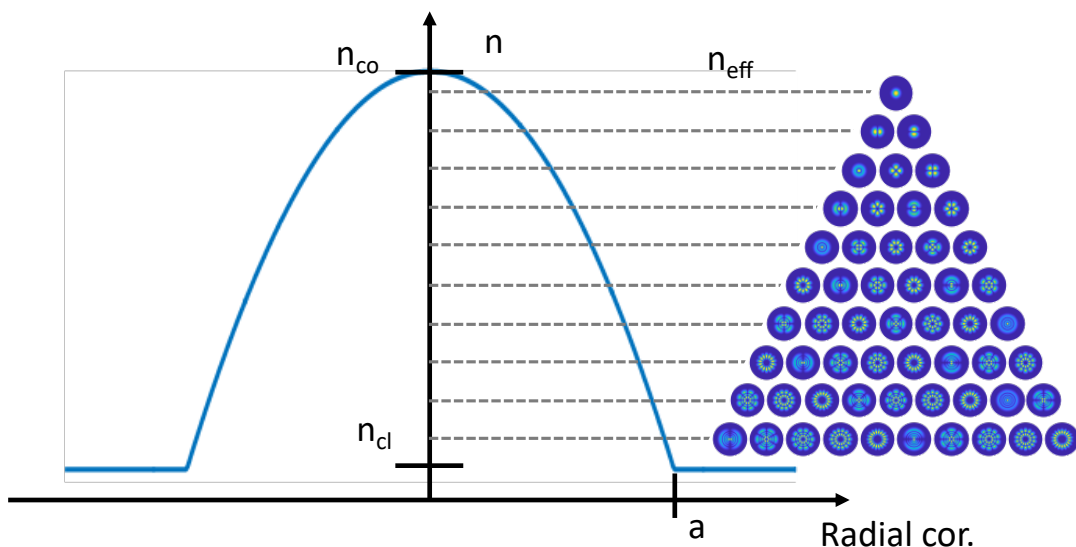


Figure 8.1 – Refractive index profile of a graded-index, 55-mode fiber and the corresponding mode-group (MG) structure.

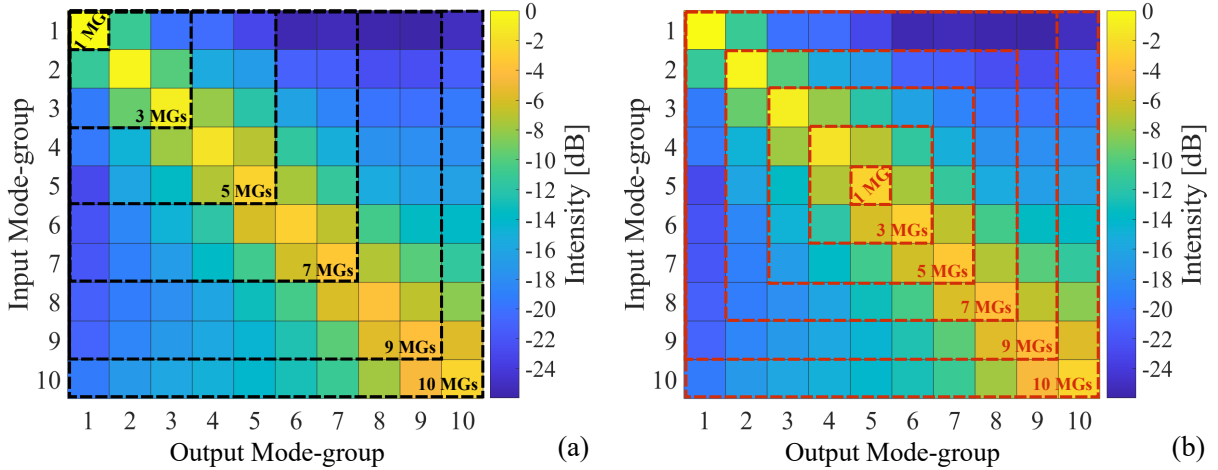


Figure 8.2 – MG-averaged crosstalk matrices after 25.9 km transmission in a 55-mode fiber (RADEMACHER *et al.*, 2022). The dashed squares indicate the investigated MG selections employed for equalization to recover (a) MG #1 and (b) MG #5.

main diagonal.

This chapter investigates the potential of reducing the MIMO equalizer complexity in a 55-mode fiber transmission system (RADEMACHER *et al.*, 2022) by strategically deactivating FIR filters corresponding to MG combinations with low coupling. The recovery of a certain output MG considering MIMO equalization with a reduced set of input MGs is evaluated. The input MGs are selected as those whose propagation constants are closest to that of the equalized output MG (HO *et al.*, 2013). As an example, Fig. 8.2a indicates the 2, 4, 6, 8, and 9 closest neighbors of MG #1, whereas Fig. 8.2b shows the 2, 4, 6, 8, and 9 closest neighbors of MG #5.

8.1 Experimental 55-mode transmission setup

The experimental setup used for reduced complexity MIMO equalization study is shown in Fig. 8.3 (RADEMACHER *et al.*, 2022). A total of 184 WDM channels are generated, comprising a test-band and a dummy-band. The test-band is generated from three 25-GHz-spaced tunable laser sources, modulated in two dual-polarization IQ-modulators. The dummy band is generated in a separate IQ-modulator, using 25 GHz-spaced laser lines from an optical comb source. Test- and dummy-band modulators were driven by 49 GSa/s arbitrary waveform generators (AWGs), producing root-raised cosine-shaped 16-QAM signals with a 0.01 roll-off factor. In this paper, only a single WDM channel at 1543 nm is investigated. 55 copies of the test-band are generated in a three-stage split-and-delay setup, where the 55 signals are delayed by multiples of 50 ns to emulate independent data signals within the delay-spread of the MMF. A multi-plane light-conversion (MPLC) based mode-selective multiplexer (MUX) (FONTAINE *et al.*, 2019) is used to launch the

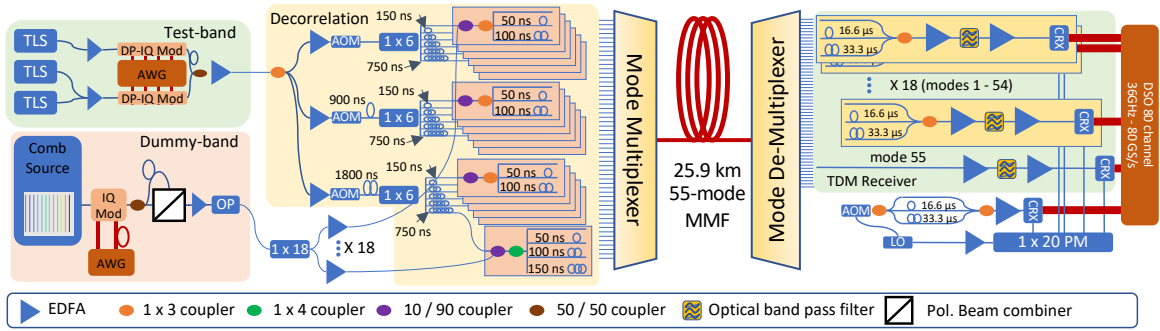


Figure 8.3 – Experimental setup for the 55-mode SDM transmission system (RADEMACHER *et al.*, 2022).

55 input signals into the 55 modes of a 25.9 km long, graded-index 55-mode fiber. After transmission, another MPLC MUX is used to demultiplex the signals into 55 SMFs. A time-domain multiplexed (TDM) receiver setup (UDEN *et al.*, 2014a) is employed to receive groups of three signals in a single coherent receiver, hence a total of 18 coherent receivers are used to receive the signals transmitted over the first 54 modes, with an additional coherent receiver used for the signal in the 55th mode. A similar TDM setup including another coherent receiver is used for the local oscillator (LO) path to detect the relative phase changes of the LO laser across the three time slots of the TDM receiver. An 80 channel real-time oscilloscope with an electrical bandwidth of 36 GHz, operating at 80 GSa/s, is used to digitize the electrical signals from the 20 coherent receivers. Further details on the transmission system can be found in (RADEMACHER *et al.*, 2022).

The DSP module starts with front-end imperfections removal and frequency offset estimation. MIMO equalization is performed by a time-domain dynamic equalizer updated by the LMS algorithm that was initialized in a data-aided mode, followed by a decision-directed mode for signal performance assessment. Phase recovery is carried out in loop-mode with dynamic equalization. Each of the 10 output MGs is obtained from the equalization of the desired MG itself, along with its 2, 4, 6, 8, and 9 nearest neighboring MGs, maintaining the length of the FIR filters fixed for all the cases. For the MGs at the extremes, MG #1 and MG #10, the nearest neighbors are selected in just one direction (increasing or decreasing propagation constants), as exemplified by the black squares in Fig. 8.2a for MG #1. For intermediate MGs, neighboring MGs are chosen in both directions, as indicated by the red squares in Fig. 8.2b for MG #5. Table 8.1 and Table 8.2 present all the configurations employed for MIMO equalization. The complexity of MIMO equalization is assessed in terms of the number of active FIR filters. The transmission performance is evaluated based on the data rate estimated from generalized mutual information (GMI) (ALVARADO *et al.*, 2018). The data rate at each MIMO equalizer configuration is obtained as

$$\text{Data rate} = \text{GMI} \times \# \text{ output modes} \times R_s. \quad (8.1)$$

OUTPUT MODE - GROUP	MODE - GROUPS EMPLOYED FOR EQUALIZATION		
	One MG	Three MGs	Five MGs
MG 1	MG 1	MGs 1, 2, 3	MGs 1, 2, 3, 4, 5
MG 2	MG 2	MGs 1, 2, 3	MGs 1, 2, 3, 4, 5
MG 3	MG 3	MGs 2, 3, 4	MGs 1, 2, 3, 4, 5
MG 4	MG 4	MGs 4, 5, 6	MGs 2, 3, 4, 5, 6
MG 5	MG 5	MGs 4, 5, 6	MGs 3, 4, 5, 6, 7
MG 6	MG 6	MGs 5, 6, 7	MGs 4, 5, 6, 7, 8
MG 7	MG 7	MGs 6, 7, 8	MGs 5, 6, 7, 8, 9
MG 8	MG 8	MGs 7, 8, 9	MGs 6, 7, 8, 9, 10
MG 9	MG 9	MGs 8, 9, 10	MGs 6, 7, 8, 9, 10
MG 10	MG 10	MGs 8, 9, 10	MGs 6, 7, 8, 9, 10

Table 8.1 – Mode-groups employed for MIMO equalization to recover each desired mode-group. Part I.

OUTPUT MODE - GROUP	MODE - GROUPS EMPLOYED FOR EQUALIZATION		
	Seven MGs	Nine MGs	Ten MGs
MG 1	MGs 1, 2, 3, 4, 5, 6, 7	MGs 1, 2, 3, 4, 5, 6, 7, 8, 9	All MGs
MG 2	MGs 1, 2, 3, 4, 5, 6, 7	MGs 1, 2, 3, 4, 5, 6, 7, 8, 9	All MGs
MG 3	MGs 1, 2, 3, 4, 5, 6, 7	MGs 1, 2, 3, 4, 5, 6, 7, 8, 9	All MGs
MG 4	MGs 1, 2, 3, 4, 5, 6, 7	MGs 1, 2, 3, 4, 5, 6, 7, 8, 9	All MGs
MG 5	MGs 2, 3, 4, 5, 6, 7, 8	MGs 1, 2, 3, 4, 5, 6, 7, 8, 9	All MGs
MG 6	MGs 3, 4, 5, 6, 7, 8, 9	MGs 2, 3, 4, 5, 6, 7, 8, 9, 10	All MGs
MG 7	MGs 4, 5, 6, 7, 8, 9, 10	MGs 2, 3, 4, 5, 6, 7, 8, 9, 10	All MGs
MG 8	MGs 4, 5, 6, 7, 8, 9, 10	MGs 2, 3, 4, 5, 6, 7, 8, 9, 10	All MGs
MG 9	MGs 4, 5, 6, 7, 8, 9, 10	MGs 2, 3, 4, 5, 6, 7, 8, 9, 10	All MGs
MG 10	MGs 4, 5, 6, 7, 8, 9, 10	MGs 2, 3, 4, 5, 6, 7, 8, 9, 10	All MGs

Table 8.2 – Mode-groups employed for MIMO equalization to recover each desired mode-group. Part II.

8.2 Results and discussion

The data rate computed as in Eq. (8.1) and averaged over the number of output modes as a function of the number of input MGs used for equalization is shown in Fig. 8.4a. For the sake of clarity, only the curves for MGs # 1, 2, 3, 4, 9, and 10 are shown. As expected, lower-order MGs exhibit a higher data rate per mode compared to high-order MGs. The curves indicate a steep increase in the average data rate going from 1 to 3 input MGs used for equalizing low-order MGs. This indicates that low-order MGs couple little to other MGs and have a higher potential for complexity reduction. Higher-order MGs, however, couple more to other MGs, requiring a significant amount of adjacent input MGs to achieve an increment in data rate. From 7 MGs, the average data rate remains roughly stable with a gradual increment until reaching the maximum value when all 10 MGs are used for equalization.

Fig. 8.4b shows the number of active FIR filters as a function of the number of MGs used for equalization, for the 10 MGs. If only one input MG is used for equalization, the number of active filters that compose the MIMO equalizer is 4, 16, 36, 64, 100, 144, 196,

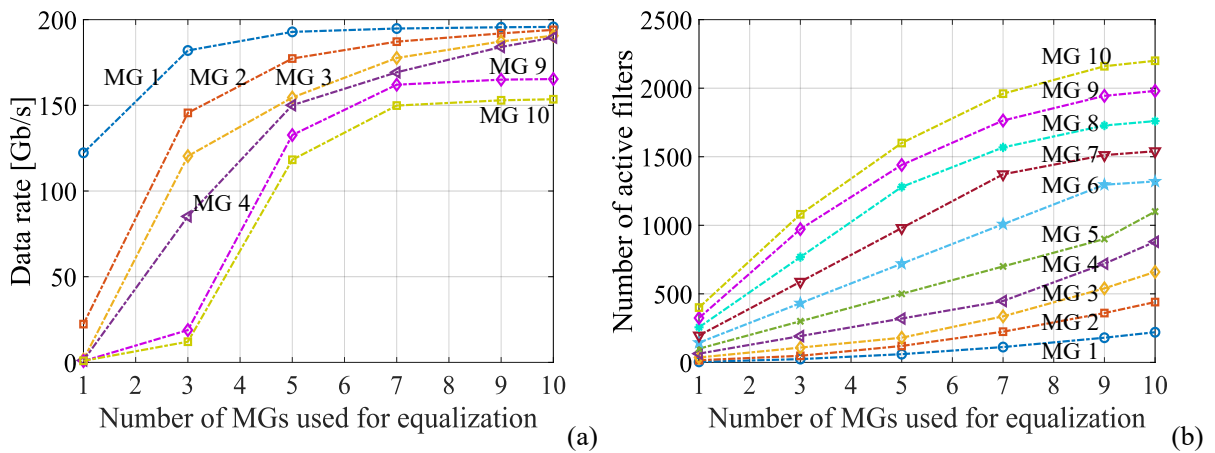


Figure 8.4 – (a) Mode-group (MG)-averaged, GMI-based data rate for different output MGs as a function of the number of input MGs, used for MIMO equalization. (b) Number of active filters for the 10 MGs as a function of the number of input MGs used for equalization.

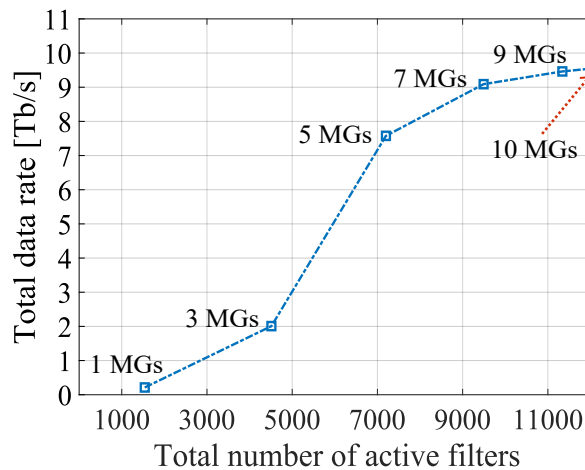


Figure 8.5 – System GMI-based data rate as a function of the number of active filters.

256, 324, and 400 for MGs from 1 to 10, respectively. The number of active filters increases with the number of MGs employed for equalization at a higher derivative for higher-order MGs. Fig. 8.4a and Fig. 8.4b show that although lower-order MGs couple less to neighbors and therefore can allow deactivation of a significant portion of its FIR filters, the impact of this deactivation on the overall complexity is limited, as low-order MGs contain relatively few modes, and thus contribute little to the overall system complexity.

Fig. 8.5 shows the overall data rate and the total number of active filters employed in each studied case. A data rate of 9.6 Tb/s is achieved by employing a full MIMO equalizer consisting of $110 \times 110 = 12100$ active FIR filters. Employing 7 input MGs for equalization of each output MG requires 2608 fewer filters for a system data rate of 9.1 Tb/s, equivalent to a data rate decrease of 4.9%. Using 5 input MGs per output MG reduces the number of active filters to 7200, leading to a data rate decrease of 20.7%. These results show that

the data rate may be flexibly traded with the number of active filters to allow a new dimension for optimization of MMF based SDM systems.

8.3 Summary

High-mode-count, coupled SDM transmission requires highly complex and computationally expensive MIMO equalizers for signal separation. Even in short-distance transmission, a high number of spatial modes makes the equalization process computationally expensive. However, in highly mode-selective SDM transmission, although modes couple within a MG, coupling between modes in different MGs may be limited. This observation instigates the possibility of strategically deactivating filters with low content. This chapter investigates the potential of reducing their complexity in an experimental 55-mode fiber SDM transmission system, by using only subsets of the received mode-groups (MGs) for MIMO equalization. In the employed 25.9 km long, graded-index 55-mode fiber, low-order MGs couple little with other MGs, but also contribute little to the overall data rate and complexity. On the other hand, high-order MGs couple more with other MGs, and also contribute significantly to the overall data rate and complexity. The investigation shows that a 21.5% complexity reduction can be achieved with only a 4.9% data rate reduction by selective filter deactivation based on understanding of the MIMO characteristics. Although not investigated here, we note that, further complexity reductions may also be achieved by using a different selection of neighbouring MGs or by simultaneously reducing the FIR filter length.

9 CONCLUSION

The fervor for electronic devices and Internet services boosts the sustained growth of data traffic through optical networks. Solutions based on space division multiplexing (SDM), either over bundles of single-mode fibers (SMFs), multi-mode fibers (MMFs), or multi-core fibers (MCFs), are being evaluated to increase the capacity of current coherent optical systems while maintaining the trend to reduce the cost per transmitted bit. Transmission over optical fibers with spatial multiplexing is subject to several channel impairments. The random power coupling among propagation modes results in crosstalk that should be compensated for by digital signal processing (DSP) using a dynamic multiple-input multiple-output (MIMO) equalizer. The computational complexity of the MIMO equalizer increases with the broadening of the channel impulse response. Then, modal dispersion and residual chromatic dispersion (CD) left over from the static equalizer must be carefully handled. Modal dispersion is managed during system design at both fiber and component levels. On the contrary, the residual CD is minimized by an accurate accumulated CD estimation and compensation through static equalization.

Long-distance SDM systems will integrate thousands of kilometers length optical fibers and multiple in-line components. Fibers, amplifiers, multiplexers, and switches, among others, introduce two perturbations known as mode-dependent loss (MDL) and mode-dependent gain (MDG), named jointly in this thesis as MDG. Besides MDG, optical amplifiers generate amplified spontaneous emission (ASE) noise. The combined effect of MDG and ASE noise fundamentally limits the capacity and transmission distance of future SDM systems.

Channel parameter estimation is essential for performance evaluation and troubleshooting. In this thesis, the estimation of channel parameters in coupled SDM transmissions using DSP-based techniques is investigated. The work focuses on the estimation of MDG and signal-to-noise ratio (SNR) employing both conventional DSP methods and artificial neural networks (ANNs). Additionally, the study covers the evaluation of scanning methods for accumulated CD estimation in the scope of SDM systems. The computational complexity of MIMO equalizers in SDM transmission is also a high-interest topic. Conventionally, MIMO equalizers are implemented using finite impulse response (FIR) filters. The complexity of the MIMO equalizer is then dictated by the number of required FIR filters and their length. Approaches to reduce the MIMO equalizer complexity with a low system performance penalty are very attractive for future SDM transmission. In this thesis, an approach to strategically reduce the number of FIR filters composing the

MIMO equalizer in SDM transmission is experimentally investigated.

In this thesis, the general diagram of an SDM transmission system was detailed. The description covered the components of the transmitter, optical channel, and receiver. Later, the mathematical model of a MIMO transmission was presented. All the algorithms of the DSP chain implemented in this thesis for impairment compensation were described. The DSP chain was applied to two case studies. Two different approaches for dynamic MIMO equalization and carrier phase recovery (CPR) were evaluated. The results evidenced that, in SDM transmission with high levels of phase noise, the MIMO equalizer updated with the least mean square (LMS) algorithm should be strategically intertwined with the CPR block so that phase mismatches do not impair the MIMO convergence. Applying the DSP chain to the case studies, simulation and experimental data were processed to show the effect of ASE noise, MDG, and nonlinearities on the system performance.

The manuscript also gathered fundamental concepts of MDG, including topics such as mathematical modeling, MDG-induced performance degradation, and MDG simulation through the well-known semi-analytical multisection model for strongly-coupled SDM transmission. Moreover, the conventional methods for MDG and SNR estimation in SDM systems were studied. The results obtained from semi-analytical and simulation data evidenced that the conventional MDG estimation method based on DSP presents a deficient performance at high levels of MDG and low SNRs. Similarly, semi-analytical results showed that the conventional method for SNR estimation presents very low accuracy at high regimes of MDG and SNR.

After evidencing the performance limitation of the conventional DSP-based MDG estimation method, an improved DSP-based technique for MDG estimation in SDM systems based on an analytical correction factor was proposed. The correction factor method was validated through simulations and experiments. The results showed that the technique substantially improves the MDG estimation accuracy, mainly for high levels of MDG and moderate levels of SNR. Furthermore, an ANN-based MDG and SNR estimator in SDM systems was proposed. The technique was validated using experimental data of a short-distance 3-mode transmission. After validation, the ANN estimator was applied to a case study of a long-haul 6-mode transmission. The results showed that the ANN-based estimator outperforms the conventional methods presenting a very high performance over all the regimes of MDG and SNR evaluated.

In addition to the estimation of MDG and SNR, this thesis evaluated the estimation of the accumulated chromatic dispersion. Three scanning-based techniques for accumulated CD estimation proposed for SMF systems were evaluated in the context of SDM transmissions. The results showed that the methods based on the signal peak-to-average

power ratio (PAPR) are critically affected by crosstalk even at low levels. Similarly, Godard's error method presented a high performance only for moderate crosstalk levels. On the contrary, the delay-tap sampling technique provided accurate estimates of accumulated CD even for very high crosstalk levels.

Finally, as a complementary topic, the selective FIR filter deactivation based on the crosstalk matrix of an experimental SDM link was evaluated to decrease the computational complexity of MIMO equalizers in high-mode count SDM transmission. MIMO complexity reduction was experimentally investigated in a 55-mode transmission over a 25.9 km long graded-index fiber. The results show that, in the employed 55-mode fiber, low-order MGs couple little with other MGs but also contribute little to the overall data rate and complexity. On the other hand, high-order MGs couple more with other MGs and contribute significantly to the overall data rate and complexity. By the strategic FIR filter deactivation, 21.5% complexity reduction can be achieved with only a 4.9% data rate reduction.

This work opens new challenges for future work. The estimation of other channel parameters, such as the mode coupling regime and modal dispersion, can also be studied. In the scope of flexible optical systems, the adaptation of the DSP algorithms and the transmitter parameters like modulation format and transmission rate based on the channel state can also be investigated. Likewise, regarding the effect of the MDG on the system performance, the MDG-induced capacity reduction in experimental SDM transmission can be studied. Finally, the validation of the proposed estimation techniques on several experimental setups with different fiber lengths is desirable.

Bibliography

- ABEDIN, K.; TAUNAY, T.; FINI, J.; BANSAL, L.; SUPRADEEPA, V.; YAN, M.; ZHU, B.; MONBERG, E.; DIGIOVANNI, D. Cladding pumped erbium-doped multicore fiber amplifiers for space division multiplexing. In: OPTICAL SOCIETY OF AMERICA. *Frontiers in Optics*. [S.l.], 2014. p. FTh3B–1. Cited on page 66.
- ABEDIN, K.; TAUNAY, T.; FISHTEYN, M.; YAN, M.; ZHU, B.; FINI, J.; MONBERG, E.; DIMARCELLO, F.; WISK, P. Amplification and noise properties of an erbium-doped multicore fiber amplifier. *Optics express*, Optica Publishing Group, v. 19, n. 17, p. 16715–16721, 2011. Cited on page 64.
- ABEDIN, K. S.; FINI, J. M.; THIERRY, T. F.; ZHU, B.; YAN, M. F.; BANSAL, L.; DIMARCELLO, F. V.; MONBERG, E. M.; DIGIOVANNI, D. J. Seven-core erbium-doped double-clad fiber amplifier pumped simultaneously by side-coupled multimode fiber. *Optics Letters*, Optica Publishing Group, v. 39, n. 4, p. 993–996, 2014. Cited on page 64.
- AGRAWAL, G. P. *Fiber-Optic Communications Systems*. Third. [S.l.]: A JOHN WILEY AND SONS, 2002. Cited 10 times on pages 45, 49, 50, 51, 55, 58, 60, 66, 73, and 74.
- AGRAWAL, G. P. Nonlinear fiber optics: its history and recent progress. *JOSA B*, Optical Society of America, v. 28, n. 12, p. A1–A10, 2011. Cited on page 54.
- AINSLIE, B.; DAY, C. A review of single-mode fibers with modified dispersion characteristics. *Journal of lightwave technology*, IEEE, v. 4, n. 8, p. 967–979, 1986. Cited on page 58.
- ALVARADO, A.; FEHENBERGER, T.; CHEN, B.; WILLEMS, F. M. Achievable information rates for fiber optics: Applications and computations. *Journal of Lightwave Technology*, IEEE, v. 36, n. 2, p. 424–439, 2018. Cited 2 times on pages 69 and 149.
- ANTONELLI, C.; MECOZZI, A.; SHTAIF, M. The delay spread in fibers for SDM transmission: dependence on fiber parameters and perturbations. *Optics express*, Optical Society of America, v. 23, n. 3, p. 2196–2202, 2015. Cited 2 times on pages 99 and 138.
- ARIK, S. O.; KAHN, J. M.; HO, K.-P. MIMO signal processing for mode-division multiplexing: An overview of channel models and signal processing architectures. *IEEE Signal Processing Magazine*, IEEE, v. 31, n. 2, p. 25–34, 2014. Cited on page 39.
- ARIKAWA, M.; NAKAMURA, K.; HOSOKAWA, K.; HAYASHI, K. Long-haul WDM/SDM transmission over coupled 4-core fiber with coupled 4-core EDFA and its mode dependent loss characteristics estimation. *Journal of Lightwave Technology*, IEEE, v. 40, n. 6, p. 1664–1671, 2021. Cited on page 35.
- BAGAD, V. S. *Optical Fiber Communications*. First. [S.l.]: Technical Publications Pune, 2007. Cited on page 56.
- BARRY, J. R.; LEE, E. A.; MESSERSCHMITT, D. G. *Digital Communications*. Third. [S.l.]: Kluwer Academic Publishers, 2004. Cited 3 times on pages 42, 44, and 68.

- BEEK, J.-J. V. D.; EDFORS, O.; SANDELL, M.; WILSON, S. K.; BORJESSON, P. O. On channel estimation in OFDM systems. In: IEEE. *1995 IEEE 45th Vehicular Technology Conference. Countdown to the Wireless Twenty-First Century*. [S.l.], 1995. v. 2, p. 815–819. Cited on page 111.
- BIRKS, T. A.; GRIS-SÁNCHEZ, I.; YEROLATSITIS, S.; LEON-SAVAL, S.; THOMSON, R. R. The photonic lantern. *Advances in Optics and Photonics*, Optical Society of America, v. 7, n. 2, p. 107–167, 2015. Cited on page 47.
- BJARKLEV, A.; RASMUSSEN, T.; LUMHOLT, O.; ROTTWITT, K.; HELMER, M. Optimal design of single-cladded dispersion-compensating optical fibers. *Optics letters*, Optical Society of America, v. 19, n. 7, p. 457–459, 1994. Cited on page 32.
- BORN, M.; WOLF, E. *Principles of optics: electromagnetic theory of propagation, interference and diffraction of light*. [S.l.]: Elsevier, 2013. Cited on page 56.
- BRILLOUIN, L. Diffusion de la lumière et des rayons x par un corps transparent homogène: Influence de l'agitation thermique. *Annals of Physics*, v. 9, n. 17, p. 88–122, 1922. Cited on page 59.
- BROMAGE, J. Raman amplification for fiber communications systems. *journal of lightwave technology*, IEEE, v. 22, n. 1, p. 79–93, 2004. Cited on page 62.
- CANTOR, G. N. *Optics after Newton: theories of light in Britain and Ireland, 1704-1840*. [S.l.]: Manchester University Press, 1983. Cited on page 58.
- CHO, H. J.; VARUGHESE, S.; LIPPIATT, D.; DESALVO, R.; TIBULEAC, S.; RALPH, S. E. Optical performance monitoring using digital coherent receivers and convolutional neural networks. *Optics Express*, Optical Society of America, v. 28, n. 21, p. 32087–32104, 2020. Cited on page 133.
- CISCO. *Cisco Annual Internet Report (2018–2023)*. 2020. Cited on page 33.
- DAS, A.; RAO, B. D. SNR and noise variance estimation for MIMO systems. *IEEE Transactions on Signal processing*, IEEE, v. 60, n. 8, p. 3929–3941, 2012. Cited 2 times on pages 102 and 116.
- DEMTRÖDER, W. *Atoms, molecules and photons: An introduction to atomic-, molecular- and quantum-physics*. 1. ed. Springer, 2005. ISBN 3-540-20631-0. Disponível em: <<http://gen.lib.rus.ec/book/index.php?md5=F781822CB3B31D7F375ABDD694AECEDE>>. Cited 2 times on pages 44 and 66.
- DOMINGUES, O. D.; MELLO, D. A.; SILVA, R. da; ARIK, S. Ö.; KAHN, J. M. Achievable rates of space-division multiplexed submarine links subject to nonlinearities and power feed constraints. *Journal of lightwave technology*, IEEE, v. 35, n. 18, p. 4004–4010, 2017. Cited 2 times on pages 34 and 70.
- DZIEDZIC, J. M.; STOLEN, R. H.; ASHKIN, A. Optical kerr effect in long fibers. *Appl. Opt.*, OSA, v. 20, n. 8, p. 1403–1406, 04 1981. Disponível em: <<http://ao.osa.org/abstract.cfm?URI=ao-20-8-1403>>. Cited on page 60.
- EDFORS, O.; SANDELL, M.; BEEK, J.-J. Van de; WILSON, S. K.; BORJESSON, P. O. OFDM channel estimation by singular value decomposition. *IEEE Transactions on communications*, IEEE, v. 46, n. 7, p. 931–939, 1998. Cited on page 111.

- ESSIAMBRE, R. J.; KRAMER, G.; WINZER, P. J.; FOSCHINI, G. J.; GOEBEL, B. Capacity limits of optical fiber networks. *Journal of Lightwave Technology*, v. 28, n. 4, p. 662–701, 02 2010. ISSN 0733-8724. Cited on page 67.
- ESSIAMBRE, R.-J.; KRAMER, G.; WINZER, P. J.; FOSCHINI, G. J.; GOEBEL, B. Capacity limits of optical fiber networks. *Journal of Lightwave Technology*, IEEE, v. 28, n. 4, p. 662–701, 2010. Cited 2 times on pages 104 and 123.
- ESSIAMBRE, R. J.; TKACH, R. W. Capacity trends and limits of optical communication networks. *Proceedings of the IEEE*, v. 100, n. 5, p. 1035–1055, 05 2012. ISSN 0018-9219. Cited on page 67.
- EZNAVEH, Z. S.; FONTAINE, N. K.; CHEN, H.; LOPEZ, J. A.; ZACARIAS, J. A.; HUANG, B.; CORREA, A. A.; GONNET, C.; SILLARD, P.; LI, G. *et al.* Ultra-low DMG multimode EDFA. In: OPTICA PUBLISHING GROUP. *Optical Fiber Communication Conference*. [S.l.], 2017. p. Th4A–4. Cited on page 64.
- FARUK, M. S.; KIKUCHI, K. Adaptive frequency-domain equalization in digital coherent optical receivers. *Optics Express*, Optical Society of America, v. 19, n. 13, p. 12789–12798, 2011. Cited 4 times on pages 10, 84, 85, and 86.
- FARUK, M. S.; SAVORY, S. J. Digital signal processing for coherent transceivers employing multilevel formats. *Journal of Lightwave Technology*, IEEE, v. 35, n. 5, p. 1125–1141, 2017. Cited 3 times on pages 82, 83, and 119.
- FATADIN, I.; IVES, D.; SAVORY, S. J. Compensation of frequency offset for differentially encoded 16- and 64-QAM in the presence of laser phase noise. *IEEE Photonics Technology Letters*, v. 22, n. 3, p. 176–178, 2 2010. ISSN 1041-1135. Cited on page 42.
- FATADIN, I.; SAVORY, S. J.; IVES, D. Compensation of quadrature imbalance in an optical QPSK coherent receiver. *IEEE Photonics Technology Letters*, IEEE, v. 20, n. 20, p. 1733–1735, 2008. Cited on page 80.
- FAUSTINI, L.; MARTINI, G. Bend loss in single-mode fibers. *Journal of lightwave technology*, IEEE, v. 15, n. 4, p. 671–679, 1997. Cited on page 56.
- FAVRE, F.; GUEN, D. le; SIMON, J. C.; LANDOUSIES, B. External-cavity semiconductor laser with 15 nm continuous tuning range. *Electronics Letters*, v. 22, n. 15, p. 795–796, 07 1986. ISSN 0013-5194. Cited on page 45.
- FERREIRA, F.; MONTEIRO, P.; SILVA, H. Semi-analytical model for linear modal coupling in few-mode fiber transmission. In: IEEE. *2012 14th International Conference on Transparent Optical Networks (ICTON)*. [S.l.], 2012. p. 1–4. Cited 2 times on pages 107 and 143.
- FERREIRA, R. M. da S. *Advanced Digital Signal Processing for Flexible Optical Access Networks*. Tese (Doutorado) — University of Aveiro, Portugal, 2017. Cited on page 83.
- FLEMING, M.; MOORADIAN, A. Spectral characteristics of external-cavity controlled semiconductor lasers. *IEEE Journal of Quantum Electronics*, v. 17, n. 1, p. 44–59, 01 1981. ISSN 0018-9197. Cited on page 45.

- FONTAINE, N. K.; CARPENTER, J.; GROSS, S.; LEON-SAVAL, S.; JUNG, Y.; RICHARDSON, D. J.; AMEZCUA-CORREA, R. Photonic lanterns, 3-D waveguides, multiplane light conversion, and other components that enable space-division multiplexing. *Proceedings of the IEEE*, IEEE, v. 110, n. 11, p. 1821–1834, 2022. Cited on page 48.
- FONTAINE, N. K.; RYF, R.; CHEN, H.; NEILSON, D. T.; KIM, K.; CARPENTER, J. Laguerre-gaussian mode sorter. *Nature communications*, Nature Publishing Group, v. 10, n. 1, p. 1–7, 2019. Cited on page 148.
- GALTAROSSA, C. R. M. A. *Polarization Mode Dispersion*. First. [S.l.]: Springer, 2005. Cited on page 57.
- GARDNER, W. B. Microbending loss in optical fibers. *The bell system technical journal*, Nokia Bell Labs, v. 54, n. 2, p. 457–465, 1975. Cited on page 56.
- GLOGE, D. Weakly guiding fibers. *Applied optics*, Optical Society of America, v. 10, n. 10, p. 2252–2258, 1971. Cited 2 times on pages 51 and 52.
- GODARD, D. Self-recovering equalization and carrier tracking in two-dimensional data communication systems. *IEEE transactions on communications*, IEEE, v. 28, n. 11, p. 1867–1875, 1980. Cited on page 142.
- GRÜNER-NIELSEN, L.; SUN, Y.; NICHOLSON, J. W.; JAKOBSEN, D.; JESPERSEN, K. G.; JR, R. L.; PÁLSDÓTTIR, B. Few mode transmission fiber with low DGD, low mode coupling, and low loss. *Journal of Lightwave Technology*, IEEE, v. 30, n. 23, p. 3693–3698, 2012. Cited on page 71.
- GRUNER-NIELSEN, L.; WANDEL, M.; KRISTENSEN, P.; JORGENSEN, C.; JORGENSEN, L. V.; EDVOLD, B.; PALSDOTTIR, B.; JAKOBSEN, D. Dispersion-compensating fibers. *Journal of Lightwave Technology*, v. 23, n. 11, p. 3566–3579, 10 2005. ISSN 0733-8724. Cited on page 58.
- HAYASHI, T.; TAMURA, Y.; HASEGAWA, T.; TARU, T. Record-low spatial mode dispersion and ultra-low loss coupled multi-core fiber for ultra-long-haul transmission. *Journal of Lightwave Technology*, IEEE, v. 35, n. 3, p. 450–457, 2017. Cited 6 times on pages 95, 109, 113, 114, 115, and 134.
- HAYKIN, S. *Adaptive filter theory*. [S.l.]: Prentice-Hall, Inc., 1996. Cited on page 84.
- HAYKIN, S. *Communication Systems*. 4th ed. ed. Wiley, 2001. ISBN 0-471-17869-1. Disponível em: <<http://gen.lib.rus.ec/book/index.php?md5=0D7B2D4C12E3B9C37D94EDCFF4698458>>. Cited 3 times on pages 41, 43, and 68.
- HEI, Y.; LI, L.; LI, W.; LI, X.; SHI, G. Channel estimation in few mode fiber mode division multiplexing transmission system. *Optical Fiber Technology*, Elsevier, v. 41, p. 182–186, 2018. Cited on page 35.
- HO, K.-P. *Phase-modulated optical communication systems*. [S.l.]: Springer Science & Business Media, 2005. Cited 2 times on pages 75 and 76.

- HO, K.-P.; KAHN, J. M. Frequency diversity in mode-division multiplexing systems. *Journal of Lightwave Technology*, IEEE, v. 29, n. 24, p. 3719–3726, 2011. Cited on page 114.
- HO, K.-P.; KAHN, J. M. Mode-dependent loss and gain: statistics and effect on mode-division multiplexing. *Optics express*, Optical Society of America, v. 19, n. 17, p. 16612–16635, 2011. Cited 10 times on pages 62, 79, 94, 103, 107, 108, 109, 110, 139, and 140.
- HO, K.-P.; KAHN, J. M. Statistics of group delays in multimode fiber with strong mode coupling. *Journal of lightwave technology*, IEEE, v. 29, n. 21, p. 3119–3128, 2011. Cited 3 times on pages 99, 138, and 139.
- HO, K.-P.; KAHN, J. M. *Optical Fiber Telecommunications VIB: Chapter 11. Mode Coupling and its Impact on Spatially Multiplexed Systems*. [S.l.]: Elsevier Inc. Chapters, 2013. Cited on page 60.
- HO, K.-P.; KAHN, J. M. Linear propagation effects in mode-division multiplexing systems. *Journal of Lightwave Technology*, v. 32, n. 4, p. 614–628, 2014. Cited on page 60.
- HO, K.-P.; KAHN, J. M.; KAMINOW, I.; LI, T.; WILLNER, A. Mode coupling and its impact on spatially multiplexed systems. *Optical Fiber Telecommunications VI*, Elsevier Amsterdam, v. 17, p. 1386–1392, 2013. Cited 5 times on pages 34, 35, 100, 122, and 148.
- HOFFMANN, S.; BHANDARE, S.; PFAU, T.; ADAMCZYK, O.; WORDEHOFF, C.; PEVELING, R.; PORRMANN, M.; NOE, R. Frequency and phase estimation for coherent qpsk transmission with unlocked dfb lasers. *IEEE Photonics Technology Letters*, v. 20, n. 18, p. 1569–1571, 09 2008. ISSN 1041-1135. Cited on page 82.
- HOUT, M. van den; OSPINA, R. S.; HEIDE, S. van der; ALVARADO-ZACARIAS, J. C.; ANTONIO-LÓPEZ, J. E.; BIGOT-ASTRUC, M.; CORREA, A. A.; SILLARD, P.; AMEZCUA-CORREA, R.; MELLO, D. A. *et al.* Experimental validation of MDL emulation and estimation techniques for SDM transmission systems. In: IEEE. *2020 European Conference on Optical Communications (ECOC)*. [S.l.], 2020. p. 1–4. Cited 4 times on pages 14, 129, 130, and 139.
- HUANG, H.; CHEN, H.; HUANG, Y.; ZHANG, Q.; CHEN, J.; FONTAINE, N. K.; MAZUR, M.; RYF, R.; SONG, Y. MIMO processing with linear beat interference cancellation for space division multiplexing self-homodyne coherent transmission. *Journal of Lightwave Technology*, IEEE, v. 40, n. 13, p. 4136–4149, 2022. Cited on page 35.
- HÁGER, C.; PFISTER, H. D. Nonlinear interference mitigation via deep neural networks. In: OPTICAL SOCIETY OF AMERICA. *Optical fiber communication conference*. [S.l.], 2018. p. W3A–4. Cited on page 133.
- INAN, B.; SPINNLER, B.; FERREIRA, F.; BORNE, D. van den; LOBATO, A.; ADHIKARI, S.; SLEIFFER, V. A.; KUSCHNEROV, M.; HANIK, N.; JANSEN, S. L. DSP complexity of mode-division multiplexed receivers. *Optics express*, Optica Publishing Group, v. 20, n. 10, p. 10859–10869, 2012. Cited on page 147.
- JATOBA-NETO, A. C.; MELLO, D. A.; ROTHENBERG, C. E.; ARIK, S. Ö.; KAHN, J. M. Scaling sdm optical networks using full-spectrum spatial switching. *IEEE/OSA*

Journal of Optical Communications and Networking, IEEE, v. 10, n. 12, p. 991–1004, 2018. Cited 2 times on pages 34 and 70.

JUNG, Y.; ALAM, S.-U.; RICHARDSON, D. J. Optical amplifiers for mode division multiplexing. Springer, 2018. Cited on page 64.

JUNG, Y.; ALAM, S.-u.; RICHARDSON, D. J.; RAMACHANDRAN, S.; ABEDIN, K. S. Multicore and multimode optical amplifiers for space division multiplexing. In: *Optical Fiber Telecommunications VII*. [S.l.]: Elsevier, 2020. p. 301–333. Cited 2 times on pages 10 and 65.

KANG, Q.; LIM, E.-L.; JUNG, F. P. Y.; BASKIOTIS, C.; ALAM, S.-u.; RICHARDSON, D. J. Minimizing differential modal gain in cladding-pumped EDFAs supporting four and six mode groups. *Optics express*, Optica Publishing Group, v. 22, n. 18, p. 21499–21507, 2014. Cited on page 64.

KAO, K. C.; HOCKHAM, G. A. Dielectric-fibre surface waveguides for optical frequencies. In: IET. *Proceedings of the Institution of Electrical Engineers*. [S.l.], 1966. v. 113, n. 7, p. 1151–1158. Cited on page 32.

KECK, D. Fundamentals of optical waveguide fibers. *IEEE Communications Magazine*, IEEE, v. 23, n. 5, p. 17–22, 1985. Cited on page 55.

KERR, J. Liv. a new relation between electricity and light: Dielectrified media birefringent (second paper). *The London, Edinburgh, and Dublin Philosophical Magazine and Journal of Science*, Taylor & Francis, v. 50, n. 333, p. 446–458, 1875. Cited on page 60.

KHAN, F. N.; ZHONG, K.; AL-ARASHI, W. H.; YU, C.; LU, C.; LAU, A. P. T. Modulation format identification in coherent receivers using deep machine learning. *IEEE Photonics Technology Letters*, IEEE, v. 28, n. 17, p. 1886–1889, 2016. Cited on page 133.

KHAN, F. N.; ZHONG, K.; ZHOU, X.; AL-ARASHI, W. H.; YU, C.; LU, C.; LAU, A. P. T. Joint OSNR monitoring and modulation format identification in digital coherent receivers using deep neural networks. *Optics express*, Optical Society of America, v. 25, n. 15, p. 17767–17776, 2017. Cited on page 133.

KIM, N.; LEE, Y.; PARK, H. Performance analysis of MIMO system with linear MMSE receiver. *IEEE Transactions on Wireless Communications*, IEEE, v. 7, n. 11, p. 4474–4478, 2008. Cited on page 111.

KINGMA, D. P.; BA, J. Adam: A method for stochastic optimization. *arXiv preprint arXiv:1412.6980*, 2014. Cited on page 135.

KOGELNIK, H.; SHANK, C. Coupled-wave theory of distributed feedback lasers. *Journal of applied physics*, AIP, v. 43, n. 5, p. 2327–2335, 1972. Cited on page 45.

KUSCHNEROV, M.; HAUSKE, F.; PIYAWANNO, K.; SPINNLER, B.; NAPOLI, A.; LANKL, B. Adaptive chromatic dispersion equalization for non-dispersion managed coherent systems. In: OPTICAL SOCIETY OF AMERICA. *Optical Fiber Communication Conference*. [S.l.], 2009. p. OMT1. Cited 2 times on pages 141 and 142.

- KUSCHNEROV, M.; HAUSKE, F. N.; PIYAWANNO, K.; SPINLER, B.; ALFIAD, M. S.; NAPOLI, A.; LANKL, B. DSP for coherent single-carrier receivers. *Journal of Lightwave Technology*, OSA, v. 27, n. 16, p. 3614–3622, 08 2009. Cited on page 83.
- LEVEN, A.; KANEDA, N.; KOC, U.-V.; CHEN, Y.-K. Frequency estimation in intradyne reception. *IEEE Photonics Technology Letters*, v. 19, n. 6, p. 366–368, 03 2007. Cited on page 73.
- LI, J.; LI, L.; TAO, Z.; HOSHIDA, T.; RASMUSSEN, J. C. Laser-linewidth-tolerant feed-forward carrier phase estimator with reduced complexity for qam. *Journal of Lightwave Technology*, v. 29, n. 16, p. 2358–2364, 08 2011. ISSN 0733-8724. Cited on page 93.
- LOBATO, A.; FERREIRA, F.; KUSCHNEROV, M.; BORNE, D. van den; JANSEN, S. L.; NAPOLI, A.; SPINLER, B.; LANKL, B. Impact of mode coupling on the mode-dependent loss tolerance in few-mode fiber transmission. *Optics express*, Optical Society of America, v. 20, n. 28, p. 29776–29783, 2012. Cited 2 times on pages 62 and 138.
- LUIS, R. S.; PUTTNAM, B. J.; RADEMACHER, G.; AWAJI, Y.; FURUKAWA, H. 372 Tb/s unrepeated 213 km transmission over a 125 μm cladding diameter, 4-core MCF. In: OPTICA PUBLISHING GROUP. *Optical Fiber Communication Conference*. [S.l.], 2022. p. M4B–3. Cited on page 34.
- LUN, H.; FU, M.; LIU, X.; WU, Y.; YI, L.; HU, W.; ZHUGE, Q. Soft failure identification for long-haul optical communication systems based on one-dimensional convolutional neural network. *Journal of Lightwave Technology*, IEEE, v. 38, n. 11, p. 2992–2999, 2020. Cited on page 133.
- MAIMAN, T. H. *et al.* Stimulated optical radiation in ruby. 1960. Cited on page 32.
- MCKAY, M. R.; COLLINGS, I. B.; TULINO, A. M. Achievable sum rate of mimo mmse receivers: A general analytic framework. *IEEE Transactions on Information Theory*, IEEE, v. 56, n. 1, p. 396–410, 2009. Cited 2 times on pages 111 and 116.
- MEARS, R. J.; REEKIE, L.; JAUNCEY, I.; PAYNE, D. N. Low-noise erbium-doped fibre amplifier operating at 1.54 μm . *Electronics Letters*, IET, v. 23, n. 19, p. 1026–1028, 1987. Cited on page 33.
- MELLO, D.; OSPINA, R.; SRINIVAS, H.; CHOUTAGUNTA, K.; CHOU, E.; KAHN, J. Impact and mitigation of mode-dependent gain in ultra-long-haul SDM systems. In: OPTICAL SOCIETY OF AMERICA. *Optical Fiber Communication Conference*. [S.l.], 2022. p. 1–3. Cited on page 116.
- MELLO, D. A.; SRINIVAS, H.; CHOUTAGUNTA, K.; KAHN, J. M. Impact of polarization-and mode-dependent gain on the capacity of ultra-long-haul systems. *Journal of Lightwave Technology*, IEEE, v. 38, n. 2, p. 303–318, 2019. Cited 6 times on pages 35, 103, 105, 110, 134, and 139.
- MELLO, D. A. de A.; BARBOSA, F. A. *Digital Coherent Optical Systems: Architecture and Algorithms*. [S.l.]: Springer Nature, 2021. Cited 4 times on pages 9, 52, 55, and 69.
- MEYR, H.; MOENECLAËY, M.; FECHTEL, S. A. *Digital Communication Receivers*. First. [S.l.]: John Wiley and Sons, Inc., 1998. Cited on page 42.

- MIYA, T.; TERUNUMA, Y.; HOSAKA, T.; MIYASHITA, T. Ultimate low-loss single-mode fibre at 1.55 μm . *Electronics Letters*, IET, v. 15, n. 4, p. 106–108, 1979. Cited on page 32.
- MIZUNO, T.; TAKARA, H.; SHIBAHARA, K.; MIYAMOTO, Y.; OGUMA, M.; ONO, H.; ABE, Y.; MATSUI, T.; MATSUO, S.; SAITOH, K. *et al.* Mode dependent loss equaliser and impact of MDL on PDM-16QAM few-mode fibre transmission. In: IEEE. *2015 European Conference on Optical Communication (ECOC)*. [S.l.], 2015. p. 1–3. Cited on page 120.
- MOORADIAN, A. *External cavity semiconductor laser*. [S.l.]: Google Patents, 1991. US Patent 5,050,179. Cited on page 45.
- MORI, T.; SAKAMOTO, T.; WADA, M.; YAMAMOTO, T.; YAMAMOTO, F. Low dmd four LP mode transmission fiber for wide-band WDM-MIMO system. In: OPTICAL SOCIETY OF AMERICA. *Optical Fiber Communication Conference*. [S.l.], 2013. p. OTh3K–1. Cited on page 71.
- MORI, Y.; ZHANG, C.; KIKUCHI, K. Novel configuration of finite-impulse-response filters tolerant to carrier-phase fluctuations in digital coherent optical receivers for higher-order quadrature amplitude modulation signals. *Optics express*, Optical Society of America, v. 20, n. 24, p. 26236–26251, 2012. Cited 5 times on pages 11, 78, 88, 89, and 112.
- MROZIEWICZ, B.; BUGAJSKI, M.; NAKWASKI, W. *Physics of semiconductor lasers*. [S.l.]: Elsevier, 2017. Cited on page 45.
- NAGAYAMA, K.; KAKUI, M.; MATSUI, M.; SAITOH, I.; CHIGUSA, Y. Ultra-low-loss (0.1484 dB/km) pure silica core fibre and extension of transmission distance. *Electronics Letters*, v. 38, n. 20, p. 1168–1169, 09 2002. ISSN 0013-5194. Cited on page 56.
- NAMIKI, S.; SEO, K.; TSUKIJI, N.; SHIKII, S. Challenges of raman amplification. *Proceedings of the IEEE*, IEEE, v. 94, n. 5, p. 1024–1035, 2006. Cited on page 62.
- ONISHI, M.; KOYANO, Y.; SHIGEMATSU, M.; KANAMORI, H.; NISHIMURA, M. Dispersion compensating fibre with a high figure of merit of 250 ps/nm/db. *Electronics Letters*, IET, v. 30, n. 2, p. 161–163, 1994. Cited on page 32.
- OSPINA, R. S.; HOUT, M. Van den; ALVARADO-ZACARIAS, J. C.; ANTONIO-LÓPEZ, J. E.; BIGOT-ASTRUC, M.; CORREA, A. A.; SILLARD, P.; AMEZCUA-CORREA, R.; OKONKWO, C.; MELLO, D. A. Mode-dependent loss and gain estimation in SDM transmission based on MMSE equalizers. *Journal of Lightwave Technology*, IEEE, v. 39, n. 7, p. 1968–1975, 2020. Cited 3 times on pages 129, 139, and 147.
- OSPINA, R. S.; HOUT, M. van den; HEIDE, S. van der; WEERDENBURG, J. van; RYF, R.; FONTAINE, N. K.; CHEN, H.; AMEZCUA-CORREA, R.; OKONKWO, C.; MELLO, D. A. MDG and SNR estimation in SDM transmission based on artificial neural networks. *Journal of Lightwave Technology*, IEEE, v. 40, n. 15, p. 5021–5030, 2022. Cited on page 133.
- OSPINA, R. S.; HOUT, M. van den; OKONKWO, C.; MELLO, D. A. Mode-dependent loss and gain emulation in coupled sdm transmission. In: *XXXVIII Simpósio Brasileiro*

de Telecomunicações e Processamento de Sinais (SBrT 2020). [S.l.: s.n.], 2020. p. 1–4. Cited on page 124.

OSPINA, R. S.; OKONKWO, C.; MELLO, D. A. DSP-based mode-dependent loss and gain estimation in coupled SDM transmission. In: OPTICAL SOCIETY OF AMERICA. *Optical Fiber Communication Conference*. [S.l.], 2020. p. W2A–47. Cited 2 times on pages 112 and 139.

OSPINA, R. S.; SANTOS, L. F. dos; MELLO, D. A.; FERREIRA, F. M. Scanning-based chromatic dispersion estimation in mode-multiplexed optical systems. In: IEEE. *2019 21st International Conference on Transparent Optical Networks (ICTON)*. [S.l.], 2019. p. 1–4. Cited on page 146.

OSPINA, R. S. B.; HOUT, M. van den; HEIDE, S. van der; OKONKWO, C.; MELLO, D. A. A. Neural-network-based MDG and optical snr estimation in SDM transmission. In: *Optical Fiber Communication Conference (OFC) 2021*. Optica Publishing Group, 2021. p. Th1A.20. Disponível em: <<http://opg.optica.org/abstract.cfm?URI=OFC-2021-Th1A.20>>. Cited 2 times on pages 133 and 136.

PFAU, T. *Development and real-time implementation of digital signal processing algorithms for coherent optical receivers*. Tese (Doutorado) — Paderborn University, 2009. Cited on page 92.

PFAU, T.; HOFFMANN, S.; NOE, R. Hardware-efficient coherent digital receiver concept with feedforward carrier recovery for m -qam constellations. *Journal of Lightwave Technology*, v. 27, n. 8, p. 989–999, 04 2009. ISSN 0733-8724. Cited 3 times on pages 83, 91, and 93.

POOLE, C. D.; WAGNER, R. E. Phenomenological approach to polarisation dispersion in long single-mode fibres. *Electronics Letters*, v. 22, n. 19, p. 1029–1030, 09 1986. ISSN 0013-5194. Cited on page 57.

PUTTNAM, B. J.; RADEMACHER, G.; LUÍS, R. S.; ERIKSSON, T. A.; KLAUS, W.; AWAJI, Y.; WADA, N.; MAEDA, K.; TAKASAKA, S.; SUGIZAKI, R. 0.715 Pb/s transmission over 2,009.6 km in 19-core cladding pumped EDFA amplified MCF link. In: OPTICAL SOCIETY OF AMERICA. *Optical Fiber Communication Conference*. [S.l.], 2019. p. Th4B–1. Cited on page 64.

RADEMACHER, G.; LUIS, R.; PUTTNAM, B.; FONTAINE, N.; MAZUR, M.; CHEN, H.; RYF, R.; NEILSON, D.; DAHL, D.; CARPENTER, J.; SILLARD, P.; ACHTEN, F.; BIGOT, M.; SAKAGUCHI, J.; FURUKAWA, H. 1.53 Peta-bit/s C-band transmission in a 55-mode fiber. In: IEEE. *2022 European Conference on Optical Communication (ECOC)*. [S.l.], 2022. p. 1–3. Cited 5 times on pages 15, 34, 147, 148, and 149.

RADEMACHER, G.; LUÍS, R. S.; PUTTNAM, B. J.; RYF, R.; HEIDE, S. van der; ERIKSSON, T. A.; FONTAINE, N. K.; CHEN, H.; ESSIAMBRE, R.-J.; AWAJI, Y. *et al.* High capacity transmission in a coupled-core three-core multi-core fiber. *Journal of Lightwave Technology*, IEEE, v. 39, n. 3, p. 757–762, 2020. Cited 2 times on pages 35 and 72.

RADEMACHER, G.; LUÍS, R. S.; PUTTNAM, B. J.; RYF, R.; HEIDE, S. Van der; ERIKSSON, T. A.; FONTAINE, N. K.; CHEN, H.; ESSIAMBRE, R.-J.; AWAJI, Y. *et al.* A comparative study of few-mode fiber and coupled-core multi-core fiber

transmission. *Journal of Lightwave Technology*, IEEE, v. 40, n. 6, p. 1590–1596, 2022. Cited on page 34.

RADEMACHER, G.; PUTTNAM, B. J.; LUÍS, R. S.; SAKAGUCHI, J.; KLAUS, W.; ERIKSSON, T. A.; AWAJI, Y.; HAYASHI, T.; NAGASHIMA, T.; NAKANISHI, T. *et al.* Highly spectral efficient C+L-band transmission over a 38-core-3-mode fiber. *Journal of Lightwave Technology*, IEEE, v. 39, n. 4, p. 1048–1055, 2020. Cited on page 116.

RADEMACHER, G.; PUTTNAM, B. J.; LUÍS, R. S.; SAKAGUCHI, J.; KLAUS, W.; ERIKSSON, T. A.; AWAJI, Y.; HAYASHI, T.; NAGASHIMA, T.; NAKANISHI, T. *et al.* 10.66 peta-bit/s transmission over a 38-core-three-mode fiber. In: OPTICAL SOCIETY OF AMERICA. *Optical Fiber Communication Conference*. [S.l.], 2020. p. Th3H–1. Cited 2 times on pages 103 and 111.

RADEMACHER, G.; RYF, R.; FONTAINE, N. K.; CHEN, H.; ESSIAMBRE, R.-J.; PUTTNAM, B. J.; LUIS, R. S.; AWAJI, Y.; WADA, N.; GROSS, S. *et al.* Long-haul transmission over few-mode fibers with space-division multiplexing. *Journal of Lightwave Technology*, IEEE, v. 36, n. 6, p. 1382–1388, 2017. Cited 3 times on pages 71, 103, and 111.

RAMAN, C. V. A change of wave-length in light scattering. *Nature*, v. 121, p. 619, 04 1928. Cited on page 59.

RAMASWAMI, R.; SIVARAJAN, K. N.; SASAKI, G. H. *Optical Networks, A Practical Perspective*. Third. [S.l.]: ELSEVIER Inc, 2010. Cited 9 times on pages 9, 44, 45, 49, 58, 60, 62, 63, and 66.

RANDEL, S.; MESTRE, M. A.; RYF, R.; WINZER, P. J. Digital signal processing in spatially multiplexed coherent communications. In: IEEE. *2012 38th European Conference and Exhibition on Optical Communications*. [S.l.], 2012. p. 1–3. Cited on page 147.

RANDEL, S.; RYF, R.; GNAUCK, A.; MESTRE, M. A.; SCHMIDT, C.; ESSIAMBRE, R.-J.; WINZER, P.; DELBUE, R.; PUPALAIKIS, P.; SUREKA, A. *et al.* Mode-multiplexed 6 x 20-GBd QPSK transmission over 1200-km DGD-compensated few-mode fiber. In: OPTICAL SOCIETY OF AMERICA. *Optical Fiber Communication Conference*. [S.l.], 2012. p. 1–3. Cited on page 71.

RASHLEIGH, S. C.; ULRICH, R. Polarization mode dispersion in single-mode fibers. *Opt. Lett.*, OSA, v. 3, n. 2, p. 60–62, 08 1978. Disponível em: <<http://ol.osa.org/abstract.cfm?URI=ol-3-2-60>>. Cited on page 57.

RENNER, H. Bending losses of coated single-mode fibers: a simple approach. *Journal of Lightwave technology*, IEEE, v. 10, n. 5, p. 544–551, 1992. Cited on page 56.

RICHARDSON, D. New optical fibres for high-capacity optical communications. *Phil. Trans. R. Soc. A*, The Royal Society, v. 374, n. 2062, p. 20140441, 2016. Cited 5 times on pages 9, 33, 47, 70, and 71.

RYF, R.; ALVARADO-ZACARIAS, J. C.; WITTEK, S.; FONTAINE, N. K.; ESSIAMBRE, R.-J.; CHEN, H.; AMEZCUA-CORREA, R.; SAKUMA, H.; HAYASHI, T.; HASEGAWA, T. Coupled-core transmission over 7-core fiber. In: OPTICAL SOCIETY OF AMERICA. *Optical Fiber Communication Conference*. [S.l.], 2019. p. Th4B–3. Cited 3 times on pages 35, 71, and 114.

- RYF, R.; ESSIAMBRE, R.; GNAUCK, A.; RANDEL, S.; MESTRE, M. A.; SCHMIDT, C.; WINZER, P.; DELBUE, R.; PUPALAIKIS, P.; SUREKA, A. *et al.* Space-division multiplexed transmission over 4200 km 3-core microstructured fiber. In: OPTICAL SOCIETY OF AMERICA. *National Fiber Optic Engineers Conference*. [S.l.], 2012. p. PDP5C-2. Cited on page 34.
- RYF, R.; ESSIAMBRE, R.-J.; RANDEL, S.; GNAUCK, A.; WINZER, P.; HAYASHI, T.; TARU, T.; SASAKI, T. MIMO-based crosstalk suppression in spatially multiplexed 3×56-Gb/s PDM-QPSK signals for strongly coupled three-core fiber. *IEEE Photonics Technology Letters*, IEEE, v. 23, n. 20, p. 1469–1471, 2011. Cited on page 71.
- RYF, R.; FONTAINE, N. K.; ESSIAMBRE, R.-J. Spot-based mode couplers for mode-multiplexed transmission in few-mode fiber. *IEEE Photonics Technology Letters*, IEEE, v. 24, n. 21, p. 1973–1976, 2012. Cited on page 48.
- RYF, R.; FONTAINE, N. K.; MESTRE, M. A.; RANDEL, S.; PALOU, X.; BOLLE, C.; GNAUCK, A. H.; CHANDRASEKHAR, S.; LIU, X.; GUAN, B. *et al.* 12× 12 MIMO transmission over 130-km few-mode fiber. In: OPTICAL SOCIETY OF AMERICA. *Frontiers in Optics*. [S.l.], 2012. p. FW6C-4. Cited on page 39.
- RYF, R.; RANDEL, S.; GNAUCK, A. H.; BOLLE, C.; SIERRA, A.; MUMTAZ, S.; ESMAEELPOUR, M.; BURROWS, E. C.; ESSIAMBRE, R.-J.; WINZER, P. J. *et al.* Mode-division multiplexing over 96 km of few-mode fiber using coherent 6 × 6 MIMO processing. *Journal of Lightwave technology*, IEEE, v. 30, n. 4, p. 521–531, 2011. Cited on page 48.
- RYF, R.; RANDEL, S.; GNAUCK, A. H.; BOLLE, C.; ESSIAMBRE, R.-J.; WINZER, P.; PECKHAM, D. W.; MCCURDY, A.; LINGLE, R. Space-division multiplexing over 10 km of three-mode fiber using coherent 6× 6 MIMO processing. In: OPTICAL SOCIETY OF AMERICA. *National Fiber Optic Engineers Conference*. [S.l.], 2011. p. PDPB10. Cited on page 34.
- SABRA, A. I. *Theories of Light - From Descartes to Newton*. Cambridge University Press, 1981. ISBN 9780521284363. Disponível em: <<http://gen.lib.rus.ec/book/index.php?md5=3240E97754F9312E8DBC224921D50C2>>. Cited on page 58.
- SAIF, W.; ESMAIL, M. A.; RAGHEB, A.; ALSHAWI, T.; ALSHEBEILI, S. Machine learning techniques for optical performance monitoring and modulation format identification: A survey. *IEEE Communications Surveys & Tutorials*, IEEE, 2020. Cited 2 times on pages 132 and 133.
- SAIF, W. S.; RAGHEB, A. M.; ALSHAWI, T. A.; ALSHEBEILI, S. A. Optical performance monitoring in mode division multiplexed optical networks. *Journal of Lightwave Technology*, IEEE, v. 39, n. 2, p. 491–504, 2021. Cited 3 times on pages 35, 132, and 133.
- SAIF, W. S.; RAGHEB, A. M.; SELEEM, H. E.; ALSHAWI, T. A.; ALSHEBEILI, S. A. Modulation format identification in mode division multiplexed optical networks. *IEEE Access*, IEEE, v. 7, p. 156207–156216, 2019. Cited 2 times on pages 35 and 133.
- SAITOH, K.; MATSUO, S. Multicore fiber technology. *Journal of Lightwave Technology*, IEEE, v. 34, n. 1, p. 55–66, 2016. Cited on page 34.

- SAKAMOTO, T.; AOZASA, S.; MORI, T.; WADA, M.; YAMAMOTO, T.; NOZOE, S.; SAGAE, Y.; TSUJIKAWA, K.; NAKAJIMA, K. Randomly-coupled single-mode 12-core fiber with highest core density. In: IEEE. *2017 Optical Fiber Communications Conference and Exhibition (OFC)*. [S.l.], 2017. p. 1–3. Cited on page 71.
- SALEH, M. C. T. B. E. A. *Fundamentals of photonics*. 1st. ed. Wiley, 1991. (Wiley series in pure and applied optics). ISBN 0471839655,9780585321479,9780471839651. Disponível em: <<http://gen.lib.rus.ec/book/index.php?md5=323CF22AA48243FC4ADAB2D63E31EE60>>. Cited 2 times on pages 55 and 83.
- SANTOS, L. F. D.; FERREIRA, F. M.; ELLIS, A. D.; MELLO, D. A. Filter bank multi-sub-band transmission for optical systems with mode multiplexing. *IEEE Photonics Journal*, IEEE, v. 11, n. 2, p. 1–12, 2019. Cited on page 147.
- SANTOS, L. F. dos; FERREIRA, F. M.; MELLO, D. A. Sub-band-based transmission for mode-multiplexed optical systems. In: IEEE. *2017 19th International Conference on Transparent Optical Networks (ICTON)*. [S.l.], 2017. p. 1–4. Cited on page 145.
- SASAKI, Y.; TAKENAGA, K.; AIKAWA, K.; MIYAMOTO, Y.; MORIOKA, T. Single-mode 37-core fiber with a cladding diameter of 248 μm . In: IEEE. *2017 Optical Fiber Communications Conference and Exhibition (OFC)*. [S.l.], 2017. p. 1–3. Cited on page 71.
- SAVORY, S. J. Digital filters for coherent optical receivers. *Optics Express*, OSA, v. 16, n. 2, p. 804–817, 01 2008. Cited 3 times on pages 83, 144, and 147.
- SAYED, A. H. *Adaptive filters*. [S.l.]: John Wiley & Sons, 2011. Cited on page 87.
- SELMİ, M.; JAOUEN, Y.; CIBLAT, P. Accurate digital frequency offset estimator for coherent polmux qam transmission systems. In: *2009 35th European Conference on Optical Communication*. [S.l.: s.n.], 2009. p. 1–2. ISSN 1550-381X. Cited on page 82.
- SHALEV-SHWARTZ, S.; BEN-DAVID, S. *Understanding machine learning: From theory to algorithms*. [S.l.]: Cambridge university press, 2014. Cited on page 132.
- SHAPIRO, A. E. Newton's definition of a light ray and the diffusion theories of chromatic dispersion. *The University of Chicago Press Journals*, v. 66, n. 2, p. 194–210, 06 1975. Cited on page 58.
- SHEMIRANI, M. B.; MAO, W.; PANICKER, R. A.; KAHN, J. M. Principal modes in graded-index multimode fiber in presence of spatial-and polarization-mode coupling. *Journal of Lightwave Technology*, IEEE, v. 27, n. 10, p. 1248–1261, 2009. Cited 2 times on pages 34 and 61.
- SHIBAHARA, K.; LEE, D.; KOBAYASHI, T.; MIZUNO, T.; TAKARA, H.; SANO, A.; KAWAKAMI, H.; MIYAMOTO, Y.; ONO, H.; OGUMA, M. *et al.* Dense SDM (12-core X 3-mode) transmission over 527 km with 33.2-ns mode-dispersion employing low-complexity parallel MIMO frequency-domain equalization. *Journal of Lightwave Technology*, IEEE, v. 34, n. 1, p. 196–204, 2016. Cited on page 84.

- SHIBAHARA, K.; MIZUNO, T.; KAWAKAMI, H.; KOBAYASHI, T.; NAKAMURA, M.; SHIKAMA, K.; NAKAJIMA, K.; MIYAMOTO, Y. Full c-band 3060-km dmd-unmanaged 3-mode transmission with 40.2-tb/s capacity using cyclic mode permutation. *Journal of Lightwave Technology*, IEEE, v. 38, n. 2, p. 514–521, 2020. Cited on page 35.
- SHYMK, J. J. *et al.* Frequency-domain and multirate adaptive filtering. *IEEE Signal processing magazine*, v. 9, n. 1, p. 14–37, 1992. Cited on page 85.
- SILLARD, P.; BENYAHYA, K.; SOMA, D.; LABROILLE, G.; JIAN, P.; IGARASHI, K.; RYF, R.; FONTAINE, N. K.; RADEMACHER, G.; SHIBAHARA, K. Few-mode fiber technology, deployments, and systems. *Proceedings of the IEEE*, IEEE, 2022. Cited on page 34.
- SILLARD, P.; MOLIN, D.; BIGOT-ASTRUC, M.; AMEZCUA-CORREA, A.; JONGH, K. de; ACHTEN, F. 50 μm multimode fibers for mode division multiplexing. *Journal of Lightwave Technology*, IEEE, v. 34, n. 8, p. 1672–1677, 2016. Cited 2 times on pages 125 and 129.
- SILLARD, P.; MOLIN, D.; BIGOT-ASTRUC, M.; JONGH, K. D.; ACHTEN, F.; VELÁZQUEZ-BENÍTEZ, A. M.; AMEZCUA-CORREA, R.; OKONKWO, C. M. Low-differential-mode-group-delay 9-lp-mode fiber. *Journal of Lightwave Technology*, IEEE, v. 34, n. 2, p. 425–430, 2016. Cited on page 71.
- SILVA, E. P. da; ZIBAR, D. Widely linear equalization for IQ imbalance and skew compensation in optical coherent receivers. *Journal of Lightwave Technology*, IEEE, v. 34, n. 15, p. 3577–3586, 2016. Cited on page 123.
- SOMA, D.; WAKAYAMA, Y.; BEPPU, S.; SUMITA, S.; TSURITANI, T.; HAYASHI, T.; NAGASHIMA, T.; SUZUKI, M.; TAKAHASHI, H.; IGARASHI, K. *et al.* 10.16 peta-bit/s dense SDM/WDM transmission over low-DMD 6-mode 19-core fibre across C+L band. In: IEEE. *2017 European Conference on Optical Communication (ECOC)*. [S.l.], 2017. p. 1–3. Cited on page 72.
- SORIANO, R. A.; HAUSKE, F. N.; GONZALEZ, N. G.; ZHANG, Z.; YE, Y.; MONROY, I. T. Chromatic dispersion estimation in digital coherent receivers. *Journal of Lightwave Technology*, IEEE, v. 29, n. 11, p. 1627–1637, 2011. Cited 2 times on pages 141 and 142.
- TAYLOR, M. G. Coherent detection method using dsp for demodulation of signal and subsequent equalization of propagation impairments. *IEEE Photonics Technology Letters*, IEEE, v. 16, n. 2, p. 674–676, 2004. Cited on page 33.
- TESSIER, R.; BURLESON, W. Reconfigurable computing for digital signal processing: A survey. *Journal of VLSI signal processing systems for signal, image and video technology*, Springer, v. 28, p. 7–27, 2001. Cited on page 90.
- TROPPER, A. C.; FOREMAN, H. D.; GARNACHE, A.; WILCOX, K. G.; HOOGLAND, S. H. Vertical-external-cavity semiconductor lasers. *Journal of Physics D: Applied Physics*, v. 37, n. 9, p. R75, 2004. Disponível em: <<http://stacks.iop.org/0022-3727/37/i=9/a=R01>>. Cited on page 45.
- UDEN, R. G. H. van. *MIMO digital signal processing for optical spatial division multiplexed transmission systems*. Tese (Doutorado) — Ph. D. dissertation, Dept. Elect. Eng., Eindhoven Univ. Technol., Eindhoven . . . , 2014. Cited on page 88.

- UDEN, R. G. V.; OKONKWO, C. M.; CHEN, H.; WAARDT, H. de; KOONEN, A. M. Time domain multiplexed spatial division multiplexing receiver. *Optics express*, Optical Society of America, v. 22, n. 10, p. 12668–12677, 2014. Cited on page 149.
- UDEN, R. V.; CORREA, R. A.; LOPEZ, E. A.; HUIJSKENS, F.; XIA, C.; LI, G.; SCHÜLZGEN, A.; WAARDT, H. D.; KOONEN, A.; OKONKWO, C. M. Ultra-high-density spatial division multiplexing with a few-mode multicore fibre. *Nature Photonics*, Nature Publishing Group, v. 8, n. 11, p. 865, 2014. Cited on page 123.
- VELÁZQUEZ-BENÍTEZ, A. M.; ANTONIO-LÓPEZ, J. E.; ALVARADO-ZACARÍAS, J. C.; FONTAINE, N. K.; RYF, R.; CHEN, H.; HERNÁNDEZ-CORDERO, J.; SILLARD, P.; OKONKWO, C.; LEON-SAVAL, S. G. *et al.* Scaling photonic lanterns for space-division multiplexing. *Scientific reports*, Nature Publishing Group, v. 8, n. 1, p. 1–9, 2018. Cited 3 times on pages 47, 121, and 122.
- WADA, M.; SAKAMOTO, T.; AOZASA, S.; MORI, T.; YAMAMOTO, T.; NAKAJIMA, K. Core-pumped 10-mode edfa with cascaded edf configuration. In: VDE. *ECOC 2016; 42nd European Conference on Optical Communication*. [S.l.], 2016. p. 1–3. Cited on page 64.
- WAKAYAMA, Y.; IGARASHI, K.; SOMA, D.; TAGA, H.; TSURITANI, T. Novel 6-mode fibre amplifier with large erbium-doped area for differential modal gain minimization. In: VDE. *ECOC 2016; 42nd European Conference on Optical Communication*. [S.l.], 2016. p. 1–3. Cited on page 64.
- WANG, D.; LU, C.; LAU, A. P. T.; HE, S. Adaptive chromatic dispersion compensation for coherent communication systems using delay-tap sampling technique. *IEEE Photonics Technology Letters*, IEEE, v. 23, n. 14, p. 1016–1018, 2011. Cited 2 times on pages 141 and 142.
- WAUTELET, X.; HERZET, C.; DEJONGHE, A.; LOUVEAUX, J.; VANDENDORPE, L. Comparison of em-based algorithms for MIMO channel estimation. *IEEE Transactions on communications*, IEEE, v. 55, n. 1, p. 216–226, 2007. Cited 3 times on pages 102, 116, and 135.
- WEERDENBURG, J. van; RYF, R.; ALVARADO-ZACARIAS, J. C.; ALVAREZ-AGUIRRE, R. A.; FONTAINE, N. K.; CHEN, H.; AMEZCUA-CORREA, R.; KOONEN, T.; OKONKWO, C. 138 Tbit/s transmission over 650 km graded-index 6-mode fiber. In: IEEE. *2017 European Conference on Optical Communication (ECOC)*. [S.l.], 2017. p. 1–3. Cited 2 times on pages 35 and 103.
- WEERDENBURG, J. van; RYF, R.; ALVARADO-ZACARIAS, J. C.; ALVAREZ-AGUIRRE, R. A.; FONTAINE, N. K.; CHEN, H.; AMEZCUA-CORREA, R.; SUN, Y.; GRÜNER-NIELSEN, L.; JENSEN, R. V. *et al.* 138-Tb/s mode-and wavelength-multiplexed transmission over six-mode graded-index fiber. *Journal of Lightwave Technology*, IEEE, v. 36, n. 6, p. 1369–1374, 2018. Cited 5 times on pages 11, 70, 98, 103, and 111.
- WEINBERGER, P. John kerr and his effects found in 1877 and 1878. *Philosophical Magazine Letters*, Taylor & Francis, v. 88, n. 12, p. 897–907, 2008. Cited on page 60.
- WIDROW, B.; HOFF, M. E. *Adaptive switching circuits*. [S.l.], 1960. Cited on page 87.

WINZER, P. J. Making spatial multiplexing a reality. *Nature Photonics*, Nature Publishing Group, v. 8, n. 5, p. 345, 2014. Cited 2 times on pages 33 and 39.

WINZER, P. J.; FOSCHINI, G. J. MIMO capacities and outage probabilities in spatially multiplexed optical transport systems. *Optics express*, Optical Society of America, v. 19, n. 17, p. 16680–16696, 2011. Cited 3 times on pages 35, 103, and 109.

WYSOCKI, P.; MAZURCZYK, V. Polarization dependent gain in erbium-doped fiber amplifiers: computer model and approximate formulas. *Journal of lightwave technology*, IEEE, v. 14, n. 4, p. 572–584, 1996. Cited on page 64.

XIA, C.; BAI, N.; AMEZCUA-CORREA, R.; ANTONIO-LOPEZ, E.; SCHULZGEN, A.; RICHARDSON, M.; ZHOU, X.; LI, G. Supermodes in strongly-coupled multi-core fibers. In: IEEE. *Optical Fiber Communication Conference and Exposition and the National Fiber Optic Engineers Conference (OFC/NFOEC), 2013*. [S.l.], 2013. p. 1–3. Cited on page 34.

XIE, C. Chromatic dispersion estimation for single-carrier coherent optical communications. *IEEE Photonics Technology Letters*, IEEE, v. 25, n. 10, p. 992–995, 2013. Cited 3 times on pages 141, 142, and 143.

XU, T.; JACOBSEN, G.; POPOV, S.; LI, J.; VANIN, E.; WANG, K.; FRIBERG, A. T.; ZHANG, Y. Chromatic dispersion compensation in coherent transmission system using digital filters. *Optics Express*, OSA, v. 18, n. 15, p. 16243–16257, 07 2010. Cited on page 83.

YEN, H.; NAKAMURA, M.; GARMIRE, E.; SOMEKH, S.; YARIV, A.; GARVIN, H. Optically pumped gas waveguide lasers with a fundamental 0.11μ corrugation feedback. *Optics Communications*, Elsevier, v. 9, n. 1, p. 35–37, 1973. Cited on page 45.

ZHOU, X. Efficient clock and carrier recovery algorithms for single-carrier coherent optical systems: A systematic review on challenges and recent progress. *IEEE Signal Processing Magazine*, v. 31, n. 2, p. 35–45, 03 2014. ISSN 1053-5888. Cited 2 times on pages 83 and 93.